Quantitative analysis of apoptotic decisions in single cells and cell populations

by

John G. Albeck

B.A., Biological Sciences
Cornell University, 2000

Submitted to the Department of Biology in partial fulfillment of the requirements for the degree of

Doctor of Philosophy in Biology
at the
Massachusetts Institute of Technology

February 2007

Signature of Author: _____
Department of Biology
February 6, 2007

Certified by: _____
Peter K. Sorger
Professor of Biology and Biological Engineering
Thesis Supervisor

Accepted by: _____
Stephen P. Bell
Professor of Biology
Chairman, Committee for Graduate Students

Quantitative analysis of apoptotic decisions
in single cells and cell populations

by

John G. Albeck

Submitted to the Department of Biology on February 6, 2007
in partial fulfillment of the requirements
for the degree of Doctor of Philosophy in Biology

Abstract

Apoptosis is a form of programmed cell death that is essential for the elimination of damaged or unneeded cells in multicellular organisms. Inactivation of apoptotic cell death is a necessary step in the development of cancer, while hypersensitivity to apoptosis is a factor in degenerative diseases. Many of the molecular components controlling apoptosis have been identified, including the central effectors of apoptosis, a family of proteases known as caspases that efficiently dismantle the cell when active. While many of the molecular details of apoptotic regulators are now understood, a major challenge is to integrate this information to understand quantitatively how sensitivity to apoptosis and the kinetics of death are determined, in both single cells and populations of cells. We have approached this problem with a combined experimental and computational approach. Using single-cell observations, genetic and pharmacological perturbations, and mechanistic mathematical modeling, we have dissected the mechanism by which cells make a binary decision between survival and apoptosis. We identified conditions under which the apoptotic decision system fails, allowing cells to survive with caspase-induced damage that may result in damage to the genome and oncogenesis. We further used live-cell imaging to identify and characterize a kinetic threshold at which slow and variable upstream signals are converted into rapid and discrete downstream caspase activation. Lastly, we examined the integration of multiple pro-and apoptotic signal transduction pathways by constructing a principal component-based model that linked apoptotic phenotypes to a compendium of signaling measurements. This approach enabled the identification of the molecular signals most important in determining the level of apoptosis across a population of cells. Together, our findings provide insight into the molecular and kinetic mechanisms by which cells integrate diverse molecular signals to make a discrete cell fate decision.

Thesis Supervisor: Peter K. Sorger
Title: Professor of Biology, Professor of Biological Engineering

Table of Contents

John G. Albeck

Education

Massachusetts Institute of Technology, Cambridge, MA
Ph.D. in Biology, expected 2006

Cornell University, Ithaca, NY
B.A. in Biological Sciences, 2000

Research Experience

Graduate Research, 2001-present
Advisor: Peter Sorger, MIT

Undergraduate Research, 1998-2000
Advisor: Richard Cerione, Cornell University

Undergraduate Research, Summer 1998
Advisor: Lonny Levin, Weill Cornell Medical College.

Teaching Experience

Spring, 2002: Teaching Assistant, Project Lab (7.16), MIT

Spring 2004: Teaching Assistant, Fundamental Limits of Biological Measurement (BEH.481), MIT

Spring 2004, 2005: Guest lecturer on "Apoptosis in Mammalian Cells", Project Lab (7.16), MIT

Awards and Honors

Magna cum laude in Biological Sciences, Cornell University, 2000
Phi Beta Kappa Society, 2000
John S. Knight Writing Award, Cornell University, 1997

Publications

Albeck J.G., Burke J.M., Zhang M., Lauffenburger D.A., and Sorger P.K. "Mathematical modeling and single-cell analysis of a snap-action feed-forward switch controlling receptor-mediated cell death." *Submitted.*

Publications (cont.)

Albeck J.G., MacBeath G., White F.M., Sorger P.K., Lauffenburger D.A., Gaudet S. (2006) "Collecting and organizing systematic sets of protein data." *Nat. Rev. Mol. Cell Biol.* 7(11):803-812.

Janes K.A., Gaudet S., Albeck J.G., Nielsen U.B., Lauffenburger D.A., and Sorger P.K. (2006) "The response of human epithelial cells to TNF involves an inducible autocrine cascade." *Cell* 124(6): 1225-1239.

Janes K.A.*, Albeck J.G.*, Gaudet S., Sorger P.K., Lauffenburger D.A., and Yaffe M.B. (2005) "A Systems Model of Signaling Identifies a Molecular Basis Set that Predicts Cytokine-Induced Apoptosis." *Science* 310(5754):1646-1653.
*These authors contributed equally to this work.

Gaudet S., Janes K.A., Albeck J.G., Pace E.A., Lauffenburger D.A., and Sorger P.K. (2005) "A compendium of signals and responses triggered by prodeath and prosurvival cytokines." *Mol. Cell. Proteomics* 10: 1569-1590.

Janes K.A., Kelly J.R., Gaudet S., Albeck J.G., Sorger P.K., and Lauffenburger D.A. (2004) "Cue-signal-response analysis of the TNF-induced apoptosis by partial least squares regression of dynamic multivariate data." *J. Comput. Biol.* 11: 544-561.

Janes K.A., Albeck J.G., Peng L.X., Sorger P.K., Lauffenburger D.A., Yaffe M.B. (2003) "A High-throughput Quantitative Multiplex Kinase Assay for Monitoring Information Flow in Signaling Networks: Application to Sepsis-Apoptosis."
Mol Cell Proteomics 2(7):463-473.

Feng Q., Albeck J.G., Cerione R.A., Yang W. (2002) "Regulation of the Cool/Pix proteins: key binding partners of the Cdc42/Rac targets, the p21-activated kinases." *J Biol Chem.* 277(7):5644-5650.

Acknowledgements

I owe a great debt of thanks to my advisor, Peter Sorger, for giving me a place in his lab, allowing me the freedom to explore my own interests, and always pushing me to take the next step forward. His endless dedication and love of science have been a great example and inspiration. I am also deeply grateful to Doug Lauffenburger for his constant enthusiastic support and tireless work to make MIT an amazing place to study quantitative biology.

I also thank my committee members Amy Keating, Chris Burge, and Drew Endy for their support, good advice, and willingness to give their time to serve on my thesis committee. You always believed in my work and supported me even when and supported my work I might have sounded crazy. I also thank Galit Lahav for graciously agreeing to participate in my thesis defense.

I am deeply indebted to Suzanne Gaudet, Kevin Janes, John Burke, Bree Aldridge, Minsheng Zhang, and Sabrina Spencer for being brilliant colleagues, the best of collaborators, and great friends throughout my time here. It has been my great privilege to work closely with such talented scientists and excellent people.

I want to thank all of my lab-mates, who have made every day in lab something to look forward to. Thanks to Paul Jasper, Rob Hagan, and Stephanie Xie for the good times we had in lab together, and the better times we had when avoiding lab together. Sean Milton, Annegret Schultze-Lutum, Aurora Burds, Emily Gillett, Jess Tytell, Peter DeWulf, Kate Leitermann, Jeremy Muhlich,and Leo Alexopoulos were great co-workers and filled our lab space with enthusiasm and good discussions. I also owe many thanks also to Viji Draviam, Dan Rines, Chris Espelin, , Ulrik Nielsen, Mike Cardone, and Andrew McAinsh for frequently offering their help and experience when I needed it.

Last, and most of all, I would like to thank my family and friends for their love and support. In particular I thank my parents, who taught me to love learning and were ever-encouraging. And finally, most of all, I thank my son Thomas and wife Alice for their constant love, support, and encouragement...without you, I never could have made it.

Chapter 1

Introduction

Chapter 1: Introduction

Table of contents

1.1 Cell death and the organism

Cell death is an essential process in the life of multicellular organisms. This fact can be easily appreciated by considering that each day in the human body, billions of new cells are created by cell division; without a corresponding subtraction of old cells, the total number of cells in the organism would quickly expand and lead to uncontrolled growth of various tissues. This balance of life and death has been appreciated by physiologists for over 100 years (Clarke and Clarke 1995) and has led, in the modern era of biology, to an intense study of the molecular mechanisms of cell death.

In animals, there are several routes to cell death (Golstein and Kroemer 2005). The most commonly recognized types of cell death are necrosis, apoptosis, and autophagy (Edinger and Thompson 2004). In general, necrosis is considered an uncontrolled form of cell death resulting from gross insults to the cell, whereas apoptosis is a more orderly process in which the cell is deliberately dismantled by a network of specific molecular effectors in response to pro-death signals from within the cell or from its environment. The role of autophagy in cell death has come to light only recently, and much remains unknown about why this adaptive response to nutrient limitation seems to serve as an alternative mechanism of cell disposal (Lum et al. 2005). These classes of cell death are not clear-cut; in many instances cells display characteristics of more than one type of cell death, such as "necroptosis" which combines features of apoptosis and necrosis (Degterev et al. 2005). It is also often observed that inhibition of one type of cell death does not prevent the cell from dying, but forces it to die by a different process (Chipuk and Green 2005). This is most strikingly observed in mice in which central effectors of apoptosis have been knocked out; although there is high embryonic mortality,

the individuals that survive to adulthood appear normal, probably because autophagic cell death compensates for the lack of apoptosis (Lindsten et al. 2000; Shimizu et al. 2004). Thus, the understanding of how cell death occurs and is regulated within living organisms continues to evolve, covering an increasingly rich spectrum of cytological processes. Nevertheless, the large majority of cell death research has focused on apoptosis and the molecules controlling it. Much is now known about this form of cell death, and its importance in development and disease is clear.

Apoptosis plays a role in controlling the shape and size of developing tissues (reviewed in (Jacobson et al. 1997)). Two frequently cited examples of this role are the development of digits and the central nervous system in mammals. In the first example, the cells between developing digits die by apoptosis, leaving each digit separate from the next (Zou and Niswander 1996). In the case of the central nervous system, many more neurons are born than will eventually make up the adult brain; the final size and connectivity of the brain is achieved by the apoptotic cell deaths of neurons that do not form proper synapses. In fact, this process is one reason for the high mortality observed in many mouse knockouts of apoptotic genes; if the number of neurons is not successfully reduced, the developing brain cannot fit inside the skull, leading to pre- or peri-natal death (Hakem et al. 1998; Kuida et al. 1998).

Apoptosis is also a factor in many diseases. The most obvious example of this is cancer, where a lack of cell death enables a hyperplasia to grow unchecked (Green and Evan 2002). Moreover, apoptosis is responsible for eliminating cells with damaged DNA; preventing apoptosis is necessary to allow damaged cells to survive and accumulate the mutations that eventually lead to malignancy (reviewed in (Zhivotovsky

and Kroemer 2004)). In the treatment of cancer, chemotherapy and radiation therapy are directed at inducing the death of tumor cells. There is much hope that by understanding the mechanisms of apoptosis, more effective means of killing cancer cells may be developed. In other disorders, excessive apoptosis can lead to degeneration of critical tissues. Some of the damage resulting from ischemia is a result of apoptosis, because cells peripheral to the site of the primary injury receive pro-death signals (Cheng et al. 1998). Pharmacological inhibitors of apoptosis are being evaluated as treatments for reducing the extent of ischemic injury to brain and cardiac tissue. Thus, there is great interest in understanding apoptosis from a clinical perspective.

1.2 Identification of cell death genes

Despite the long-standing appreciation of the necessity of cell death for homeostasis, nearly all of the specific connections between apoptosis and disease have been made only in the last 20 years. The enabling factor for these discoveries was the groundbreaking identification of a core set of genes necessary for apoptosis in the nematode worm *Caenorhabditis elegans* (Ellis and Horvitz 1986; Hengartner et al. 1992). Remarkably, the essential features of this core apoptotic machinery were found to be conserved throughout vertebrates. The first molecular link between apoptosis and cancer was made when it was discovered that the oncogene B-cell lymphoma 2 (Bcl-2) did not affect the proliferative capacity of cells but instead promoted their survival (Vaux et al. 1988). It was subsequently discovered that Bcl-2 was homologous to one of the *C. elegans* cell death genes, ced-9 (Hengartner and Horvitz 1994). Also among the cell death genes of the worm was ced-3; this gene was found to encode a cysteine protease,

leading to the identification of the caspases, the core effectors of apoptosis in all animal cells (Yuan et al. 1993).

Although much was learned from the *C elegans* cell death pathway, the apoptotic pathway in mammalian cells has turned out to be significantly more complex than the simple linear pathway found in the worm (Danial and Korsmeyer 2004). Additional families of proteins, not present in the worm, add layers of regulation to apoptosis in mammalian cells. Moreover, the families of apoptotic genes present in the worm have expanded significantly throughout evolution. In the worm, the caspase family is represented by one gene and the Bcl-2 family by two; in humans, there are 11 known caspases and over 20 Bcl-2 family proteins. In the next section, I review the major classes of apoptotic effector and regulatory proteins in mammalian cells.

1.3 The apoptosis parts list

1.3.1 Effector Caspases

Caspases- 3, -6, and -7 are known as the effector caspases, because these proteases cleave a broad set of cellular substrates to induce cell death. Caspases-3 and -7 are the most closely related and cleave very similar sets of substrates, with an optimal substrate cleavage sequence of DEVD, while caspase-6 cleaves a different set of substrates, with an optimal substrate cleavage sequence of VEID (Talanian et al. 1997; Thornberry et al. 1997). Over 300 substrates for the effector caspases have been identified, and these include proteins involved in signal transduction, metabolic regulation, DNA repair, and cellular structure (Fischer et al. 2003). One key substrate is ICAD, the inhibitor of caspase-activated DNAses. This protein is typically bound to the

DFF40/CAD, the caspase-activated DNAse; when ICAD is cleaved, CAD is released and creates double-stranded breaks in chromosomal DNA, resulting in genomic degradation (Liu et al. 1998; Inohara et al. 1999). Perhaps the best-known substrate of the effector caspases is poly-ADP-ribose polymerase (PARP), a caspase-3/7 substrate. Since this was one of the first identified effector caspase substrates, its cleavage has long been used as an indicator of caspase activity (Kaufmann 1989; Tewari et al. 1995).

Effector caspases are normally present in the cell as inactive dimers (Pop et al. 2001). The transition to the active form requires main-chain cleavage of each monomer at a site that separates the N-terminus from the C-terminus. This cleavage enables a conformational change in the caspase dimer (which is converted to a hetero-tetramer by the cleavage of each monomer) that opens the active site and increases activity by 200-fold (Tewari et al. 1995; Bose et al. 2003). The activating cleavage of effector caspases is performed by the initiator caspases (discussed below), or by granzyme B (Darmon et al. 1995; Li et al. 1997; Abreu et al. 2001). While it was long thought that effector caspases might process their own precursors autocatalytically to form a feedback amplification loop, this hypothesis has been disproven (Liu et al. 2005). However, it has been observed that effector caspases may activate certain initiator caspases (see next section), forming a more extended positive feedback loop (Slee et al. 1999; Fujita et al. 2001; Cowling and Downward 2002).

1.3.2 Initiator caspases

These caspases act mainly as signal transducers. Caspases 2, 8, 9, and 10 can be activated by numerous stimuli; once active, they activate the effector caspases as

discussed above. Initiator caspases can be activated by proteolytic cleavage (Sohn et al. 2005), but they can also be stimulated by conformational changes in the absence of cleavage when they are forced to form homo-dimers (Boatright et al. 2003; Chang et al. 2003b; Donepudi et al. 2003). In contrast to effector caspases, initiator caspases are normally monomeric, and contain one or more domains that mediate interaction with upstream regulators. These domains allow the initiator caspases to be recruited to protein complexes, where dimerization is induced and allosteric activation occurs. Several initiator caspase-activating complexes have been identified. The most well known is the apoptosome, in which the adaptor protein Apaf-1 recruits and activates caspase-9 (Li et al. 1997); this complex is stimulated by the release of cytochrome c from the mitochondria, which is discussed below. Caspase-8 is primarily activated by the Death-Inducing Signaling Complex (DISC), which is formed by death receptor activation, leading to the recruitment of the adaptor protein FADD (Kischkel et al. 1995; Medema et al. 1997). FADD recruits caspase-8 via a homotypic death effector domain (DED) interaction; allosteric activation of caspase-8 within the DISC leads to its autocatalytic processing and the release of mature, active caspase-8 into the cytosol (Chang et al. 2003a).

1.3.3 Inhibitor of Apoptosis Proteins (IAPs)

The Inhibitor of Apoptosis Proteins (IAPs) are inhibitors of caspases, that occur in many species and play a particularly important role in apoptosis in *Drosophila*. IAPs are characterized by containing one or more Baculoviral IAP repeat (BIR) domains. However, while nine BIR-containing genes have been identified in the human genome,

only one of these, X-linked inhibitor of apoptosis (XIAP), is a direct inhibitor of caspases. XIAP, containing 3 BIR domains, is a potent inhibitor of caspases-3, -7, and -9, binding to each of these caspases with a K_d of 1 nM or less (Deveraux et al. 1997). The mode of XIAP inhibition of caspase-9 differs from that of caspases-3/7. In the case of caspase-3/7, the linker region between BIR2 and BIR3 occupies the active site of the caspase, but cannot be cleaved because it lies in the opposite direction of natural peptide substrates (Huang et al. 2001; Shiozaki et al. 2003). In the case of caspase-9, XIAP binds to the homodimerization interface to prevent activation of caspase-9 by the apoptosome (Shiozaki et al. 2003). Other human IAP proteins, including ML-IAP, ILP, cIAP-1, and cIAP-2 also appear to regulate apoptosis, but are not direct inhibitors of caspases (Eckelman and Salvesen 2006) . Instead, these proteins appear to antagonize negative regulators of XIAP such as Smac (Shin et al. 2005; Vucic et al. 2005), and they may play a role in regulating the activity of the DISC. Other IAP proteins, such as Survivin, display very weak inhibition of apoptosis, and their role in regulating apoptosis is still unclear. Some IAPs, such as XIAP, also carry RING domains and have been shown to act as ubiquitin E3 ligases for the caspases they inhibit, targeting these caspases for degradation by the proteasome (Suzuki et al. 2001; Chen et al. 2003). However, IAPs also appear to regulate their own levels by auto-ubiquitination (Yang et al. 2000). The ultimate importance of these ubiquitination reactions remains unclear, but it may explain in part why proteasome inhibitors can act potently both as inhibitors and as sensitizers to apoptosis (Sohn et al. 2006).

1.3.4 Proteins of the mitochondrial intermembrane space

A number of pro-apoptotic proteins typically reside in the mitochondrial intermembrane space, where they pose no threat to the cell. However, in response to many apoptotic stimuli, the mitochondrial outer membrane undergoes a permeability transition, allowing these intermembrane space proteins to be released into the cytosol. The first such protein to be identified was cytochrome c, a component of the electron transport chain. When released into the cytosol, cytochrome c transiently interacts with Apaf-1 to induce a conformational change, allowing Apaf-1 to assemble into a complex known as the apoptosome (Li et al. 1997; Kim et al. 2005). Procaspase-9 is also recruited to the apoptosome, where it is activated by enforced dimerization. Thus, assembled apoptosome complexes act as activation platforms for procaspase-9 (Rodriguez and Lazebnik 1999). Apoptosomes assembled *in vitro* are remarkably large heptameric complexes (Yu et al. 2005); however, the stoichiometry of apoptosomes *in vivo* is likely somewhat different (Hill et al. 2004; Twiddy et al. 2004). Another important protein released from the mitochondrial compartment is Smac, which binds to XIAP to prevent XIAP from inhibiting caspases (Du et al. 2000; Verhagen et al. 2000). Other proteins, such as Omi/HtrA2 and Apoptosis Inducing Factor (AIF), are also released when mitochondrial permeabilization occurs; however, the importance of these proteins in the apoptotic program is still debated.

1.3.4 Bcl-2 family proteins

Permeability of the mitochondrial outer membrane is controlled by the Bcl-2 family of proteins. This family contains both pro- and anti-apoptotic proteins, which are identified by containing one or more Bcl-2 homology (BH) domains (Spierings et al. 2005). The pro-apoptotic members are further subdivided into effector (also known as multidomain), activator, and sensitizer categories, and the identification of these subtypes has refined the widely-held "rheostat" model of the mitochondrial pathway (Korsmeyer et al. 1993; Letai et al. 2002; Certo et al. 2006). In this model, the effectors Bax and Bak are required for the induction of large, non-selective pores in the mitochondrial outer membrane, which allow the release of proteins such as Smac and cytochrome c into the cytosol (Wei et al. 2001; Kuwana et al. 2002). To induce permeabilization, Bax and Bak must be activated by one of the activator class of pro-apoptotic Bcl-2 proteins, which include Bid and Bim (Wei et al. 2000). However, the anti-apoptotic Bcl-2 family proteins, which include Bcl-2, Bcl-X_L, and Mcl-1, block the effects of both effector and activator pro-apoptotic family members by binding to them (Oltvai et al. 1993; Cheng et al. 2001). Therefore, the levels of anti-apoptotic Bcl-2 proteins are thought to set a threshold for permeabilization; pores will be formed only when pro-apoptotic family members are in excess of the anti-apoptotic family members. However, this threshold can be altered by the sensitizer family members. Sensitizers are structurally similar to activators, containing only a single BH domain, but they cannot directly activate Bax and Bak. Instead, sensitizers bind to free anti-apoptotic Bcl-2 proteins, preventing the anti-apoptotic proteins from binding to other activators or effectors, and effectively lowering

the threshold. Together, this control system is thought to constitute the "central control point" for apoptosis (Spierings et al. 2005).

1.3.5 The death receptors

The death receptors are members of the Tumor Necrosis Factor (TNF) superfamily of receptors and include Fas (receptor for FasL), TNF-R1 and TNF-R2 (for TNFa), and DR4/DR5 (for TRAIL). Both death receptors and death ligands form homo-trimers (Smith and Baglioni 1987). Binding of a trimeric ligand to its receptor induces receptor activation, but it is not yet clear whether binding induces receptor trimerization, or instead induces a conformational change in a pre-formed receptor trimer (Siegel et al. 2000). In either case, ligand binding stimulates the recruitment to the receptor of several adaptor proteins to form the DISC (Death-inducing signaling complex)(Kischkel et al. 1995; Medema et al. 1997); interaction of receptors and adaptor proteins is mediated by homotypic interactions of death domains, which are present in both the cytoplasmic region of the receptor and in the adaptor proteins. It the cases of Fas, DR4, and DR5, the only adaptor protein recruited is FADD (Fas-associated, death domain-containing)(Chinnaiyan et al. 1995; Chaudhary et al. 1997); in the case of TNF, TRADD (TNF receptor-associated, death domain containing) is first recruited and then subsequently recruits FADD and the TRAF (TNF receptor-associated factors) family of adaptors (Rothe et al. 1994; Hsu et al. 1995; Hsu et al. 1996). Once FADD has been recruited to the DISC, it recruits caspases-8 and -10 through the homotypic interaction of death effector domains (DEDs), which occur in both FADD and in the caspase -8 and -10 prodomains. Inside the DISC, caspases-8 and -10 are first activated by conformational

changes resulting from induced dimerization (Boatright et al. 2003; Donepudi et al. 2003). Autocatalytic processing of the initiator caspases then ensues, resulting in the release of activated caspase-8 or -10 dimers into the cytosol (Chang et al. 2003a). This activation of caspase-8/10 is regulated by Flip, a protein that is highly similar to caspases-8 and -10, but which lacks catalytic activity (Irmler et al. 1997). Regulation of caspase-8/10 activation by Flip is bi-functional; at low concentrations Flip can be recruited to the DISC to serve as a dimerization partner for caspase-8 or -10, allowing activation of that caspase, but at high concentrations Flip inhibits caspase-8/10 activation by competing for binding to the DISC (Chang et al. 2002; Micheau et al. 2002).

1.4 The core pathways of apoptosis

1.4.1 The extrinsic pathway

The extrinsic apoptotic pathway refers to induction of effector caspase activity by the death ligands. In some cells, this pathway is thought to be relatively simple. Activation of the death receptor leads to DISC formation and caspase-8 activation. Caspase-8 then activates caspases-3 and -7 to kill the cell. However, in a number of cell types, this linear cascade is not sufficient for cell death (Scaffidi et al. 1998). In such cells, the mitochondrial pathway must also be activated through caspase-8/10-mediated cleavage of the pro-apoptotic Bcl-2 family protein Bid (Li et al. 1998; Luo et al. 1998). Once Bid has been cleaved, it activates Bax to induce mitochondrial permeabilization. The mitochondrial pathway is likely required either to amplify the amount of cleaved caspase-3 when caspase-8 acitivity is very weak (Scaffidi et al. 1998; Scaffidi et al. 1999), or to remove the inhibitory effect of XIAP on caspase-3 by the release of Smac

(Zhang et al. 2001; Deng et al. 2002; Li et al. 2002; Sun et al. 2002). Thus, in many cells, essentially all of the apoptotic regulators discussed above come into play when the death receptors are stimulated.

1.4.2 The intrinsic pathway

The intrinsic apoptotic pathway refers to induction of apoptosis in response to DNA damage, changes in pH, growth factor withdrawal, and other cellular stresses. In general, apoptotic signaling under these circumstances begins with the mitochondrial pathway. p53 activation in response to DNA damage or loss of growth factor signaling result in changes in the relative levels of pro- and anti-apoptotic Bcl-2 family proteins, leading to mitochondrial permeabilization (Miyashita and Reed 1995; Maurer et al. 2006). Thus, in these cases, caspases are activated only downstream of the mitochondrial release of cytochrome c and apoptosome formation. However, in heat- and stress-induced apoptosis, caspase-2 is activated upstream of the mitochondria and is required for mitochondrial permeabilization (Lassus et al. 2002; Tu et al. 2006).

1.5 Regulation of apoptosis by pro-survival signaling

The molecules discussed above consititute the central machinery responsible for either dismantling the cell or directly holding back the destructive caspases when not necessary. However, many more molecular pathways have been found to influence the entry of the cell into apoptosis. Among these molecules are kinases and transcription factors that impinge directly upon the core machinery; kinases phosphorylate and thereby alter the activity of certain components of the machinery, while transcription factors

adjust the expression levels of core components. These changes can affect the sensitivity of a cell to apoptosis, determining whether or not a given pro-apoptotic stimulus is sufficient to induce apoptosis. Thus, these pathways form an additional layer of regulation surrounding the core machinery of apoptosis. Among these pathways are some of the central signal transduction pathways of the cell, such as the mitogen-activated protein kinase (MAPK), phosphoinositide-3 kinase (PI3K), and NF-κB pathways, which also control cell growth, proliferation, and stress response. Thus, this outer layer of regulation serves to connect the apoptotic decision process to other central cellular processes. With such pervasive routes of regulation, it could be argued that few, if any, functions of the cell are not connected to apoptosis in some way.

1.5.1 The PI3K pathway

The PI3K/Akt pathway is perhaps the best-known survival signaling pathway, and it affects apoptosis through numerous connections. Akt is known to phosphorylate Bad, a Bcl-2 family pro-apoptotic sensitizer protein (Datta et al. 1997; Datta et al. 2002). When phosphorylated by Akt, Bad can be bound by 14-3-3 proteins, which sequester Bad away from the mitochondria and prevent it from exerting its pro-apoptotic effect (Datta et al. 2000). Similarly, Akt phosphorylates the Forkhead family of transcription factors; this phosphorylation results in sequestration away from the nucleus by 14-3-3 proteins (Brunet et al. 1999). Since the Forkhead family transcriptionally activates pro-apoptotic genes such as FasL, phosphorylation by Akt again produces an anti-apoptotic effect. Akt can also inactivate caspase-9 by directly phosphorylating it (Cardone et al. 1998), and can stabilize XIAP through direct phosphorylation (Dan et al. 2004). Akt can also

phosphorylate and inactivate GSK3 (Cross et al. 1995); it was recently found that GSK3 can target the anti-apoptotic Bcl-2 family member Mcl-1 for ubiquitin-mediated degradation by phosphorylating it (Maurer et al. 2006). Thus, Akt activation would lead to an increase in protective Mcl-1 levels. Together, the many anti-apoptotic functions of Akt make it a potent pro-survival signal; aberrant up-regulation of this pathway is central to the ability of tumor cells to resist apoptosis.

1.5.2 The NF-κB pathway

NF-κB is a transcription factor that upregulates numerous anti-apoptotic genes at the mRNA level. Among its transcriptional targets are XIAP, cIAP1/2, Bcl-2, and Flip (Stehlik et al. 1998; Tsukahara et al. 1999; Micheau et al. 2001). NF-κB is typically kept inactive because it is held in the cytoplasm by the constitutively bound Inhibitor of kB (IκB). However, the IκB family of kinases (IKKs) stimulate NF-κB translocation to the nucleus by phosphorylating IkB and targeting it for proteasome-mediated degradation (Ghosh and Baltimore 1990). The nuclear translocation of NF-κB leads to transcriptional activation of its target genes. This pathway is activated by numerous cytokines, such as TNF and the interleukins, and is usually associated with inflammation. Recent work has demonstrated that NF-κB can play an important role in cancer cell survival as well (reviewed in (Karin 2006)).

1.5.3 MAPK pathways

The mitogen-activated protein (MAP) kinases also play a central role in controlling apoptosis. It was initially reported that the ERK MAPK pathway played a

pro-survival role and the p38 and JNK MAPK pathways played a pro-apoptotic role (Xia et al. 1995), but subsequent studies have been conflicting. For example, the ERK 1/2 pathway is an important survival pathway; its targets include caspase-9, which it inhibits by direct phosphorylation (Allan et al. 2003), and Bad, which is a substrate of the ERK target ribosomal S6 kinase (RSK) (Bonni et al. 1999). It has also been reported that ERK inhibits death receptor signaling upstream of caspase-8, although the direct target for this function remains unknown (Tran et al. 2001; Soderstrom et al. 2002). However, ERK has also been found to play a pro-death role in some situations, such as in neuronal degeneration associated with Parkinson's disease (Kulich and Chu 2001). Even more ambiguous are the roles of the JNK and p38 MAPK pathways. While these pathways are required for pro-apoptotic signaling in many cases (Kuan et al. 1999), in other contexts they appear to act as pro-survival factors (Yu et al. 2004). Thus, it appears that the roles of MAPK pathways in regulating apoptosis, while very important, are complex and highly context-dependent.

1.6 Apoptosis at the population and single cell level

To be understood fully, apoptosis must be studied at both the population and the single-cell level. Within a population, each individual cell may or may not commit apoptosis. Therefore, it is typical to study apoptosis using assays that distinguish between healthy and apoptotic cells, thus allowing the percentage of apoptotic cells within the population to be quantitated. This measure, also known as the "apoptotic index" of a tissue or population, is commonly reported as a measure of the response to a particular stimulus or genetic alteration. As is often noted, this is not a perfect measure,

because it depends on the rate at which apoptotic cells break down or are cleared from the tissue and the rate at which healthy cells are produced by cell division; these rates can vary with time and context. Moreover, the heterogeneity of individual cellular responses complicates the use of biochemical methods such as immunoblotting that homogenize the entire population; such methods must be used with the caveat that both healthy and apoptotic cells are included within the cell lysates being analyzed. Thus, a number of studies have focused on apoptosis in single cells and have observed the real-time dynamics of apoptotic events at this level. These studies have led to interesting insights into how apoptosis is executed. However, it is difficult to assess the sensitivity to apoptosis by observing a single cell, which either dies or does not. To accurately compare the sensitivity of cells under two or more conditions, it is more useful to compare the apoptotic indices measured across larger populations. Thus, understanding a process like apoptosis necessitates the use of both population- and cellular-level measurements.

Numerous apoptotic events have been imaged in single living cells. Morphological changes such as cell shrinkage and membrane blebbing are visible via basic light microscopy (Goldstein et al. 2000a). Other changes, such as DNA fragmentation, membrane permeablization, or mitochondrial depolarization, can be imaged using fluorescent dyes. Specific molecular events involving proteins can be detected using the appropriate green fluorescent protein (GFP) fusions, and this approach has been the most informative in observing the dynamics of apoptotic signaling. For example, a cytochrome c-GFP fusion revealed that cytochrome c release from the mitochondria during apoptosis is always a rapid and complete event, taking only 5-10

minutes to complete once it begins (Goldstein et al. 2000b; Goldstein et al. 2005). Subsequent studies have shown that this dynamic behavior is also true of Smac and other proteins of the mitochondrial intermembrane space and that all of these proteins are released simultaneously when mitochondrial permeabilization occurs (Rehm et al. 2003; Munoz-Pinedo et al. 2006). Interestingly, however, mitochondrial membrane depolarization is a distinct event from cytochrome c/Smac release. Depolarization follows cytochrome c release and is dependent on the downstream activation of caspases (Munoz-Pinedo et al. 2006).

Single-cell studies have also revealed much about the regulation of caspases. Most of these studies have employed GFP-based Förster resonance energy transfer (FRET) sensors sensitive to caspase activity. These sensors are constructed by linking together two fluorescent proteins capable of undergoing FRET (CFP and YFP are the most common) with a caspase cleavage sequence in between; the proximity of the two fluorescent proteins within the fusion protein enables FRET to occur. When the caspase specific for the cleavage sequence is active, it cleaves apart the two fluorescent proteins and the FRET interaction is lost, resulting in a shift in the ratio of intensities of CFP and YFP emission. Using this technique it was found that, like cytochrome c/Smac release, the cleavage of a caspase-3 FRET substrate begins suddenly after a delay phase and is rapidly completed (within 5-10 minutes) (Tyas et al. 2000; Rehm et al. 2002). Moreover, this rapid cleavage follows the release of Smac by 10-15 minutes (Rehm et al. 2003). Morphological changes such as cell shrinkage quickly follow effector caspase activation. Thus, single cell studies indicate that once the mitochondrial outer membrane is

permeabilized, downstream events occur in rapid succession; the execution of the cell is complete within 10 minutes in some cases (Green 2005).

Live-cell studies have also shown that the time preceding mitochondrial permeabilization is variable and can be at least as long as 12 hours. Much less is known about the dynamics of signaling during this period. Several attempts have been made to observe caspase-8 activity, but these have produced conflicting results (Luo et al. 2003; Kawai et al. 2004). It has also been reported that a transient increase in cellular calcium can be observed prior to permeabilization, but the role of this signal is unclear. Thus, signaling dynamics upstream of the mitochondrial pathway remain obscure.

1.7 Quantitative challenges in apoptosis

The emerging field of systems biology seeks to develop a quantitative, system-level understanding of biological pathways and networks. A central approach in systems biology is to create/ models that capture system-level behavior while retaining the details of the underlying molecular mechanisms. Apoptosis presents a rather unique quantitative challenge for systems biology. It is not a gross oversimplification to state that apoptosis is a cell fate that is ultimately linked directly to a single quantity: the effector caspase activity in the cell. All apoptotic signals eventually converge on the effector caspases, and the extent to which these enzymes become active determines whether the cell lives or dies (at least in the cases where other forms of cell death are not available). In contrast, in a differentiation circuit, rather than converging on one effector, the signal diverges to many effectors, such as genes that are transcriptionally activated, most of which are still unknown, making accurate mechanistic modeling a distant goal. However, it is currently

realistic to consider mechanistic modeling of the time-dependent activity of an enzyme such as caspase-3. Mathematical models for systems controlling enzymatic activity are well-developed, and the structure of the biochemical pathways regulating effector caspase activity have been well described, to some extent even in quantitative terms It should thus be possible to construct a model that accurately describes the enzymatic activity of the effector caspases. Indeed, several attempts have been made to capture caspase regulation by mathematical modeling (Fussenegger et al. 2000; Bentele et al. 2004; Eissing et al. 2004; Bagci et al. 2005; Stucki and Simon 2005). These models have begun to address a number of interesting questions in apoptosis, but as of yet have provided few definitive answers. However, by approaching apoptosis from a quantitative perspective, these studies have helped to raise a number of interesting unanswered questions in the field of apoptosis. Some of these questions have not yet been considered by those approaching apoptosis from a traditional biology perspective. Thus, there is much interesting work to be done in applying mathematical modeling to apoptosis.

1.7.1 Quantitating the lethality of caspases

How much effector caspase activity is needed to cause a cell to die? In other words, what percentage of effector caspases in each cell must be activated, and for how long must they remain active, in order to ensure cell death? A complementary question is, what percentage of effector caspase substrates must be cleaved to kill the cell? These are essentially experimental questions; to answer them will require the examination of cells in which caspases have been activated at different levels and the determination of their resulting fates. To date, this has not been possible, because all stimuli examined

appear to activate caspases in an all-or-none manner, regardless how low of a stimulus concentration is used. Thus, to answer this question, a method will have to be developed to bypass all-or-none caspase activation. Doing so will likely require an understanding of the mechanism of all-or-none caspase activation. However, it will be essential to answer this question in order to connect quantitative models of caspase activation to cell fate.

1.7.2 All-or-none caspase activation

Why is caspase activation all-or-none? It is probably important for the cell to avoid partial activation of caspases, since this would lead to an uncertain cell fate. Some formal hypotheses for all-or-none mechanisms have been proposed by the caspase models constructed so far. One hypothesis is that this results from the positive feedback loop mediated by caspase-6 (Eissing et al. 2004). Positive feedback has been shown to mediate all-or-none behavior in other systems (Ferrell and Xiong 2001). A second possibility is that some type of allosteric regulation of the caspases is involved. For example, it has been proposed that the assembly of the heptameric apoptosome may be a highly cooperative event that combines with positive feedback to form a bistable caspase switch (Bagci et al. 2005). A third possibility, based on single-cell data, is that the all-or-none release of cytochrome c and other proteins from the mitochondria drives all-or-none caspase activation (Goldstein et al. 2000b; Green 2005). However, it is still unknown why cytochrome c release is all-or-none; since it is released by Bax-mediated pores, it might be expected that the rate of release would be dependent on the number of Bax proteins present in the mitochondrial membrane. Differentiating among these

possibilities will likely require both single-cell experimentation and quantitative modeling.

1.7.3 Integration of apoptotic signals

As described above, many pathways regulate apoptosis in some way, but caspase activation is still all-or-none. How is all of this information integrated, and which pathways are the most important for the fate of the cell? One hypothesis is that this integrating function is performed by the Bcl-2 family proteins of the mitochondria (Spierings et al. 2005). In this scenario, pro and anti-apoptotic signals increase and decrease the levels of pro and anti apoptotic Bcl-2 family proteins accordingly; if the number of activated pro-apoptotic Bcl-2 exceeds the number of anti-apoptotic proteins, then the release of cytochrome c and other mitochondrial proteins occurs rapidly and completely. Thus, each signal gets a number of "votes" corresponding to the number of pro- or anti-apoptotic proteins it produces or inactivates, with the mitochondria serving as the ballot box. It is also interesting to ask how all regulatory pathways affect apoptosis in such a way that all-or-none caspase activation is maintained. This would appear to be important, if it is indeed true that partial caspase activation is detrimental.

1.7.4 Thresholds in apoptosis

Given that apoptosis is an all-or-none event, there must be some threshold for pro-apoptotic signaling that must be crossed to initiate apoptosis. One model has suggested that the number of Flip molecules in the cell creates a threshold for death ligand concentration (Bentele et al. 2004). Other work has suggested that the number of anti-

apoptotic Bcl-2 family members in the cell sets a threshold for the release of cytochrome c (Certo et al. 2006). It is quite possible that there is more than one threshold; there may be multiple points in the pathway at which the signal must exceed a certain value in order to trigger downstream events. However, answering this question will require an understanding of how thresholds are created in general. In an ideal threshold, the output response for a given signal is zero below a certain level of signal, and non-zero above that point. It is often tempting to state that an inhibitory molecule "sets a threshold" for the signaling molecule that it inhibits; for example, in the FLIP threshold model, each Flip binds to and inhibits one activated receptor. If this mechanism created an ideal threshold, then the presence of 10^3 Flip molecules in the cell would imply that the downstream signaling from the receptor would remain off until greater than 10^3 receptors had been activated. However, a simple binding reaction like this creates an effective threshold only when the Kd of the association reaction is extremely tight (< 1 nM). Indeed the, Flip model assumes a Flip-receptor Kd of 1 pM. However, protein-protein interactions are rarely this tight. Thus, it is unlikely that simple binding reactions are responsible for most biological thresholds. Instead, thresholds likely arise in more complex ways, such as through distributed phosphorylation (Gunawardena 2005) or zero-order ultrasensitivity (Goldbeter and Koshland 1981). It will be important to definitively identify components of the apoptotic pathway that create thresholds.

1.7.5 The relationship between timing of death and apoptotic sensitivity

Quantifying the sensitivity of a given cell type to apoptosis is an important question. This is particularly critical in relation to clinical studies, where the goal may be

to identify treatments stimuli that effectively induce death in a particular cell type, such as tumor cells (Lowe et al. 2004). In many studies, the sensitivity of cells to a particular is assessed by treating cells continuously with a pro-apoptotic stimulus and measuring the apoptotic index at one or several time points afterwards. One criticism of this approach is that it does not reveal the true fate of cells. To determine whether cells ultimately live or die in response to a stimulus, it is necessary to examine their long-term behavior; this can be done by colony-forming assays, for example. However, such assays should not be considered the final word; it is highly unlikely that cells in vivo are subjected to a single, continuous dose of a given stimuli for days or weeks. Since apoptotic stimuli are likely transient, the timing of cell death in response to a given stimulus is also an important aspect of the cellular response. Thus, the response of a population of cells to a given apoptotic stimulus cannot be summarized by a simple percentage or rate. Summarizing the apoptotic response can best be done by mathematical models that consider both the timing and extent of cell death, and perhaps the rates of other processes such as mitosis (Byrne et al. 2006).

1.7.6 Asychronicity and variability in individual responses.

The apoptotic response is known to be highly variable from cell to cell (Tyas et al. 2000). It is not yet clear whether this is a feature unique to apoptosis, or whether it is simply more obvious in apoptosis then in other cellular processes due to the distinctive morphology of apoptotic cells. Moreover, recent studies have also revealed significant cell-to-cell variability in the NF-κB and p53 signaling systems, which feed into the central apoptotic pathways (Nelson et al. 2004; Geva-Zatorsky et al. 2006). Thus, cell-

to-cell variability plays an important role in apoptotic responses. It can been hypothesized that this is a beneficial feature, allowing populations of cells in the body to respond in a graded manner to stimuli. However, it is also possible that the high level of heterogeneity observed in cell death is an artifact of the deranged tumor cell lines used in many *in vitro* studies of apoptosis. Quantifying this heterogeneity and understanding its mechanism and function will be essential for building accurate models of apoptotic responses.

1.7.7 Interaction networks with high combinatorial complexity

Many steps in apoptotic signaling involve the formation of protein complexes, such as DISC and apoptosome formation, and the interaction of Bcl-2 pro- and anti-apoptotic proteins. In many of these cases, the number of possible different combinations of subunits is very high. For example, in the Bcl-2 family there are at least 8 pro-apoptotic proteins and 6 anti-apoptotic proteins, making for 48 possible heterodimer combinations. Recent studies have undercovered binding preference profiles for several of these proteins (Chen et al. 2005; Kuwana et al. 2005). However, the temptation has been to view these binding profiles as binary – e.g. Bak binds to Mcl-1 and Bcl-X_L, but not to Bcl-2 – rather than taking into account the K_d for each interaction. As this biochemical interaction data continues to be improved, mathematical models may be able to predict the abundance of each of the possible heterodimers, and hopefully will improve understanding of which interactions are critical and which are less important. This has already been attempted on a smaller scale by one study that concluded that Bcl-2 likely

exerts its anti-apoptotic effect by binding to both Bax and Bid rather than either one alone (Hua et al. 2005).

1.8 Conclusion

To achieve the goal of improving treatments for diseases such as cancer, apoptosis must be understood at multiple levels. At the molecular level, the challenge is to understand the molecular details of enzyme reactions and protein interactions so that the effects of mutations can be understood and so that inhibitors can be designed to target specific functions. At the single-cell level, the challenge is to understand how apoptosis is successfully executed or carefully suppressed, so that the cell accurately and certainly chooses the fate that is required of it; failure of even a single damaged cell to die can result in cancer. At the tissue level, the challenge is to understand how the death and survival of many cells are coordinated accurately, so that the right number of cell deaths occurs to maintain homeostasis. These levels of organization are interconnected; for example, individual cells must be calibrated properly so that they respond in the correct proportion to tissue-level signaling. Thus, future advances in the field of apoptosis will rely on approaches that can integrate quantitative information across multiple levels of organization. Thus, as much as apoptosis is an interesting challenge for systems biology, systems modeling may become an essential tool in understanding cell death.

1.9 References

Abreu MT, Arnold ET, Chow JY, Barrett KE (2001) Phosphatidylinositol 3-kinase-dependent pathways oppose Fas-induced apoptosis and limit chloride secretion in human intestinal epithelial cells. Implications for inflammatory diarrheal states. J Biol Chem 276(50): 47563-47574.

Allan LA, Morrice N, Brady S, Magee G, Pathak S et al. (2003) Inhibition of caspase-9 through phosphorylation at Thr 125 by ERK MAPK. Nat Cell Biol 5(7): 647-654.

Bagci EZ, Vodovotz Y, Billiar TR, Ermentrout GB, Bahar I (2005) Bistability in Apoptosis: Roles of Bax, Bcl-2 and Mitochondrial Permeability Transition Pores. Biophys J.

Bentele M, Lavrik I, Ulrich M, Stosser S, Heermann DW et al. (2004) Mathematical modeling reveals threshold mechanism in CD95-induced apoptosis. J Cell Biol 166(6): 839-851.

Boatright KM, Renatus M, Scott FL, Sperandio S, Shin H et al. (2003) A unified model for apical caspase activation. Mol Cell 11(2): 529-541.

Bonni A, Brunet A, West AE, Datta SR, Takasu MA et al. (1999) Cell survival promoted by the Ras-MAPK signaling pathway by transcription-dependent and -independent mechanisms. Science 286(5443): 1358-1362.

Bose K, Pop C, Feeney B, Clark AC (2003) An uncleavable procaspase-3 mutant has a lower catalytic efficiency but an active site similar to that of mature caspase-3. Biochemistry 42(42): 12298-12310.

Brunet A, Bonni A, Zigmond MJ, Lin MZ, Juo P et al. (1999) Akt promotes cell survival by phosphorylating and inhibiting a Forkhead transcription factor. Cell 96(6): 857-868.

Byrne HM, Alarcon T, Owen MR, Webb SD, Maini PK (2006) Modelling aspects of cancer dynamics: a review. Philos Transact A Math Phys Eng Sci 364(1843): 1563-1578.

Cardone MH, Roy N, Stennicke HR, Salvesen GS, Franke TF et al. (1998) Regulation of cell death protease caspase-9 by phosphorylation. Science 282(5392): 1318-1321.

Certo M, Del Gaizo Moore V, Nishino M, Wei G, Korsmeyer S et al. (2006) Mitochondria primed by death signals determine cellular addiction to antiapoptotic BCL-2 family members. Cancer Cell 9(5): 351-365.

Chang DW, Xing Z, Capacio VL, Peter ME, Yang X (2003a) Interdimer processing mechanism of procaspase-8 activation. Embo J 22(16): 4132-4142.

Chang DW, Ditsworth D, Liu H, Srinivasula SM, Alnemri ES et al. (2003b) Oligomerization is a general mechanism for the activation of apoptosis initiator and inflammatory procaspases. J Biol Chem 278(19): 16466-16469.

Chang DW, Xing Z, Pan Y, Algeciras-Schimnich A, Barnhart BC et al. (2002) c-FLIP(L) is a dual function regulator for caspase-8 activation and CD95-mediated apoptosis. Embo J 21(14): 3704-3714.

Chaudhary PM, Eby M, Jasmin A, Bookwalter A, Murray J et al. (1997) Death receptor 5, a new member of the TNFR family, and DR4 induce FADD-dependent apoptosis and activate the NF-kappaB pathway. Immunity 7(6): 821-830.

Chen L, Smith L, Wang Z, Smith JB (2003) Preservation of caspase-3 subunits from degradation contributes to apoptosis evoked by lactacystin: any single lysine or lysine pair of the small subunit is sufficient for ubiquitination. Mol Pharmacol 64(2): 334-345.

Chen L, Willis SN, Wei A, Smith BJ, Fletcher JI et al. (2005) Differential targeting of prosurvival Bcl-2 proteins by their BH3-only ligands allows complementary apoptotic function. Mol Cell 17(3): 393-403.

Cheng EH, Wei MC, Weiler S, Flavell RA, Mak TW et al. (2001) BCL-2, BCL-X(L) sequester BH3 domain-only molecules preventing BAX- and BAK-mediated mitochondrial apoptosis. Mol Cell 8(3): 705-711.

Cheng Y, Deshmukh M, D'Costa A, Demaro JA, Gidday JM et al. (1998) Caspase inhibitor affords neuroprotection with delayed administration in a rat model of neonatal hypoxic-ischemic brain injury. J Clin Invest 101(9): 1992-1999.

Chinnaiyan AM, O'Rourke K, Tewari M, Dixit VM (1995) FADD, a novel death domain-containing protein, interacts with the death domain of Fas and initiates apoptosis. Cell 81(4): 505-512.

Chipuk JE, Green DR (2005) Do inducers of apoptosis trigger caspase-independent cell death? Nat Rev Mol Cell Biol 6(3): 268-275.

Clarke PG, Clarke S (1995) Historic apoptosis. Nature 378(6554): 230.

Cowling V, Downward J (2002) Caspase-6 is the direct activator of caspase-8 in the cytochrome c-induced apoptosis pathway: absolute requirement for removal of caspase-6 prodomain. Cell Death Differ 9(10): 1046-1056.

Cross DA, Alessi DR, Cohen P, Andjelkovich M, Hemmings BA (1995) Inhibition of glycogen synthase kinase-3 by insulin mediated by protein kinase B. Nature 378(6559): 785-789.

Dan HC, Sun M, Kaneko S, Feldman RI, Nicosia SV et al. (2004) Akt phosphorylation and stabilization of X-linked inhibitor of apoptosis protein (XIAP). J Biol Chem 279(7): 5405-5412.

Danial NN, Korsmeyer SJ (2004) Cell death: critical control points. Cell 116(2): 205-219.

Darmon AJ, Nicholson DW, Bleackley RC (1995) Activation of the apoptotic protease CPP32 by cytotoxic T-cell-derived granzyme B. Nature 377(6548): 446-448.

Datta SR, Dudek H, Tao X, Masters S, Fu H et al. (1997) Akt phosphorylation of BAD couples survival signals to the cell-intrinsic death machinery. Cell 91(2): 231-241.

Datta SR, Katsov A, Hu L, Petros A, Fesik SW et al. (2000) 14-3-3 proteins and survival kinases cooperate to inactivate BAD by BH3 domain phosphorylation. Mol Cell 6(1): 41-51.

Datta SR, Ranger AM, Lin MZ, Sturgill JF, Ma YC et al. (2002) Survival factor-mediated BAD phosphorylation raises the mitochondrial threshold for apoptosis. Dev Cell 3(5): 631-643.

Degterev A, Huang Z, Boyce M, Li Y, Jagtap P et al. (2005) Chemical inhibitor of nonapoptotic cell death with therapeutic potential for ischemic brain injury. Nat Chem Biol 1(2): 112-119.

Deng Y, Lin Y, Wu X (2002) TRAIL-induced apoptosis requires Bax-dependent mitochondrial release of Smac/DIABLO. Genes Dev 16(1): 33-45.

Deveraux QL, Takahashi R, Salvesen GS, Reed JC (1997) X-linked IAP is a direct inhibitor of cell-death proteases. Nature 388(6639): 300-304.

Donepudi M, Sweeney AM, Briand C, Grutter MG (2003) Insights into the regulatory mechanism for caspase-8 activation. Mol Cell 11(2): 543-549.

Du C, Fang M, Li Y, Li L, Wang X (2000) Smac, a mitochondrial protein that promotes cytochrome c-dependent caspase activation by eliminating IAP inhibition. Cell 102(1): 33-42.

Eckelman BP, Salvesen GS (2006) The human anti-apoptotic proteins cIAP1 and cIAP2 bind but do not inhibit caspases. J Biol Chem 281(6): 3254-3260.

Edinger AL, Thompson CB (2004) Death by design: apoptosis, necrosis and autophagy. Curr Opin Cell Biol 16(6): 663-669.

Eissing T, Conzelmann H, Gilles ED, Allgower F, Bullinger E et al. (2004) Bistability analyses of a caspase activation model for receptor induced apoptosis. J Biol Chem.

Ellis HM, Horvitz HR (1986) Genetic control of programmed cell death in the nematode C. elegans. Cell 44(6): 817-829.

Ferrell JE, Xiong W (2001) Bistability in cell signaling: How to make continuous processes discontinuous, and reversible processes irreversible. Chaos 11(1): 227-236.

Fischer U, Janicke RU, Schulze-Osthoff K (2003) Many cuts to ruin: a comprehensive update of caspase substrates. Cell Death Differ 10(1): 76-100.

Fujita E, Egashira J, Urase K, Kuida K, Momoi T (2001) Caspase-9 processing by caspase-3 via a feedback amplification loop in vivo. Cell Death Differ 8(4): 335-344.

Fussenegger M, Bailey JE, Varner J (2000) A mathematical model of caspase function in apoptosis. Nat Biotechnol 18(7): 768-774.

Geva-Zatorsky N, Rosenfeld N, Itzkovitz S, Milo R, Sigal A et al. (2006) Oscillations and variability in the p53 system. Mol Syst Biol 2: 2006 0033.

Ghosh S, Baltimore D (1990) Activation in vitro of NF-kappa B by phosphorylation of its inhibitor I kappa B. Nature 344(6267): 678-682.

Goldbeter A, Koshland DE, Jr. (1981) An amplified sensitivity arising from covalent modification in biological systems. Proc Natl Acad Sci U S A 78(11): 6840-6844.

Goldstein JC, Kluck RM, Green DR (2000a) A single cell analysis of apoptosis. Ordering the apoptotic phenotype. Ann N Y Acad Sci 926: 132-141.

Goldstein JC, Waterhouse NJ, Juin P, Evan GI, Green DR (2000b) The coordinate release of cytochrome c during apoptosis is rapid, complete and kinetically invariant. Nat Cell Biol 2(3): 156-162.

Goldstein JC, Munoz-Pinedo C, Ricci JE, Adams SR, Kelekar A et al. (2005) Cytochrome c is released in a single step during apoptosis. Cell Death Differ 12(5): 453-462.

Golstein P, Kroemer G (2005) Redundant cell death mechanisms as relics and backups. Cell Death Differ 12 Suppl 2: 1490-1496.

Green DR (2005) Apoptotic pathways: ten minutes to dead. Cell 121(5): 671-674.

Green DR, Evan GI (2002) A matter of life and death. Cancer Cell 1(1): 19-30.

Gunawardena J (2005) Multisite protein phosphorylation makes a good threshold but can be a poor switch. Proc Natl Acad Sci U S A 102(41): 14617-14622.

Hakem R, Hakem A, Duncan GS, Henderson JT, Woo M et al. (1998) Differential requirement for caspase 9 in apoptotic pathways in vivo. Cell 94(3): 339-352.

Hengartner MO, Horvitz HR (1994) C. elegans cell survival gene ced-9 encodes a functional homolog of the mammalian proto-oncogene bcl-2. Cell 76(4): 665-676.

Hengartner MO, Ellis RE, Horvitz HR (1992) Caenorhabditis elegans gene ced-9 protects cells from programmed cell death. Nature 356(6369): 494-499.

Hill MM, Adrain C, Duriez PJ, Creagh EM, Martin SJ (2004) Analysis of the composition, assembly kinetics and activity of native Apaf-1 apoptosomes. Embo J 23(10): 2134-2145.

Hsu H, Xiong J, Goeddel DV (1995) The TNF receptor 1-associated protein TRADD signals cell death and NF-kappa B activation. Cell 81(4): 495-504.

Hsu H, Shu HB, Pan MG, Goeddel DV (1996) TRADD-TRAF2 and TRADD-FADD interactions define two distinct TNF receptor 1 signal transduction pathways. Cell 84(2): 299-308.

Hua F, Cornejo MG, Cardone MH, Stokes CL, Lauffenburger DA (2005) Effects of Bcl-2 levels on Fas signaling-induced caspase-3 activation: molecular genetic tests of computational model predictions. J Immunol 175(2): 985-995.

Huang Y, Park YC, Rich RL, Segal D, Myszka DG et al. (2001) Structural basis of caspase inhibition by XIAP: differential roles of the linker versus the BIR domain. Cell 104(5): 781-790.

Inohara N, Koseki T, Chen S, Benedict MA, Nunez G (1999) Identification of regulatory and catalytic domains in the apoptosis nuclease DFF40/CAD. J Biol Chem 274(1): 270-274.

Irmler M, Thome M, Hahne M, Schneider P, Hofmann K et al. (1997) Inhibition of death receptor signals by cellular FLIP. Nature 388(6638): 190-195.

Jacobson MD, Weil M, Raff MC (1997) Programmed cell death in animal development. Cell 88(3): 347-354.

Karin M (2006) Nuclear factor-kappaB in cancer development and progression. Nature 441(7092): 431-436.

Kaufmann SH (1989) Induction of endonucleolytic DNA cleavage in human acute myelogenous leukemia cells by etoposide, camptothecin, and other cytotoxic anticancer drugs: a cautionary note. Cancer Res 49(21): 5870-5878.

Kawai H, Suzuki T, Kobayashi T, Mizuguchi H, Hayakawa T et al. (2004) Simultaneous imaging of initiator/effector caspase activity and mitochondrial membrane potential during cell death in living HeLa cells. Biochim Biophys Acta 1693(2): 101-110.

Kim HE, Du F, Fang M, Wang X (2005) Formation of apoptosome is initiated by cytochrome c-induced dATP hydrolysis and subsequent nucleotide exchange on Apaf-1. Proc Natl Acad Sci U S A 102(49): 17545-17550.

Kischkel FC, Hellbardt S, Behrmann I, Germer M, Pawlita M et al. (1995) Cytotoxicity-dependent APO-1 (Fas/CD95)-associated proteins form a death-inducing signaling complex (DISC) with the receptor. Embo J 14(22): 5579-5588.

Korsmeyer SJ, Shutter JR, Veis DJ, Merry DE, Oltvai ZN (1993) Bcl-2/Bax: a rheostat that regulates an anti-oxidant pathway and cell death. Semin Cancer Biol 4(6): 327-332.

Kuan CY, Yang DD, Samanta Roy DR, Davis RJ, Rakic P et al. (1999) The Jnk1 and Jnk2 protein kinases are required for regional specific apoptosis during early brain development. Neuron 22(4): 667-676.

Kuida K, Haydar TF, Kuan CY, Gu Y, Taya C et al. (1998) Reduced apoptosis and cytochrome c-mediated caspase activation in mice lacking caspase 9. Cell 94(3): 325-337.

Kulich SM, Chu CT (2001) Sustained extracellular signal-regulated kinase activation by 6-hydroxydopamine: implications for Parkinson's disease. J Neurochem 77(4): 1058-1066.

Kuwana T, Bouchier-Hayes L, Chipuk JE, Bonzon C, Sullivan BA et al. (2005) BH3 domains of BH3-only proteins differentially regulate Bax-mediated mitochondrial membrane permeabilization both directly and indirectly. Mol Cell 17(4): 525-535.

Kuwana T, Mackey MR, Perkins G, Ellisman MH, Latterich M et al. (2002) Bid, Bax, and lipids cooperate to form supramolecular openings in the outer mitochondrial membrane. Cell 111(3): 331-342.

Lassus P, Opitz-Araya X, Lazebnik Y (2002) Requirement for caspase-2 in stress-induced apoptosis before mitochondrial permeabilization. Science 297(5585): 1352-1354.

Letai A, Bassik M, Walensky L, Sorcinelli M, Weiler S et al. (2002) Distinct BH3 domains either sensitize or activate mitochondrial apoptosis, serving as prototype cancer therapeutics. Cancer Cell 2(3): 183.

Li H, Zhu H, Xu CJ, Yuan J (1998) Cleavage of BID by caspase 8 mediates the mitochondrial damage in the Fas pathway of apoptosis. Cell 94(4): 491-501.

Li P, Nijhawan D, Budihardjo I, Srinivasula SM, Ahmad M et al. (1997) Cytochrome c and dATP-dependent formation of Apaf-1/caspase-9 complex initiates an apoptotic protease cascade. Cell 91(4): 479-489.

Li S, Zhao Y, He X, Kim TH, Kuharsky DK et al. (2002) Relief of extrinsic pathway inhibition by the Bid-dependent mitochondrial release of Smac in Fas-mediated hepatocyte apoptosis. J Biol Chem 277(30): 26912-26920.

Lindsten T, Ross AJ, King A, Zong WX, Rathmell JC et al. (2000) The combined functions of proapoptotic Bcl-2 family members bak and bax are essential for normal development of multiple tissues. Mol Cell 6(6): 1389-1399.

Liu H, Chang DW, Yang X (2005) Interdimer processing and linearity of procaspase-3 activation. A unifying mechanism for the activation of initiator and effector caspases. J Biol Chem 280(12): 11578-11582.

Liu X, Li P, Widlak P, Zou H, Luo X et al. (1998) The 40-kDa subunit of DNA fragmentation factor induces DNA fragmentation and chromatin condensation during apoptosis. Proc Natl Acad Sci U S A 95(15): 8461-8466.

Lowe SW, Cepero E, Evan G (2004) Intrinsic tumour suppression. Nature 432(7015): 307-315.

Lum JJ, Bauer DE, Kong M, Harris MH, Li C et al. (2005) Growth factor regulation of autophagy and cell survival in the absence of apoptosis. Cell 120(2): 237-248.

Luo KQ, Yu VC, Pu Y, Chang DC (2003) Measuring dynamics of caspase-8 activation in a single living HeLa cell during TNFalpha-induced apoptosis. Biochem Biophys Res Commun 304(2): 217-222.

Luo X, Budihardjo I, Zou H, Slaughter C, Wang X (1998) Bid, a Bcl2 interacting protein, mediates cytochrome c release from mitochondria in response to activation of cell surface death receptors. Cell 94(4): 481-490.

Maurer U, Charvet C, Wagman AS, Dejardin E, Green DR (2006) Glycogen synthase kinase-3 regulates mitochondrial outer membrane permeabilization and apoptosis by destabilization of MCL-1. Mol Cell 21(6): 749-760.

Medema JP, Scaffidi C, Kischkel FC, Shevchenko A, Mann M et al. (1997) FLICE is activated by association with the CD95 death-inducing signaling complex (DISC). Embo J 16(10): 2794-2804.

Micheau O, Lens S, Gaide O, Alevizopoulos K, Tschopp J (2001) NF-kappaB signals induce the expression of c-FLIP. Mol Cell Biol 21(16): 5299-5305.

Micheau O, Thome M, Schneider P, Holler N, Tschopp J et al. (2002) The long form of FLIP is an activator of Caspase-8 at the Fas death-inducing signaling complex. J Biol Chem 4: 4.

Miyashita T, Reed JC (1995) Tumor suppressor p53 is a direct transcriptional activator of the human bax gene. Cell 80(2): 293-299.

Munoz-Pinedo C, Guio-Carrion A, Goldstein JC, Fitzgerald P, Newmeyer DD et al. (2006) Different mitochondrial intermembrane space proteins are released during apoptosis in a manner that is coordinately initiated but can vary in duration. Proc Natl Acad Sci U S A 103(31): 11573-11578.

Nelson DE, Ihekwaba AE, Elliott M, Johnson JR, Gibney CA et al. (2004) Oscillations in NF-kappaB signaling control the dynamics of gene expression. Science 306(5696): 704-708.

Oltvai ZN, Milliman CL, Korsmeyer SJ (1993) Bcl-2 heterodimerizes in vivo with a conserved homolog, Bax, that accelerates programmed cell death. Cell 74(4): 609-619.

Pop C, Chen YR, Smith B, Bose K, Bobay B et al. (2001) Removal of the pro-domain does not affect the conformation of the procaspase-3 dimer. Biochemistry 40(47): 14224-14235.

Rehm M, Dussmann H, Prehn JH (2003) Real-time single cell analysis of Smac/DIABLO release during apoptosis. J Cell Biol 162(6): 1031-1043.

Rehm M, Dussmann H, Janicke RU, Tavare JM, Kogel D et al. (2002) Single-cell fluorescence resonance energy transfer analysis demonstrates that caspase activation during apoptosis is a rapid process. Role of caspase-3. J Biol Chem 277(27): 24506-24514.

Rodriguez J, Lazebnik Y (1999) Caspase-9 and APAF-1 form an active holoenzyme. Genes Dev 13(24): 3179-3184.

Rothe M, Wong SC, Henzel WJ, Goeddel DV (1994) A novel family of putative signal transducers associated with the cytoplasmic domain of the 75 kDa tumor necrosis factor receptor. Cell 78(4): 681-692.

Scaffidi C, Schmitz I, Zha J, Korsmeyer SJ, Krammer PH et al. (1999) Differential modulation of apoptosis sensitivity in CD95 type I and type II cells. J Biol Chem 274(32): 22532-22538.

Scaffidi C, Fulda S, Srinivasan A, Friesen C, Li F et al. (1998) Two CD95 (APO-1/Fas) signaling pathways. Embo J 17(6): 1675-1687.

Shimizu S, Kanaseki T, Mizushima N, Mizuta T, Arakawa-Kobayashi S et al. (2004) Role of Bcl-2 family proteins in a non-apoptotic programmed cell death dependent on autophagy genes. Nat Cell Biol 6(12): 1221-1228.

Shin H, Renatus M, Eckelman BP, Nunes VA, Sampaio CA et al. (2005) The BIR domain of IAP-like protein 2 is conformationally unstable: implications for caspase inhibition. Biochem J 385(Pt 1): 1-10.

Shiozaki EN, Chai J, Rigotti DJ, Riedl SJ, Li P et al. (2003) Mechanism of XIAP-Mediated Inhibition of Caspase-9. Mol Cell 11(2): 519-527.

Siegel RM, Frederiksen JK, Zacharias DA, Chan FK, Johnson M et al. (2000) Fas preassociation required for apoptosis signaling and dominant inhibition by pathogenic mutations. Science 288(5475): 2354-2357.

Slee EA, Harte MT, Kluck RM, Wolf BB, Casiano CA et al. (1999) Ordering the cytochrome c-initiated caspase cascade: hierarchical activation of caspases-2, -3, -6, -7, -8, and -10 in a caspase-9-dependent manner. J Cell Biol 144(2): 281-292.

Smith RA, Baglioni C (1987) The active form of tumor necrosis factor is a trimer. J Biol Chem 262(15): 6951-6954.

Soderstrom TS, Poukkula M, Holmstrom TH, Heiskanen KM, Eriksson JE (2002) Mitogen-activated protein kinase/extracellular signal-regulated kinase signaling in activated T cells abrogates TRAIL-induced apoptosis upstream of the mitochondrial amplification loop and caspase-8. J Immunol 169(6): 2851-2860.

Sohn D, Schulze-Osthoff K, Janicke RU (2005) Caspase-8 can be activated by interchain proteolysis without receptor-triggered dimerization during drug-induced apoptosis. J Biol Chem 280(7): 5267-5273.

Sohn D, Totzke G, Essmann F, Schulze-Osthoff K, Levkau B et al. (2006) The proteasome is required for rapid initiation of death receptor-induced apoptosis. Mol Cell Biol 26(5): 1967-1978.

Spierings D, McStay G, Saleh M, Bender C, Chipuk J et al. (2005) Connected to death: the (unexpurgated) mitochondrial pathway of apoptosis. Science 310(5745): 66-67.

Stehlik C, de Martin R, Kumabashiri I, Schmid JA, Binder BR et al. (1998) Nuclear factor (NF)-kappaB-regulated X-chromosome-linked iap gene expression protects endothelial cells from tumor necrosis factor alpha-induced apoptosis. J Exp Med 188(1): 211-216.

Stucki JW, Simon HU (2005) Mathematical modeling of the regulation of caspase-3 activation and degradation. J Theor Biol 234(1): 123-131.

Sun XM, Bratton SB, Butterworth M, MacFarlane M, Cohen GM (2002) Bcl-2 and Bcl-xL inhibit CD95-mediated apoptosis by preventing mitochondrial release of Smac/DIABLO and subsequent inactivation of X-linked inhibitor-of-apoptosis protein. J Biol Chem 277(13): 11345-11351.

Suzuki Y, Nakabayashi Y, Takahashi R (2001) Ubiquitin-protein ligase activity of X-linked inhibitor of apoptosis protein promotes proteasomal degradation of

caspase-3 and enhances its anti-apoptotic effect in Fas-induced cell death. Proc Natl Acad Sci U S A 98(15): 8662-8667.

Talanian RV, Quinlan C, Trautz S, Hackett MC, Mankovich JA et al. (1997) Substrate specificities of caspase family proteases. J Biol Chem 272(15): 9677-9682.

Tewari M, Quan LT, O'Rourke K, Desnoyers S, Zeng Z et al. (1995) Yama/CPP32 beta, a mammalian homolog of CED-3, is a CrmA-inhibitable protease that cleaves the death substrate poly(ADP-ribose) polymerase. Cell 81(5): 801-809.

Thornberry NA, Rano TA, Peterson EP, Rasper DM, Timkey T et al. (1997) A combinatorial approach defines specificities of members of the caspase family and granzyme B. Functional relationships established for key mediators of apoptosis. J Biol Chem 272(29): 17907-17911.

Tran SE, Holmstrom TH, Ahonen M, Kahari VM, Eriksson JE (2001) MAPK/ERK overrides the apoptotic signaling from Fas, TNF, and TRAIL receptors. J Biol Chem 276(19): 16484-16490.

Tsukahara T, Kannagi M, Ohashi T, Kato H, Arai M et al. (1999) Induction of Bcl-x(L) expression by human T-cell leukemia virus type 1 Tax through NF-kappaB in apoptosis-resistant T-cell transfectants with Tax. J Virol 73(10): 7981-7987.

Tu S, McStay GP, Boucher LM, Mak T, Beere HM et al. (2006) In situ trapping of activated initiator caspases reveals a role for caspase-2 in heat shock-induced apoptosis. Nat Cell Biol 8(1): 72-77.

Twiddy D, Brown DG, Adrain C, Jukes R, Martin SJ et al. (2004) Pro-apoptotic proteins released from the mitochondria regulate the protein composition and caspase-processing activity of the native Apaf-1/caspase-9 apoptosome complex. J Biol Chem 279(19): 19665-19682.

Tyas L, Brophy VA, Pope A, Rivett AJ, Tavare JM (2000) Rapid caspase-3 activation during apoptosis revealed using fluorescence-resonance energy transfer. EMBO Rep 1(3): 266-270.

Vaux DL, Cory S, Adams JM (1988) Bcl-2 gene promotes haemopoietic cell survival and cooperates with c-myc to immortalize pre-B cells. Nature 335(6189): 440-442.

Verhagen AM, Ekert PG, Pakusch M, Silke J, Connolly LM et al. (2000) Identification of DIABLO, a mammalian protein that promotes apoptosis by binding to and antagonizing IAP proteins. Cell 102(1): 43-53.

Vucic D, Franklin MC, Wallweber HJ, Das K, Eckelman BP et al. (2005) Engineering ML-IAP to produce an extraordinarily potent caspase 9 inhibitor: implications for Smac-dependent anti-apoptotic activity of ML-IAP. Biochem J 385(Pt 1): 11-20.

Wei MC, Lindsten T, Mootha VK, Weiler S, Gross A et al. (2000) tBID, a membrane-targeted death ligand, oligomerizes BAK to release cytochrome c. Genes Dev 14(16): 2060-2071.

Wei MC, Zong WX, Cheng EH, Lindsten T, Panoutsakopoulou V et al. (2001) Proapoptotic BAX and BAK: a requisite gateway to mitochondrial dysfunction and death. Science 292(5517): 727-730.

Xia Z, Dickens M, Raingeaud J, Davis RJ, Greenberg ME (1995) Opposing effects of ERK and JNK-p38 MAP kinases on apoptosis. Science 270(5240): 1326-1331.

Yang Y, Fang S, Jensen JP, Weissman AM, Ashwell JD (2000) Ubiquitin protein ligase activity of IAPs and their degradation in proteasomes in response to apoptotic stimuli. Science 288(5467): 874-877.

Yu C, Minemoto Y, Zhang J, Liu J, Tang F et al. (2004) JNK suppresses apoptosis via phosphorylation of the proapoptotic Bcl-2 family protein BAD. Mol Cell 13(3): 329-340.

Yu X, Acehan D, Menetret JF, Booth CR, Ludtke SJ et al. (2005) A structure of the human apoptosome at 12.8 A resolution provides insights into this cell death platform. Structure (Camb) 13(11): 1725-1735.

Yuan J, Shaham S, Ledoux S, Ellis HM, Horvitz HR (1993) The C. elegans cell death gene ced-3 encodes a protein similar to mammalian interleukin-1 beta-converting enzyme. Cell 75(4): 641-652.

Zhang XD, Zhang XY, Gray CP, Nguyen T, Hersey P (2001) Tumor necrosis factor-related apoptosis-inducing ligand-induced apoptosis of human melanoma is regulated by smac/DIABLO release from mitochondria. Cancer Res 61(19): 7339-7348.

Zhivotovsky B, Kroemer G (2004) Apoptosis and genomic instability. Nat Rev Mol Cell Biol 5(9): 752-762.

Zou H, Niswander L (1996) Requirement for BMP signaling in interdigital apoptosis and scale formation. Science 272(5262): 738-741.

Chapter 2

Modeling the snap-action behavior and failure modes of a switch controlling extrinsic cell death

This chapter has been submitted for publication. J.M. Burke played a major role in developing the computational model and running the simulations shown throughout the study. M.S. Zhang performed western blots of caspase-3 in response to TRAIL and proteasome inhibitor.

Albeck, J.G.[1,3], Burke, J.M.[1,2], Zhang, M.[1,3], Lauffenburger, D.A.[1,2], and Sorger, P.K.[1,2,3] 2007 (Submitted) Modeling the snap-action behavior and failure modes of a switch controlling extrinsic cell death.

Chapter 2

Modeling the snap-action behavior and failure modes of a switch controlling extrinsic cell death.

Table of contents

2.1 Abstract

Caspases, the proteases that dismantle apoptotic cells, are normally regulated via an all-or-none switch that enforces an unambiguous choice between life and death. To understand the operation of this switch in quantitative terms we constructed a mathematical model using mass-action kinetics and verified it by observation of single cells perturbed by protein depletion, over-expression, or inhibition. Receptor-mediated cell death is characterized by rapid caspase activation and efficient caspase substrate cleavage, but only after a remarkably long delay (up to 12 hr), whose mean duration and variance depend on ligand dose. Modeling must therefore account for both snap-action behavior and variable delay: it is not sufficient that all processes be fast. Moreover, activation reactions operating on distinct time scales must be reconciled with the requirement that caspases be held safely in check under most circumstances. Our analysis establishes that cell death is dependent on a multi-step feed-forward circuit involving several parallel processes, rather than on simple feedback. Through simulation and experimentation we identify distinct failure modes in the apoptosis switch and suggest that at least one has the potential to promote genomic instability and oncogenic transformation.

2.2 Introduction

Activation of executioner caspases (caspases-3 and-7; hereafter C3), the hallmark of apoptosis, is triggered by intracellular events such as DNA damage, oxidative stress, and chemical insult (intrinsic cell death), and by extracellular stimuli such as TNF (Tumor necrosis factor), TRAIL (TNF -related apoptosis-inducing ligand), and Fas ligand (extrinsic cell death). Apoptosis is essential for many developmental processes but is misregulated in diseases as diverse as cancer and autoimmunity (Green and Evan 2002). Caspases directly cleave essential cellular proteins and activate specialized DNAses, thereby dismantling both the proteome and genome (Fischer et al. 2003). At the single-cell level, caspase activation occurs in an all-or-none manner (Tyas et al. 2000; Rehm et al. 2002) ensuring that once begun, DNA and protein degradation are carried to completion. Otherwise, sub-lethal cellular damage, indeterminant physiological states, and severe genomic instability might result. Quantitative understanding of all-or-none caspase activation is incomplete, despite a variety of competing informal and mathematical models that seek to explain the regulation of cell death (Fussenegger et al. 2000; Bentele et al. 2004; Eissing et al. 2004; Bagci et al. 2005; Hua et al. 2005; Stucki and Simon 2005).

In this paper we combine time-resolved measurement of apoptosis in single TRAIL- or TNF-treated cells with perturbation of specific proteins by RNAi or over-expression to construct an experimentally-validated mathematical model of receptor-mediated apoptosis. We use simulation to derive insight into the control of extrinsic apoptosis under normal circumstances and concepts derived from the engineering field of failure analysis (failure mechanism modeling) to understand how control can break down.

We identify several distinct forms of failure with the potential to contribute to human disease.

2.3 Results

2.3.1 A quantitative description of caspase activation in single cells

As a first step in describing receptor-mediated apoptosis quantitatively, we measured the response of cells to TNF and TRAIL. When HeLa cell cultures were exposed to either ligand, a graded dose-dependent response was observed in which the number of dead cells increased gradually over a period of ~24 hr (see also Chapter 4) (Janes et al. 2005). However, when C3 activation was monitored by fluorescence microscopy of cells carrying a FRET-based cleavage reporter, all-or-none activation was observed at the single-cell level. FRET reporter cleavage occurred within a few minutes of morphological manifestations of apoptosis, such as cell shrinkage and membrane blebbing, demonstrating that C3 activation was indeed concomitant with death (Fig 2.1A,B) (Rehm et al. 2002). As previously shown, the amount of C3 substrate cleaved in single cells at time *t* can be represented by a Boltzman equation with three parameters: T_d, the delay time preceding cleavage; T_s, the switch time from minimum to maximum cleavage; and *f*, the final fraction of substrate cleaved (Eq 1; Fig 2.1C):

$$[cPARP(t)] = \frac{f}{1 + e^{-4.0\frac{t - T_d}{T_s}}} \qquad \text{Eq. 1 (Rehm et al. 2002)}$$

T_d, T_s, and *f* were determined by monitoring FRET signals in cells exposed to TNF or TRAIL at concentrations ranging from saturating to roughly physiological (with >100 cells monitored per condition). T_s was found to be short and nearly constant (15-30 min, see Table S1 for actual values) and *f* high (~1.0) regardless of the concentration or identity of the ligand (Fig 2.1D). Conversely, T_d was highly variable from cell to cell (60

- >720 min) and both its mean and variance were sensitive to ligand concentration (Fig 2.1E). Low doses of TRAIL were associated with long and variable T_d relative to saturating TRAIL, as were all concentrations of TNF (Fig 2.1E, Table S1). Thus, the caspase activation network triggered by TNF and TRAIL constitutes a switch that waits for a variable interval before transitioning rapidly and irreversibly from open to closed – a so-called irreversible, snap-action, variable-delay switch. Integration of live-cell imaging data over many cells reveals the importance of variability in T_d for a graded response to death ligand at the population level, given that T_s and f are essentially constant (Fig. S1). The importance of these findings from the perspective of modeling is that they impose more complex requirements on the apoptosis regulatory circuit than rapid caspase activation alone.

Live-cell imaging allows the behavior of single cells to be monitored in detail but is relatively low-throughput relative to flow cytometry, another single-cell technique. Flow cytometry also allows cleavage of endogenous substrates (rather than artificial reporters) to be monitored, albeit with loss of information on the history of single cells (Irish et al. 2006). When cells were treated with TNF or TRAIL over a range of concentrations, stained with antibody against the cleaved form of the endogenous C3 substrate PARP (cPARP) (Li and Darzynkiewicz 2000), and subjected to flow cytometry, a bimodal distribution was observed in which PARP was entirely full length in a subset of cells and entirely cleaved in others (Fig. 1F). Very few cells (<5%) were present in which a fraction of PARP was cleaved. Application of a simple data model to the flow cytometry results (see Fig. 2.S2) made it possible to derive switching values ($T_s \sim 20$ min, $T_d \sim$ 60-400 min, and $f \sim 1.0$ Fig. 1F) that were very close to values obtained by live cell imaging, thereby confirming that data derived from the two methods can be fused.

Very similar results were obtained by flow cytometry with an antibody against cleaved cytokeratin, another C3 substrate (data not shown), suggesting that the behavior of cPARP is generally representative of endogenous executioner caspase substrates.

Data modeling also revealed that flow cytometry profiles for cPARP should show distinctive changes with variation in T_d, T_s, or f (Fig 2.S2): (i) when T_d increases with T_s and f constant, so that efficient snap-action switching is retained, cPARP-positive cells accumulate more slowly, but there is no increase in cells with intermediate cPARP; (ii) if T_s increases with f constant, there is a breakdown of snap-action behavior and the appearance of cells in which PARP is partially cleaved at short, but not at long, times ($f \rightarrow 1.0$ as $t \rightarrow \infty$); (iii) if f decreases with or without changes in T_d and T_s, a steady accumulation of cells with partially cleaved PARP is observed. Scenario (i) corresponds to effective regulation of cell death, albeit at an altered sensitivity to death ligand, whereas scenarios (ii) and (iii) represent failure modes.

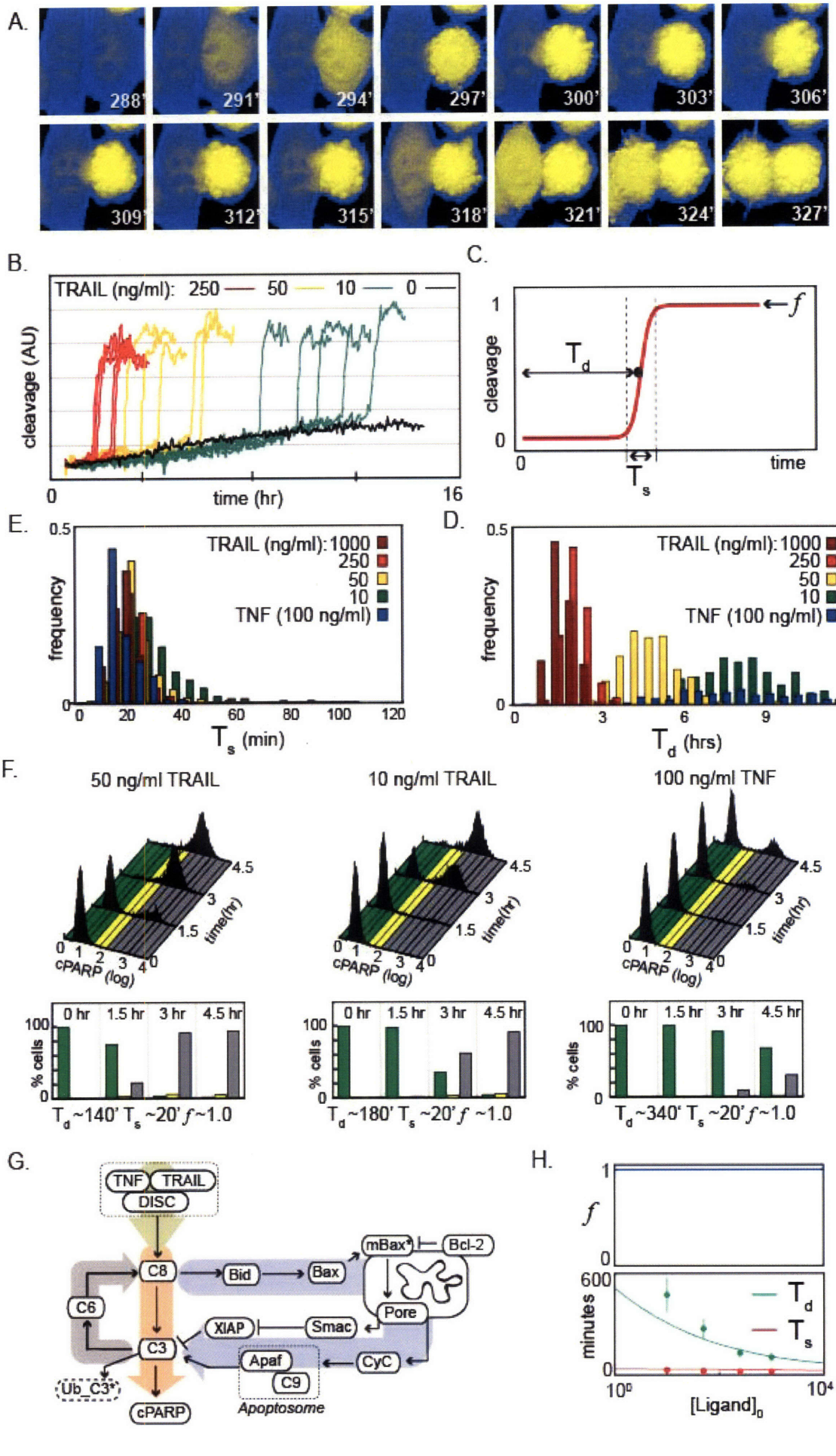
A.
288'
291'
294'
297'
300'
303'
306'
309'
312'
315'
318'
321'
324'
327'
B.
TRAIL (ng/ml): 250 50 10 0
cleavage (AU)
0
time (hr)
16
C.
1
cleavage
0
f
T_d
0
time
T_s
E.
0.5
frequency
0
TRAIL (ng/ml): 1000
250
50
10
TNF (100 ng/ml)
0 20 40 60 80 100 120
T_s (min)
D.
0.5
frequency
0
TRAIL (ng/ml): 1000
250
50
10
TNF (100 ng/ml)
0 3 6 9 12
T_d (hrs)
F.
50 ng/ml TRAIL
10 ng/ml TRAIL
100 ng/ml TNF
4.5
3
1.5
time(hr)
0
cPARP (log)
0 1 2 3 4
0 hr 1.5 hr 3 hr 4.5 hr
100
% cells
0
T_d~140' T_s~20' f~1.0
T_d~180' T_s~20' f ~1.0
T_d~340' T_s~20' f~1.0
G.
TNF
TRAIL
DISC
C8
Bid
Bax
mBax
Bcl-2
Pore
C6
XIAP
Smac
C3
Apaf
CyC
C9
Ub_C3*
cPARP
Apoptosome
H.
1
f
0
600
minutes
0
T_d
T_s
10^0
10^4
[Ligand]_0

Figure 2.1. Properties of receptor-mediated cell death in single cells. A. Ratiometric images of HeLa cells carrying a stably expressed caspase reporter, in which cleavage alters the FRET signal, treated with 50 ng/ml TRAIL. Loss of FRET signal, indicative of substrate cleavage, is shown by a shift in color from blue to yellow. B. Plots of substrate cleavage for individual cells treated with varying amounts of TRAIL or TNF (as indicated by color code). The slow rise in FRET signal prior to a sudden increase appears to represent a photobleaching effect that is independent of caspase activation C. Idealized time course of substrate cleavage in a single cell as represented by the Boltzmann equation (see Eq.1 in text). D,E. T_s and T_d were measured by live-cell microscopy of HeLa cells treated with varying concentrations of death ligand (n>100 for each condition); frequency distributions based on a binning interval of 30 min. F. cPARP levels were measured by flow cytometry at various timepoints after treatment with TNF or TRAIL as indicated. The colored regions underlying each histogram represent cells with approximate levels of PARP cleavage of <5% (green), 5-20% (yellow), or >20% (grey). Bar graphs below each set of histograms represent a discretization of the flow data in which the percent of cells falling into each PARP cleavage class are quantitated. G. Schematic diagram of TRAIL-induced apoptotic pathways; the major features of the network are indicated as large colored arrows: beige – receptor module; red – direct caspase cascade; grey – positive feedback loop; blue – mitochondrial feedforward loop. H. Simulation of T_d, T_s, and f values as functions of ligand concentration using our ODE model.

2.3.2 A mathematical model of extrinsic cell death

To determine how caspases and their regulators set T_d, T_s, and f, we constructed a mathematical model of protein pathways activated by TNF and TRAIL receptors. The model was based on mass-action chemical kinetics involving uni- or bi-molecular elementary reactions as represented by a coupled set of non-linear ordinary differential equations (ODEs; see Section 2.6). No arbitrary or fitted algebraic forms were introduced that might generate cooperativity or ultrasensitivity *a priori*. Moreover, since ODE models are very sensitive to errors in connectivity, we included only well-

substantiated reactions in the model, at the cost of excluding some interesting processes. The ODE model included four sets of reactions whose components and connectivity were derived from the literature (Fig 2.1G): (i) a lumped-parameter receptor module linking binding of TNF and TRAIL ligands to their cognate receptors and then to activation of caspase-8 (C8) to form cleaved caspase-8 (C8*); (ii) an enzyme cascade in which C8* cleaves C3 and activates it to form C3*, which then cleaves PARP to form cPARP; (iii) a positive feedback loop in which caspase-6 (C6) is cleaved by C3* to form C6*, which then activates additional C8; and (iv) a mitochondrial feed-forward pathway, in which C8*, via its substrate Bid, promotes formation of Bax-containing pores in the mitochondrial membrane, through which cytochrome c (CyC) and Smac translocate to the cytosol to form the apoptosome (which also generates C3*) and neutralize the C3* inhibitor XIAP. In its granularity, the model aims to be reasonably complete with respect to biochemical mechanism, but three simplifications were made to reduce the number of biochemical species and associated free parameters. First, receptor-dependent "death-inducing signaling complexes" (DISCs) were not modeled in detail; second, proteins with similar biochemical activities were lumped into a single species (e.g. C8 and C10 are represented by C8 alone; C3 and C7 by C3 alone; see Section 2.6); and third, transcription was omitted because all experiments were performed in the presence of cycloheximide (which is commonly used to sensitize cells to the action of TNF but in our experiments serves to simplify the overall reaction network). Values for kinetic parameters and initial protein concentrations were determined from the literature, by direct measurement, and by induction, as described in detail in Section 2.7. It is important to note however, that our model, like virtually all physico-chemical models of mammalian cell signaling, has not yet been formally calibrated against data so as to

rigorously constrain parameter values. Thus, in the absence of other information, kinetic rate constants and initial conditions in the model were set to intermediate values within a range that was physically plausible. The final model contained 58 species (corresponding to 18 distinct gene products with non-zero initial conditions, and 40 additional species representing complexed, cleaved, or differentially localized forms) and 28 reactions described by 70 non-zero rate constants (including forward, reverse, and catalytic rates for each reaction).

To ensure that our model accurately reflected the mechanisms of snap-action switching in Hela cells, we applied an iterative process of experimental perturbation and model regression. Experimentally, proteins throughout the network were depleted by siRNA (typically, three independent siRNA oligos were examined for each gene) or were stably overexpressed as retroviral constructs under the control of a viral promoter. For each perturbation, levels of depleted or over-expressed proteins were determined by immunoblotting (Fig 2.S3), and T_d, T_s, and f were estimated by flow cytometry following treatment with TRAIL. Changes in protein concentrations correspond in the model to changes in the initial concentration of that species (denoted as $[X]_0$ for species X). Thus, for each experiment, the initial conditions in the model were adjusted to reflect measured changes in concentration of a depleted or overexpressed protein, and changes in T_d, T_s, and f were determined by simulation. Importantly, the final model correctly predicted the dependence of T_d, and independence of T_s and f, on ligand dose (Fig 2.1H). The constrained model was therefore studied further for insight into the mechanisms and failure modes of C3 regulation, as described in detail below.

2.3.3 Feedforward control of snap-action behavior

Because positive feedback plays a role in many all-or-none biological transitions (Ferrell and Xiong 2001; Eissing et al. 2004), we examined the role played by the C6 positive feedback loop in C3 activation (Cowling and Downward 2002). 10-fold depletion of C6 by RNAi did not significantly alter the dynamics of cPARP accumulation in cells treated with TNF or TRAIL (relative to control depletions; T_d,~70 min; T_s,~20 min; f.~ 1.0, Fig 2.2A, B). Independence on C6 was also captured by the model: snap-action PARP cleavage was retained even when C6 was removed completely (Fig 2.2C). Remarkably, however, simulation shows that C6* nonetheless plays a major role in determining overall levels of C8* in dying cells (Fig 2.2D). If the generation of C8* is separated into its two sources, DISC and C6*, it is apparent that a dramatic acceleration in C8* formation is induced upon C6* activation. *A priori,* it might be assumed that this acceleration would constitute a key feature of snap-action switching. However, C8* generated by C6* lags temporally behind C8* generated by DISC and is present only after rapid cleavage of PARP has begun, making it inconsequential for the dynamics of TRAIL-mediated cell death (Fig 2.2D). Although parameter values can be found in which the kinetics of PARP cleavage do depend substantially on the C6* feedback loop (either $[C6]_0$, or the rate of C8 cleavage by C6* must be high) these conditions do not appear to pertain to unperturbed or RNAi-treated Hela cells. However, they might occur in cells with a different form of caspase regulation. Importantly, however, C6-mediated positive feedback does not appear to be essential for snap-action C3 activation under our conditions.

We therefore turned to the mitochondrial feed-forward circuit. Bcl-2 over-expression (Fig 2.2E) or Bid depletion by RNAi (data not shown), both of which prevent

formation of Bax-containing pores in the mitochondrial membrane (Fig 2.S4), strongly blocked PARP cleavage (f<0.04) and cell death in response to TNF or TRAIL. However, when Bcl-2-overexpressing cells were examined by Western blotting, efficient processing of C3 to its active form C3* was observed (Fig 2.2F). C3 processing was C8*-dependent (as demonstrated by RNAi of C8, Fig 2.S5), even though C3* catalytic activity and PARP cleavage were absent. The absence of C3* activity despite processing of C3 to its active form suggested that C3* must be held in check by an inhibitor. In Hela cells this protein is most likely XIAP, which binds to and blocks C3* activity, and also acts as a ubiquitin-targeting E3 enzyme. Bax-mediated mitochondrial permeabilization blocks the inhibitory activity of XIAP (thereby activating C3*) by mediating the release of the XIAP-binding protein Smac. In Bcl-2-overexpressing cells, Smac is retained in mitochondria and cytosolic XIAP is free to inhibit C3* (Zhang et al. 2001; Deng et al. 2002; Li et al. 2002; Sun et al. 2002). The logic of these binding and translocation events is such that the block on apoptosis imposed by Bcl-2 overexpression should be overcome by XIAP depletion (Wilkinson et al. 2004). To confirm this prediction, Bcl-2-overexpressing cells were treated with siRNA against XIAP and the response to TRAIL examined. As expected, PARP cleavage was restored, but strikingly, snap-action switching failed, with T_s increasing dramatically to ~120 minutes and f falling to ~0.1 (Fig 2.2F,G). Even at the 24hr time point PARP cleavage was incomplete and virtually all cells displayed partial PARP cleavage, appearing as a single peak with median f~0.1 (Fig 2.2H). Remarkably, 45% of cells from this experimental condition were viable when replated into fresh medium, demonstrating that they had sustained a sub-lethal level of C3-mediated damage (Fig 2.2G). Thus, inactivation of the mitochondrial feedforward pathway is associated with two distinct failures in the control of apoptosis: cells activate

effector caspases only slowly (long T_s) and they do not commit decisively to apoptosis (low f).

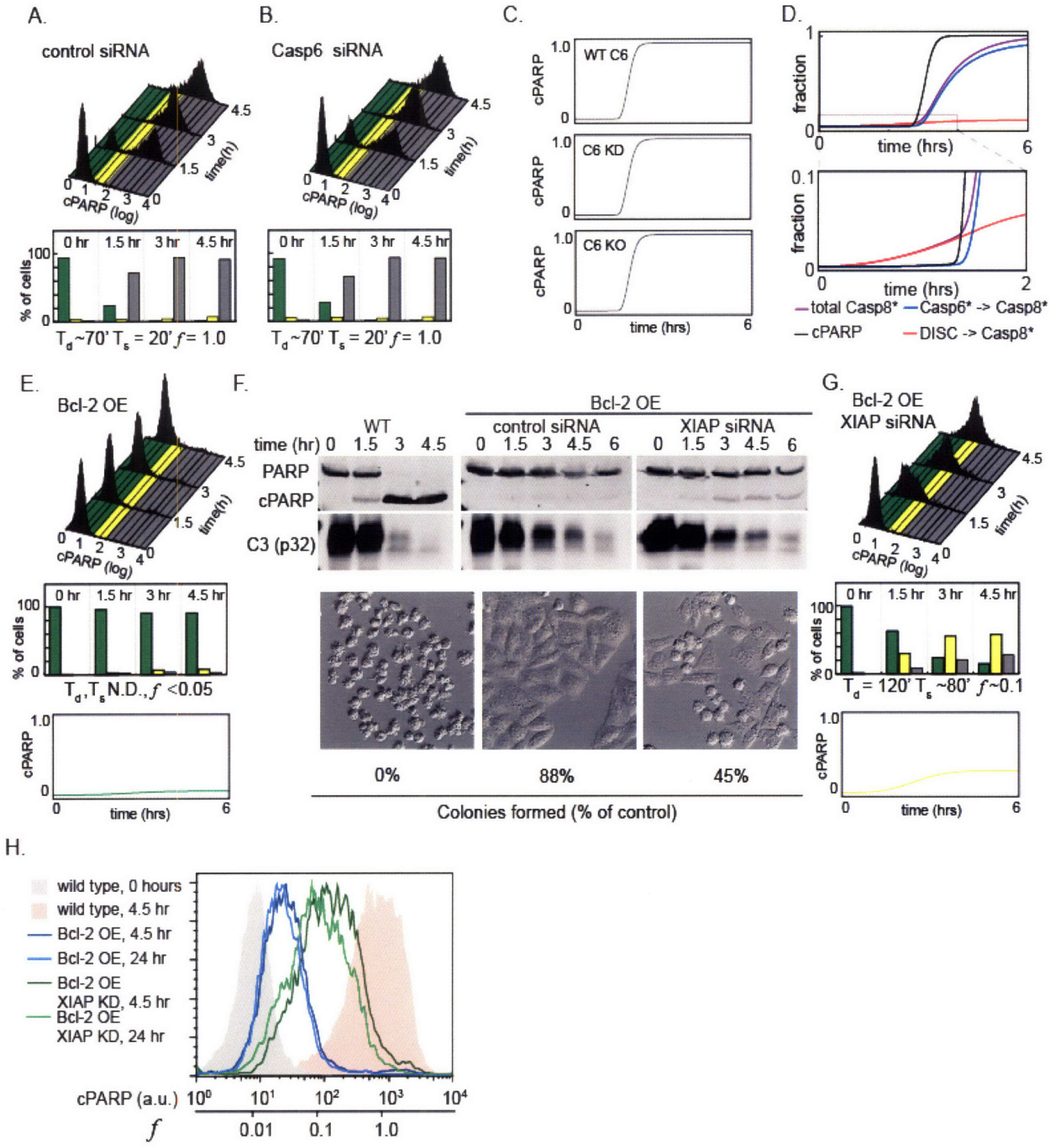

Figure 2.2. The mitochondrial pathway is critical for snap-action PARP cleavage. A, B. HeLa cells transfected with control or C6-targeting siRNA oligos were treated with 50 ng/ml TRAIL, and cPARP was measured as in Fig. 1. C. Simulations of PARP

cleavage in response to TRAIL in cells with $[C6]_0$ at wild type levels (WT), 10-fold knockdown (KD), or completely absent (KO). D. Simulated time courses of cPARP, total C8*, C8* produced by the DISC, and C8* produced by C6*. E. Bcl-2-overexpressing cells transfected with control siRNA were treated with 50 ng/ml TRAIL and cPARP was measured as in Fig. 1. Simulation of PARP cleavage in Bcl-2 overexpressing cells is shown at bottom. F. Control or Bcl-2-overexpressing HeLa cells were transfected with the indicated siRNA oligos and treated with 50 ng/ml TRAIL. PARP and C3 processing were analyzed by immunoblot. Differential interference contrase images of each condition were taken at 4.5 hours, and clonogenic survival was assessed by a colony-forming assay after 4.5 hours of treatment; percentages denote the number of colonies after TRAIL treatment relative to untreated controls. G. Bcl-2-overexpressing cells transfected with $XIAP_{0.15}$ siRNA were treated with 50 ng/ml TRAIL and cPARP was measured as in Fig. 1. Simulation of PARP cleavage in Bcl-2 overexpressing, XIAP-depleted cells is shown at bottom. H. Control or Bcl-2-overexpressing HeLa cells were transfected with control or $XIAP_{0.15}$ siRNA, and treated with 50 ng/ml TRAIL. HeLa cells were treated as indicated and cPARP levels were analyzed by flow cytometry at 4.5 and 24 hours. Levels of cPARP are indicated by two x-scales, one showing arbitrary units of fluorescence, and one showing the calculated value of f, which was determined by normalizing the fluorescence units to the peak intensity of cells with complete PARP cleavage (shown in pink).

2.3.4 Mechanism of partial PARP cleavage

The failure of Bcl-2-overexpressing/ XIAP-depleted cells, to fully cleave PARP after many hours was initially puzzling; C3* is a very potent enzyme, present at $\sim 10^4$ copies/cell (Stennicke et al. 1998). Simulation confirmed our impression *a priori* that activating even 1% of the C3 in a Hela cell (i.e. $\sim 10^2$ C3*) should be sufficient for full PARP cleavage over a period of several hours (data not shown). However, analysis of Bcl-2-overexpressing/ XIAP-depleted conditions revealed a possible mechanism by

which PARP cleavage might never go to completion. C3* (but not C3) is degraded via XIAP-dependent ubiquitination and subsequent proteasomal proteolysis (Suzuki et al. 2001; Chen et al. 2003). Under conditions in which mitochondria are not permeabilized due to Bcl-2 overexpression and XIAP is depleted to 15% of its normal level, the rate of C3* production by C8* is only slightly greater than its rate of degradation, and only a small amount of active enzyme accumulates (Fig 2.3A). Eventually, precursor C3 is exhausted, with the net effect that C3* is generated in a pulse of limited duration and magnitude sufficient to partially, but not fully, cleave PARP. In sum, in our model, short C3* half life and efficient inhibition of C3* by XIAP (ensured by a K_d of 10^{-9}M), are both preconditions for partial PARP cleavage (Fig 2.3A). Moreover, cell survival requires that cPARP levels be quite low, since we estimate an LD_{50}(cPARP) of 0.1 (Fig. 2F, 2.S6).

A testable prediction from modeling is that *f* should be very sensitive to the rate of C3* degradation and the consequent size of the C3* pulse in Bcl-2-overexpressing cells (Fig 2.3B). Cells overexpressing Bcl-2 were therefore treated with a constant level of TRAIL and varying concentrations of the proteasome inhibitor MG-132, followed by flow cytometric analysis of cPARP (Fig 2.3C). With increasing MG-132 (and decreasing C3* degradation – data not shown), *f* was observed to increase in a dose-dependent manner from ~0.05 to ~1.0. Under some conditions, *f* reached its limit value more rapidly in cells than in simulation (within 6 rather than 12 hr., Fig 2.S6) probably because details of C3* degradation were absent from the ODE model. Nonetheless, good overall agreement between simulation and experiment supports the conclusion that partial PARP cleavage and incomplete cell killing represents a distinctive form of failure in the regulation of apoptosis. In Bcl-2-overexpressing/XIAP-depleted cells, incomplete death

arises because C8* alone does not generate sufficient C3* to counteract the combined effects of C3* degradation and residual XIAP-mediated C3* inhibition.

While proteasome inhibition and gross alteration of Bcl-2 and XIAP protein levels abolished snap-action behavior, it was unclear how sensitive switching was to smaller changes in these parameters. We therefore simulated f in TRAIL-treated cells across a wide range of physically reasonable values of $[Bcl\text{-}2]_0$, $[XIAP]_0$ and the rate of XIAP-mediated C3* degradation (Fig 2.3D,E). We found that many conditions were compatible with efficient cell killing ($f \sim 1.0$, gray areas) whereas others corresponded to an inactive death pathway ($f \sim 0$, green areas). However, failure of snap action switching ($0<f<1.0$) occurred over a fairly broad region in the $[Bcl\text{-}2]_0$ vs. $[XIAP]_0$ landscape (denoted by yellow). At high levels of $[Bcl\text{-}2]_0$, in particular, f increased gradually as XIAP levels decreased (Fig 2.3D, red arrow). To confirm this prediction, we searched for an siRNA oligo that would deplete XIAP to ≤5% of its original level ($XIAP_{0.05}$; Fig 2.S7) as compared to the $XIAP_{0.15}$ oligo used in the experiments of Fig 2.2G, which depleted XIAP to ~15% of its original level. We observed that transfection of Bcl-2-overexpressing cells with $XIAP_{0.05}$ resulted in $f \sim 0.6$, as compared to $f \sim 0.1$ with $XIAP_{0.15}$, confirming our prediction (these points are denoted by positions 4 and 3, respectively, in Fig. 3D). A landscape divided between regions of high, low, and intermediate values for f was also observed when $[Bcl\text{-}2]_0$ was plotted against the rate of XIAP-mediated C3* degradation (Fig 2.3E), explaining our ability to vary f in a dose-dependent manner with MG-132 (Figure 2.3E, red arrow). Thus, data and simulation suggest that when the mitochondrial pathway is not efficiently activated, f is a continuous variable of $[XIAP]_0$ and the rate of C3* degradation, leaving the apoptotic network vulnerable to partial activation over a fairly wide range of conditions.

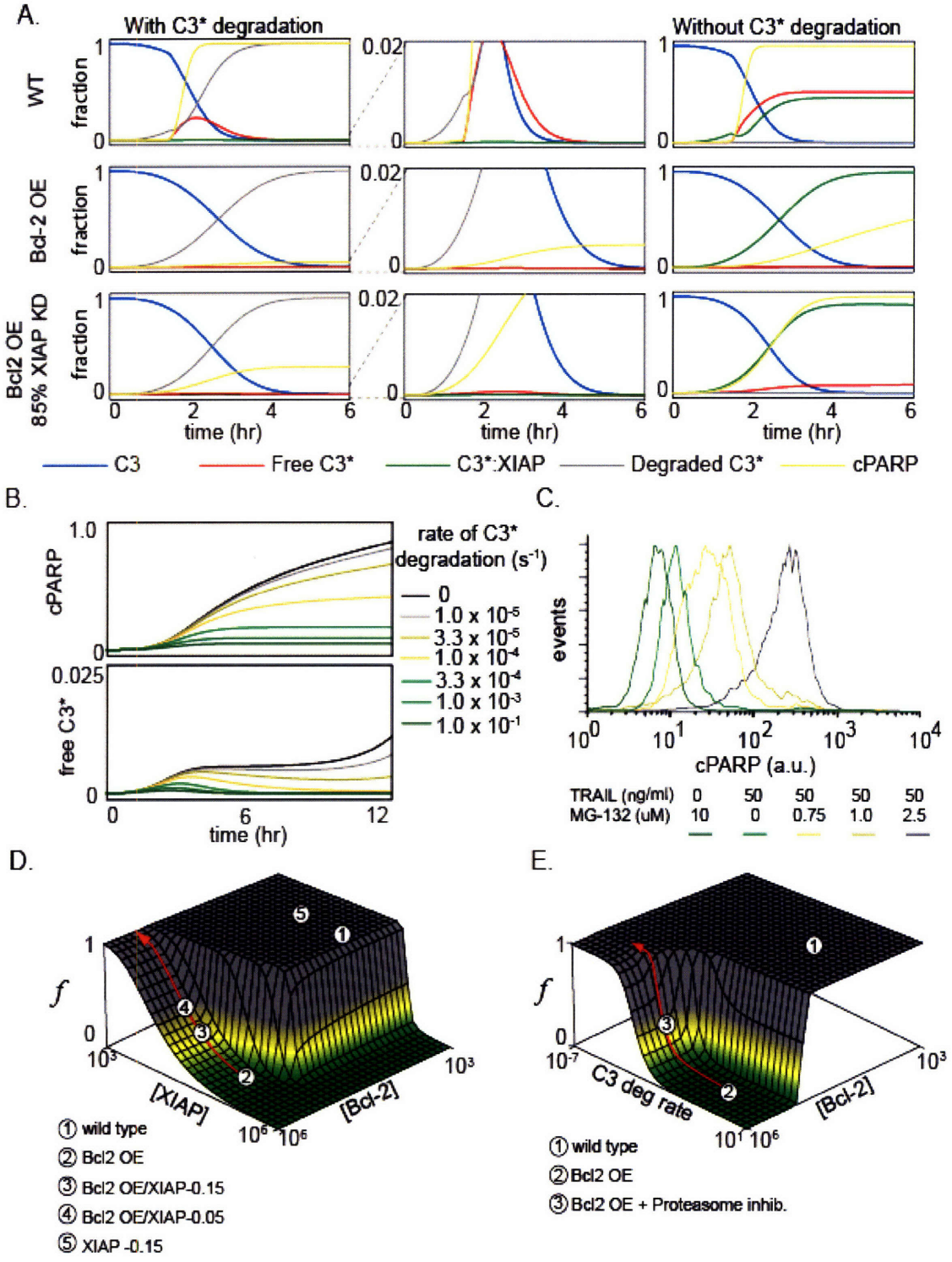

Figure 2.3. Role of C3 degradation and XIAP in switching parameters. A. Simulation of time courses for C3, C3* (divided into free/active, XIAP-bound, and degraded forms), and PARP for the indicated conditions; simulations are shown at full scale (left column),

at magnified scale to highlight low-abundance species (center column), and in the absence C3 degradation (right column). B. Simulation of the time courses of cPARP and C3*, in which the rate of XIAP-mediated C3* degradation was varied as indicated. C. Bcl-2- overexpressing HeLa cells were co-treated with 50 ng/ml TRAIL and the indicated concentrations of MG-132; cPARP levels were measured by flow cytometry after 6 hours, a time sufficient to reach steady state in all conditions (see Fig 2.S6). D,E. Simulation of f as a function of $[Bcl\text{-}2]_0$ and $[XIAP]_0$ (D), or of f as a function of $[Bcl\text{-}2]_0$ and the rate of C3* degradation by XIAP (E); numbered circles denote points corresponding to the indicated experimental conditions. Red arrows denote a region of parameter space in which f is a continuous function of (D) $[XIAP]_0$ or (E) rate of C3* degradation.

2.3.5 Signal transmission and ratiometric control of snap-action behavior

Because mitochondrial feedforward is essential for snap-action switching, the proteins responsible for transmitting the signal from mitochondrial permeabilization to C3 activation should also be important. We observed that RNAi-mediated depletion of Smac (to ~10% of initial levels) resulted in $f \sim 0.1$ in TRAIL-treated cells (Fig 2.4A). This represents a phenocopy of Bcl-2 overexpression/XIAP-depletion (Fig 2.2E) except that the Smac depletion was more heterogeneous in terms of f values. That XIAP is indeed the critical target for Smac was demonstrated by the observation that simultaneous RNAi-mediated depletion of Smac and XIAP restores rapid, efficient PARP cleavage ($f \sim 1.0$; $T_s \sim 20'$; $T_d \sim 60'$; Fig 2.4B).

The effects of RNAi-mediated depletion of Smac alone or of Smac and XIAP together can be understood in terms of movement along a landscape of predicted f values from an unperturbed state in which switching was efficient (position 1 in Figure 4C), to a second state at which switching was inefficient (position 2), and then to a third efficient

state with short T_s and high f but in which $[Smac]_0$ and $[XIAP]_0$ are both ~10-fold lower, (position 3). The value of f is also predicted to be highly sensitive to Smac levels near the $[Smac]_0=[XIAP]_0$ threshold, providing an explanation for the heterogeneity in f following RNAi of Smac: cell-to-cell variations in Smac concentrations are an inevitable consequence of RNAi-mediated protein depletion. Overall, our data are consistent with the hypothesis that states in which $[Smac]_0/[XIAP]_0 < 1.0$ are associated with a disruption of the mitochondrial feedforward signal and inefficient commitment to apoptosis. However, it is possible that under these conditions caspase-independent cell death might occur, as has been observed in cells in which mitochondria permeabilize but caspases are inhibited (Chipuk and Green 2005).

The apoptosome, a complex whose assembly is triggered by cytosolic translocation of CyC and subsequent association of Apoptosis-activating factor-1 (Apaf-1) and C9, is known to play a role in apoptosis via C9*-mediated cleavage of C3 to C3* (Zou et al. 1997). Depletion of Apaf-1 by RNAi appeared to phenocopy RNAi-mediated depletion of Smac by increasing T_s and decreasing f, an effect that was reversed by simultaneous depletion of XIAP (although results with multiple Apaf-1 oligos produced highly variable results, Fig 2.S8). Our model contains a simplified version of the apoptosome, since much remains unknown about its stoichiometry *in vivo*. Simulation suggested however, that the C3-processing activity of C9* in the apoptosome was not critical for snap-action switching, since inactivation of this function resulted in only a moderate decrease in T_s (Fig 2.S9). Instead the XIAP-binding activity of the apoptosome (Bratton et al. 2002; Hill et al. 2004) was necessary for both low T_s and high f because it sequesters XIAP away from C3* (Fig 2.S9). This is an intriguing hypothesis, but remains speculative in the absence of an experimental analysis that separates the catalytic

activity of C9 from its XIAP-binding function. Regardless of the specifics of apoptosome activity, when f was plotted as a function of $[Smac]_0$ and the concentration of the apoptosome (for simplicity, we set $[C9]_0$, = $[Apaf\text{-}1]_0$ in this simulation), f was high only if the sum of the two XIAP-binding species was greater than $[XIAP]_0$ (Fig 2.4D). This explains why snap-action switching was abrogated by depletion of either Smac or Apaf-1, since either reduced the total XIAP-sequestering activity (see Fig 2.S8 for further discussion of this point).

The potential for coordinate action between the apoptosome and Smac is also observed in a plot of f as a function of $[XIAP]_0$ and $[Smac]_0$ (Fig 2.4C). The transition between high and low f falls along the line where $[XIAP]_0$=$[Smac]_0$, down to $[Smac]_0$ = 10^4 per cell, at which point f is no longer sensitive to further reduction in Smac levels. This discontinuity at $[Smac]_0 = 10^4$ represents the point at which the apoptosome becomes the primary determinant of XIAP inactivation. Depending on where on these surfaces the initial conditions lie, either Apaf-1, Smac, or the combination of Smac and Apaf-1 could be the dominant suppressor of XIAP activity, perhaps explaining why Smac appears critical in some cell types (Zhang et al. 2001; Deng et al. 2002; Li et al. 2002; Sun et al. 2002; Chipuk and Green 2005), but the Apaf-1/XIAP ratio is determinative in others (Wright et al. 2004; Potts et al. 2005).

While many regions in the plots of f as a function of $[XIAP]_0$, $[Smac]_0$, C3* degradation rate, etc. are flat, implying insensitivity to changes in parameter values, f changes rapidly in other areas. Cells living in regions of rapidly changing f will be highly sensitive to small changes in protein concentration. An oft-stated assumption about cellular networks is that they are "robust" to changes in parameters (Stelling et al. 2004) but our data strongly suggest that, with respect to apoptosis, Hela cells do not exhibit this

type of robustness for several key variables. Whether this proves true in general remains to be determined, but we speculate that sensitivity rather than robustness may be important for a process such as apoptosis that is regulated by many physiological stimuli.

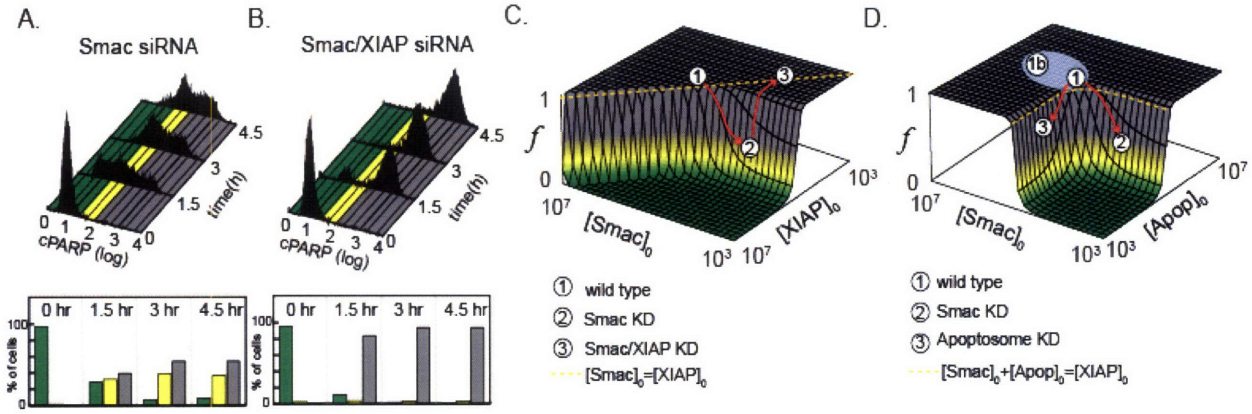

Figure 2.4. Transmission of the mitochondrial signal by Smac and apoptosome formation. A,B. HeLa cells transfected with Smac siRNA oligo or Smac and $XIAP_{0.05}$ siRNA oligos in combination, were treated with 50 ng/ml TRAIL and cPARP levels were analyzed as in Fig. 1. C, D. Simulation of *f* as a function of $[Smac]_0$ and $[XIAP]_0$ (C), or of *f* as a function of $[Smac]_0$ and $[Apop]_0$ ($[Apop]_0$ is equivalent to $[C9]_0$ and $[Apaf\text{-}1]_0$, which were assumed to be equal) (D). Dotted lines denote regions of parameter space in which (C) $[Smac]_0$ equals $[XIAP]_0$ or (D) the sum of $[Smac]_0$ and $[Apop]_0$ equals $[XIAP]_0$. The numbered circles correspond to points sampled experimentally; see text for details. The blue region surrounding point 1 in D denotes a region of uncertaintyand "1b" an alternate location for the wild type condition. These ambiguities arise from uncertainity in the extent of Apaf-1 depletion by siRNA (see Fig 2.S8).

2.3.6 Dynamic masking of XIAP depletion phenotypes

XIAP appears to play a governing role in controlling snap-action activation of apoptosis. It is essential for preventing PARP cleavage prior to mitochondrial

permeabilization, and it must be efficiently inhibited by proteins released from the mitochondria for PARP cleavage to proceed. Given this role, it is surprising that previous studies have observed only a mild phenotype associated with XIAP deletion (Harlin et al. 2001). Simulation suggested that completely removing XIAP should alter sensitivity to TRAIL (Fig 2.5A). Indeed, with $[XIAP]_0 = 0$ in our model, noise rejection was greatly diminished and T_d was short at even very low TRAIL concentrations. This is consistent with data showing that Hct-116 cell lines lacking XIAP are abnormally responsive to TRAIL (Cummins et al. 2004). Low XIAP levels are also predicted to allow (premature) cleavage of PARP in the time preceding mitochondrial permeabilization (Fig 2.5B). To confirm this prediction, XIAP-depleted and unperturbed cells were treated with TRAIL and cPARP levels determined (Fig 2.5C). At early times (1.5 hr after TRAIL addition), flow cytometry of XIAP-depleted, but not of control cells, revealed a clear subpopulation in which PARP was partially cleaved (f ~0.02 to 0.1, Fig 2.5B, shaded orange area) as well as a population in which PARP was fully cleaved (f ~1.0). f eventually reached 1.0 in all cells by 3 hr (Fig 2.S10). Modeling suggested that premature cPARP cleavage arose because low levels of C3* generated by C8* prior to mitochondrial permeabilization were only weakly inhibited by residual XIAP, leading to conversion of ~ 5% of PARP to cPARP (Fig 2.5B). Complete conversion to cPARP eventually occurs because mitochondrial feedforward kicks in normally (Fig 2.5B, red star). Thus, substantial differences between normal and XIAP-depleted cells early in signaling were obscured by an overwhelming later signal. We refer to this phenomenon as dynamic masking. While we observe in TRAIL-treated HeLa cells that the XIAP phenotype is masked by rapid firing of the mitochondrial pathway, it is possible that,

under other conditions, delayed mitochondrial permeabilization might actually allow states of partial PARP cleavage to persist.

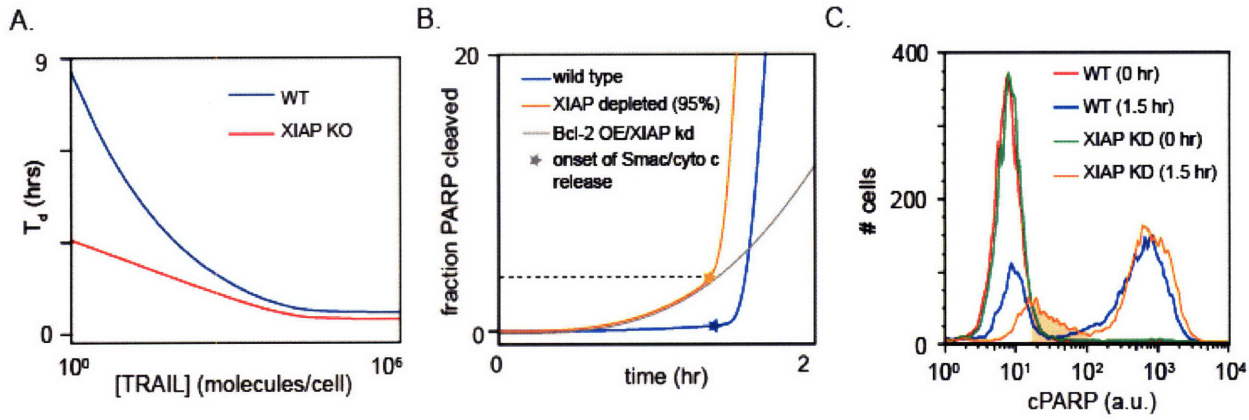

Figure 2.5. Dynamic masking of the XIAP depletion phenotype. A. Simulation of T_d as a function of TRAIL concentration for wild type conditions, or with $[XIAP]_0$=0, as indicated. B. Simulation of the time course of cPARP in wild type, XIAP-depleted, and Bcl-2-overexpressing/XIAP-depleted conditions. Stars denote the time at which Smac/cytochrome c release begins, and dashed lines drawn to the Y-axis indicate the amount of PARP cleavage that preceded Smac/cytochrome c release in each condition. C. HeLa cells transfected with control or $XIAP_{0.05}$ siRNA oligos were treated with 50 ng/ml TRAIL, and cPARP levels were analyzed by flow cytometry at 0 or 1.5 hours.

2.3.7 Mechanistic insights into snap-action, variable delay switching

Simulation makes it possible to infer the dynamics of pro-apoptotic signaling at multiple points in a protein network in a single-cell, something that cannot be accomplished experimentally. In figure 2.6A-K we show the time-dependent evolution of nine biochemical species critical in C3 regulation (calculated, for simplicity, in the absence of C6). Our use of mass-action kinetics makes it possible to interpret these plots by inspection, but the salient features are also amenable to formal mathematical analysis,

something we will describe elsewhere. Apoptotic signaling begins with DISC formation (not shown) and the slow but steady accumulation of C8* (Fig. 2.6B), processing of tBid (Fig. 2.6C), and translocation of Bax (Fig. 2.6D) from the cytosol to the mitochondrial membrane (with 10-fold amplification in the number of molecules involved). Multimerization of membrane-bound Bax (Bax^*_m, Fig. 6F) is inhibited by Bcl-2. Simulation suggests that the relatively slow $C8^* \rightarrow tBid \rightarrow Bax^*_m$ reaction is important for the remarkably long duration of T_d, as is the inhibition of Bax^*_m by relatively abundant Bcl-2. A threshold is reached when $[Bax^*_m]$ exceeds [Bcl-2] (Fig. 6E, denoted by a pink vertical line in Fig 2.6), at which point pores suddenly form in a higher-order reaction, followed by Smac and CyC translocation to the cytosol (Fig. 6G, which is essentially irreversible because it involves diffusion down a steep concentration gradient (Kuwana et al. 2002)). From the perspective of maintaining short T_s, it is necessary that pore formation be at least second-fourth order in Bax^*_m so that the possibility of Bax^*_m-Bcl-2 binding is exhausted prior to the formation of pores. However, when pore formation exceeds sixth order, T_s again becomes longer. These observation are consistent with biochemical evidence that the Bax-containing pore is a 2-8 mer (Antonsson et al. 2001). Translocation of Smac and CyC involves dramatic amplification in the number of molecules (~500 fold) and acceleration in rates of evolution driven by high V_{max}: as few as 10-50 pores appear sufficient to transport 10^5 Smac and CyC molecules in ~10 min. It is noteworthy that pores continue to form hours after their transport task is complete, probably because overshoot is an inevitable consequence of rapid and complete activation. The amount of cytosolic Smac and newly assembled apoptosome are considerably in excess of levels needed to neutralize XIAP (Fig. 6H). At this point de-amplification of the cascade by 10-50 fold is observed in formation of active C3* (Fig.

6I), but the amount of enzyme remains well in excess of what is needed to fully convert PARP to cPARP (Fig. 6K).

Several general points can be deduced from this reaction scheme. First, very few if any reactions in the pathway reach steady state before cell death occurs. Second, signaling does not involve a chain of successively amplified steps, as observed, for example, in glycogen breakdown triggered by protein kinase A. Instead, both amplification (e.g. C8* → Bid → Bax^*_m) and deamplification (e.g. Smac → XIAP → C3*) of rates and number of molecules are observed, but critical steps are mediated by processes with high catalytic capacity. Third, the relative timing of events is frequently critical: a small amount of an active species present at an early time (DISC→C8*) is often more important in determining outcome than a larger quantity later (C6*→C8*). This point is noteworthy because quantitative analysis of cell signaling frequently focuses on differences in protein levels or localization at steady-state and not on transient signals. Fourth, generating a switch that allows for long T_d and short T_s requires interplay between reactions occurring on both long and short time scales (the essence of a stiff system); a variable-delay, snap-action switch cannot occur if every process is fast. Finally, although an analysis of cell death inevitably focuses on the mechanisms of caspase activation, the mechanisms responsible caspase inhibition are at least as complex: C3* is a lethal enzyme that must remain <<1% active for cell survival.

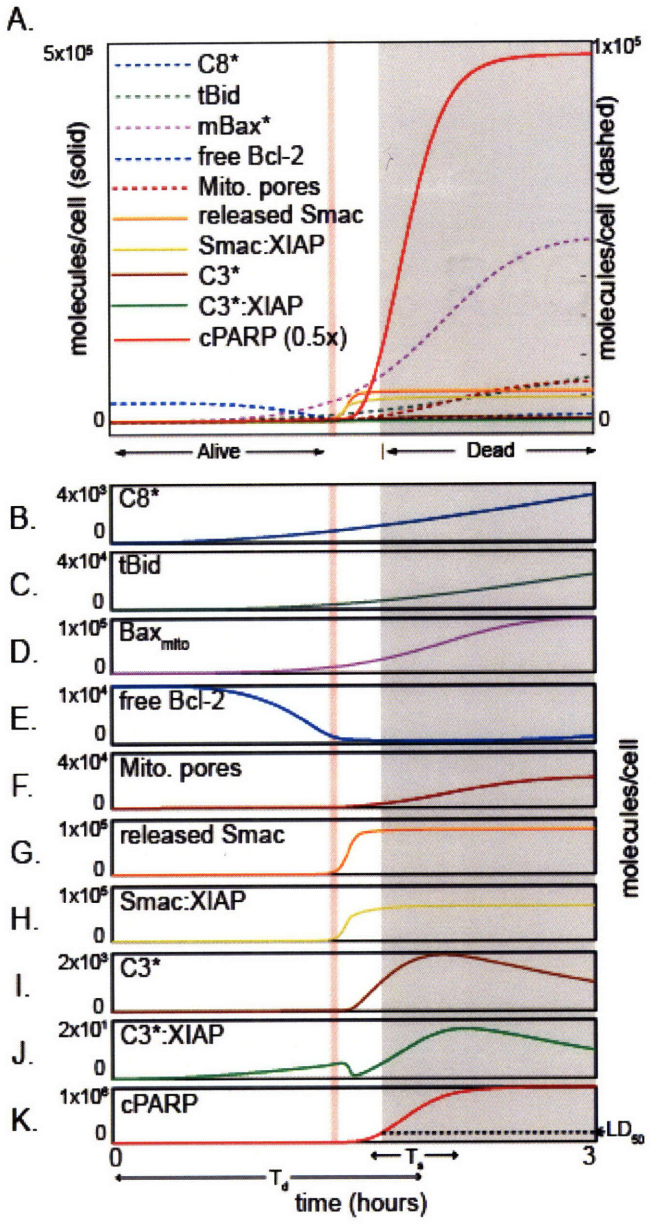

Figure 2.6. Simulation of the levels of key proteins controlling caspase activation in response to TNF and TRAIL. For clarity, positive feedback was omitted by setting $[C6]_0=0$. In (A), all species are overlaid, but three different vertical scales are used to fit species on one graph; the axis on the left is associated with species in solid lines, except for cPARP, which is shown at half-scale; the axis on the right, whose maximum value is 5-fold lower, is associated with species in dashed lines. In the bottom panels (B-K), each species is shown separately, with each vertical axis scaled as indicated. The pink vertical line denotes the time at which all free Bcl-2 is depleted, resulting in the release of CyC/Smac. The LD_{50} for caspase activity (corresponding to ~10% PARP cleavage) is

denoted by a dashed line in the cPARP plot; the gray shaded region denotes time points after this lethal dose has been reached and cells are dead.

2.4 Discussion

Here we describe the use of mathematical modeling and single-cell analysis to derive mechanistic insight into the operation of a highly efficient, snap-action, variable delay switch controlling extrinsic cell death. Accommodating both snap-action and variable delay behaviors is surprisingly demanding, as is the requirement that caspases normally be held safely in check. Our successful inclusion of these features of apoptosis in a mathematical model distinguishes this work from previous efforts. Also valuable, in our opinion, is the decision to restrict modeling to first-order reactions involving mass-action kinetics, thereby avoiding phenomenological forms such as Hill functions and other polynomial expressions. Interesting non-linear behavior in the model arises from the interconnectivity of elementary reactions rather than from *a priori* assumptions.

Hitherto, it has usually been asserted that the key to control of apoptosis is bistability (a local, steady-state phenomenon) (Eissing et al. 2004; Bagci et al. 2005). However, our analysis shows that transient caspase activation seals the fate of a cell long before steady-state is reached. Moreover, a quasi-steady state with very low C3* does not necessarily correspond to sustained survival (given the potency of executioner caspases). The extrinsic cell death pathway achieves a binary outcome through parallel transient reactions whose relative strengths and timing determine C3* activity. The circuit controlling receptor-mediated apoptosis is also unusual in relying on feedforward and successive steps of negative regulation to make switching rapid and delay time long. Variability in delay is probably involved in the dose-response of cell populations to death

ligand but we do not yet know precisely how it arises. Preliminary experiments suggest that differences in rates of reaction upstream of mitochondrial permeabilization are involved (data not shown).

When perturbed by RNAi or small molecules, the C3* regulatory network is characterized by poor noise rejection, loss of snap-action behavior, and low efficiency. The last of these failures, in which $f<1.0$, is the most interesting because it has the potential to generate indeterminate physiological states (Vaughan et al. 2002). Genomic instability is also likely to arise through partial degradation of the genome, mediated by the DFF40 nuclease (Samejima and Earnshaw 2005). Indeed, sub-lethal pro-apoptotic stimuli have previously been linked to induction of chromosomal translocations typical of leukemia (Aplan et al. 1996; Stanulla et al. 1997a; Stanulla et al. 1997b; Vaughan et al. 2005). Moreover, overexpressed Bcl-2, which we identify as a key condition for $f<1.0$ failure, is a potent oncogene in lymphocytes (McDonnell and Korsmeyer 1991). Thus, the oncogenic potential of Bcl-2 overexpression could result not only from extended cell survival, but also accelerated accumulation of genetic lesions induced by the cell's own apoptotic machinery.

In contrast to the focus on robustness in many contemporary efforts to model biological pathways, our work focuses on sensitivity in the apoptosis network and modes of failure. Apoptosis is a highly regulated process associated with a wide range of physiological transformations (Spierings et al. 2005) and the cost of this regulability may be higher susceptibility to failure in the face of mutation. More generally, we believe that a rigorous application of failure analysis to biological circuits (something we have not yet achieved) may prove valuable in understanding how quantitative changes in protein levels or activities contribute to human disease.

2.5 Materials and Methods

Reagents and cell culture

HeLa cells stably expressing pMIG-Bcl-2 or pMIG (empty vector control) were kind gifts of Dr. Fei Hua and Dr. Michael Cardone. Antibodies against cleaved PARP, cleaved caspase-3, XIAP, and Apaf-1 were obtained from BD Biosciences. The antibody against caspase-6 was obtained from Cell Signaling; the antibody against Smac was obtained from Calbiochem. Secondary antibodies for flow cytometry and western blotting were from Molecular Probes (Invitrogen) and Rockland. SuperKiller TRAIL was obtained from Alexis Biochemicals, and cycloheximide (CHX) and MG-132 were from Sigma. siRNA oligos were purchased from Dharmacon.

Inclusion of cycloheximide in death assays

All treatments with TRAIL or TNF were carried out in the presence of 2.5 μg/ml CHX. This treatment retards protein synthesis, and is widely used in the study of TNF and TRAIL-induced apoptosis (Wajant et al. 2000; Munshi et al. 2001). Moreover, all published single-cell observations of all-or-none caspase FRET reporter cleavage in response to death receptor stimulation have been performed in the presence of CHX (Rehm et al. 2002; Luo et al. 2003; Takemoto et al. 2003; Kawai et al. 2004). Cells treated with 2.5μg/ml CHX alone showed no evidence of PARP cleavage or cell death for at least 24 hr.

Generation of HeLa cells expressing a caspase-3 FRET reporter.

Venus YFP was ligated into pECFP-C1 downstream of a linker encoding the sequence `SGLRSSGDEVDGTSGSGST`; the sequence DEVD is a consensus caspase-3 cleavage site present in PARP which has been used in other similar reporters (*3,4,6*). The

use of Venus as the FRET acceptor in place of EYFP is important, since EYFP displays significant pH sensitivity (*4*). The resulting plasmid, pECFP-DEVD-Venus, was transfected into HeLa cells, and stable transfectants were isolated by selection with G418 followed by flow cytometry sorting for Venus (YFP)-positive cells.

Live cell microscopy

HeLa cells stably expressing pECFP-DEVD-Venus were grown in chambered coverglass slides (LabTek) for 24-48 hr. Immediately prior to imaging, medium was replaced with CO_2-independent medium (Gibco) containing the appropriate doses of SuperKiller TRAIL and CHX. Cells were then imaged at 37° C on a Deltavision Spectris AX71 equipped with a temperature control chamber using a 20X objective. CFP and YFP images were acquired at 3-minute intervals for 12 hours. Cleavage of the reporter by caspase-3 results in a separation of the CFP and YFP proteins, which thereby abrogates intramolecular FRET. Reporter cleavage was monitored by the change in CFP:YFP ratio. The change in CFP:YFP ratio over time and the T_d and T_s for individual cells were measured using ImageJ software with a custom-made plugin, which is available from the authors. While our results are qualitatively very consistent with previous studies (e.g. Rehm et.al. 2002), we note that relatively minor quantitative differences are likely a result of differences in the FRET reporter and in data processing.

Flow cytometry assay.

After treatment for the appropriate length of time with SuperKiller TRAIL, HeLa cells were trypsinized (taking care to collect both floating and adherent cells) and fixed with 4% paraformaldehyde in PBS for 10 minutes at room temperature. Following a PBS wash, cells were permeablized in 100% methanol. We found that fixation with formaldehyde was essential to maintaining the specificity of the anti-cleaved PARP

antibody. Prior to staining for flow cytometry, cells were stored for up to 5 days at -20 C in 100% methanol. Cells were stained with primary antibodies (1:250 anti-cleaved PARP or 1:500 anti-cleaved caspase-3 in PBS-T+1%BSA) for 1 hour at room temperature, followed by staining with secondary antibodies (1:250 in PBS-T+1%BSA) for 1 hour. Cells were then analyzed on a Becton Dickinson FACSCalibur. Analysis was performed using the FlowJo software package (Treestar); in each experiment the gate for partial PARP cleavage was set to be 160 channels wide and approximately centered between the positive and negative peaks for the control sample, and thus contained cells in which approximately 5-20% of PARP was cleaved. Positive and negative gates were then defined as all the remaining channels above and below the intermediate gate, respectively. For each experiment, the same gates were used for all samples. In cases where single-cell behavior (T_d, T_s, and f) was estimated, this estimate was made by comparing the observed frequencies of negative, intermediate, and positive cells with simulated flow cytometry experiments generated in Matlab (see below).

Simulation of flow cytometry data

Simulated flow cytometry data were produced using the Matlab script contained in Appendix E, where the process used to generate the simulated data is described in detail.

siRNA transfection

siRNA transfections were performed as described (Meraldi et al. 2004), with a final concentration of 3-5 nM for each oligo in the growth medium. Medium was

changed 1 day after transfection, and TRAIL treatment was performed on the second day after transfection. Oligo sequences are shown in Table S2.

Western blotting

Western blots were carried out as described (Gaudet et al. 2005) and detected using an Odyssey Scanner (Li-Cor Instruments, Omaha NE).

Colony-forming assays

After treatment with CHX alone or TRAIL+CHX, cells were harvested as described for flow cytometry, collecting both floating and adherent cells. Cells were then plated at a density of ~10^2-10^3 in 10-cm plates. After 2 weeks of growth, colonies were stained with crystal violet and counted. The viability percentages reported were determined by dividing the number of colonies on the TRAIL+CHX-treated plate by the number of colonies on a CHX-treated plate transfected with the same siRNA oligos.

Mathematical modeling

All network model simulations were carried out in Matlab (The Mathworks, Natick, MA). Since our model is a stiff system (that is, containing processes that occur on multiple time scales), numerical simulations were performed using Matlab's ODE15s solver, which is a multistep, variable-order differential equation solver recommended for stiff systems. Absolute tolerances were set to 10^{-10}, and relative tolerances were set to 10^{-8}. Further details of model construction and simulation are discussed below.

2.6 Construction of the mathematical model

Biochemical reaction equations were derived from the canonical death receptor network (see (Bouralexis et al. 2005) for review). For each given binary reaction, i, the biochemical equation is represented by one of following general mass-action paradigms:

$$E + S \underset{k_{-i}}{\overset{k_i}{\rightleftharpoons}} E:S \xrightarrow{\kappa_i} E + P \qquad \begin{cases} \frac{d[E]}{dt} &= -k_i[E][S] + k_{-i}[E:S] + \kappa_i[E:S] \\ \frac{d[S]}{dt} &= -k_i[E][S] + k_{-i}[E:S] \\ \frac{d[E:S]}{dt} &= k_i[E][S] - k_{-i}[E:S] - \kappa_i[E:S] \\ \frac{d[P]}{dt} &= \kappa_i[E:S] \end{cases} \tag{1}$$

$$E + S \underset{k_{-i}}{\overset{k_i}{\rightleftharpoons}} E:S \xrightarrow{\kappa_i} P \qquad \begin{cases} \frac{d[E]}{dt} &= -k_i[E][S] + k_{-i}[E:S] \\ \frac{d[S]}{dt} &= -k_i[E][S] + k_{-i}[E:S] \\ \frac{d[E:S]}{dt} &= k_i[E][S] - k_{-i}[E:S] - \kappa_i[E:S] \\ \frac{d[P]}{dt} &= \kappa_i[E:S] \end{cases} \tag{2}$$

$$E + S \underset{k_{-i}}{\overset{k_i}{\rightleftharpoons}} E:S \qquad \begin{cases} \frac{d[E]}{dt} &= -k_i[E][S] + k_{-i}[E:S] \\ \frac{d[S]}{dt} &= -k_i[E][S] + k_{-i}[E:S] \\ \frac{d[E:S]}{dt} &= k_i[E][S] - k_{-i}[E:S] \end{cases} \tag{3}$$

where an enzyme or other protein, E, reacts with its substrate or binding partner, S, forming complex, E:S, and depending on the specific reaction, i, forming product, P, such that k_i, k_{-i}, and κ_i are the forward, backward, and catalytic rates, respectively. The list of species that are used in the biochemical equations are in Table S3.

Mathematical Model

Assume the cytosolic and mitochondrial compartments (see below) are each well mixed. Let $[X]$ represent the number of molecules of species X in each compartment. Let the rate at which the number of molecules per compartment of species x changes with respect to time t, in seconds, be represented by $\dot{x} = dx/dt$. Using the rates found in Table

S5, and the state variables and initial conditions in Table S7, the biochemical reactions in Table S4 are modeled by the system of ordinary differential equations found in Table S8.

Simulation and Visualization

Matlab stiff solver ODE15s was used to numerically solve the system of ODEs. This is a variable order solver that employs numerical differentiation formulas (NDFs). Graphs and visualizations were made using Matlab and Axum software packages.

Experimental over-expression and knockdown perturbations are simulated in the model by adjusting the initial conditions appropriately in accordance with experimental data. For example, a Bcl-2 over-expression of 30-fold would be represented by multiplying the initial condition for Bcl-2 by 30, with all other initial conditions and parameters unchanged.

Signaling Redundancy:

For simplicity, proteins which perform redundant or similar functions were represented as single lumped species. Thus, "C8" represents both caspase-8 and -10, and "C3" represents caspase-3 and -7. Mcl-1 represents all Bcl-2 antiapoptotic proteins in the cytosolic compartment that bind to Bid, and Bcl-2 represents all Bcl-2 antiapoptotic proteins in the mitochondrial compartment that bind to Bax^*_m. PARP represents all substrates of cleaved caspase-3 (other than C6).

Cytosolic and mitochondrial compartments

Since many of the biochemical processes of the mitochondrial pathway occur on or in the outer membrane of the mitochondria, these processes are effectively physically separated from processes occurring in the cytosol. To reflect this segregation, the model is comprised of two compartments, cytosolic and mitochondrial. Each compartment is a separate, well-mixed volume; specific molecules, such as cytochrome c, may move from

one compartment to another at a defined rate. Based on measurements of the mitochondrial and cytosolic volume of HeLa cells (Posakony et al. 1977), the volume of the mitochondrial compartment is estimated to be 7% of the volume of the cytosolic compartment. The rates of second-order (or higher-order) reactions, in which two (or more) molecules must collide with each other, increase as volume decreases, due to the increased likelihood of a collision. To reflect this, the reaction rates of intermolecular reactions occurring in the mitochondrial compartment are divided by the ratio of the mitochondrial compartment volume to the cytosolic compartment volume (0.07).

Rate Constants

Assume that a cell is 10^{-12} liters (1 pL), and that bimolecular reaction rate constants, k_i, are diffusion limited. Therefore the forward reactions are bound by $k_i \leq 1 \text{x} 10^6$ M^{-1} sec^{-1}, for all reactions i (Berg 1985; Zhou 1993). All dissociation rates are approximately 10^{-3} sec^{-1}, resulting in dissociation constants in the range of 1-10 nM (with one exception: activation of receptor the dissociation rate is 10^{-5} sec^{-1}, since this is a lumped parameter fit to match data). All catalytic rates are 0, 1, 0.1, or 10 sec^{-1}. All translocation reactions (between cytosol and mitochondrial compartments) have a rate of 10^{-2} sec^{-1}.

Initial protein concentrations

Relatively few references for initial concentrations of proteins are available. However, many signaling proteins have been found to be present in the range of 1nM to 1μM (~10^3-10^6 copies/cell) (*48,49*). Therefore, we restricted initial protein concentrations to fall within these bounds (with the exception of Flip, which does not figure significantly in the model and was estimated to be present at lower levels).

Consistent with these bounds, procaspase-3 has been reported to be present at 10^4-10^5 copies/cell (*20,50*), and was therefore set conservatively as 10^4 copies/cell.

Protein synthesis

In all the experiments presented in this study, the cells were treated with CHX to retard protein synthesis. To reflect this, the mathematical model contains no source terms. Understanding and modeling the additional layers of control imposed by transcriptional or translational regulation will be an important question for further study.

Protein Degradation

We assume that protein degradation is slow compared to signaling dynamics, so with one exception, the model contains no sink terms. The one exception is the case of C3* degradation by XIAP, which we have experimentally determined to occur at significant levels on the timescale of the experiment (Fig 3). In this case, degradation is approximated by assuming that ubiquitinated caspase-3 is catalytically inactive.

2.7 Supplemental figures and tables

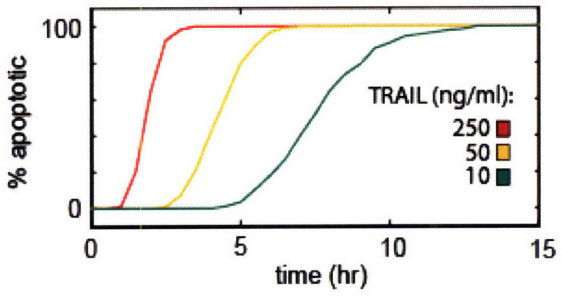

Figure 2.S1 Graded response in the accumulation of apoptotic cells. The cumulative percentage of cells entering apoptosis (as measured by FRET reporter cleavage) was calculated from the live-cell data shown in Fig 2.1. Apoptotic cells accumulate over the course of hours, and the rate of accumulation is dependent on the strength of the stimulus. Thus, at the population level, the apoptotic response is slow and can be controlled in a graded manner, even though each individual cell exhibits an all-or-none response.

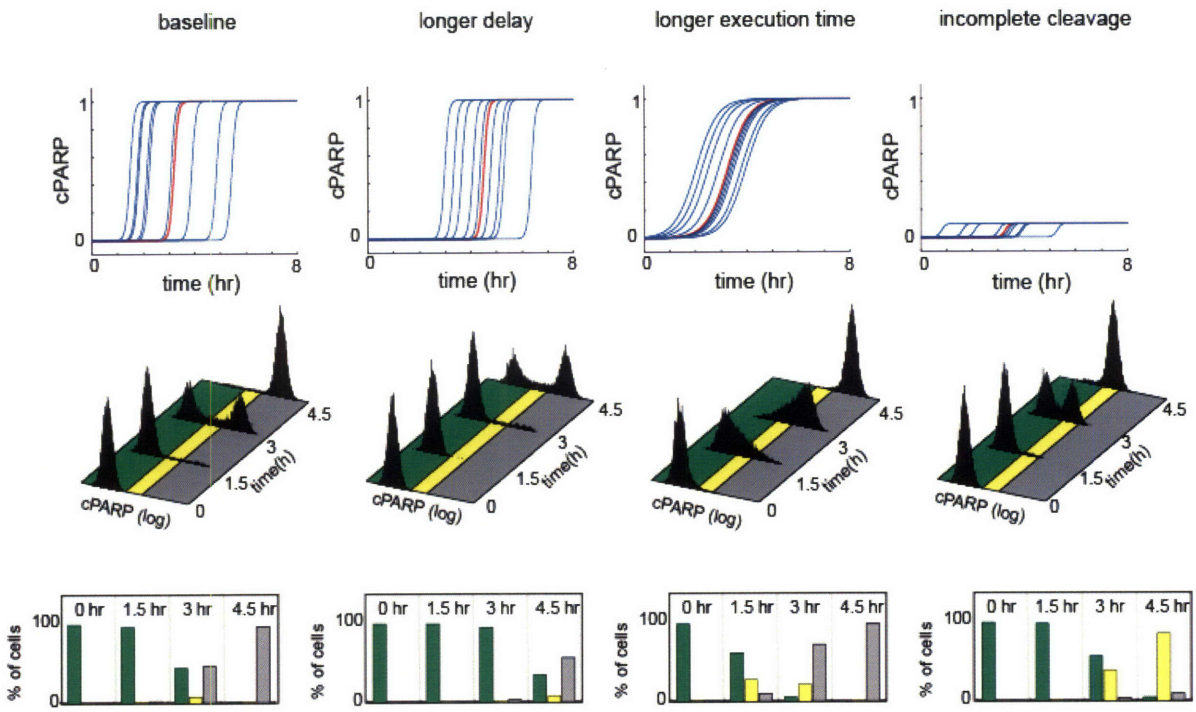

Figure 2.S2 A data model linking live-cell and flow cytometry data. Hypothetical live-cell data were modeled by creating families of Boltzmann equation curves for each condition, where f and T_s were held at a constant value, while T_d was chosen at random from a normal distribution (see Methods section). In the top row, ten such curves for each condition are shown, with the red curve representing the mean T_d. For each condition, 10,000 curves were generated and converted to the predicted flow cytometry profile by 1) choosing values at discrete times, 2) adding simulated measurement noise, and 3) displaying histograms of these values on a logarithmic scale. The second row of plots shows the predicted FACS data for each condition. The predicted FACS data were then gated into regions of low, intermediate, or high fluorescence intensity (colored green, yellow, and gray, respectively), and the percent of cells falling into each region is plotted on a bar graph (bottom row of plots), as was done for flow cytometry experiments throughout the study. By using this process, live-cell and flow cytometric data can be

directly compared. From experimental flow cytometry data, the underlying single-cell behavior can be estimated. As discussed in the text, three major classes of deviation are possible from the typically-observed baseline condition (a change in either T_d, T_s, or f), and each of these changes results in a distinct change in the expected flow cytometry profile.

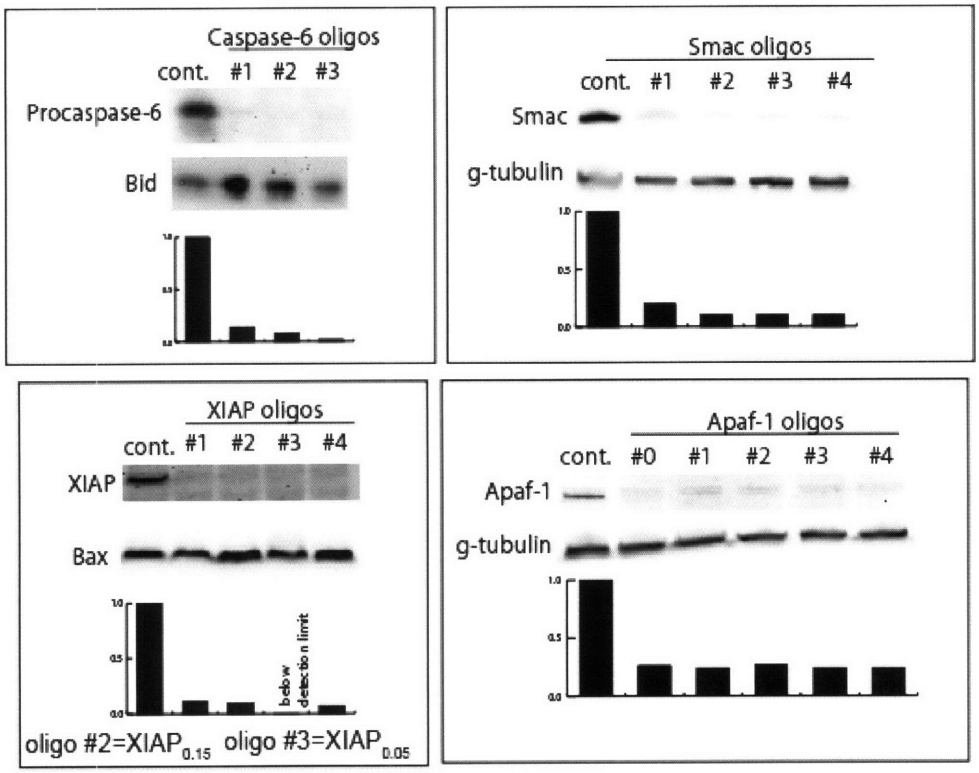

Figure 2.S3 Quantitation of protein depletion by immunoblot. For each siRNA oligo used, HeLa cells were transfected as described in the Methods section. After two days, cells were lysed in sample buffer and separated by SDS-PAGE. Blots were then probed with an antibody against the targeted protein (top image in each panel) and an antibody against a non-targeted protein as a loading control (bottom image in each panel). Percent depletion for each oligo (relative to a control oligo) was quantitated using ImageJ software. The percent knockdown in each case was then used to determine new intitial conditions for simulation of the corresponding behavior of the mathematical model. Bcl-

2 overexpression was found to be 30-fold relative to wild-type conditions (not shown, K.Leitermann and P.K.S., unpublished data).

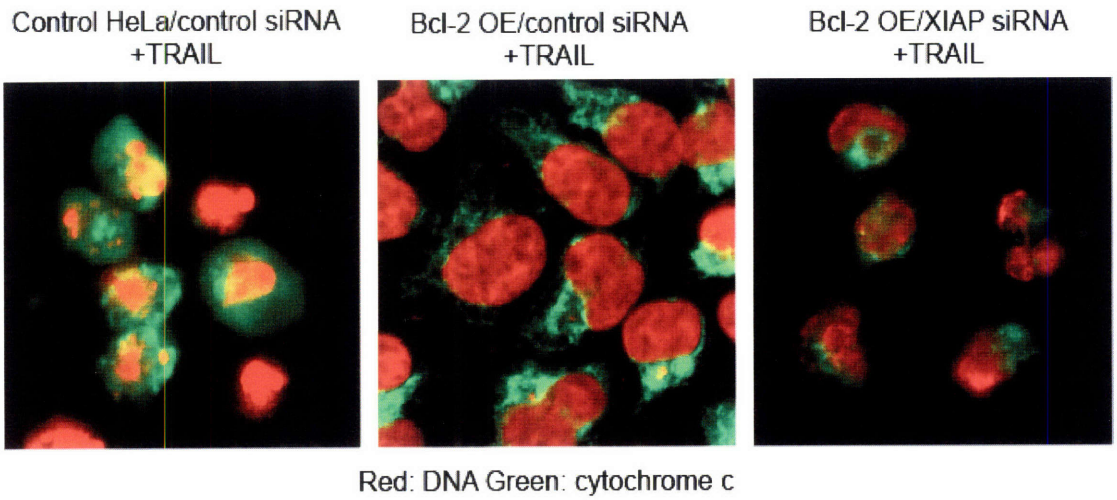

Figure 2.S4 Bcl-2 overexpression blocks mitochondrial permeabilization under all conditions. Control and Bcl-2-overexpressing HeLa cells were transfected with either control or XIAP siRNA and then treated with 50 ng/ml TRAIL for 4 hours. Cells were then fixed, and cytochrome c was detected by immunofluorescence microscopy; DNA was co-stained with Hoechst 33342. In control HeLa cells, cytochrome c redistributes from the mitochondria to the cytosol, resulting in a diffuse staining pattern (left). In Bcl-2 overexpressing cells, cytochrome c remains in a punctate mitochondrial pattern even after TRAIL treatment (center). The punctate pattern of cytochrome c staining is maintained even in XIAP -depleted cells, where caspase activation has resulted in nuclear condensation and cell death (right).

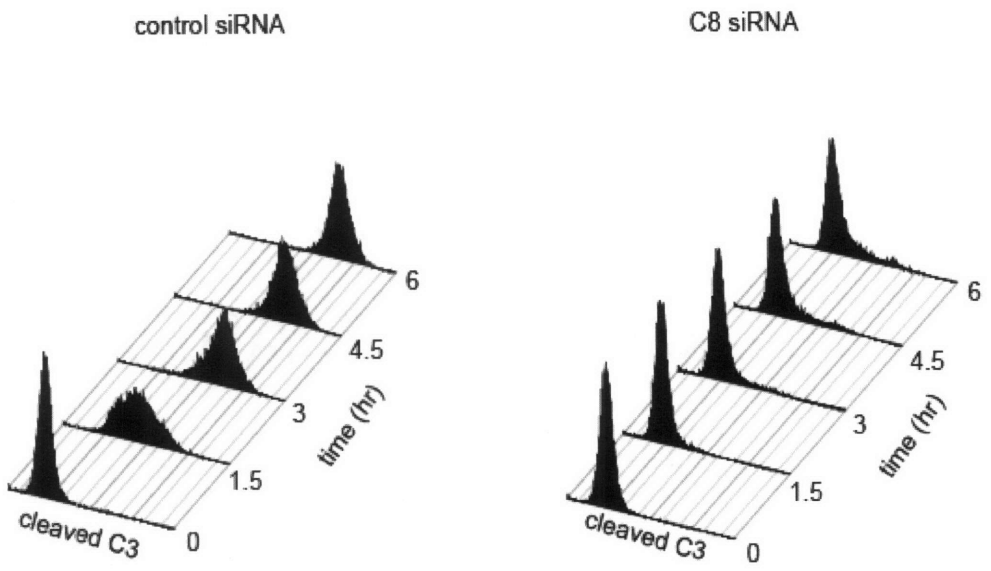

Figure 2.S5 C8 is required for C3 cleavage in Bcl-2-overexpressing cells. Bcl-2 overexpressing cells were transfected with control or C8 siRNA and then treated with 50 ng/ml TRAIL. Cells were fixed at the indicated times, and C3 cleavage was assayed by flow cytometry. While a significant increase in C3 cleavage is detected in control cells, C8 depletion abrogates this cleavage.

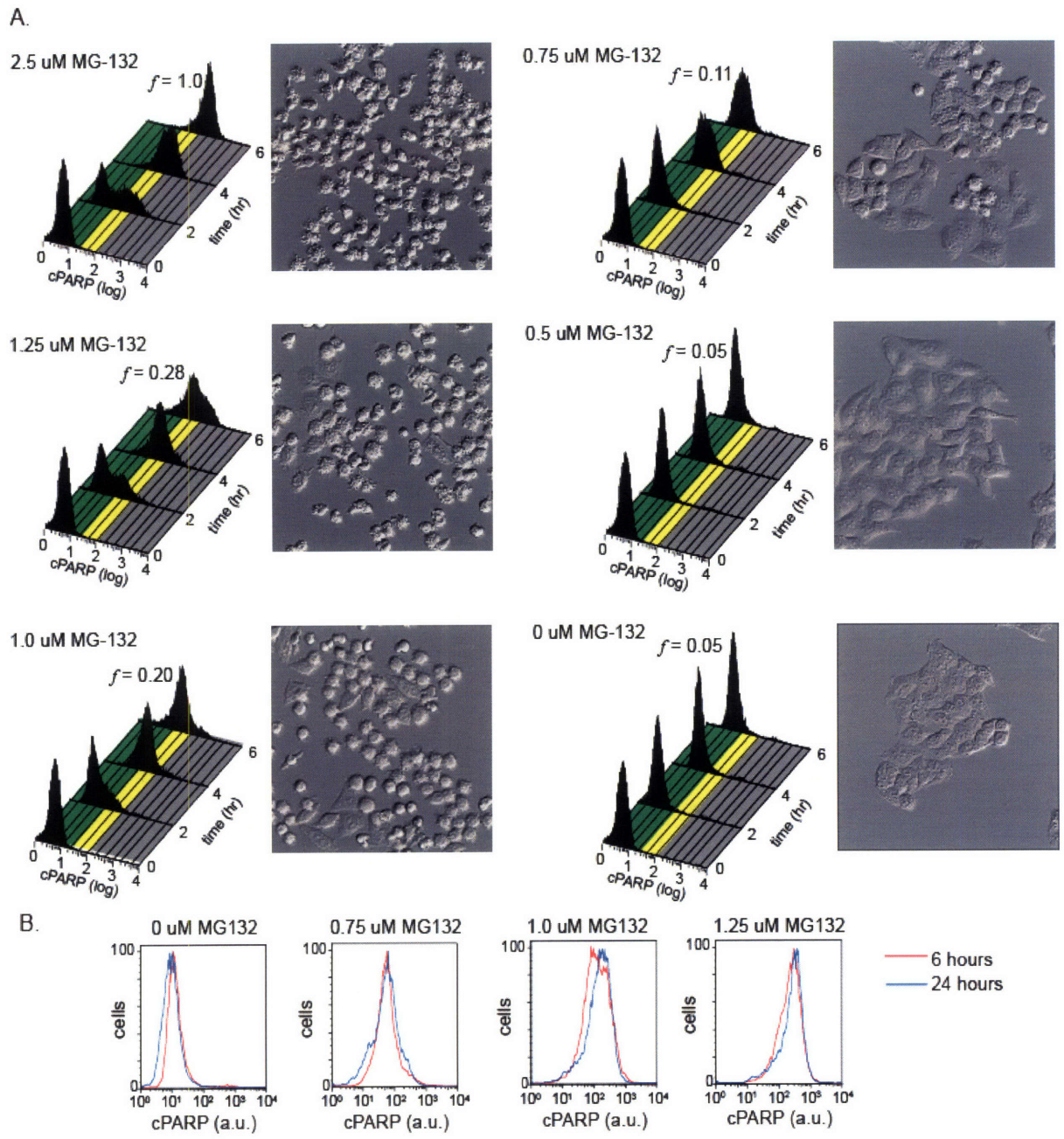

Figure 2.S6 Continuous variation of *f* in response to proteasome inhibitor. A. Bcl-2-overexpressing HeLa cells were co-treated with 50 ng/ml TRAIL and the indicated concentration of MG-132, fixed at the indicated times, and analyzed for cPARP by flow cytometry. Representative DIC images of cells are shown for cells at 6 hours in each

condition. B. Cells were treated and analyzed as in A, and the cPARP staining at 6 and 24 hours was compared. From this we conclude that under the TRAIL and MG-132 conditions tested here, cPARP reaches its final value (*f*) by 6 hours of treatment. DIC images of the cells indicate that ~50% of the cells under the TRAIL+0.75uM MG-132 treatment display apoptotic morphology, and the number of apoptotic-appearing cells increases with MG-132 concentration. The *f* value at which ~50% of cells appear apoptotic occurs is 0.11, which is similar to the *f* value in Bcl-2-overexpressing, XIAP-depleted cells at which ~50% of cells appear apoptotic and viability is reduced to ~50% (Fig 2.2F,G). Therefore, these data support the finding that, in the absence of mitochondrial permeabilization, a pulse of C3* activity sufficient to cleave ~10% of PARP and other substrates represents the LD_{50} for cumulative C3* activity.

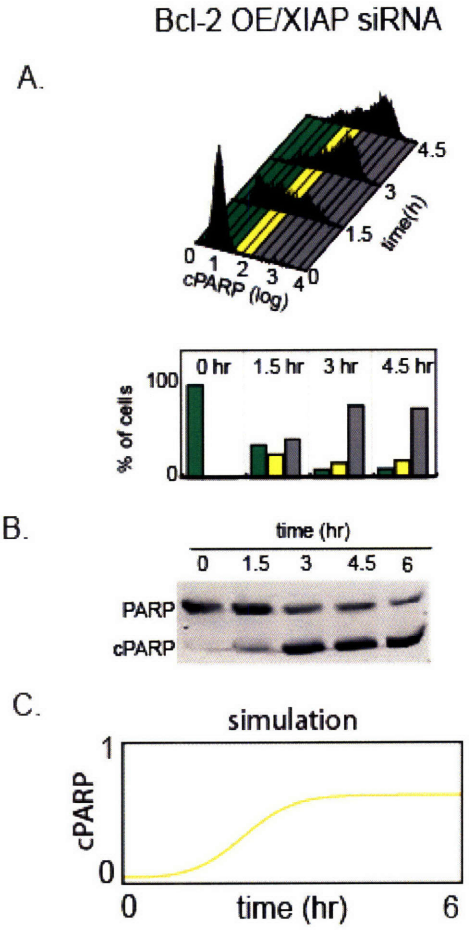

Figure 2.S7 Highly efficient depletion of XIAP leads to higher *f*. Bcl-2 overexpressing HeLa cells were transfected with the $XIAP_{0.05}$ oligo, which produces >95% XIAP depletion (Fig 2.S3), and then treated with 50 ng/ml TRAIL; cPARP levels were analyzed by flow cytometry (A) and by western blotting (B). Under these conditions, a higher *f* is reached (~0.6) relative to Bcl-2-overexpressing cells in which XIAP has been depleted to a lesser extent (~0.15, Fig 2.2F,G). This increase in *f* agrees with our analysis by simulation (C), which predicts that *f* varies inversely with XIAP expression level in Bcl-2-overexpressing cells (See also Fig 2.3D).

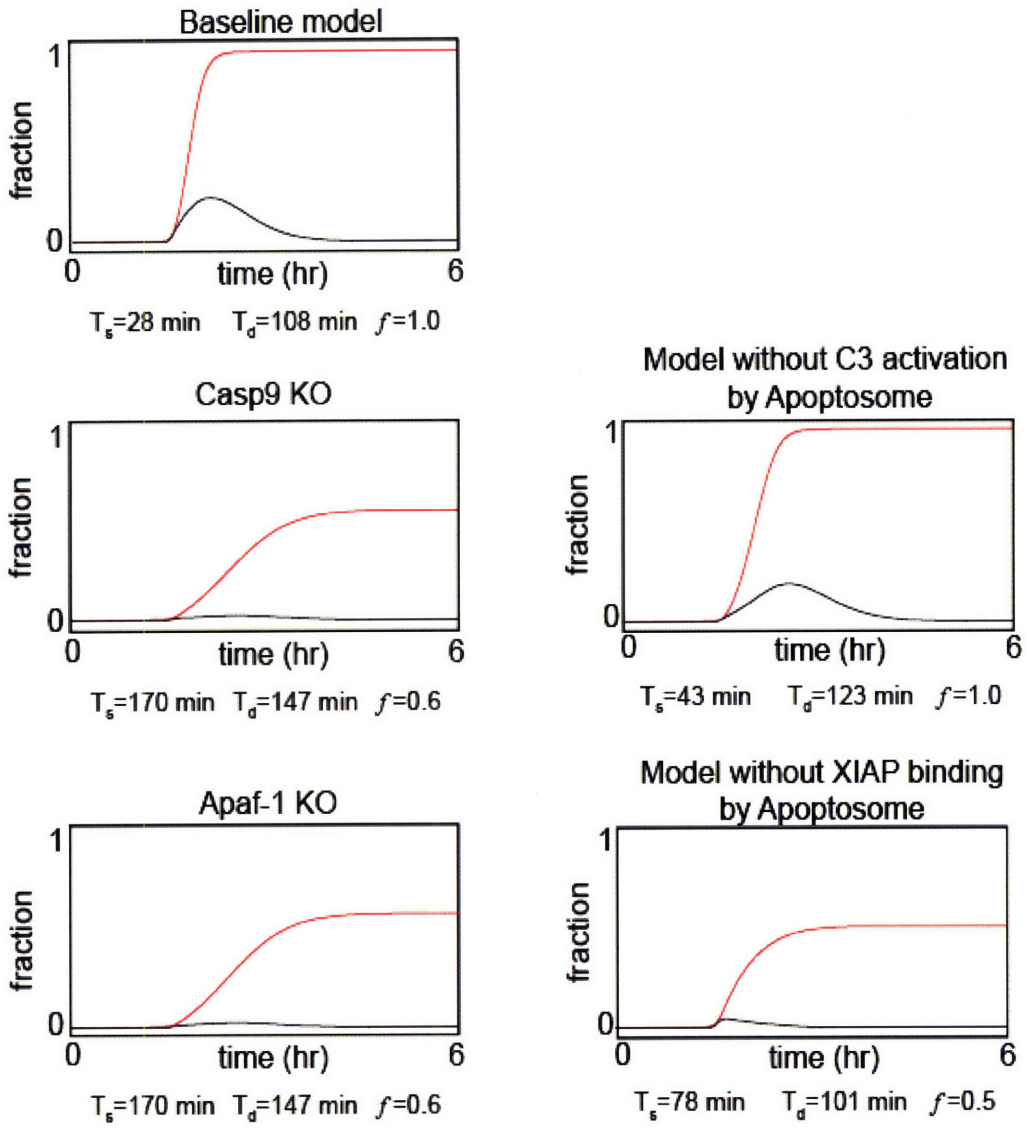

Figure 2.S8 XIAP-sequestering activity of the apoptosome is essential for high *f*. cPARP and C3* time courses were simulated in the baseline model and in models in which the indicated changes were made. In the absence of either of the apoptosome components, C9 and Apaf-1, $f<1$ and T_s is high. Removing the ability of the apoptosome to process C3 does not affect *f* and has only a moderate effect on T_s, while removing the ability of the apoptosome to bind XIAP does affect *f* to the same extent as the knockouts. Therefore, the role of the apoptosome in reaching $f=1$ is mediated by its XIAP-sequestering activity.

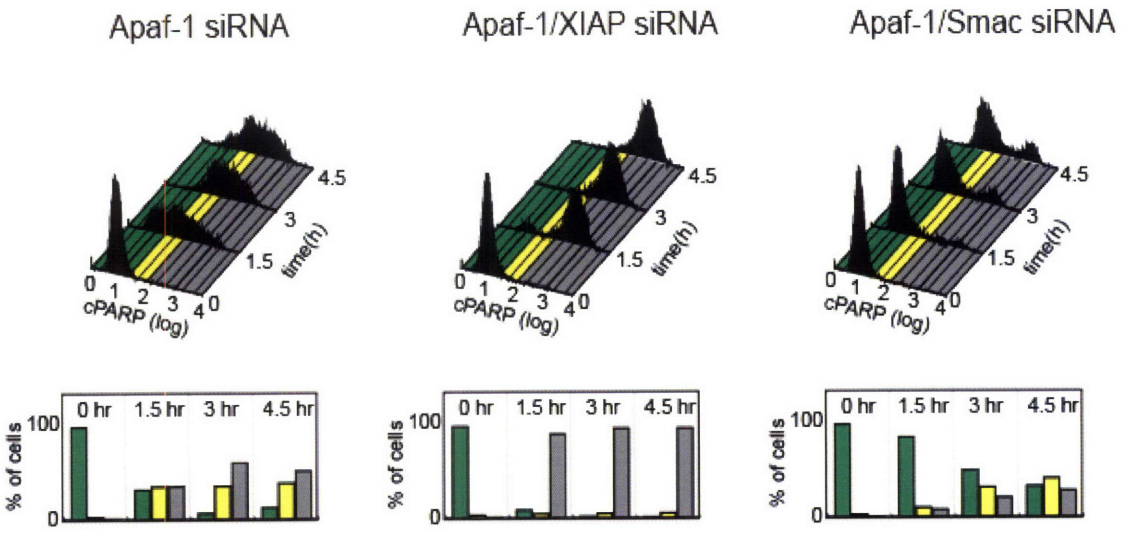

Figure 2.S9 Apaf-1 depletion phenocopies Smac depletion. HeLa cells were transfected with siRNA oligos targeting Apaf-1, Apaf-1/XIAP, or Apaf-1/Smac, treated with 50 ng/ml TRAIL, and assayed for cPARP by flow cytometry. Apaf-1 depletion appears to phenocopy Smac depletion, resulting in decreased *f*. Co-depletion of XIAP and Apaf-1 restores efficient PARP cleavage. Moreover, co-depletion of Smac and Apaf-1 has an additive inhibitory effect on PARP cleavage; more cPARP-negative cells persist at longer times. These results favor a model in which both Smac and the apoptosome cooperate to antagonize XIAP, so that depletion of either Smac or the apoptosome component Apaf-1 results in a decrease in *f* (points 2 and 3, respectively in Fig. 4C). The Apaf-1 oligo used in these experiments has been previously used in other studies (Lassus et al. 2002; Burek et al. 2006). However, other Apaf-1 oligos, which appeared to deplete Apaf-1 with similar efficiency, did not produce a significant change in *f*, and did not act in an additive manner with Smac co-depletion (not shown). This difference may be due to differences in Apaf-1 depletion that were below the detection limit of our assay, or differences in the depletion of other Apaf-1 isoforms that were not detected. The specificity of the results seen with the oligo shown here, including rescue by XIAP and additive effect with Smac, argues against an off-target effect, although this remains a formal possibility. However, if it is true that Apaf-1 depletion does not significantly affect *f*, the implication for our model is that wild type cells fall at a different point (position 1b) on the surface in Fig. 4C, so that Smac depletion, but not Apaf-1 depletion, results in decreased *f*.

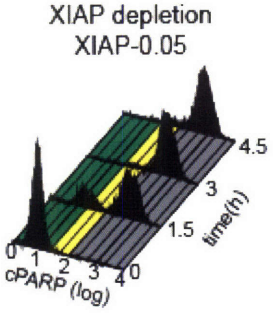

Figure 2.S10 XIAP-depleted cells achieve complete cleavage of PARP. HeLa cells were transfected with an XIAP oligo ($XIAP_{0.05}$), and then treated with 50 ng/ml TRAIL; cPARP levels were analyzed by flow cytometry. While partial PARP cleavage is observed in a subpopulation of cells at early times (1.5 hr, see Fig. 5C), full PARP cleavage is reached at later times (3-4.5 hr).

Table S1: T_d and T_s values determined by live-cell microscopy

TRAIL (ng/ml)	Mean T_d (min)	Std.Dev. T_d (min)	Mean T_s (min)	Std. Dev. T_s(min)
1000	104	25.6	19.1	5.3
250	129	26.6	19.9	5.7
50	273	56.6	21.7	8.9
10	472	103.6	27	9.9

Table S2: siRNA oligo sequences

	target sequence	**source**
Capase-6		
oligo 1	aattcatgaggtgtcaactgt	designed
oligo 2	nnttgcctcaatgctaactaa	designed
oligo 3	nnacattaactggcttgttca	designed
Caspase-8		
oligo 1	aactaccagaaaggtatacct	Chun et al. 2002
Smac		
oligo 1	nngaccacatatgcgttgatt	designed
oligo 2	nntgcgttgattgaagctatt	designed
oligo 3	nnacttctctttaccgacaat	designed
oligo 4	nngcagaagctgcatatcaaa	designed
XIAP		
oligo 1	aaacttgtgtacctgcagaca	designed
oligo 2	aaccgtgcggtgctttagttg	designed
oligo 3	aaggcgacactttcctaattg	designed
oligo 4	aaaatagtgccacgcagtcta	designed
Apaf-1		
oligo 0	aattggtgcacttttacgtga	Lassus et. al. 2002
oligo 1	aatgatggcattcctgttgtc	designed
oligo 2	aacacggttggatcaggatga	designed
oligo 3	nnacaactttctggcctatca	designed
oligo 4	nnggtcgataatggaatgctt	designed
control		
EGFP-1	aaagcagaagaacggcatcaa	designed
EGFP-2	aagctcaagcttcgaattctg	designed

Table S3: List of Species

Species	Description (all species are located in cellular compartment (CC) unless otherwise stated.)
L	death ligand, such as TRAIL and TNF
R	inactive receptor, for example limiting factor of Death Inducing Signaling Complex (DISC) formation
R^*	active receptor
$flip$	binds to active receptor acting as an inhibitor
$X:Y = Y:X$	complex formed by species X and Y, for example, $L:R$ is the ligand-receptor complex
$C8$	procaspase-8 and procaspase-10, inactive form of caspase-8 and caspase-10
$C8^*$	cleaved caspase-8 and caspase-10, active form of caspase-8 and caspase-10
Bar	binds to $Casp8$ and acts as an inhibitor
$C3$	procaspase-3 and procaspase-7, inactive form of caspase-3 and caspase-7
$C3^*$	cleaved caspase-3 and caspase-7, active form of caspase-3 and caspase-7
$C6$	procaspase-6, inactive form of caspase-6
$C6^*$	cleaved caspase-6, active form of caspase-6
$XIAP$	X-linked Inhibitor of Apoptosis (XIAP) in the cell
$PARP$	all substrates of $C3^*$
$cPARP$	cleaved $PARP$, and represents single cell death
Bid	substrate of cleaved caspase-8, inactive form
$tBid$	cleaved Bid, active form of Bid
$Mcl1$	represents the family of antiapoptotic Bcl-2 proteins in the CC, it binds to $tBid$ and acts as in inhibitor
Bax	substrate of $tBid$, inactive form
Bax^*	active form of Bax
Bax_m^*	Bax^* in the mitochondrial compartment (MC)
Bax_2	represents $Bax_m^* : Bax_m^*$ in the MC
Bax_4	represents $Bax_2 : Bax_2$ in the MC
$Bcl2$	represents all antiapoptotic Bcl-2 proteins in the MC
M	the number of unoccupied Bax_4 binding sites on outer membrane of the mitochondria, in MC
M^*	the number of pores Bax_4 created on the outer membrane of the mitochondria, in MC
CyC_m	cyotochrome c inside the mitochondria, in MC
CyC_r	cytochrome c released from the mitochondria, but remaining in the MC
CyC	cytochrome c in the CC
$Smac_m$	Smac/Diablo inside the mitochondria, in MC
$Smac_r$	Smac/Diablo released from the mitochondria, but remaining in the MC
$Smac$	Smac/Diablo in the CC
$Apaf$	Apoptosis Activating Factor (Apaf-1), substrate of CyC, inactive form
$Apaf^*$	active form of Apaf-1
$C9$	inactive form of procaspase-9
$Apop$	the apoptosome, which is the complex $Apaf^* : C9$
$C3^*_{Ub}$	$C3^*$ ubiquitinated and targeted for degradation. Assumed inactive

Table S4: Biochemical Equations

Reaction	Ref
$L + R \underset{k_{-1}}{\overset{k_1}{\rightleftharpoons}} L:R \xrightarrow{\kappa_1} R^*$	(16)
$R^* + flip \underset{k_{-2}}{\overset{k_2}{\rightleftharpoons}} R^*:flip$	(17)
$R^* + C8 \underset{k_{-3}}{\overset{k_3}{\rightleftharpoons}} R^*:C8 \xrightarrow{\kappa_3} R^* + C8^*$	(18)
$C8^* + Bar \underset{k_{-4}}{\overset{k_4}{\rightleftharpoons}} C8^*:Bar$	(19)
$C8^* + C3 \underset{k_{-5}}{\overset{k_5}{\rightleftharpoons}} C8^*:C3 \xrightarrow{\kappa_5} C8^* + C3^*$	(20)
$C3^* + C6 \underset{k_{-6}}{\overset{k_6}{\rightleftharpoons}} C3^*:C6 \xrightarrow{\kappa_6} C3^* + C6^*$	(21)
$C6^* + C8 \underset{k_{-7}}{\overset{k_7}{\rightleftharpoons}} C6^*:C8 \xrightarrow{\kappa_7} C6^* + C8^*$	(22)
$C3^* + XIAP \underset{k_{-8}}{\overset{k_8}{\rightleftharpoons}} C3^*:XIAP \xrightarrow{\kappa_8} C3^*_{Ub} + XIAP$	(23.24)
$C3^* + PARP \underset{k_{-9}}{\overset{k_9}{\rightleftharpoons}} C3^*:PARP \xrightarrow{\kappa_9} C3^* + cPARP$	(25)
$C8^* + Bid \underset{k_{-10}}{\overset{k_{10}}{\rightleftharpoons}} C8^*:Bid \xrightarrow{\kappa_{10}} C8^* + tBid$	(26.27)
$Bid + Mcl1 \underset{k_{-11}}{\overset{k_{11}}{\rightleftharpoons}} Bid:Mcl1$	(28)
$tBid + Bax \underset{k_{-12}}{\overset{k_{12}}{\rightleftharpoons}} tBid:Bax \xrightarrow{\kappa_{12}} tBid + Bax^*$	(29)
$Bax^* \underset{k_{-13}}{\overset{k_{13}}{\rightleftharpoons}} Bax^*_m$	(29)
$Bax^*_m + Bcl2 \underset{k_{-14}}{\overset{k_{14}}{\rightleftharpoons}} Bax^*_m:Bcl2$	(30)
$Bax^*_m + Bax^*_m \underset{k_{-15}}{\overset{k_{15}}{\rightleftharpoons}} Bax_2$	(31)
$Bax_2 + Bcl2 \underset{k_{-16}}{\overset{k_{16}}{\rightleftharpoons}} Bax_2:Bcl2$	
$Bax_2 + Bax_2 \underset{k_{-17}}{\overset{k_{17}}{\rightleftharpoons}} Bax_4$	(31)
$Bax_4 + Bcl2 \underset{k_{-18}}{\overset{k_{18}}{\rightleftharpoons}} Bax_4:Bcl2$	
$Bax_4 + M \underset{k_{-19}}{\overset{k_{19}}{\rightleftharpoons}} Bax_4:M \xrightarrow{\kappa_{19}} M^*$	(32)
$M^* + CyC_m \underset{k_{-20}}{\overset{k_{20}}{\rightleftharpoons}} M^*:CyC_m \xrightarrow{\kappa_{20}} M^* + CyC_r$	(33)
$M^* + Smac_m \underset{k_{-21}}{\overset{k_{21}}{\rightleftharpoons}} M^*:Smac_m \xrightarrow{\kappa_{21}} M^* + Smac_r$	(34.35)
$CyC_r \underset{k_{-22}}{\overset{k_{22}}{\rightleftharpoons}} CyC$	
$CyC + Apaf \underset{k_{-23}}{\overset{k_{23}}{\rightleftharpoons}} CyC:Apaf \xrightarrow{\kappa_{23}} CyC + Apaf^*$	(36)
$Apaf^* + C9 \underset{k_{-24}}{\overset{k_{24}}{\rightleftharpoons}} Apop$	(33)
$Apop + C3 \underset{k_{-25}}{\overset{k_{25}}{\rightleftharpoons}} Apop:C3 \xrightarrow{\kappa_{25}} Apop + C3^*$	(33)
$Smac_r \underset{k_{-26}}{\overset{k_{26}}{\rightleftharpoons}} Smac$	
$Apop + XIAP \underset{k_{-27}}{\overset{k_{27}}{\rightleftharpoons}} Apop:XIAP$	(37.38)
$Smac + XIAP \underset{k_{-28}}{\overset{k_{28}}{\rightleftharpoons}} Smac:XIAP$	(34.35)

Table S5: Rate Constant Values

i	k_i $((\#/CC)^{-1}\cdot sec^{-1})$	k_{-i} (sec^{-1})	κ_i (sec^{-1})
1	4×10^{-7}	10^{-3}	10^{-5}
2	10^{-6}	10^{-3}	
3	10^{-6}	10^{-3}	1
4	10^{-6}	10^{-3}	
5	10^{-7}	10^{-3}	1
6	10^{-6}	10^{-3}	1
7	3×10^{-8}	10^{-3}	1
8	2×10^{-6}	10^{-3}	0.1
9	10^{-6}	10^{-3}	1
10	10^{-7}	10^{-3}	1
11	10^{-6}	10^{-3}	
12	10^{-7}	10^{-3}	1
13	10^{-2} (sec^{-1})	10^{-2}	
14	10^{-6} $((\#/CC)^{-1}\cdot sec^{-1})$	10^{-3}	
15	10^{-6} $((\#/CC)^{-1}\cdot sec^{-1})$	10^{-3}	
16	10^{-6} $((\#/CC)^{-1}\cdot sec^{-1})$	10^{-3}	
17	10^{-6} $((\#/CC)^{-1}\cdot sec^{-1})$	10^{-3}	
18	10^{-6} $((\#/CC)^{-1}\cdot sec^{-1})$	10^{-3}	
19	10^{-6} $((\#/CC)^{-1}\cdot sec^{-1})$	10^{-3}	1
20	2×10^{-6} $((\#/CC)^{-1}\cdot sec^{-1})$	10^{-3}	10
21	2×10^{-6} $((\#/CC)^{-1}\cdot sec^{-1})$	10^{-3}	10
22	10^{-2} (sec^{-1})	10^{-2}	
23	5×10^{-7}	10^{-3}	1
24	5×10^{-8}	10^{-3}	
25	5×10^{-9}	10^{-3}	1
26	10^{-2} (sec^{-1})	10^{-2}	
27	2×10^{-6}	10^{-3}	
28	7×10^{-6}	10^{-3}	

Reaction rate constants for the i^{th} reaction found in Table S4. CC and MC denote the cytosolic and mitochondrial compartments, respectively.

Table S6: Selected Initial Condition and Rate References

Enzymatic Reaction	Km (#/cell)	k_{cat} (sec^{-1})	k_{cat}/Km	Ref	substrate
*C8**					
Garcia-Calvo *et.al.* 1999	4.2×10^7	0.37	8.8×10^{-9}	(39)	LETD
Stennicke *et.al.* 1998			1.5×10^{-6}	(20)	*C3*
Stennicke *et.al.* 2000	1.1×10^7	0.69	6.4×10^{-8}	(40)	DEVDG
*C3**					
Bose *et.al.* 2003	1.3×10^6	0.4	3.0×10^{-7}	(41)	DEVD
Casciola-Rosen *et.al.* 1996			8.6×10^{-6}	(42)	PARP
Casciola-Rosen *et.al.* 1996			1.2×10^{-5}	(42)	DNA-PK
Casciola-Rosen *et.al.* 1996			3.8×10^{-6}	(42)	UI-70K
Garcia-Calvo *et.al.* 1999	6.0×10^6	14	2.3×10^{-6}	(39)	DEVD
Margolin *et.al.* 1997	6.0×10^6	23	3.8×10^{-6}	(43)	PARP
Stennicke *et.al.* 2000	7.8×10^6	2.5	3.2×10^{-7}	(40)	DEVDG
Talanian *et.al.* 1997	6.6×10^6	2.4	3.6×10^{-7}	(44)	DEVD
*C6**					
Garcia-Calvo *et.al.* 1999	1.0×10^8			(39)	VEHD
Casp9					
Garcia-Calvo *et.al.* 1999	4.7×10^8	0.1	2.6×10^{-10}	(39)	LEHD
Talanian *et.al.* 1997	1.8×10^7	5	2.7×10^{-7}	(44)	VEID
Binding Reaction	kon ($(\#/cell)^{-1} \cdot sec^{-1}$)	k_{off} (sec^{-1})	K_d (#/cell)	Ref	protein fragments
XIAP : *C3**/*7*					
Huang *et.al* 2003	3.5×10^{-6}	0.0021	600	(45)	caspase-7/linkerBIR2
Riedl *et.al* 2001	4.2×10^{-6}	0.0024	570	(46)	caspase-3/BIR2
Riedl *et.al* 2001	2.3×10^{-5}	0.0014	61	(46)	caspase-7/BIR2
XIAP : *Casp9*					
Sun *et.al* 2000			6700	(47)	BIR2-RF(aa 241-497) of XIAP
Smac : *XIAP*					
Huang *et.al* 2003	1.2×10^{-5}	0.0022	180	(45)	Smac/linker_BIR2_BIR3

Table S7: Variables and Initial Conditions

variable	state	model IC (#/CC)
x_1	$[L]$	10^3
x_2	$[R]$	10^4
x_3	$[L:R]$	0
x_4	$[R^*]$	0
x_5	$[flip]$	10^2
x_6	$[flip:R^*]$	0
x_7	$[C8]$	10^4
x_8	$[C8:R^*]$	0
x_9	$[C8^*]$	0
x_{10}	$[Bar]$	10^3
x_{11}	$[C8^*:Bar]$	0
x_{12}	$[C3]$	10^4
x_{13}	$[C8^*:C3]$	0
x_{14}	$[C3^*]$	0
x_{15}	$[C6]$	10^4
x_{16}	$[C3^*:C6]$	0
x_{17}	$[C6^*]$	0
x_{18}	$[C6^*:C8]$	0
x_{19}	$[XIAP]$	10^5
x_{20}	$[XIAP:C3^*]$	0
x_{21}	$[PARP]$	10^6
x_{22}	$[C3^*:PARP]$	0
x_{23}	$[cPARP]$	0
x_{24}	$[Bid]$	4×10^4
x_{25}	$[C8^*:Bid]$	0
x_{26}	$[tBid]$	0
x_{27}	$[Mcl1]$	5×10^3
x_{28}	$[tBid:Mcl1]$	0

Table S7 (Cont): Variables and Initial Conditions

variable	state	model IC (#/CC)
x_{29}	$[Bax]$	10^5
x_{30}	$[tBid : Bax]$	0
x_{31}	$[Bax^*]$	0
x_{32}	$[Bax^*_m]$	0 (#/MC)
x_{33}	$[Bcl2]$	10^4 (#/MC)
x_{34}	$[Bax^*_m : Bcl2]$	0 (#/MC)
x_{35}	$[Bax_2]$	0 (#/MC)
x_{36}	$[Bax_2 : Bcl2]$	0 (#/MC)
x_{37}	$[Bax_4]$	0 (#/MC)
x_{38}	$[Bax_4 : Bcl2]$	0 (#/MC)
x_{39}	$[M]$	5×10^5 (#/MC)
x_{40}	$[Bax_4 : M]$	0 (#/MC)
x_{41}	$[M^*]$	0 (#/MC)
x_{42}	$[CyC_m]$	5×10^5 (#/MC)
x_{43}	$[M^* : CyC_m]$	0 (#/MC)
x_{44}	$[CyC_r]$	0 (#/MC)
x_{45}	$[Smac_m]$	10^5 (#/MC)
x_{46}	$[M^* : Smac_m]$	0 (#/MC)
x_{47}	$[Smac_r]$	0 (#/MC)
x_{48}	$[CyC]$	0
x_{49}	$[Apaf]$	10^5
x_{50}	$[Apaf : CyC]$	0
x_{51}	$[Apaf^*]$	0
x_{52}	$[C9]$	10^5
x_{53}	$[Apop]$	0
x_{54}	$[Apop : C3]$	0
x_{55}	$[Smac]$	0
x_{56}	$[Apop : XIAP]$	0
x_{57}	$[Smac : XIAP]$	0
x_{58}	$[C3^*_{Ub}]$	0

All initial conditions are in number per cytosolic compartment (#/CC) unless otherwise noted as number per mitochondrial compartment (#/MC).

2.8 Acknowledgements

We thank F. Hua and M. Cardone for reagents, G. Lu for siRNA oligo design, and K. Janes, B. Schoeberl, S. Gaudet, and B. Aldridge for valuable help.

2.9 References

Antonsson B, Montessuit S, Sanchez B, Martinou JC (2001) Bax is present as a high molecular weight oligomer/complex in the mitochondrial membrane of apoptotic cells. J Biol Chem 276(15): 11615-11623.

Aplan PD, Chervinsky DS, Stanulla M, Burhans WC (1996) Site-specific DNA cleavage within the MLL breakpoint cluster region induced by topoisomerase II inhibitors. Blood 87(7): 2649-2658.

Bagci EZ, Vodovotz Y, Billiar TR, Ermentrout GB, Bahar I (2005) Bistability in Apoptosis: Roles of Bax, Bcl-2 and Mitochondrial Permeability Transition Pores. Biophys J.

Bentele M, Lavrik I, Ulrich M, Stosser S, Heermann DW et al. (2004) Mathematical modeling reveals threshold mechanism in CD95-induced apoptosis. J Cell Biol 166(6): 839-851.

Berg OG (1985) Orientation constraints in diffusion-limited macromolecular association. The role of surface diffusion as a rate-enhancing mechanism. Biophys J 47(1): 1-14.

Bose K, Pop C, Feeney B, Clark AC (2003) An uncleavable procaspase-3 mutant has a lower catalytic efficiency but an active site similar to that of mature caspase-3. Biochemistry 42(42): 12298-12310.

Bouralexis S, Findlay DM, Evdokiou A (2005) Death to the bad guys: targeting cancer via Apo2L/TRAIL. Apoptosis 10(1): 35-51.

Bratton SB, Lewis J, Butterworth M, Duckett CS, Cohen GM (2002) XIAP inhibition of caspase-3 preserves its association with the Apaf-1 apoptosome and prevents CD95- and Bax-induced apoptosis. Cell Death Differ 9(9): 881-892.

Burek M, Maddika S, Burek CJ, Daniel PT, Schulze-Osthoff K et al. (2006) Apoptin-induced cell death is modulated by Bcl-2 family members and is Apaf-1 dependent. Oncogene 25(15): 2213-2222.

Casciola-Rosen L, Nicholson DW, Chong T, Rowan KR, Thornberry NA et al. (1996) Apopain/CPP32 cleaves proteins that are essential for cellular repair: a fundamental principle of apoptotic death. J Exp Med 183(5): 1957-1964.

Chaudhary PM, Eby M, Jasmin A, Bookwalter A, Murray J et al. (1997) Death receptor 5, a new member of the TNFR family, and DR4 induce FADD-dependent apoptosis and activate the NF-kappaB pathway. Immunity 7(6): 821-830.

Chen L, Smith L, Wang Z, Smith JB (2003) Preservation of caspase-3 subunits from degradation contributes to apoptosis evoked by lactacystin: any single lysine or lysine pair of the small subunit is sufficient for ubiquitination. Mol Pharmacol 64(2): 334-345.

Chipuk JE, Green DR (2005) Do inducers of apoptosis trigger caspase-independent cell death? Nat Rev Mol Cell Biol 6(3): 268-275.

Chun HJ, Zheng L, Ahmad M, Wang J, Speirs CK et al. (2002) Pleiotropic defects in lymphocyte activation caused by caspase-8 mutations lead to human immunodeficiency. Nature 419(6905): 395-399.

Clohessy JG, Zhuang J, de Boer J, Gil-Gomez G, Brady HJ (2006) Mcl-1 interacts with truncated Bid and inhibits its induction of cytochrome c release and its role in receptor-mediated apoptosis. J Biol Chem 281(9): 5750-5759.

Cowling V, Downward J (2002) Caspase-6 is the direct activator of caspase-8 in the cytochrome c-induced apoptosis pathway: absolute requirement for removal of caspase-6 prodomain. Cell Death Differ 9(10): 1046-1056.

Cummins JM, Kohli M, Rago C, Kinzler KW, Vogelstein B et al. (2004) X-linked inhibitor of apoptosis protein (XIAP) is a nonredundant modulator of tumor necrosis factor-related apoptosis-inducing ligand (TRAIL)-mediated apoptosis in human cancer cells. Cancer Res 64(9): 3006-3008.

Deng Y, Lin Y, Wu X (2002) TRAIL-induced apoptosis requires Bax-dependent mitochondrial release of Smac/DIABLO. Genes Dev 16(1): 33-45.

Deveraux QL, Takahashi R, Salvesen GS, Reed JC (1997) X-linked IAP is a direct inhibitor of cell-death proteases. Nature 388(6639): 300-304.

Du C, Fang M, Li Y, Li L, Wang X (2000) Smac, a mitochondrial protein that promotes cytochrome c-dependent caspase activation by eliminating IAP inhibition. Cell 102(1): 33-42.

Eissing T, Conzelmann H, Gilles ED, Allgower F, Bullinger E et al. (2004) Bistability analyses of a caspase activation model for receptor induced apoptosis. J Biol Chem.

Eskes R, Desagher S, Antonsson B, Martinou JC (2000) Bid induces the oligomerization and insertion of Bax into the outer mitochondrial membrane. Mol Cell Biol 20(3): 929-935.

Ferrell JE, Xiong W (2001) Bistability in cell signaling: How to make continuous processes discontinuous, and reversible processes irreversible. Chaos 11(1): 227-236.

Fischer U, Janicke RU, Schulze-Osthoff K (2003) Many cuts to ruin: a comprehensive update of caspase substrates. Cell Death Differ 10(1): 76-100.

Fussenegger M, Bailey JE, Varner J (2000) A mathematical model of caspase function in apoptosis. Nat Biotechnol 18(7): 768-774.

Garcia-Calvo M, Peterson EP, Rasper DM, Vaillancourt JP, Zamboni R et al. (1999) Purification and catalytic properties of human caspase family members. Cell Death Differ 6(4): 362-369.

Gaudet S, Janes KA, Albeck JG, Pace EA, Lauffenburger DA et al. (2005) A compendium of signals and responses triggered by prodeath and prosurvival cytokines. Mol Cell Proteomics 4(10): 1569-1590.

Green DR, Evan GI (2002) A matter of life and death. Cancer Cell 1(1): 19-30.

Harlin H, Reffey SB, Duckett CS, Lindsten T, Thompson CB (2001) Characterization of XIAP-deficient mice. Mol Cell Biol 21(10): 3604-3608.

Hill MM, Adrain C, Duriez PJ, Creagh EM, Martin SJ (2004) Analysis of the composition, assembly kinetics and activity of native Apaf-1 apoptosomes. Embo J 23(10): 2134-2145.

Hua F, Cornejo MG, Cardone MH, Stokes CL, Lauffenburger DA (2005) Effects of Bcl-2 levels on Fas signaling-induced caspase-3 activation: molecular genetic tests of computational model predictions. J Immunol 175(2): 985-995.

Huang Y, Rich RL, Myszka DG, Wu H (2003) Requirement of both the second and third BIR domains for the relief of X-linked inhibitor of apoptosis protein (XIAP)-mediated caspase inhibition by Smac. J Biol Chem 278(49): 49517-49522.

Irish JM, Kotecha N, Nolan GP (2006) Mapping normal and cancer cell signalling networks: towards single-cell proteomics. Nat Rev Cancer 6(2): 146-155.

Janes KA, Albeck JG, Gaudet S, Sorger PK, Lauffenburger DA et al. (2005) A systems model of signaling identifies a molecular basis set for cytokine-induced apoptosis. Science 310(5754): 1646-1653.

Kawai H, Suzuki T, Kobayashi T, Mizuguchi H, Hayakawa T et al. (2004) Simultaneous imaging of initiator/effector caspase activity and mitochondrial membrane potential during cell death in living HeLa cells. Biochim Biophys Acta 1693(2): 101-110.

Kim HE, Du F, Fang M, Wang X (2005) Formation of apoptosome is initiated by cytochrome c-induced dATP hydrolysis and subsequent nucleotide exchange on Apaf-1. Proc Natl Acad Sci U S A 102(49): 17545-17550.

Kuwana T, Mackey MR, Perkins G, Ellisman MH, Latterich M et al. (2002) Bid, Bax, and lipids cooperate to form supramolecular openings in the outer mitochondrial membrane. Cell 111(3): 331-342.

Lassus P, Opitz-Araya X, Lazebnik Y (2002) Requirement for caspase-2 in stress-induced apoptosis before mitochondrial permeabilization. Science 297(5585): 1352-1354.

Lee E, Salic A, Kruger R, Heinrich R, Kirschner MW (2003) The roles of APC and Axin derived from experimental and theoretical analysis of the Wnt pathway. PLoS Biol 1(1): E10.

Li H, Zhu H, Xu CJ, Yuan J (1998) Cleavage of BID by caspase 8 mediates the mitochondrial damage in the Fas pathway of apoptosis. Cell 94(4): 491-501.

Li P, Nijhawan D, Budihardjo I, Srinivasula SM, Ahmad M et al. (1997) Cytochrome c and dATP-dependent formation of Apaf-1/caspase-9 complex initiates an apoptotic protease cascade. Cell 91(4): 479-489.

Li S, Zhao Y, He X, Kim TH, Kuharsky DK et al. (2002) Relief of extrinsic pathway inhibition by the Bid-dependent mitochondrial release of Smac in Fas-mediated hepatocyte apoptosis. J Biol Chem 277(30): 26912-26920.

Li X, Darzynkiewicz Z (2000) Cleavage of Poly(ADP-ribose) polymerase measured in situ in individual cells: relationship to DNA fragmentation and cell cycle position during apoptosis. Exp Cell Res 255(1): 125-132.

Luo KQ, Yu VC, Pu Y, Chang DC (2003) Measuring dynamics of caspase-8 activation in a single living HeLa cell during TNFalpha-induced apoptosis. Biochem Biophys Res Commun 304(2): 217-222.

Luo X, Budihardjo I, Zou H, Slaughter C, Wang X (1998) Bid, a Bcl2 interacting protein, mediates cytochrome c release from mitochondria in response to activation of cell surface death receptors. Cell 94(4): 481-490.

Margolin N, Raybuck SA, Wilson KP, Chen W, Fox T et al. (1997) Substrate and inhibitor specificity of interleukin-1 beta-converting enzyme and related caspases. J Biol Chem 272(11): 7223-7228.

McDonnell TJ, Korsmeyer SJ (1991) Progression from lymphoid hyperplasia to high-grade malignant lymphoma in mice transgenic for the t(14; 18). Nature 349(6306): 254-256.

Medema JP, Scaffidi C, Kischkel FC, Shevchenko A, Mann M et al. (1997) FLICE is activated by association with the CD95 death-inducing signaling complex (DISC). Embo J 16(10): 2794-2804.

Meraldi P, Draviam VM, Sorger PK (2004) Timing and checkpoints in the regulation of mitotic progression. Dev Cell 7(1): 45-60.

Mikhailov V, Mikhailova M, Pulkrabek DJ, Dong Z, Venkatachalam MA et al. (2001) Bcl-2 prevents Bax oligomerization in the mitochondrial outer membrane. J Biol Chem 276(21): 18361-18374.

Munshi A, Pappas G, Honda T, McDonnell TJ, Younes A et al. (2001) TRAIL (APO-2L) induces apoptosis in human prostate cancer cells that is inhibitable by Bcl-2. Oncogene 20(29): 3757-3765.

Oltvai ZN, Milliman CL, Korsmeyer SJ (1993) Bcl-2 heterodimerizes in vivo with a conserved homolog, Bax, that accelerates programmed cell death. Cell 74(4): 609-619.

Posakony JW, England JM, Attardi G (1977) Mitochondrial growth and division during the cell cycle in HeLa cells. J Cell Biol 74(2): 468-491.

Potts MB, Vaughn AE, McDonough H, Patterson C, Deshmukh M (2005) Reduced Apaf-1 levels in cardiomyocytes engage strict regulation of apoptosis by endogenous XIAP. J Cell Biol 171(6): 925-930.

Rehm M, Dussmann H, Janicke RU, Tavare JM, Kogel D et al. (2002) Single-cell fluorescence resonance energy transfer analysis demonstrates that caspase activation during apoptosis is a rapid process. Role of caspase-3. J Biol Chem 277(27): 24506-24514.

Riedl SJ, Renatus M, Schwarzenbacher R, Zhou Q, Sun C et al. (2001) Structural basis for the inhibition of caspase-3 by XIAP. Cell 104(5): 791-800.

Samejima K, Earnshaw WC (2005) Trashing the genome: the role of nucleases during apoptosis. Nat Rev Mol Cell Biol 6(9): 677-688.

Scaffidi C, Schmitz I, Krammer PH, Peter ME (1999) The role of c-FLIP in modulation of CD95-induced apoptosis. J Biol Chem 274(3): 1541-1548.

Slee EA, Harte MT, Kluck RM, Wolf BB, Casiano CA et al. (1999) Ordering the cytochrome c-initiated caspase cascade: hierarchical activation of caspases-2, -3, -6, -7, -8, and -10 in a caspase-9-dependent manner. J Cell Biol 144(2): 281-292.

Spierings D, McStay G, Saleh M, Bender C, Chipuk J et al. (2005) Connected to death: the (unexpurgated) mitochondrial pathway of apoptosis. Science 310(5745): 66-67.

Stanulla M, Wang J, Chervinsky DS, Aplan PD (1997a) Topoisomerase II inhibitors induce DNA double-strand breaks at a specific site within the AML1 locus. Leukemia 11(4): 490-496.

Stanulla M, Wang J, Chervinsky DS, Thandla S, Aplan PD (1997b) DNA cleavage within the MLL breakpoint cluster region is a specific event which occurs as part of higher-order chromatin fragmentation during the initial stages of apoptosis. Mol Cell Biol 17(7): 4070-4079.

Stegh AH, Barnhart BC, Volkland J, Algeciras-Schimnich A, Ke N et al. (2002) Inactivation of caspase-8 on mitochondria of Bcl-xL-expressing MCF7-Fas cells: role for the bifunctional apoptosis regulator protein. J Biol Chem 277(6): 4351-4360.

Stelling J, Sauer U, Szallasi Z, Doyle FJ, 3rd, Doyle J (2004) Robustness of cellular functions. Cell 118(6): 675-685.

Stennicke HR, Renatus M, Meldal M, Salvesen GS (2000) Internally quenched fluorescent peptide substrates disclose the subsite preferences of human caspases 1, 3, 6, 7 and 8. Biochem J 350 Pt 2: 563-568.

Stennicke HR, Jurgensmeier JM, Shin H, Deveraux Q, Wolf BB et al. (1998) Pro-caspase-3 is a major physiologic target of caspase-8. J Biol Chem 273(42): 27084-27090.

Stucki JW, Simon HU (2005) Mathematical modeling of the regulation of caspase-3 activation and degradation. J Theor Biol 234(1): 123-131.

Sun C, Cai M, Meadows RP, Xu N, Gunasekera AH et al. (2000) NMR structure and mutagenesis of the third Bir domain of the inhibitor of apoptosis protein XIAP. J Biol Chem 275(43): 33777-33781.

Sun XM, Bratton SB, Butterworth M, MacFarlane M, Cohen GM (2002) Bcl-2 and Bcl-xL inhibit CD95-mediated apoptosis by preventing mitochondrial release of Smac/DIABLO and subsequent inactivation of X-linked inhibitor-of-apoptosis protein. J Biol Chem 277(13): 11345-11351.

Suzuki Y, Nakabayashi Y, Takahashi R (2001) Ubiquitin-protein ligase activity of X-linked inhibitor of apoptosis protein promotes proteasomal degradation of caspase-3 and enhances its anti-apoptotic effect in Fas-induced cell death. Proc Natl Acad Sci U S A 98(15): 8662-8667.

Takemoto K, Nagai T, Miyawaki A, Miura M (2003) Spatio-temporal activation of caspase revealed by indicator that is insensitive to environmental effects. J Cell Biol 160(2): 235-243.

Talanian RV, Quinlan C, Trautz S, Hackett MC, Mankovich JA et al. (1997) Substrate specificities of caspase family proteases. J Biol Chem 272(15): 9677-9682.

Tewari M, Quan LT, O'Rourke K, Desnoyers S, Zeng Z et al. (1995) Yama/CPP32 beta, a mammalian homolog of CED-3, is a CrmA-inhibitable protease that cleaves the death substrate poly(ADP-ribose) polymerase. Cell 81(5): 801-809.

Twiddy D, Brown DG, Adrain C, Jukes R, Martin SJ et al. (2004) Pro-apoptotic proteins released from the mitochondria regulate the protein composition and caspase-processing activity of the native Apaf-1/caspase-9 apoptosome complex. J Biol Chem 279(19): 19665-19682.

Tyas L, Brophy VA, Pope A, Rivett AJ, Tavare JM (2000) Rapid caspase-3 activation during apoptosis revealed using fluorescence-resonance energy transfer. EMBO Rep 1(3): 266-270.

Vaughan AT, Betti CJ, Villalobos MJ (2002) Surviving apoptosis. Apoptosis 7(2): 173-177.

Vaughan AT, Betti CJ, Villalobos MJ, Premkumar K, Cline E et al. (2005) Surviving apoptosis: a possible mechanism of benzene-induced leukemia. Chem Biol Interact 153-154: 179-185.

Verhagen AM, Ekert PG, Pakusch M, Silke J, Connolly LM et al. (2000) Identification of DIABLO, a mammalian protein that promotes apoptosis by binding to and antagonizing IAP proteins. Cell 102(1): 43-53.

Wajant H, Haas E, Schwenzer R, Muhlenbeck F, Kreuz S et al. (2000) Inhibition of death receptor-mediated gene induction by a cycloheximide-sensitive factor occurs at the level of or upstream of Fas-associated death domain protein (FADD). J Biol Chem 275(32): 24357-24366.

Wilkinson JC, Cepero E, Boise LH, Duckett CS (2004) Upstream regulatory role for XIAP in receptor-mediated apoptosis. Mol Cell Biol 24(16): 7003-7014.

Wright KM, Linhoff MW, Potts PR, Deshmukh M (2004) Decreased apoptosome activity with neuronal differentiation sets the threshold for strict IAP regulation of apoptosis. J Cell Biol 167(2): 303-313.

Wu JQ, Pollard TD (2005) Counting cytokinesis proteins globally and locally in fission yeast. Science 310(5746): 310-314.

Zhang XD, Zhang XY, Gray CP, Nguyen T, Hersey P (2001) Tumor necrosis factor-related apoptosis-inducing ligand-induced apoptosis of human melanoma is regulated by smac/DIABLO release from mitochondria. Cancer Res 61(19): 7339-7348.

Zhou HX (1993) Brownian dynamics study of the influences of electrostatic interaction and diffusion on protein-protein association kinetics. Biophys J 64(6): 1711-1726.

Zou H, Henzel WJ, Liu X, Lutschg A, Wang X (1997) Apaf-1, a human protein homologous to C. elegans CED-4, participates in cytochrome c-dependent activation of caspase-3. Cell 90(3): 405-413.

Chapter 3

The mitochondrial apoptotic pathway sets the threshold for apoptosis initiation by variable upstream signals

I performed all experiments and computational simulations shown in this chapter. John Burke assisted with this work by sharing unpublished model analysis results. Bree Aldridge played a major role in constructing the novel caspase-3 FRET reporter (see also Appendix D).

Chapter 3: The mitochondrial pathway sets a threshold for apoptosis initiation by variable upstream signals

Table of contents

3.1 Abstract

Release of cytochrome c and other pro-apoptotic proteins from the mitochondria is a central event in apoptosis and is regulated by the Bcl-2 family of proteins. While it is known that death receptor-induced caspase-8 activation induces the rapid release of cytochrome c through the Bcl-2 family proteins Bid and Bax, little is known about kinetics of this process. Using live-cell imaging to detect caspase-8 activity and mitochondrial permeabilization in single cells, we show that cleavage of caspase-8 substrates upstream of the mitochondria is a gradual process with variable rate, which suddenly induces the rapid release of mitochondrial proteins when a certain threshold is reached. We measure the level of this threshold under various conditions, and find that the time at which cells commit to apoptosis can be controlled in two ways, depending on the stimulus:1) changes in the level of caspase-8 activity, or 2) changes in the level of the threshold. Furthermore, we show that similar measurements can be made with a high-throughput flow cytometry assay, which enables rapid diagnosis of network behavior. Our findings identify the point at which the apoptotic network converts graded stimuli into an all-or-non response and provide important tools for the further study of how the mitochondrial threshold determines apoptotic sensitivity.

3.2 Introduction

The mitochondrial apoptotic pathway plays a essential role in the induction of apoptosis by many stimuli (Spierings et al. 2005). This pathway is required for death receptor-mediated apoptosis in HeLa cells and is required for the all-or-none regulation of effector caspase substrate cleavage ((Yang et al. 1997), Ch. 2). Permeabilization of the mitochondrial outer membrane results in the release of pro-apoptotic proteins such as Smac and cytochrome c from the mitochondrial intermembrane space to the cytosol. The permeabilization process is tightly controlled by the Bcl-2 family of proteins, which include both pro- and anti- apoptotic members. The interactions between Bcl-2 family proteins are elaborate (see section 1.3.4), but the central regulatory concept is believed to be a stoichiometric titration process analogous to a rheostat (Korsmeyer et al. 1993): certain pro-apoptotic family members stimulate pore formation in the outer mitochondrial membrane (Kuwana et al. 2002), while anti-apoptotic Bcl-2 proteins bind to these pro-apoptotic proteins and prevent them from doing so (Oltvai et al. 1993; Cheng et al. 2001). Therefore, the level of anti-apoptotic Bcl-2 proteins present in the cell determines the number of pro-apoptotic proteins that must be generated by a death stimulus to enable permeabilization, effectively setting the position of the rheostat. If the number of available anti-apoptotic Bcl-2 proteins is high, then many pro-apoptotic proteins are needed to overwhelm the pool of anti-apoptotic proteins, and thus only prolonged or intense pro-apoptotic stimuli will result in cell death. Conversely, if few anti-apoptotic proteins are present, then relatively low numbers of pro-apoptotic proteins are needed to reach the threshold set by the anti-apoptotic proteins, and thus weaker stimuli are sufficient to induce apoptosis. Therefore, in the rheostat model, the levels of various Bcl-

2 members in the cell are critical determinants of a cell's sensitivity to apoptosis, and the interactions of these proteins create a threshold for apoptotic signaling.

While the Bcl-2 family is clearly an important factor in determining whether a given stimulus results in cell death, an equally significant factor is the signal upstream of the mitochondrial pathway. (Here, we define the mitochondrial pathway as the steps beginning with modification of the levels or activities of the Bcl-2 family proteins and ending in he release of Smac and cytochrome c from the mitochondria). The Bcl-2 family proteins may set the threshold for apoptosis, but the strength of the signal that induces the activation of the pro-apoptotic Bcl-2 proteins determines whether or not this threshold is reached. However, much remains unknown about these upstream signals. This is partly because much less is known about the molecules involved, and partly because these signals are subtle and difficult to observe experimentally. The best-characterized upstream signal for the mitochondrial pathway is the cleavage of Bid by caspase-8 in the death receptor pathway (Li et al. 1998; Luo et al. 1998). Activation of the death receptor by ligand induces DISC formation and activation of caspase-8. Caspase-8 then cleaves Bid, which in turn activates Bax, an effector pro-apoptotic Bcl-2 protein that translocates to the mitochondria to induce permeabilization (Eskes et al. 2000). Therefore, this chain of events – from receptor to caspase-8 to Bid - regulates the amount and rate at which active Bax is produced, and modulation of this pathway in part determines whether enough Bax is activated to induce mitochondrial permeabilization.

Measuring the signals upstream of the mitochondria is the key to understanding many things that have remained obscure about the process leading from the initial pro-apoptotic stimulus to mitochondrial permeabilization:

- Does the mitochondrial pathway create a threshold for apoptotic signaling, as suggested in the rheostat model? An alternative possibility is that the threshold lies upstream (for example at the level of receptor activation), and that the mitochondrial pathway simply amplifies once the upstream threshold has been reached.
- If the mitochondrial pathway does set a threshold for mitochondrial permeabilization, how much caspase-8 activity is required to reach the threshold?
- What is the kinetic behavior of the caspase-8 signal, and what is its dynamic range in response to different strengths of stimuli?
- How do survival signals block mitochondrial permeabilization - by changing the threshold for permeabilization, or by affecting the upstream signal?
- Where does cell-to-cell variability in response to apoptotic stimuli originate - from cell-to-cell differences in the threshold for permeabilization or from differences in the strength or kinetics of the upstream signal?

To answer these questions we need methods for accurately assaying both the caspase-8 signal and mitochondrial permeabilization, so that the temporal relationship of these two processes can be directly observed. There are a number of methods available for assaying the activity of caspase-8, but the majority of these are based on biochemical techniques that produce population-average data. The work already described in this thesis (see Chapter 2) shows that population-average data can obscure essential features of the behavior of apoptotic systems. This is due in part to the highly asynchronous nature of apoptotic responses (Tyas et al. 2000), and in part to the fact that the myriad

biochemical events and positive feedback loops set in motion downstream of mitochondrial permeabilzation can overshadow the more subtle events that occur upstream (Green 2005). Thus, a single-cell approach is essential to answer these questions.

In this chapter, we examine the relationship of death receptor-induced caspase-8 activity and mitochondrial permeabilization in single living cells. Using fluorescent protein reporters for caspase-8 activity and mitochondrial permeabilization, we simultaneously observe these two events under a range of treatments. We find that caspase-8 cleavage of its substrates is initially a slow process that is detectable shortly after stimulation with TNF or TRAIL. The sudden onset of mitochondrial permeabilization occurs later, once the level of caspase-8 substrate cleavage has reached a certain threshold. Moreover, we find that the time of cell death can be modulated either by altering the level of caspase-8 activity or by adjusting the permeabilization threshold. We also develop a flow cytometry-based assay that enables high-throughput observation of the relative dynamics of caspase-8 activity and mitochondrial permeabilization and use this assay to observe network behavior in response to a number of genetic perturbations. Together, our findings provide a clearer picture of how graded upstream signals are converted into a discrete all-or-none cell decision.

3.3 Results

3.3.1 Modeling upstream events in receptor-induced apoptosis

In the current understanding of death receptor-induced apoptosis, caspase-8 and Bid are both required for induction of mitochondrial permeabilization in the death

receptor pathway (Li et al. 2002). However, some reports have suggested that this is not always the case (Deng et al. 2003). To verify that caspase-8 and Bid are indeed required in our experimental system, we depleted these proteins 10-fold by siRNA (Fig 3.1A). After treatment with TNF and cycloheximide (CHX), cytochrome c localization was determined by immunofluorescence (Fig 3.1 B). In cells not treated with siRNA, TNF/CHX treatment stimulated the translocation of cytochrome c from the mitochondria to the cytosol, a hallmark event of mitochondrial permeabilization. However, in caspase-8 or Bid-depleted cells, cytochrome c translocation did not occur under TNF/CHX treatment. Cleavage of PARP, which requires mitochondrial permeabilization in HeLa cells, was also blocked by caspase-8 or Bid depletion (data not shown). Therefore, caspase-8 and Bid are essential for the induction of mitochondrial permeabilization in HeLa cells, making these cells an appropriate model system in which to examine the relationship of caspase-8 activity and the mitochondrial pathway.

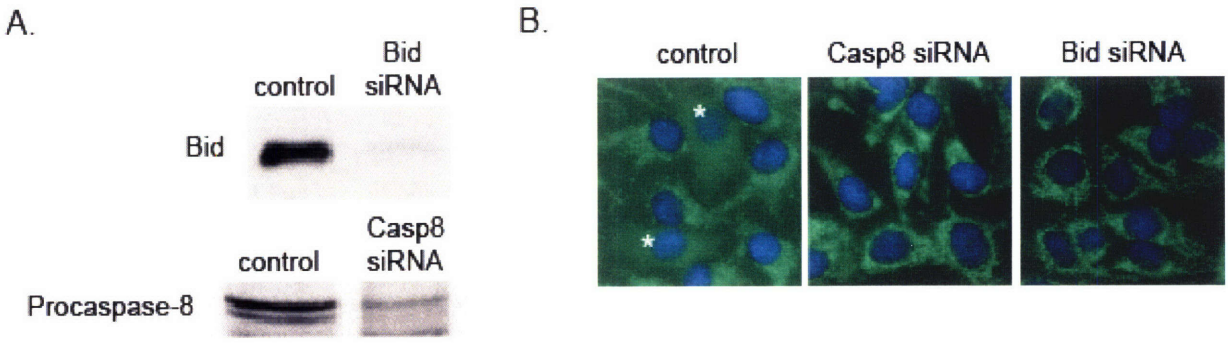

Figure 3.1 Caspase-8 and Bid are required for TNF-induced mitochondrial permeabilization in HeLa cells. A. Immunoblot analysis of Bid and caspase-8 depletion by siRNA. B. HeLa cells were transfected with the indicated siRNA oligos and then

treated with 50 ng/ml TNF + 2.5 ug/ml CHX for 4 hours. Cytochrome c (green) was detected by immunofluorescence, and DNA (blue) was stained with Hoechst 33342. Cells displaying redistribution of cytochrome c from mitochondria to the cytosol are indicated with stars.

As an aid to understanding the quantititative behavior of caspase-8 signaling and mitochondrial permebilization, we examined our mathematical model of receptor-induced apoptosis in HeLa cells (Fig 3.2 A). In the mathematical model, the ratio of activated Bax (Bax*) to Bcl-2 played a central role in controlling mitochondrial permeabilization (J.M.Burke., unpublished results). In simulations, when this ratio exceeded 1 (Fig 3.2 B, green line and star), indicating an excess of Bax* relative to Bcl-2, and Smac/cytochrome c were suddenly released (Fig 3.2 B, red curves). The release of Smac and cytochrome c was then quickly followed by PARP cleavage (Fig 3.2.B, yellow curves). Thus, the mathematical model is consistent with the rheostat analogy discussed above, since the Bax*/Bcl-2 ratio sets a sharp threshold for the onset of permeabilization. In simulation, the buildup of Bax* was directly dependent on the production of tBid by caspase-8 (Fig 3.2.B, blue curve), which was gradual up until the point of mitochondrial permeabilization. However, the kinetics of Bid cleavage in the model were poorly constrained, since there are few data on the behavior of caspase-8 activity or Bid cleavage in single cells, and further model validation necessitates experimental examination of Bid cleavage.

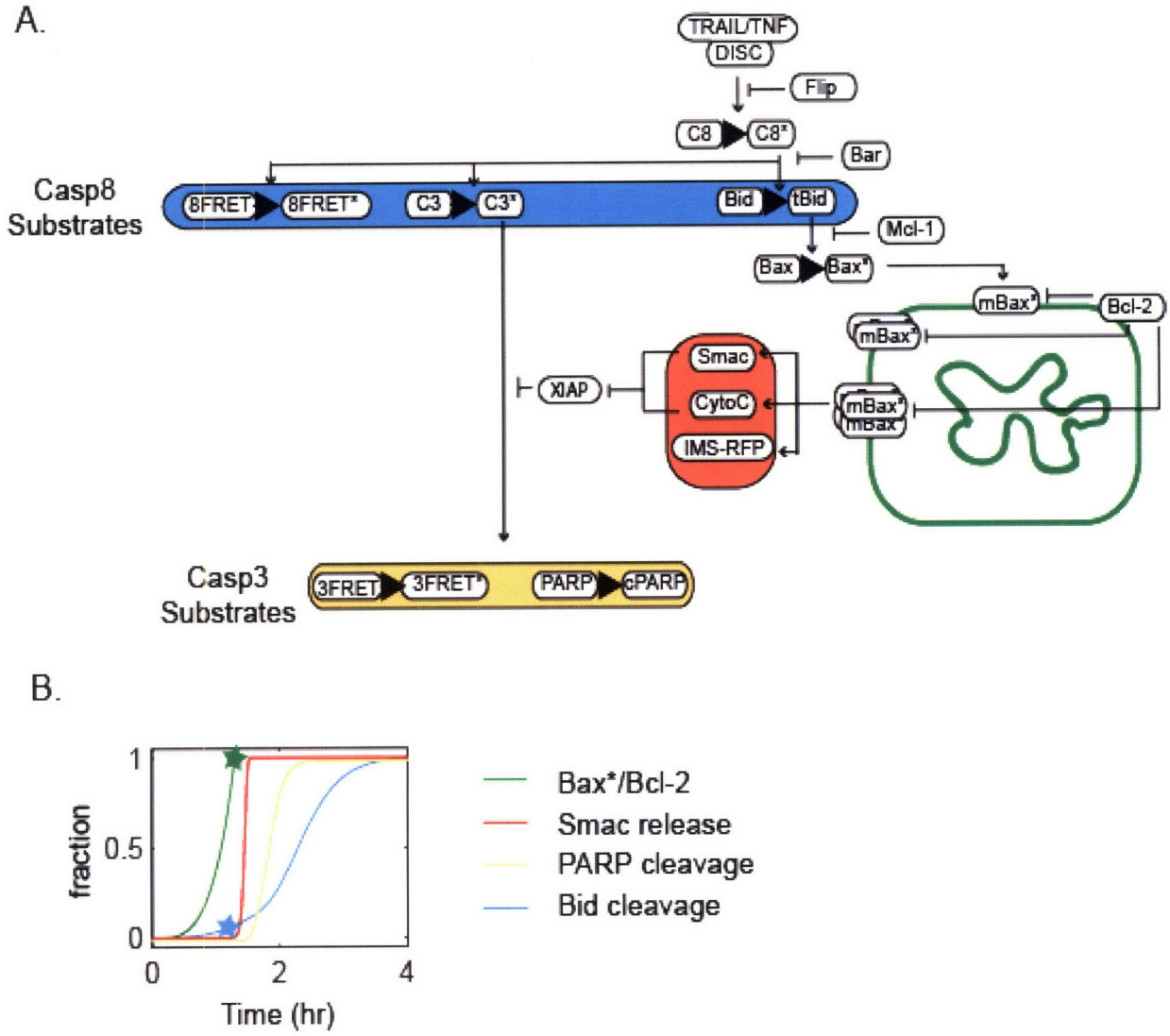

Figure 3.2 Mathematical model of mitochondrial permeabilization. A. Schematic diagram of the mathematical model. Colored ovals indicate reactions that are catalyzed by the same upstream regulator, which are assumed to have similar kinetics. Note that caspases are abbreviated: C3=Proaspase-3, C3*=active Caspase-3, etc. B. Model simulation of the response to TRAIL. Line colors correspond to the colored sections in A. The green star indicates the time at which the Bax*/Bcl-2 ratio reaches 1; the blue star indicates the level of Bid cleavage at the time that the Bax*/Bcl-2 ratio reaches 1.

3.3.2 Simultaneous imaging of multiple apoptotic events

To simultaneously observe the relative kinetics of caspase activity and mitochondrial permeabilzation, we used a combination of live-cell reporters. First, caspase activity was observed using GFP-based FRET reporters, a widely used technique (Fig 2.1, (Luo et al. 2001; Rehm et al. 2002; Luo et al. 2003; Takemoto et al. 2003; Kawai et al. 2004)). For this study, we employed newly-constructed, and more specific, caspase-3 and -8 reporters (see Appendix D). The kinetics of cleavage of the caspase-8 reporter should closely follow that of Bid cleavage because they are both substrates of the same protease (Fig 3.2 A, blue oval). Second, to monitor mitochondrial permeabilization, we used IMS-RFP, a novel reporter that accurately indicates the onset of mitochondrial permeabilization. Unlike Smac or cytochrome c, IMS-RFP can be overexpressed without altering mitochondrial signaling (Fig 3.2 A, red oval and App. D).

To verify our ability to accurately measure the relative kinetics of caspase activity and mitochondrial permeabilization, we examined the temporal relationship between caspase-3 activity and mitochondrial permeablization. In HeLa cells treated with TRAIL, caspase-3 is not activated until after mitochondrial permeabilization (see Fig 2.2). When HeLa cells expressing both the caspase-3 FRET reporter and IMS-RFP were treated with TRAIL/CHX, individual cells displayed both a sudden redistribution of IMS-RFP, indicating mitochondrial permeabilization, and a rapid increase in CFP:YFP ratio, indicating caspase-3 activity (Fig 3.3 A). In all cells imaged, the rapid increase of CFP:YFP ratio did not begin until after the first frame of IMS-RFP release. Therefore, caspase-3 was activated only after mitochondrial permeabilization, consistent with our previous findings, and demonstrating that our live-cell techniques can accurately detect

the relative timing of caspase activity and mitochondrial permeabilization. Moreover, as we had observed previously (Fig 2.1), individual cells displayed high variability in the time at which rapid FRET reporter cleavage occurred. However, when responses of the caspase-3 FRET reporter for multiple single cells were aligned by the time at which IMS-RFP redistribution began, a striking overlap between all cells was observed (Fig 3.3.C). This overlap confirms that, in HeLa cells, the events following mitochondrial permeabilization and leading to caspase-3 activation are highly stereotypical and nearly invariable from cell to cell. Therefore, cell-to-cell variability in the response to TRAIL likely occurs upstream of mitochondrial permeabilization.

We next examined the temporal relationship between mitochondrial permeabilization and upstream caspase-8 activity. For this, we performed time-lapse imaging of TRAIL-stimulated cells expressing both IMS-RFP and the caspase-8 FRET reporter. In contrast to the caspase-3 FRET reporter, we observed a significant change in caspase-8 FRET reporter cleavage prior to the first frame of IMS-RFP release (Fig 3.3.B). In each cell, a slow rise in cleavage occurred in the 1-4 hours preceding IMS-RFP release, reaching 20-30% of maximum cleavage at the onset of release (Fig 3.3 B). After IMS-RFP release, cleavage accelerated, so that the remaining ~70% of cleavage occurred in only ~30 minutes. The slow initial rise in cleavage indicates that a significant amount of caspase-8 activity occurs before IMS-RFP release; this component of the signal is likely produced by direct activation of caspase-8 by the DISC. After IMS-RFP release, the accelerated rate of caspase-8 reporter cleavage is likely due to the increase in caspase-8 activity that results from the caspase-6-mediated positive feedback loop, but it may also reflect cleavage of the reporter by related caspases such as caspase-9, which

become active during the post-release phase. This biphasic behavior was a general characteristic of all cells examined, as becomes clear by the overlap of trajectories when multiple cells are aligned by the time at which IMS-RFP release began (Fig 3.3.D). This experimentally observed behavior supports the hypothesis that the mitochondrial pathway sets a signaling threshold, because we observed that caspase-8 activity is a gradual signal that triggers mitochondrial permeabilization suddenly when it reaches a certain level. Moreover, the rise in FRET reporter cleavage prior to permeabilization is essentially linear, consistent with a first-order cleavage reaction by caspase-8, as was assumed by our model. Together, these results suggest that the kinetics of Bid cleavage and permeabilization triggering in the mathematical model are a good approximation of cellular behavior.

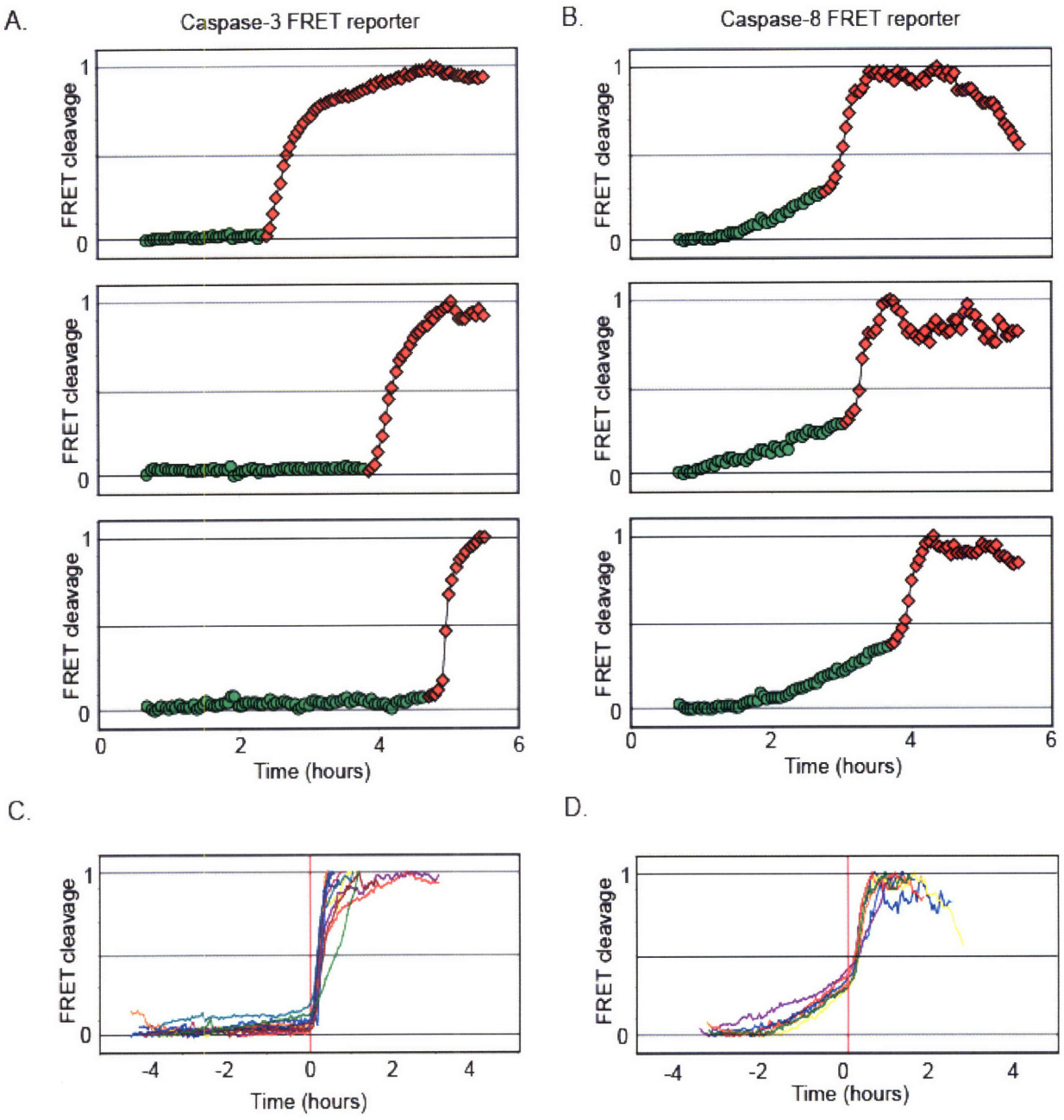

Figure 3.3 Simultaneous live-cell imaging of caspase-activity and mitochondrial permeabilization. A, B HeLa cells were transfected with IMS-RFP and the caspase-3 FRET reporter (A) or the caspase-8 FRET reporter (B) and then monitored by live-cell microscopy during treatment with 50 ng/ml TRAIL + 2.5 ug/ml CHX. The responses of three individual cells are shown for each. Green points indicate frames occurring before the first frame of IMS-RFP release; red points indicate frames occurring at or after the first frame of IMS-RFP release. C, D. Individual cell responses from A and B,

respectively,were synchronized by the first frame of IMS-RFP release (which is set to time 0 and indicated by the red vertical line) and overlaid.

3.3.3 Control of the timing of mitochondrial permeabilization

To further characterize the mitochondrial threshold, we examined multiple individual HeLa cells in populations treated with different concentrations of TRAIL and CHX. Using live-cell microscopy, we determined the percentage of caspase-8 FRET reporter cleavage at the time of IMS-RFP release; for conciseness we hereafter refer to this measurement as the "threshold value". When different concentrations of TRAIL were applied in the presence of CHX, the average time at which IMS-RFP was released increased substantially as the TRAIL concentration was decreased (Fig 3.4 A). This was also observed for PARP cleavage under similar conditions (see Fig 2.1). However the average threshold value did not vary substantially, remaining at 23-25%, with similar standard deviations, across a 25-fold range of TRAIL concentration. This indicates that the differences in the delay preceding IMS-RFP release result from changes in the rate at which cells reach the threshold value, and not from changes in the threshold value itself. In contrast, when cells were treated with TRAIL in the absence of CHX, a significant increase in the average threshold value (to 44%) was observed, along with an increase in the average delay preceding IMS-RFP, relative to cells treated with the same concentration of TRAIL in the presence of CHX (Fig 3.4 A). Together, these results suggest that the timing of mitochondrial permeabilization can be adjusted in two ways. First, changes in the rate of Bid cleavage (from different amounts of active caspase-8, for example) can affect how long it takes to reach the threshold for mitochondrial

permeabilization (Fig 3.4.B, red star). Second, the threshold itself can be adjusted (such as by changes in Bcl-2 family protein levels, Fig 3.4.B, blue star).

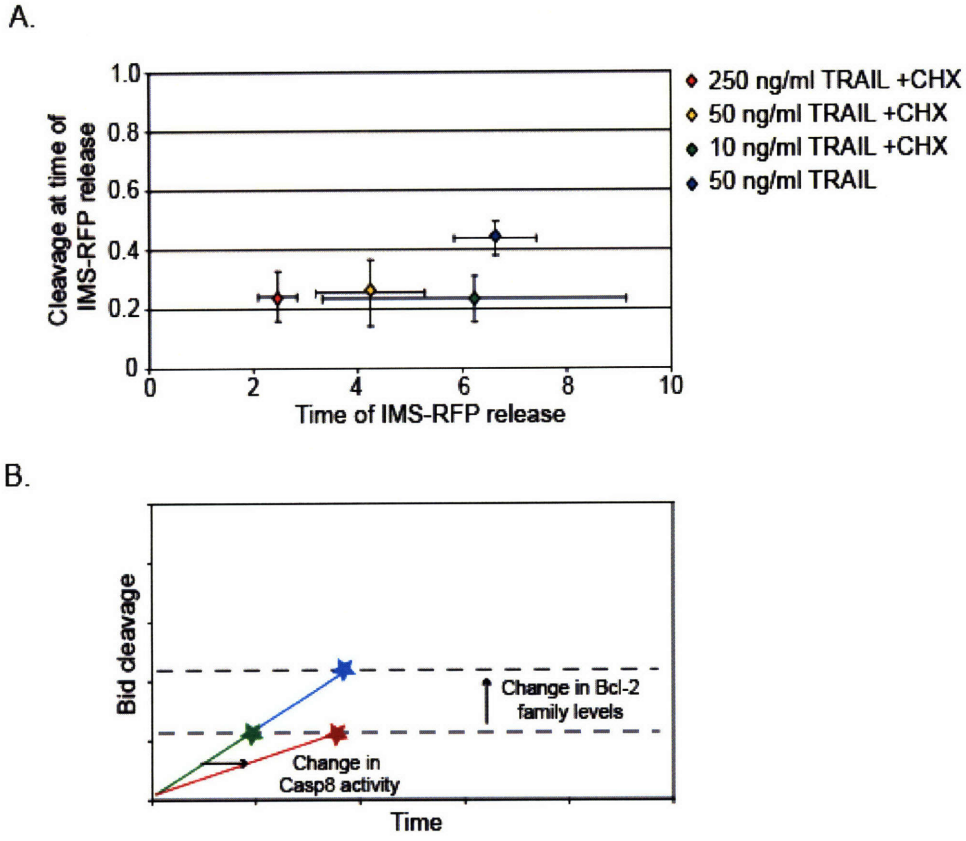

Figure 3.4 Variation in the upstream signal and in the threshold level. A. HeLa cells were transfected with caspase-8 FRET reporter and IMS-RFP and then treated with the indicated doses of TRAIL and CHX. The fraction of reporter cleavage at the first frame of IMS-RFP release (threshold value) and the time of release were measured for 9-10 cells in each condition. For each treatment, the threshold value is plotted against the time of release. B. Schematic diagram of how the timing of mitochondrial permeabilization can be delayed. Relative to a baseline condition (green line and star), a lower slope of Bid cleavage (such as would result from lower caspase-8 activity, red line) would result in reaching the threshold at a later time (red star). Raising the threshold value (such as would result from an increase in Bcl-2 levels, blue line) would also delay permeabilization (blue star), even if the slope of Bid cleavage was not altered.

We next examined whether the observed changes in delay time were consistent with our mathematical model. When ligand concentration was reduced in model simulations, fewer caspase-8 molecules were activated, and Bid cleavage was slower, Consequently, it took longer to reach the Bax*/Bcl-2=1 threshold, and a delay in permeabilization resulted (Fig 3.5 A). However, Bid cleavage at the time of permeabilization remained approximately the same, consistent with our experimental observations. A delay in permeabilziation time was also observed when Bcl-2 family proteins were increased, such as Mcl-1, which in the model bound to tBid and prevented it from activating Bax (Fig 3.5.B). In this case, caspase-8 activity was unaffected, and thus Bid cleavage reached a significantly higher level by the time permeabilization is initiated (Fig 3.5.B blue stars). Therefore, model and experiment agree that either changes in the threshold or the upstream signal can produce substantial changes in the timing of permeabilization. The model also indicated that only the threshold, and not the upstream signal, can be changed such that permeabilization never occurs. For example if Bcl-2 levels are higher than the pool of Bax that is available to be activated, the threshold is unreachable and even complete activation of Bax will never result in permeabilization (J.M. Burke, unpublished data). Conversely, if the threshold is reachable, then even a very small upstream signal will, in theory, eventually allow the threshold to be reached. The only way to adjust the upstream signal to entirely prevent permeabilization would be to remove it completely.

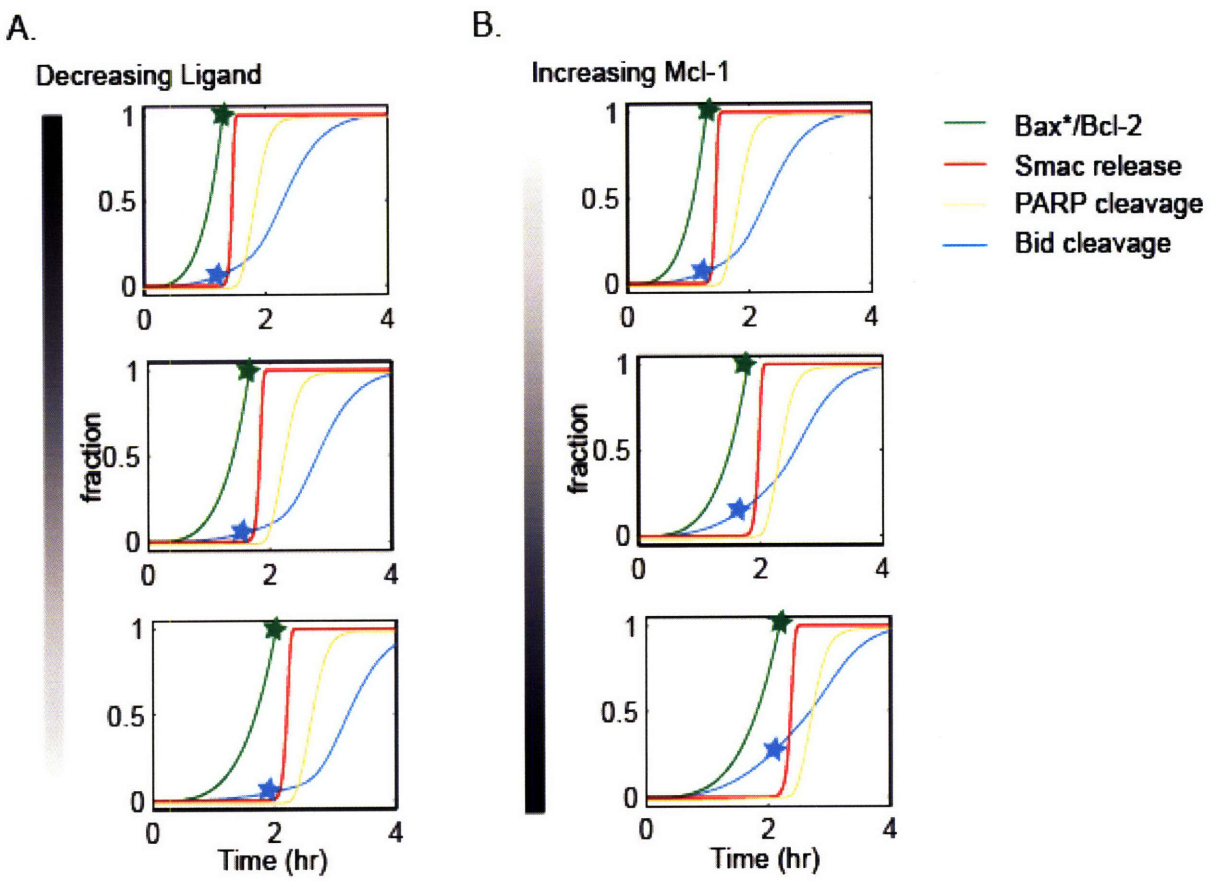

Figure 3.5 Modeling delay in mitochondrial permeabilization. A, B. Simulations of the response to decreasing concentrations of death ligand (A, gray bar) or increasing concentrations of Mcl-1 (B, gray bar). Green star indicates the time at which the Bax*/Bcl-2 ratio reaches 1; blue star indicates the level of Bid cleavage at the time the Bax*/Bcl-2 ratio reaches 1.

It is clear from the mathematical model that changes in threshold value, such as the difference observed between cells treated with TRAIL/CHX or TRAIL alone, likely result from changes in the abundance of Bcl-2 family members. Therefore, we examined the levels of Mcl-1, a key anti-apoptotic Bcl-2 family protein, in HeLa cells treated with TRAIL+CHX or TRAIL alone. While Mcl-1 protein levels remained constant throughout 6 hours of treatment with TRAIL, a >2-fold decrease in Mcl-1 levels occurred

within 2 hours of TRAIL+CHX co-treatment (Fig 3.6). A likely explanation for this drop in levels in the presence of CHX is that Mcl-1 has a half-life of ~40 minutes (Nijhawan et al. 2003), and inactivating protein synthesis by using CHX allows this degradation to occur without replenishment of the protein. Thus, at least one key Bcl-2 family member changes in a manner consistent with the shift in permeabilization threshold between TRAIL and TRAIL+CHX-treated HeLa cells.

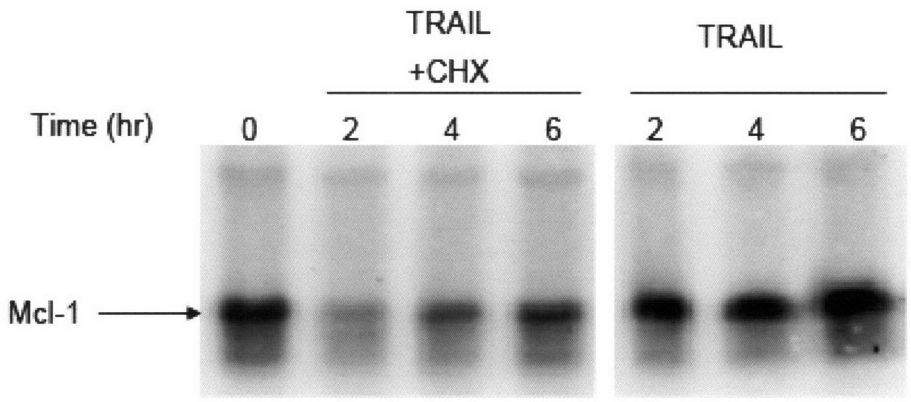

Figure 3.6 Mcl-2 levels are reduced during cotreatment with CHX. HeLa cells were treated with 50 ng/ml TRAIL in the presence or absence of 2.5 ug/ml CHX. Mcl-1 levels were determined by immunoblot at the indicated times.

3.3.4 Input-output relationship of initiator and effector caspase activity

Because both caspase-8 and caspase-3 activities were determined in relation to IMS-RFP release, the relationship of these two signals could also be determined. We averaged the IMS-RFP-aligned signals for each FRET reporter and plotted them on a common timescale, with t=0 set at the time of IMS-RFP release (Fig 3.7 A). From this plot, it is clear that mitochondrial permeabilization divides apoptosis into two phases: an initial phase (for $t<0$) in which only initiator caspases are active, and a later phase ($t>0$)

characterized by high activity of both initiator and effector caspases. These data can also be plotted as the level of caspase-8 reporter cleavage vs. the level of caspase-3 reporter cleavage, to form an input-output plot (Fig 3.7 B). Again, we can observe two phases: initially, cleavage of the initiator caspase substrate increases while effector caspase substrate is mostly unchanged (green circles), corresponding to a rightward shift with little change in the vertical direction. Then, when a certain level of input (caspase-8 signal) is reached, mitochondrial permeabilization occurs (red squares), and both caspase-8 and caspase-3 increase in activity, indicated by a shift upward and to the right.

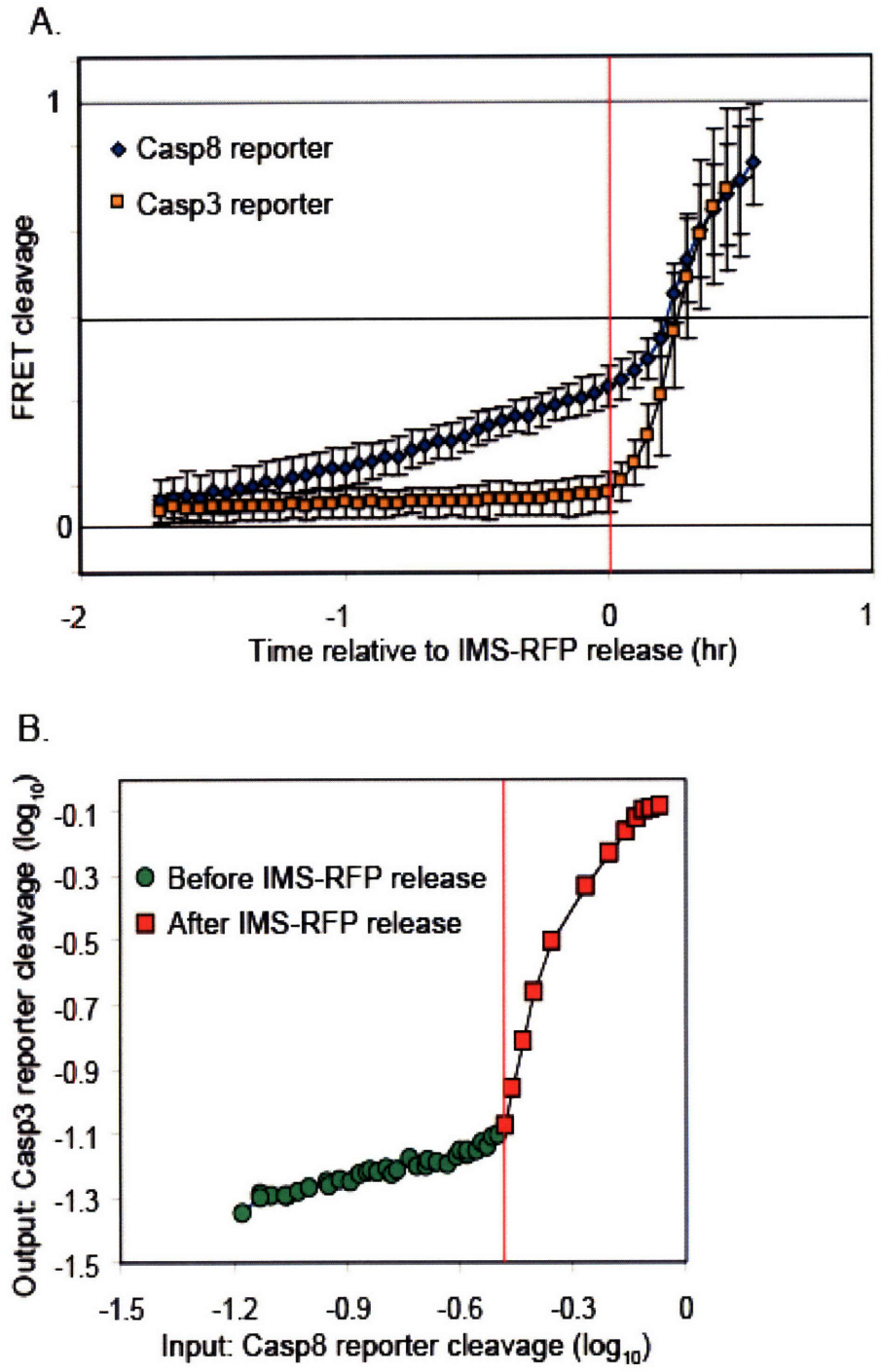

Figure 3.7 Input-output relationship of caspase-8 and caspase-3 activity. A. For each FRET reporter, 9-12 individual cell responses were synchronized by the first frame of IMS-RFP release (indicated by the red vertical line) and averaged at each time point;

error bars represent +/- 1 standard deviation. B. The average values for caspase-3 and caspase-8 reporter cleavage are plotted against each other on logarithmic axes.

3.3.5 Measuring caspase input-output by flow cytometry

Live cell microscopy provides detailed time course data, but is relatively low-throughput and relies on exogenous fluorescent reporter proteins. Conversely, immunofluorescence measurements by flow cytometry sacrifice temporal resolution, but are higher-throughput and can reveal the behavior of endogenous proteins. Therefore, we aimed to develop a flow cytometry assay for simultaneously detecting multiple apoptotic events. The antibody against cleaved PARP used in Chapter 2 provides a highly specific measurement of the level of effector caspase substrate cleavage, a measurement analogous to the caspase-3 reporter (Fig 3.2 A, yellow oval). Another commercially available antibody, directed against the caspase-3 epitope that is exposed when caspase-3 is cleaved by caspase-8 or -9 at Asp175, could provides a means for quantifying the cleavage of initiator caspase substrates (Li et al. 1997; Stennicke et al. 1998). In principle, the signal from this antibody is analogous to the caspase-8 FRET reporter, since the FRET reporter contains a cleavage site that is identical to the caspase-8/9 cleavage site in caspase-3 (IETD). We had previously observed that in Bcl-2-overexpressing cells, staining with this antibody increases upon TRAIL treatment, and that this increase is prevented by caspase-8 depletion (Fig 2.S5). However, because it is known that cleaved caspase-3 is degraded after several hours, it was somewhat puzzling that the signal from this antibody remained high after several hours (Fig 2.S5). A likely explanation is that this antibody may also recognize similar epitopes on other caspase-8

substrates. Since caspase-8 cleaves multiple proteins at sites with similar sequences, caspase-8 activity would lead to the production of several different proteins with similar cleaveage-dependent epitopes. Thus, the specificity of the cleaved caspase-3 antibody is likely somewhat broader than is generally assumed, and staining with this antibody probably reflects the aggregate levels of multiple caspase-8 cleaved proteins. Nonetheless, this antibody provides a useful indication of the activity of caspase-8, and thus we refer to it henceforth as "cleaved Casp8 substrate" antibody.

We combined the cPARP and Casp8 substrate antibodies in a two-color flow cytometry experiment. To validate the two-color assay, we compared staining in the presence and absence of mitochondrial permeabilization, using Hct-116 Bax +/- and Bax-/- cells. Deletion of Bax in these cells effectively blocks mitochondrial permeabilization in response to TRAIL (Deng et al. 2002). We did not use Bcl-2-overexpressing HeLa cells because they also express GFP, which complicates flow cytometric analysis. When Hct-116 Bax -/- cells were treated with TRAIL, the plot of cleaved Casp8 substrate vs. cPARP indicated that over time the majority of cells increased in cleaved Casp8 substrate signal but not in Casp3 substrate signal (Fig 3.8). This behavior , consistent with the live cell data, indicates that in the period preceding mitochondrial permeabilization, caspase-8 is active while caspase-3 is not. In Hct-116 Bax +/- cells treated with TRAIL, a subpopulation of cells showed a similar increase in cleaved Casp8 substrates with no increase in cPARP signal. Another subpopulation displayed a larger increase in cleaved Casp8 substrate signal as well as an increase in cPARP signal. Over time, the cleaved Casp8 substrate-positive, cPARP-negative population disappeared, while the double-positive population increased. This progression indicates that, in response to TRAIL

treatment, Hct-116 cells first enter a phase in which only caspase-8 is active, and later enter a phase in which both caspase-8 and caspase-3 are active. The transition to the second phase is dependent on mitochondrial permeabilization, since it does not occur frequently in Bax-/- cells. Overall, this behavior is very similar to that observed by live-cell microscopy (compare Fig 3.7.B and Fig 3.8). Thus, it is also possible from these data to obtain an estimate of the threshold value for cleaved Casp8 substrate at which mitochondrial permeabilization occurs, by determining the highest level of cleaved Casp8 substrate signal that occurs in cPARP-negative cells. In Hct-116 Bax +/- cells, this value was 25% of the maximum signal (Fig 3.8). Thus, the cleaved Casp8 substrate/cPARP two-color cytometry assay provides a high throughput method for measuring input-output behavior in the caspase network.

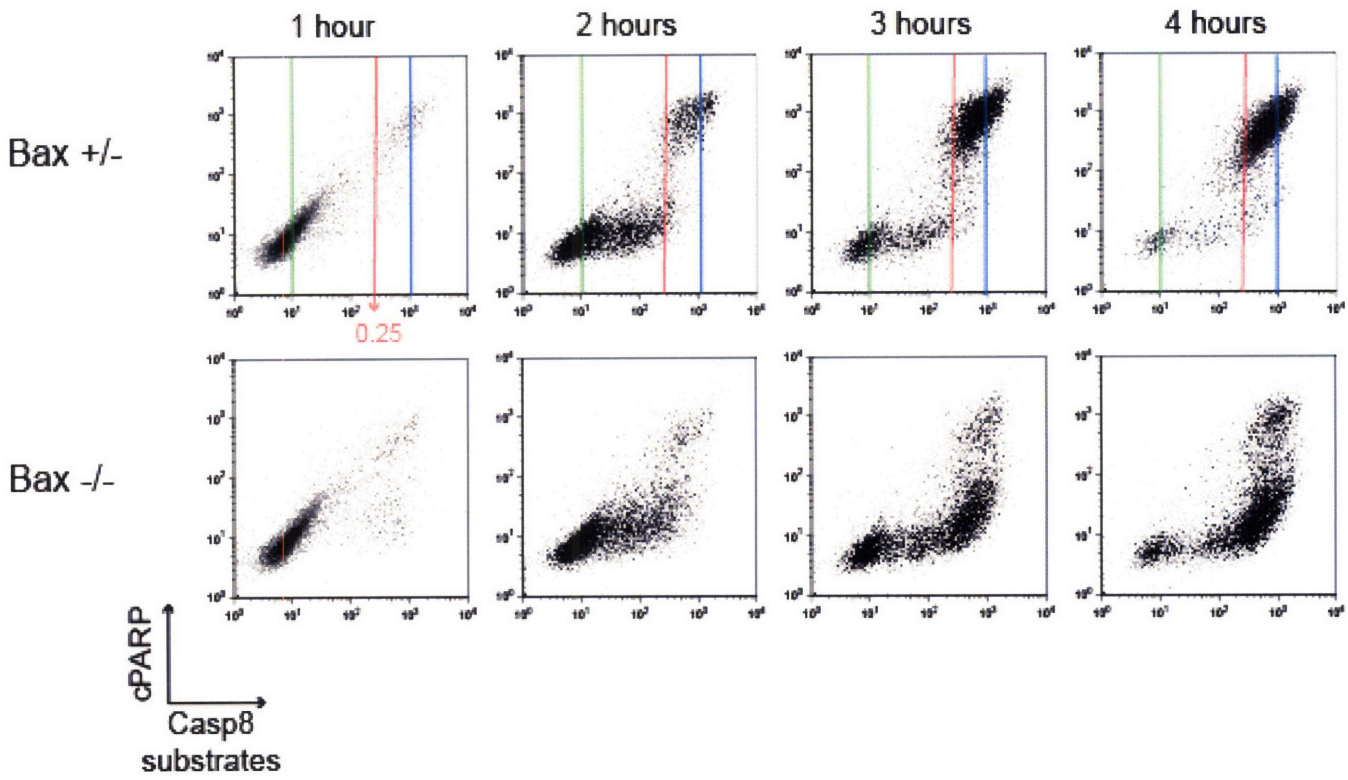

Figure 3.8 Flow cytometric observation of the input-output relationship of caspase-8 and caspase-3. Bax+/- and Bax-/- Hct-116 colon carcinoma cells were treated with 20 ng/ml TRAIL + 2.5 ug/ml CHX for the indicated times. Cells were fixed and analyzed by flow cytometry for cPARP and cleaved caspase-8 substrates. For Bax +/- cells, colored lines indicate the basal (green), threshold (red), and maximum (blue) values of cleaved caspase-8 substrate signal, respectively. The magnitude of the threshold signal, as a fraction of the maximum signal, is indicated under the left-most plot. Lines are not shown for Bax -/- cells because there is no clearly defined threshold value.

We then used the cleaved Casp8 substrate/cPARP assay to examine the threshold value in HeLa cells. We first examined HeLa cells treated with different concentrations of TRAIL or TNF in the presence of CHX (Fig 3.9.A). In each case, the cleaved Casp8 substrate/cPARP pattern observed was similar to that in Hct-116 cells; cells first

increased in cleaved Casp8 substrate signal alone until a threshold point was reached, and then became positive for both antibodies. The threshold value of cleaved Casp8 substrate was calculated for each condition and was found to range from 10-14% in each case. In cells treated with TRAIL in the absence CHX, the threshold value rose to 25% (Fig 3.9.B). Thus, the general behavior of the threshold value measured by cytometry is in good agreement with that measured by live-cell microscopy. However, the absolute values measured by flow cytometery were consistently lower than the values observed by live-cell microscopy (~12% vs. ~24% with CHX and ~25% vs. ~44% without). One possible reason for this discrepancy is that caspase-8 cleaves the FRET reporter and the pool of substrates detected by the Casp8 substrates antibody at different rates. Another possibility is errors in calibration; in both methods, the threshold values are determined as a percentage of the maximum value, and therefore measurements are highly sensitive to errors in the estimation of the maximum value. Nonetheless, the two methods provide a narrow range of estimates for the level of cleavage of Bid that is necessary to cross the mitochondrial pathway threshold. In the future, more accurate calibration and knowledge of the extent to which each method over- or under-estimates the actual rate of Bid cleavage should yield a better estimate.

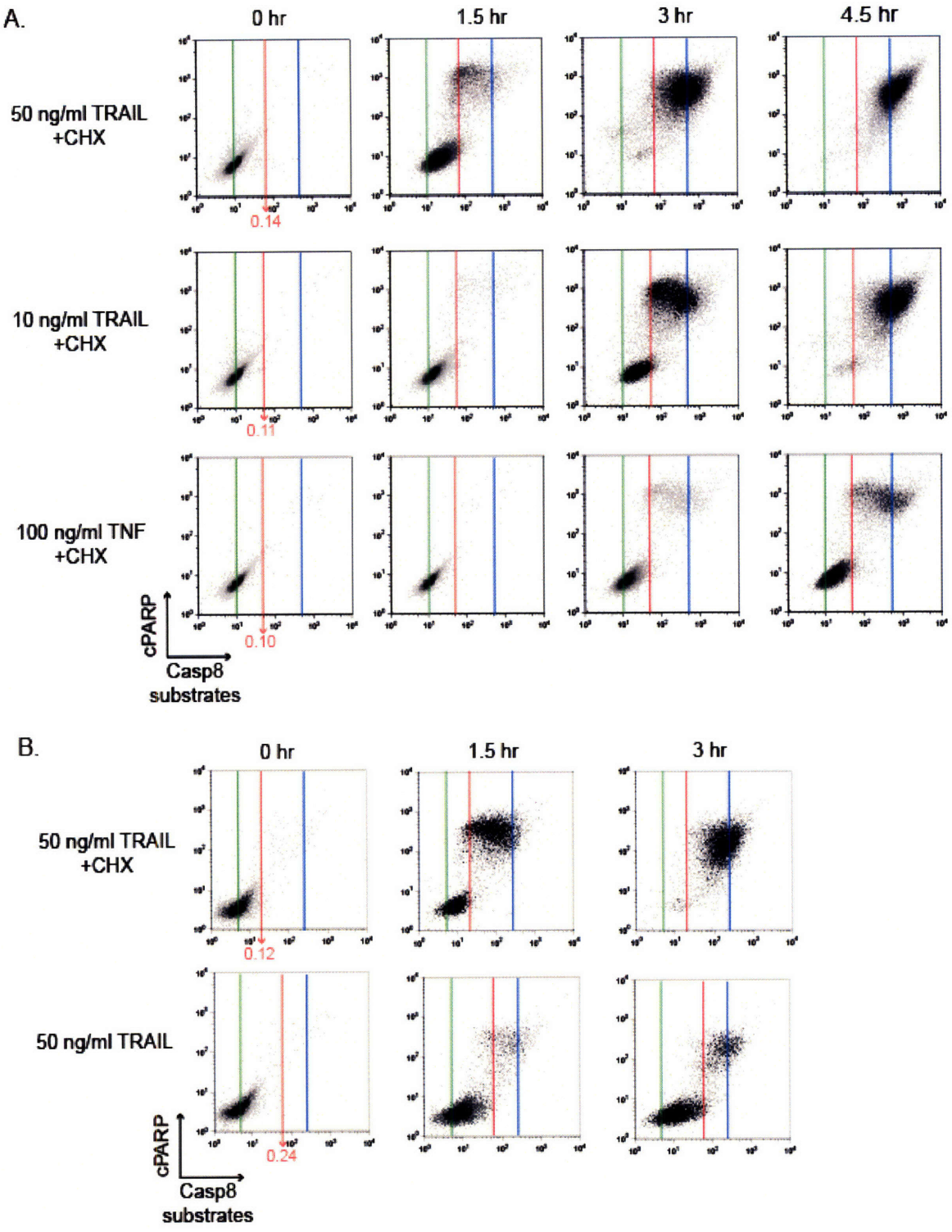

Figure 3.9 Flow cytometric determination of threshold value in HeLa cells. A,B. HeLa cells were treated as indicated and analyzed by flow cytometry for cPARP and cleaved

caspase-8 substrates as in Fig. 3.7. Colored lines indicate the basal (green), threshold (red), and maximum (blue) values of cleaved caspase-8 substrate signal, respectively.

3.3.6 Diagnosis of network behavior by flow cytometry

Next, we examined the effects of perturbation of the network by siRNA depletion on the mitochondrial pathway threshold (Fig 3.10). We first examined the depletion of Bid, the link between Casp8 activity and mitochondrial permeabilization. When Bid was depleted by 10-fold, the pattern of Casp8 substrate/cPARP staining observed by flow cytometry shifted so that the threshold for mitochondrial permeabilization increased to ~50% of the maximum cleaved Casp8 substrate signal. This shift is consistent with our model results; when fewer Bid proteins are present, Bax activation is slower and thus it will take longer to reach the point at which free Bcl-2 is exhausted. Consequently, mitochondrial permeabilization is delayed, and more caspase-8 substrates are cleaved before permeabilization occurs.

Conversely, when caspase-8 was depleted by siRNA (by 10-fold), the initial phase of caspase-8 substrate cleavage was strongly attenuated, and cells were unable to reach the threshold for mitochondrial permeabilization (Fig 3.10). Even more strikingly, when Bid and XIAP were depleted simultaneously, the apparent threshold was destroyed; under these conditions, cPARP signal always increased in proportion to cleaved Casp8 substrate. This pattern is consistent with the mechanism of snap-action switching described in Chapter 2, since both XIAP and the mitochondrial pathway are required for effective switching. Furthermore, Smac depletion, another perturbation that resulted in a loss of snap-action switching (Ch. 2), produced a similar pattern with no apparent threshold (Fig 3.10). Therefore, at least 3 different cases can be distinguished by the two-

color cPARP/cleaved Casp8 substrate assay: 1) regulation of the upstream signal (e.g. caspase-8 depletion), 2) alteration of the threshold for mitochondrial permeabilization (e.g. Bid depletion), and 3) breakdown of switching behavior (e.g. Smac depletion).

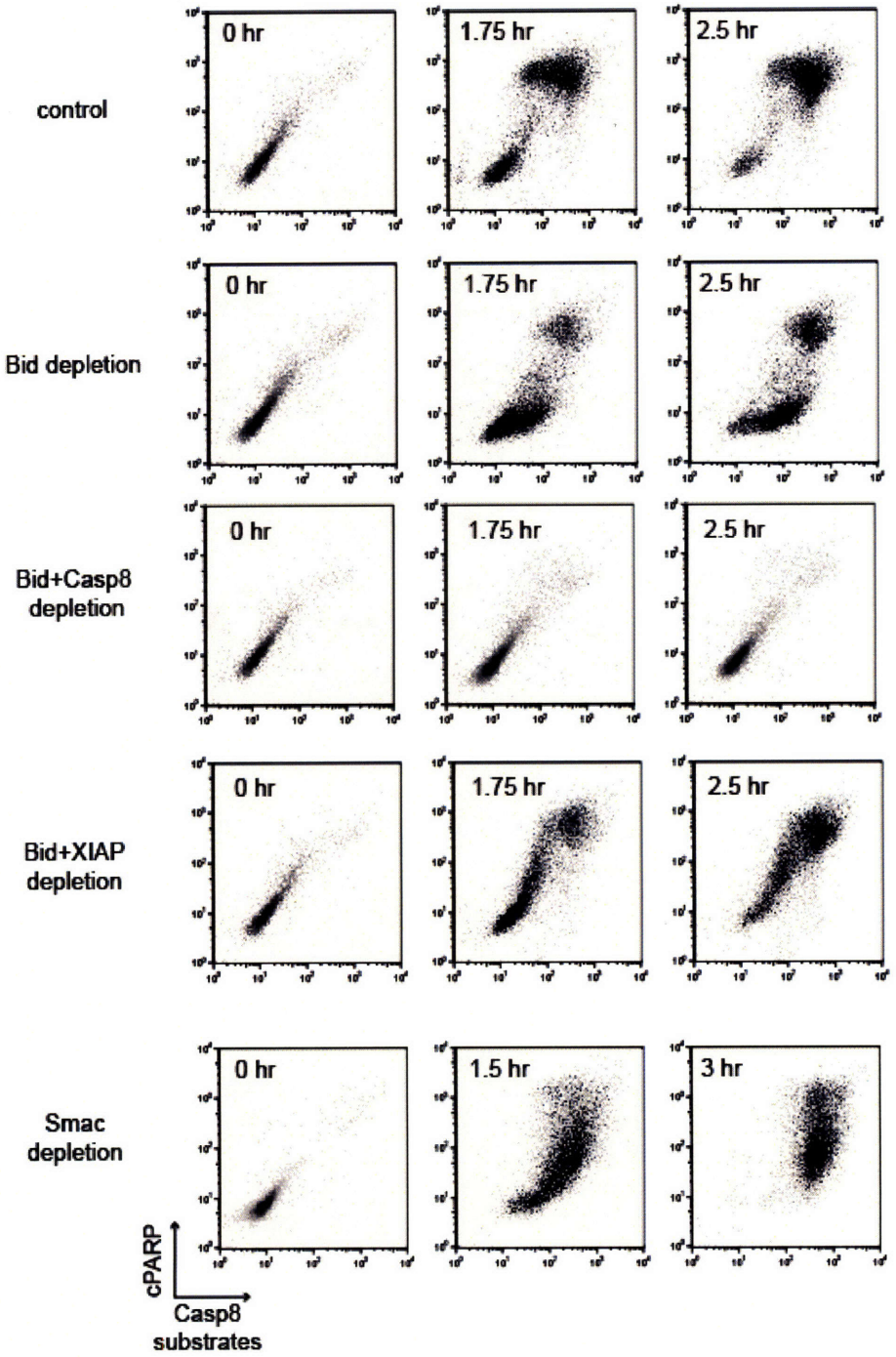

Figure 3.10 Observation of network behavior by flow cytometry. HeLa cells were transfected with the indicated with the indicated siRNA oligos, and then treated with 50 ng/ml TRAIL + 2.5 ug/ml CHX. cPARP and cleaved caspase-8 substrates were measured by flow cytometry.

Next, we studied the effect of TNF, in the absence of CHX, on caspase-8 and caspase-3 activity in HeLa cells. In the absence of CHX, TNF treatment did not produce a significant increase in either cPARP or cleaved Casp8 substrate (3.11), similar to the effect of caspase-8 depletion in TNF+CHX-treated cells (Fig 3.10). Therefore, in the case of TNF stimulation, the pro-survival pathway inhibited by CHX must act at or upstream of the level of caspase-8. This is consistent with the general hypothesis that TNF strongly stimulates the NF-kB pathway, which upregulates the DISC regulator Flip (Micheau et al. 2001); treatment with CHX blocks this upregulation. Interestingly, our results suggest that the pro-survival mechanisms inhibited by CHX in the cases of TRAIL and TNF stimulation are different. Under TRAIL stimulation, CHX blocks a pathway that regulates the threshold for the mitochondrial pathway, while under TNF stimulation, CHX blocks a pathway that inhibits caspase-8 activation at the DISC. Thus, within the same cell type, different ligands induce different survival pathways, which intervene in apoptotic signaling in distinct ways.

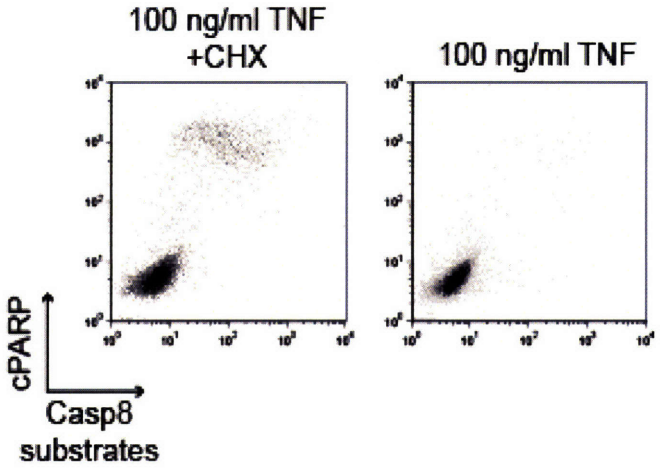

Figure 3.11 Suppression of Caspase-8 activity in cells treated with TNF in the absence of CHX. HeLa cells were treated for 4 hours with 100 ng/ml TNF in the presence or absence of 2.5 ug/ml CHX. cPARP and cleaved caspase-8 substrates were analyzed by flow cytometry.

3.4 Discussion

In this chapter, we studied the junction between upstream death receptor-induced signaling and mitochondrial permeabilization. Using live-cell microscopy, we showed that upstream of the mitochondrial pathway, cleaved caspase-8 substrates accumulate gradually, and upon reaching a certain threshold level, they trigger the sudden and rapid release of proteins from the mitochondrial intermembrane space. This supports the hypothesis put forward in Chapter 2 that permeabilization of the mitochondria is the critical threshold event in death receptor-induced apoptosis.

Importantly, our data support a quantitative model for how different concentrations and types of death ligand induce apoptosis with very different timing. The number of death receptors engaged by ligand determines the number of caspase-8

molecules that are activated; this in turn determines the rate at which tBid is cleaved and the rate at which Bax* reaches the threshold level set by anti-apoptotic Bcl-2 proteins. Under the conditions we examined, the cleavage of caspase-8 substrates increased with monotonic and approximately linear kinetics until the threshold was reached. However, after permeabilization, the rate of caspase-8 substrate cleavage increased markedly. This second phase of cleavage, likely a result of positive feedback, may explain the discrepancies in previous studies of caspase-8 activation in response to death receptor stimulation (Luo et al. 2003; Kawai et al. 2004). In the absence of information about mitochondrial permeabilization, interpreting the kinetics of capase-8 activity would be difficult. However, by simultaneously imaging caspase-8 activity and mitochondrial permeabilization, we were able to clearly distinguish these two phases.

It should be emphasized that the apparent threshold that we observe experimentally is likely an indirect measurement of the true threshold for mitochondrial permeabilization. In the current model, the true threshold is set by the ratio of Bax* to Bcl-2. However, we made surrogate measurements of the level of tBid, which is one step upstream of Bax*. The relationship of our measurements to the true threshold will therefore depend on the amount of signal amplification in the tBid to Bax* step. In future work, it may be possible to directly measure Bax* levels in relation to both tBid production and mitochondrial permeabilization; this will enable an even more accurate quantitative model of signal transduction in this pathway. Nonetheless, the measurements reported here have significant value, because they clearly distinguish events that affect the signal upstream of Bid from events that affect Bid and Bax directly. In interpreting our data, it must be remembered that the apparent (or experimentally

observed) threshold can be affected both by molecules that interact directly with Bax* and molecules that interact only with tBid, whereas the true threshold would only be affected by the former. Interestingly, because some Bcl-2 anti-apoptotic proteins may interact with tBid and not with Bax*, the apparent threshold we observe may actually be a more informative measure of the total activity level of anti-apoptotic Bcl-2 proteins than direct measures the threshold for Bax*.

The sensitivity of cells to a given apoptotic stimuli is widely thought to depend on the threshold set by the ratio of Bcl-2 family proteins. This threshold is believed to play a critical role in the resistance of cancer cells to apoptosis (Lowe et al. 2004). By measuring the input and the output to the mitochondrial pathway, we report the first single-cell measurements of where on the continuum of input values the threshold lies in a widely-used cancer cell line. Although the measurements reported here are relative values, calculated as a percentage of the maximum signal, it should be possible, using quantitative calibration methods, to determine the absolute number of tBid (and eventually, Bax*) molecules needed to cross the threshold. Moreover, it will be interesting to make similar measurements in other cell types, and to determine how their threshold values relate to their sensitivity to various apoptotic stimuli. Our flow cytometry results with HeLa and Hct-116 cells indicate a 2-fold difference in threshold value between these cell lines, confirming that substantial variation among cell lines exists. We also demonstrate that changes in this threshold value result from anti-apoptotic signaling. Detecting such changes will be useful in evaluating the effects of pro-survival pathways; the relative effectiveness of multiple survival pathways may be quantitatively compared by examining the extent to which they alter the threshold.

We find that similar measurements of the mitochondrial threshold, and of general network dynamics, can made either by live-cell microscopy or by flow cytometry. While live-cell microscopy provides better temporal resolution and is likely more accurate, the flow cytometry assay is much higher throughput. Flow cytometry measurements of at least 11 parameters are now possible (Irish et al. 2004), but we find that even a 2-parameter experiment provides a highly information-rich assay of network behavior, when it is interpreted in the context of a quantitative mechanistic model. This would suggest that flow cytometry experiments with more than two parameters could yield a remarkable amount of mechanistic information from a single sample, when experimental analysis is coupled with an appropriate modeling approach. Yet, even in its current stage, the 2-parameter experiment described here will provide an excellent means for high-content, high-throughput measurement of death receptor-induced responses in multiple cell lines. Moreover, it can be used to screen libraries of drugs or genetic reagents for molecules that specifically affect the death receptor-induced signal, the mitochondrial threshold, or snap-action switching.

Our results highlight the interesting relationship between the timing of cell death and apoptotic sensitivity. It could be argued that setting the threshold of input signal required for cell death is equivalent to setting the delay time in response to a given stimulus. This may be true in many cases, but our model suggests that the threshold can be changed in two ways. First, it is possible to set the threshold so high that it can never be reached by pro-apoptotic signals of any strength; this requires a high level of overexpression of Bcl-2 family proteins. Second, the threshold can be raised to a high, but still attainable level, resulting in a delayed mitochondrial pemeabilization in response

to any given stimulus. This could also ultimately reduce the senstitivity of the cell, because it could enable the cell to "wait out" transient pro-apoptotic stimuli without committing to apoptosis. The existence of these two distinct forms of resistance to apoptosis raises the question of whether it is necessary for cancer cells to set the threshold so high that it is unattainable, or whether they can survive effectively simply by delaying death. In many studies, when sensitivity to apoptosis is measured, the distinction between delaying death and preventing it indefinitely is not made. Our model suggests that closer attention to this detail will be important in understanding tumor cell behavior.

3.5 Materials and Methods

Reagents and cell culture

HeLa cell lines were maintained in DMEM supplemented with 10% fetal bovine serum and glutamine. Hct-116 cell lines, a kind gift of Dr. Bert Vogelstein, were maintained in McCoy's 5A medium supplemented with 10% fetal bovine serum. siRNA oligos were obtained from Dharmacon. Construction of the plasmids pExchange1-IMS-RFP, pECFP-DEVDR-Venus, and pECFP-IETD2X-Venus are described in Appendix D. SuperKiller TRAIL was obtained from Alexis, and TNF was from Peprotech. Anti-cytochrome c, anti-cPARP, and anti-cleaved caspase-3 were from BD Biosciences. Secondary antibodies were obtained from Molecular Probes. Oligofectamine was obtained from Invitrogen, and Fugene 6 was from Roche.

Transfection

siRNA transfections were performed as previously described using Oligofectamine. The concentrations of siRNA oligos in complex were between 4 and 16 nM. Plasmid DNA transfections were performed with Fugene 6 according to the manufacturer's instructions.

Immunofluorescence microscopy

HeLa cells were cultured on chambered slides (LabTek), transfected with siRNA oligos for 48 hours, and treated as indicated. Fixation was the performed using 4% formaldehyde in PBS at room temperature for 10 minutes. Cells were blocked and permeabilzed in Perm/Wash solution. Primary antibody (anti-cytochrome c) was diluted 1:250 or 1:500 in Perm/Wash and incubated on the samples for 1 hour at room temperature or 4° C overnight. Secondary antibody and Hoechst 33342 were diluted in Perm/Wash buffer and incubated with the samples for 1 hour at room temperature. Slides were mounted with coverslips and imaged using a Deltavision Spectris AX71 fluorescence microscope.

Live cell microscopy

HeLa cells transfected with fluorescent reporters were seeded in chamberered cover glass slides (LabTek). Immediately prior to imaging, medium was replaced with CO_2-independent medium (Gibco) containing the appropriate doses of SuperKiller TRAIL and CHX. Cells were then imaged at 37° C on a Deltavision Spectris AX71 equipped with a temperature control chamber using a 20X objective. CFP, YFP, and RFP images were acquired at 3-minute intervals for 12 hours. Image analysis was performed in ImageJ.

Flow cytometry

After treatment for the appropriate length of time with SuperKiller TRAIL, HeLa cells were trypsinized (taking care to collect both floating and adherent cells) and fixed with 4% paraformaldehyde in PBS for 10 minutes at room temperature. Following a PBS wash, cells were permeablized in 100% methanol. Prior to staining for flow cytometry, cells were stored for up to 5 days at -20 C in 100% methanol. Cells were stained with primary antibodies (1:250 anti-cleaved PARP and 1:500 anti-cleaved caspase-3 in PBS-T+1%BSA) for 1 hour at room temperature, followed by staining with secondary antibodies (1:250 in PBS-T+1%BSA) for 1 hour. Cells were then analyzed on a Becton Dickinson FACSCalibur. Analysis was performed using the FlowJo software package. Measurements of the mitochondrial threshold value for the cleaved Casp8 substrate antibody were made by first estimating the average maximum fluorescence level across all time points for that experiment and the approximate position of the threshold fluorescence intensity for the time point that was closest to the average cPARP T_d for that condition. Threshold values were then calculated by dividing the fluorescence intensity of at the threshold by the maximum fluorescence intensity.

Mathematical modeling

Model simulations were performed in Matlab using the model and the procedures described in Chapter 2.

3.6 Acknowledgements

I thank Suzanne Gaudet and Sabrina Spencer for helpful comments on this chapter.

3.7 References

Cheng EH, Wei MC, Weiler S, Flavell RA, Mak TW et al. (2001) BCL-2, BCL-X(L) sequester BH3 domain-only molecules preventing BAX- and BAK-mediated mitochondrial apoptosis. Mol Cell 8(3): 705-711.

Deng Y, Lin Y, Wu X (2002) TRAIL-induced apoptosis requires Bax-dependent mitochondrial release of Smac/DIABLO. Genes Dev 16(1): 33-45.

Deng Y, Ren X, Yang L, Lin Y, Wu X (2003) A JNK-dependent pathway is required for TNFalpha-induced apoptosis. Cell 115(1): 61-70.

Eskes R, Desagher S, Antonsson B, Martinou JC (2000) Bid induces the oligomerization and insertion of Bax into the outer mitochondrial membrane. Mol Cell Biol 20(3): 929-935.

Green DR (2005) Apoptotic pathways: ten minutes to dead. Cell 121(5): 671-674.

Irish JM, Hovland R, Krutzik PO, Perez OD, Bruserud O et al. (2004) Single cell profiling of potentiated phospho-protein networks in cancer cells. Cell 118(2): 217-228.

Kawai H, Suzuki T, Kobayashi T, Mizuguchi H, Hayakawa T et al. (2004) Simultaneous imaging of initiator/effector caspase activity and mitochondrial membrane potential during cell death in living HeLa cells. Biochim Biophys Acta 1693(2): 101-110.

Korsmeyer SJ, Shutter JR, Veis DJ, Merry DE, Oltvai ZN (1993) Bcl-2/Bax: a rheostat that regulates an anti-oxidant pathway and cell death. Semin Cancer Biol 4(6): 327-332.

Kuwana T, Mackey MR, Perkins G, Ellisman MH, Latterich M et al. (2002) Bid, Bax, and lipids cooperate to form supramolecular openings in the outer mitochondrial membrane. Cell 111(3): 331-342.

Li H, Zhu H, Xu CJ, Yuan J (1998) Cleavage of BID by caspase 8 mediates the mitochondrial damage in the Fas pathway of apoptosis. Cell 94(4): 491-501.

Li P, Nijhawan D, Budihardjo I, Srinivasula SM, Ahmad M et al. (1997) Cytochrome c and dATP-dependent formation of Apaf-1/caspase-9 complex initiates an apoptotic protease cascade. Cell 91(4): 479-489.

Li S, Zhao Y, He X, Kim TH, Kuharsky DK et al. (2002) Relief of extrinsic pathway inhibition by the Bid-dependent mitochondrial release of Smac in Fas-mediated hepatocyte apoptosis. J Biol Chem 277(30): 26912-26920.

Lowe SW, Cepero E, Evan G (2004) Intrinsic tumour suppression. Nature 432(7015): 307-315.

Luo KQ, Yu VC, Pu Y, Chang DC (2001) Application of the fluorescence resonance energy transfer method for studying the dynamics of caspase-3 activation during UV-induced apoptosis in living HeLa cells. Biochem Biophys Res Commun 283(5): 1054-1060.

Luo KQ, Yu VC, Pu Y, Chang DC (2003) Measuring dynamics of caspase-8 activation in a single living HeLa cell during TNFalpha-induced apoptosis. Biochem Biophys Res Commun 304(2): 217-222.

Luo X, Budihardjo I, Zou H, Slaughter C, Wang X (1998) Bid, a Bcl2 interacting protein, mediates cytochrome c release from mitochondria in response to activation of cell surface death receptors. Cell 94(4): 481-490.

Micheau O, Lens S, Gaide O, Alevizopoulos K, Tschopp J (2001) NF-kappaB signals induce the expression of c-FLIP. Mol Cell Biol 21(16): 5299-5305.

Nijhawan D, Fang M, Traer E, Zhong Q, Gao W et al. (2003) Elimination of Mcl-1 is required for the initiation of apoptosis following ultraviolet irradiation. Genes Dev 17(12): 1475-1486.

Oltvai ZN, Milliman CL, Korsmeyer SJ (1993) Bcl-2 heterodimerizes in vivo with a conserved homolog, Bax, that accelerates programmed cell death. Cell 74(4): 609-619.

Rehm M, Dussmann H, Janicke RU, Tavare JM, Kogel D et al. (2002) Single-cell fluorescence resonance energy transfer analysis demonstrates that caspase activation during apoptosis is a rapid process. Role of caspase-3. J Biol Chem 277(27): 24506-24514.

Spierings D, McStay G, Saleh M, Bender C, Chipuk J et al. (2005) Connected to death: the (unexpurgated) mitochondrial pathway of apoptosis. Science 310(5745): 66-67.

Stennicke HR, Jurgensmeier JM, Shin H, Deveraux Q, Wolf BB et al. (1998) Pro-caspase-3 is a major physiologic target of caspase-8. J Biol Chem 273(42): 27084-27090.

Takemoto K, Nagai T, Miyawaki A, Miura M (2003) Spatio-temporal activation of caspase revealed by indicator that is insensitive to environmental effects. J Cell Biol 160(2): 235-243.

Tyas L, Brophy VA, Pope A, Rivett AJ, Tavare JM (2000) Rapid caspase-3 activation during apoptosis revealed using fluorescence-resonance energy transfer. EMBO Rep 1(3): 266-270.

Yang J, Liu X, Bhalla K, Kim CN, Ibrado AM et al. (1997) Prevention of apoptosis by Bcl-2: release of cytochrome c from mitochondria blocked. Science 275(5303): 1129-1132.

Chapter 4

A Systems Model of Signaling Identifies a Molecular Basis Set for Cytokine-Induced Apoptosis

This chapter was adapted, with permission, from:

Janes K.A.*, Albeck J.G.*, Gaudet S., Sorger P.K., Lauffenburger D.A., Yaffe M.B. A systems model of signaling identifies a molecular basis set for cytokine-induced apoptosis. Science. 2005 Dec 9;310(5754):1646-53.
* These authors contributed equally to this work.

In this study, I performed all of the flow cytometry apoptosis measurements analyzed throughout the paper. K.Janes performed the PLS modeling analysis, phospho-JNK western blotting, and cytokine analysis. S.Gaudet performed western blotting analysis of caspase cleavage.

Chapter 4

A Systems Model of Signaling Identifies a Molecular Basis Set for Cytokine-Induced Apoptosis

Table of contents

4.1 Abstract

Signal transduction pathways control cellular responses to stimuli, but it is unclear how molecular information is processed as a network. We constructed a systems model of 7980 intracellular signaling events that directly links measurements to 1440 response outputs associated with apoptosis. The model accurately predicted multiple time-dependent apoptotic responses induced by a combination of the death-inducing cytokine tumor necrosis factor (TNF) with the pro-survival factors epidermal growth factor (EGF) and insulin. By capturing the role of unsuspected autocrine circuits activated by TGF-α and IL-1α, the model revealed new molecular mechanisms connecting signaling to apoptosis. The model derived two groupings of intracellular signals that constitute fundamental dimensions (molecular "basis axes") within the apoptotic signaling network. Projection along these axes captures the entire measured apoptotic network, suggesting that cell survival is determined by signaling through this canonical basis set.

4.2 Introduction

Despite extensive molecular-level information on how external stimuli affect cell fate, there is minimal understanding of how such intracellular processing occurs at a system-wide level. Most extracellular "inputs" initiate complex signaling patterns that propagate through an intracellular network to change the response "outputs" that determine a cell's phenotype (Downward 2001). Molecular signaling through this network is branched (fig. 4.S1) and dynamically interconnected to the molecular history of the prior inputs, signals, and outputs (Dumont et al. 2002). Thus, we sought to develop a mathematical formalism to connect signals and outputs in such a way that cellular responses could be predicted from molecular signaling patterns alone.

To reduce the biological complexity of cellular signal processing, experimental systems usually monitor changes in one defined extracellular stimulus (for example, a soluble cytokine) and one output response (such as apoptosis). However, physiological input stimuli are not processed in isolation, because signaling networks constantly receive additional inputs from changing environmental conditions, such as nutrient availability, cell density, and exposure to the extracellular matrix (Bissell and Radisky 2001). To investigate multi-input signal processing, large-scale "systems biology" approaches have been proposed. However, most of the analyses to date have concentrated on characterizing signals downstream of individual inputs (Bouwmeester et al. 2004; Zhu et al. 2004).

4.3 Results

Studying multiple input stimuli requires information about the network as a whole; otherwise, intracellular changes in signal transduction molecules (called "molecular signals" hereafter) can appear paradoxical. For example, c-jun N-terminal kinase (JNK) is a protein that has been reported to be proapoptotic (Lei and Davis 2003), antiapoptotic (Lamb et al. 2003), or uninvolved in apoptosis (Abreu-Martin et al. 1999)in different cell systems. To investigate this JNK-apoptosis link further, we added multiple combinations of tumor necrosis factor (TNF) and epidermal growth factor (EGF) to HT-29 human colon adenocarcinoma cells and then measured the amounts of phosphorylated JNK (P-JNK) and apoptosis (Fig. 4.1A). A plot of the TNF and EGF input stimuli and corresponding P-JNK signal and apoptosis outputs established a four-dimensional signal-response "surface" (Fig. 4.1B). "Slices" through this surface mimicking single TNF or EGF inputs could recapitulate any of the previously reported correlations between P-JNK and apoptosis (Fig. 4.1, C–E) (Abreu-Martin et al. 1999; Lamb et al. 2003; Lei and Davis 2003). This indicated that individual molecular signals like P-JNK cannot uniquely determine a cell's commitment to apoptosis, a complex output response. Quantitative experiments that dynamically sample many critical signals would be needed (Janes et al. 2003).

4.3.1 Dense experimental sampling of 7980 molecular signals and 1440 response outputs for cytokine-induced apoptosis.

To investigate how signaling networks coordinate cellular output responses, we used an established multi-input system where HT-29 cells are stimulated with three biologically relevant cytokines: TNF, EGF, and insulin (Gaudet et al. 2005a; Janes et al. 2006). The intracellular protein network downstream of these cytokine inputs is understood in reasonable detail (fig. 4.S1). Within well-recognized network branches, 19 intracellular measurements of key receptor, kinase, caspase, and adaptor proteins were collected (Table 4.1 and fig. 4.S1) (Janes et al. 2006). Using nine distinct pairwise combinations of TNF, EGF, and insulin (Fig. 4.1F), we sampled each molecular signal in triplicate at 13 time points between 0 and 24 hr to compile 7980 distinct molecular signals from the shared intracellular network (Janes et al. 2006). TNF and EGF or insulin are opposing cytokine inputs that promote or inhibit apoptosis, respectively (Abreu-Martin et al. 1995; Remacle-Bonnet et al. 2000), and the intracellular measurements thus identified which molecular signals were activated en route to the cellular decision to die or to survive. However, it remained unclear how EGF- and insulin-induced molecular signals antagonized TNF-induced apoptosis.

To test whether apoptosis could be connected to the measured signaling network (Janes et al. 2006), we measured the cell-death phenotype for each combinatorial cytokine stimulus (Fig. 4.1F). The apoptotic response itself involves various cellular changes (outputs) that can be regulated independently (Del Bino et al. 1999). Individual parameters used to characterize cell death (such as loss of membrane asymmetry) only

partially reflect the overall cellular response. Therefore, we selected four distinct apoptotic outputs (phosphatidylserine exposure, membrane permeability, nuclear fragmentation, and caspase substrate cleavage) and measured each output response by flow cytometry 12, 24, and 48 hr after stimulation (Fig. 4.1, G–O). Together, these output measurements constituted an apoptotic "signature" that characterized early (phosphatidylserine exposure), middle (caspase substrate cleavage and membrane permeability), and late (nuclear fragmentation) responses of apoptosis (the biological outputs in our system).

Table 4.1. Signaling network measurements

Protein name	Function*	Molecular signal†	Assay‡
Inhibitor of nuclear factor-kappaB kinase (IKK)	Ser kinase	Kinase activity	Kinase assay
c-jun N-terminal kinase 1 (JNK1)	Ser-Thr kinase	Kinase activity	Kinase assay
Mitogen-activated protein kinase-associated protein kinase 2 (MK2)	Ser-Thr kinase	Kinase activity	Kinase assay
Epidermal growth factor receptor (EGFR)	Receptor Tyr kinase	Phosphorylation (Tyr1068)	Ab microarray
		Total amount	Ab microarray
		Phospho/total ratio	Ab microarray
Mitogen-activated protein kinase and extracellular regulated kinase kinase (MEK)	Dual-specificity kinase	Phosphorylation (Ser217/Ser221)	Western blot
Extracellular regulated kinase (ERK)	Ser-Thr kinase	Kinase activity	Kinase assay
Insulin receptor substrate 1 (IRS1)	Adaptor-scaffold	Phosphorylation (Ser636)	Western blot
		Phosphorylation (Tyr896)	Western blot
Akt	Ser-Thr kinase	Phosphorylation (Ser473)	Ab microarray
		Total amount	Ab microarray
		Kinase activity	Kinase assay
		Phosphorylation (Ser 473)	Western blot
		Phospho/total ratio	Ab microarray
Forkhead (FKHR)	Transcription factor	Phosphorylation (Ser256)	Western blot
Caspase-8	Cys protease	Zymogen amount	Western blot
		Cleaved amount	Western blot
Caspase-3	Cys protease	Zymogen amount	Western blot

*Biological functions were assigned based upon the most recognized property of the protein.
†Signals indicate the biochemical property of the protein that was measured.
‡Assay indicates whether the protein was measured by high-throughput kinase activity assay (*10*), antibody microarray (*33*), or quantitative Western blotting (*12*).

Apoptotic signatures were measured for the nine cytokine input combinations (Fig. 4.1F), revealing temporal and cytokine dose-dependent features that would have been missed by examining single apoptotic outputs alone. Membrane permeability (red) and caspase substrate cleavage (purple) measured dead cells cumulatively (Darzynkiewicz et al. 1997). Therefore, these outputs increased monotonically with time and TNF dose (Fig. 4.1, G, J, and M). In contrast, phosphatidylserine exposure (loss of membrane asymmetry before membrane permeability) and nuclear fragmentation (digestion of DNA before complete cellular fragmentation) were transient cell states (Darzynkiewicz et al. 1997) that could increase and decrease with time and input dose (Fig. 4.1, G–O).

High concentrations of EGF and insulin antagonized TNF-induced cell death in a similar manner, particularly reducing apoptotic responses at early times (Fig. 4.1, M–O; Fig. 4.S2). Low concentrations of EGF and insulin elicited different output responses. EGF reduced TNF-induced membrane permeability at 48 h but increased transient phosphatidylserine exposure at 12 h (Fig. 4.1, J and L; $p < 0.05$, Student's t-test with Bonferroni correction). In contrast, insulin reduced TNF-induced membrane permeability at 12 and 48 h, and phosphatidylserine exposure was decreased at 12 h but higher at 48 h (Fig. 4.1, J and K; $p < 0.05$). These measured apoptotic signatures provide evidence that different apoptotic outputs can be controlled separately, depending upon the input stimulus. For example, membrane permeability is most commonly associated with secondary production of reactive oxygen species (Vanden Berghe et al. 2004), whereas phosphatidylserine exposure is thought to involve caspase- and Ca^{2+}-dependent processes

(Fadok et al. 1998). The JNK family protein kinases (Fig. 4.1A) have been implicated in reactive oxygen signaling (Ventura et al. 2004; Kamata et al. 2005) but are thought to be largely independent of Ca^{2+} signaling (Cruzalegui et al. 1999). Thus, relating the intracellular network dynamics to the complete apoptotic signature requires more information than can be provided by individual molecular signals, like JNK1.

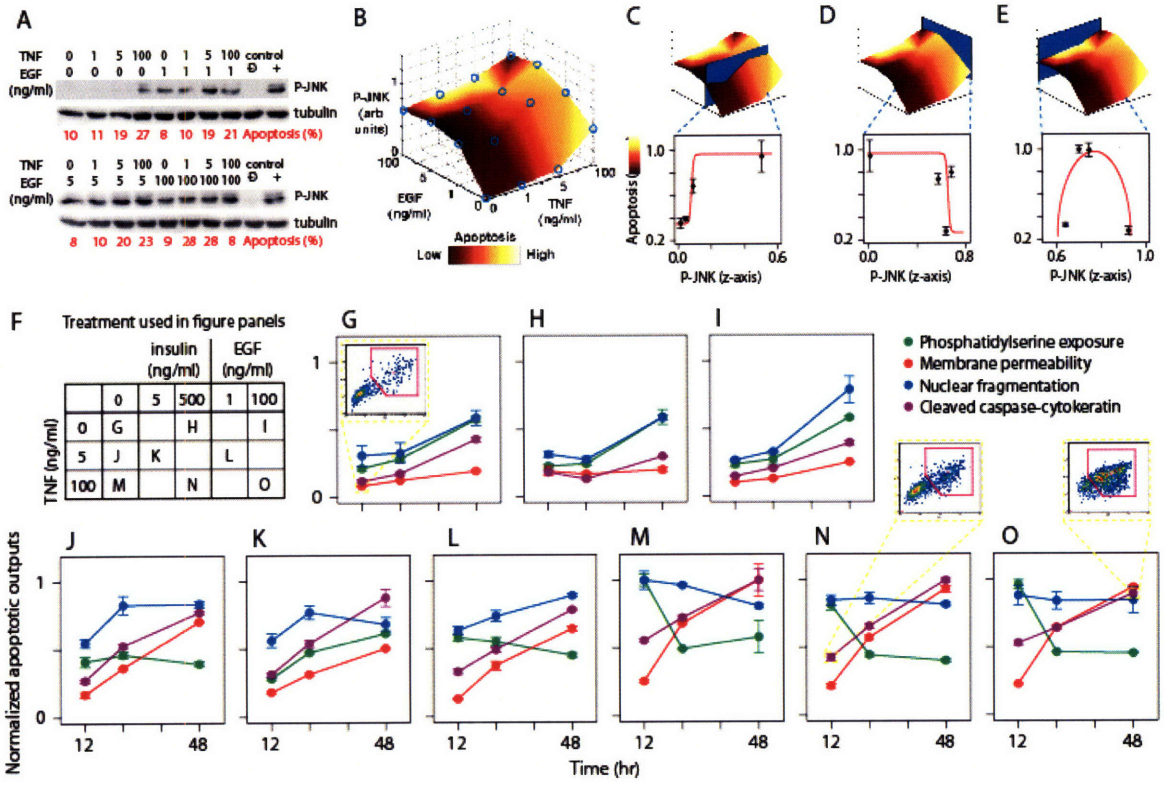

Figure 4.1. JNK phosphorylation after multi-input cytokine stimulation fails to correlate with apoptotic responses. **(A)** JNK phosphorylation and apoptosis in HT-29 cells treated with TNF, EGF, or both. Phospho-JNK (P-JNK) was analyzed at 15 min by quantitative Western blotting with tubulin as a loading control, and apoptosis was measured at 24 hr by cleaved caspase-cytokeratin staining and flow cytometry. **(B)** Response surface for P-JNK (z-axis) and apoptosis (color bar) induced by the input described in (A). **(C–E)**

Lack of a correlation between JNK phosphorylation and apoptosis. P-JNK appeared to be (C) proapoptotic, (D) antiapoptotic, or (E) uninvolved in apoptosis depending upon the experimental "slice" through the TNF-EGF signaling space. **(F)** Experimental design for TNF, EGF, and insulin stimulation. Letters correspond to the experimental treatment, used in the respective figure panels, for which 19 molecular signals (Table 4. 1) (Janes et al. 2006) and apoptotic outputs were measured. In addition, signals and apoptotic outputs were measured in cells stimulated with 0.2 ng/ml TNF and 1 ng/ml insulin. The carrier was always 0.02% DMSO. **(G–O)** Apoptotic outputs by flow cytometry. In (G), (N), and (O), the insets depict representative density plots of the cleaved caspase$^+$-cleaved cytokeratin$^+$ population. All flow cytometry measurements were normalized to the maximum observed apoptosis for phosphatidylserine exposure (25%), membrane permeability (67%), nuclear fragmentation (21%), and cleaved caspase-cytokeratin (77%). Data are presented as the mean ± S.E.M. of triplicate biological samples.

4.3.2 A partial least squares model predicts the 12 cytokine-induced apoptotic outputs from a 660-element signaling vector.

We sought to determine whether multiple molecular signals in combination could quantitatively capture the entire apoptotic signature as a response and predict apoptosis more globally. We designed a mathematical formalism that could identify the information content within each molecular signal that most closely mapped onto the output responses. The resulting mapping of lumped signals to corresponding responses might then allow us to identify the most relevant "information variables" for apoptosis and use these variables to predict apoptotic responses to stimuli outside the training set.

It was unclear what aspect of a dynamically sampled molecular signal should fill the role of an information variable for apoptosis. For example, in addition to

measurements of kinase activity at various time points, it was not known if other data such as the maximum activity, the rate of rise of activity, or the time when peak activity occurred also contained useful information. Therefore, we defined a panel of time-dependent signaling "metrics" that could be derived empirically from any dynamic signal (Fig. 4.2A). Each of the metrics [for example, activity of the mitogen-associated protein kinase (MAPK) ERK at 5 min, ERK activity at 15 min, peak ERK activity, and the abundance of phosphorylated (active) the MAPK kinase MEK (P-MEK) at 5 min] can then be represented by an "axis" along which particular multi-input stimuli project (Fig. 4.2C).

In total, we extracted 30 to 40 metrics (Table 4. S1) from each time course of a molecular signal to form a composite "metric set" (Fig. 4.2A). Metric sets were defined for all 19 molecular signals, forming a group of individual axes that together define a 660-dimensional signaling space. The projection of a multi-input stimulus along these axes creates a "signaling vector" of 660 column elements corresponding to the 30–40 metrics from each of the 19 measured molecular signals (Fig. 4.2B). The apoptotic outputs were similarly concatenated to form an apoptosis vector, where the 12 column elements are the four apoptotic outputs at three time points each (Fig. 4.2A). Each input stimulus has its own particular signaling and apoptosis vectors, so these were calculated separately for each of the nine treatment combinations (Fig. 4.1F).

We sought to identify the best mapping of the 660-dimensional signaling metric space onto the 12-dimensional output response space. A simple linear mapping would require the 7920-element coefficient matrix (12 rows × 660 columns) that best

transformed the signaling space into the response space (Fig. 4.2B), a calculation that would be impossible to solve uniquely given only nine multi-input conditions. To simplify the signal to response mapping and retain biological meaning, we first assumed that some of the signaling metric dimensions were either redundant or irrelevant. For instance, the peak activity of ERK contains the same information as the ERK activity at 5 min, when the ERK peak often occurred (Fig. 4.2C). Likewise, other axes (e.g., metrics at 0 min, prior to stimulus) merely scrambled the projections since they pointed in directions unrelated to apoptosis (Fig. 4.2C). These redundant and uninformative axes could be deemphasized or eliminated without any loss of information about the apoptotic outputs. Second, we assumed that the remaining informative axes could be compressed by linear combination into a small number of dimensions that retained the critical apoptotic information and thus constituted a biologically relevant basis set for the signal to response mapping. For instance, proteins like MEK and ERK are part of the same signaling pathway and were thus activated similarly. Although not identical, the information in many MEK and ERK metrics pointed in collinear directions that could be combined into a MEK-ERK "super axis" that retained the projection with fewer dimensions (Fig. 4.2C).

To reduce unnecessary axes and condense important axes mathematically, we used partial least squares (PLS) regression, which simplifies dimensions based upon their covariance with a specified dependent variable (P.Geladi and Kowalski 1986; Janes et al. 2004). The original 660-dimensional signaling space was reduced to a series of super axes that together best orient the measured apoptotic-output elements within the

apoptosis vector (Fig. 4.2, A and C). PLS modeling, like singular value decomposition (Alter et al. 2000), calculates super axes as an orthogonal set of "principal components", which contain linear combinations of the original 660 metric dimensions weighted by their contribution to the apoptotic outputs (Fig. 4.2C). Principal components are calculated iteratively so that successive PLS dimensions are regressed against the apoptotic-output information not captured by the preceding component. After several iterations, including more dimensions becomes undesirable, because the residual information is so small that new principal components capture spurious fluctuations in the outputs, like measurement error and noise, rather than meaningful data (Janes et al. 2004).

To optimize the number of model dimensions, we examined the root mean-squared error (RMSE) between the measured apoptosis vector and the values from models with increasing numbers of principal components. All of the input treatments were included in the initial model training to assess the RMSE of data fitting (calibration). Each treatment was then individually withheld from the training set to construct a cross-validation model, in which an RMSE of prediction could be assessed by predicting the withheld sample. The calibrated RMSE decreased monotonically, but the predicted RMSE was minimized with just three principal components (Fig. 4.2D). Using the resulting three-component apoptosis model, we examined the correlation between the measured apoptotic outputs and the cross-validated predictions for each treatment (Janes et al. 2004). If the correct signaling information was retained by the principal components in the model, then the apoptotic outputs for TNF, EGF, and insulin stimuli

not included during the model training should also be predicted. Indeed, we found a high correlation for all 12 apoptotic outputs, with predictions that were accurate to within 94% of the measured values overall (Fig. 4.2, E–J). Although the 12 individual apoptotic outputs differed quantitatively from one another (Fig. 4.1, G–O), their stimulus-dependent changes were almost entirely captured by a single PLS model of the intracellular network (Fig. 4.2, E–J). The 660 dimensions of the original signaling space (Fig. 4.2C) had thus been condensed to three dimensions, which were enriched in the molecular signals most useful for predicting the apoptotic outputs. Furthermore, specifying the dynamic state of the intracellular signaling network was absolutely essential—an equivalent PLS model given only cytokine-input concentrations (Fig. 4.1F) rather than intracellular signaling metrics could not correctly predict the apoptotic outputs (45% accuracy) (K.A.J., unpublished data).

The original measurements (Janes et al. 2006) of the signaling network contained several direct effectors of apoptosis, such as caspases (Table 4. 1) (Nicholson and Thornberry 1997). The model would obviously be less valuable if these late-effector signals were providing all of the predictive power to the model. To test whether caspase metrics were required for accurate predictions, we removed all of the caspase signals from the model and rederived the principal component axes. The resulting predictions were essentially identical (Fig. 4.2, E–J). Thus, non-caspase signals in the network contained more than enough information to predict the apoptotic outputs quantitatively. Furthermore, molecular signals activated before the initial onset of apoptosis were themselves sufficient for predicting the apoptotic signature. We found that a separate

PLS apoptosis model derived exclusively from signaling measurements made at 0 to 4 hours after cytokine addition was accurate to within 81% (Fig. 4.S3).

To examine the relationship between other molecular signals and late effector caspases directly, we next removed the apoptotic outputs altogether and defined the procaspase-8, cleaved caspase-8, and procaspase-3 time-point measurements as a new set of cellular outputs (Fig. 4.2K). Using the remaining network measurements, the PLS model predicted the caspase response dynamics within 81% accuracy (Fig. 4.2K). Together, this suggested that both the caspase effector signals and the final cellular output responses were encoded by the upstream signaling network.

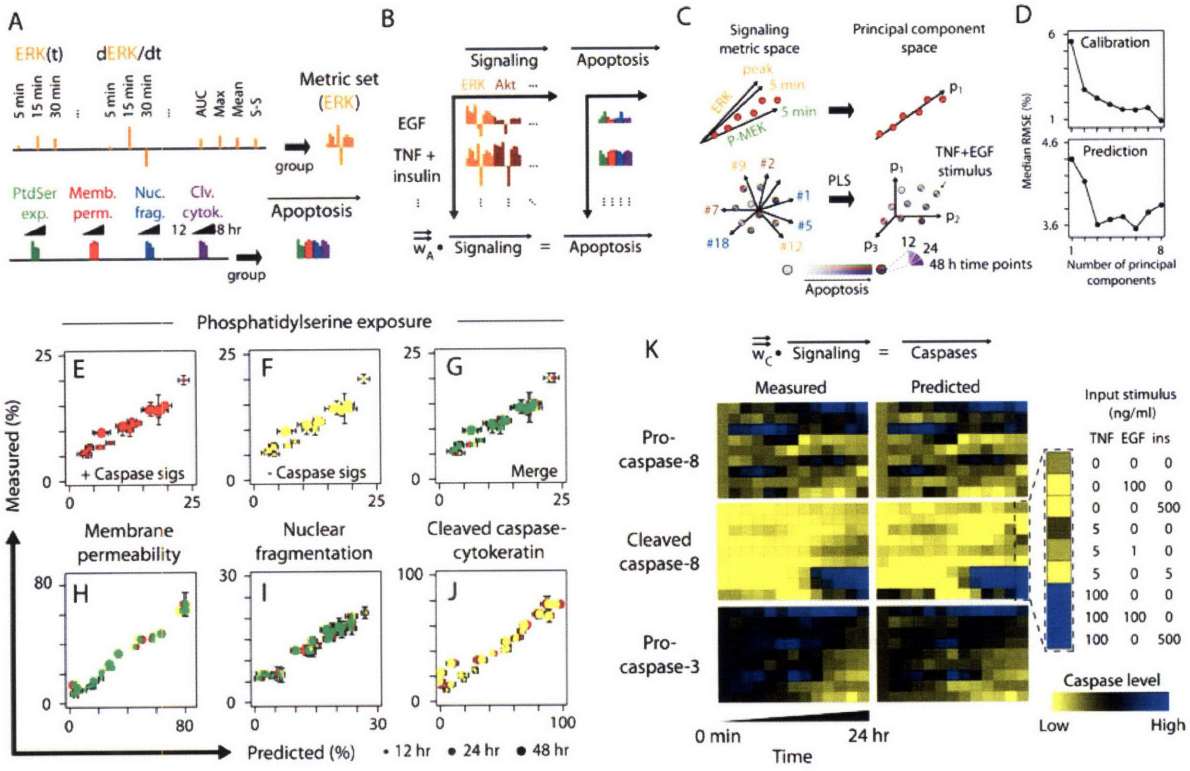

Figure 4.2. A data-driven principal components-based model correctly predicts apoptosis and caspase activation from molecular signals activated by multi-input TNF, EGF, and insulin stimulation. **(A)** Extraction of signaling and response metrics. Upper panel: time course measurements () of the signaling network were used to group individual time points (t), instantaneous derivatives (d/dt), area under the curve (AUC), and the maximum, mean, and steady-state (S-S) values and form a signaling metric set, in this example for ERK. The activation slope and decay rates for signaling peaks were also incorporated. Bottom panel: individual apoptotic output time points were concatenated for each treatment into an apoptosis vector. **(B)** Construction of the partial least squares apoptosis model. Individual signaling metric sets were concatenated into a single signaling vector for each treatment condition and these vectors then regressed against the corresponding apoptotic response vectors (Janes et al. 2004). w_A is the coefficient matrix of the apoptosis regression model. **(C)** PLS-based supervised decomposition of signaling vector space into principal components. Upper panel: a simplified example of

dimensionality reduction by principal components analysis. In this example, collinear axes like peak ERK activity, ERK activity at 5 min, and P-MEK levels at 5 min could be reduced into a single principal component axis (p_1). Lower panel: principal component axes were captured in a supervised manner to maximize prediction of apoptotic responses. In the full PLS model, the four apoptotic outputs (red, green, blue, and purple quandrants of each data point) at three time points (12, 24, and 48 hr slices within quadrants) were oriented along three principal component axes (p_1, p_2, and p_3) determined to contain the essential signaling information for predicting apoptosis. Each point corresponds to one multi-input stimulus, such as TNF + EGF, and the shading of the point corresponds qualitatively to the extent of measured apoptosis. The numbered axes (left) indicate separate metrics extracted from different molecular signals, shown in (A). **(D)** RMSE of calibration and prediction of apoptotic outputs by the PLS model as a function of increasing number of principal components. An optimum model with three components was selected. **(E–G)** Correlation plots between measured phosphatidylserine exposure (y-axis) and cross-validated predictions of phosphatidylserine exposure (x-axis) by the PLS model with (red) and without (yellow) caspase signals included. The merged overlay is shown in green. Marker size (• • ●) corresponds to the response time point at 12, 24, and 48 hr. Data are presented as the mean ± S.E.M., and model uncertainties were estimated by jack-knifing (Janes et al. 2004). **(H–J)** Correlation plots between measured and cross-validated predictions of membrane permeability, nuclear fragmentation, and caspase substrate cleavage. Data are presented as in (E–G). **(K)** Comparisons between measured caspase levels and cross-validated predictions from a specific PLS model of caspase activation. Signaling metric vectors from non-caspase molecular signals were regressed against the 0–24 hr time-point measurements of procaspase-8, cleaved caspase-8, and procaspase-3. w_C is the coefficient matrix of the caspase regression model. The nine rows in the measured and predicted color coding correspond to the nine treatment combinations shown in Fig. 4.1F. Each region of the heat map was normalized separately for comparison.

4.3.3 Model-driven discovery of apoptosis regulation via autocrine circuits.

In HT-29 cells, two regulated autocrine stimuli—transforming growth factor-α (TGF-α) and interleukin-1α (IL-1α)—cooperate with TNF to activate molecular signals in the network (Fig. 4.3A) (Janes et al. 2006). Whether these autocrine circuits contribute significantly to TNF-induced apoptosis is not known. We therefore used the PLS model to predict what the apoptotic signature would be when autocrine TGF-α and IL-1α circuits were disrupted with either an antibody to the EGFR (C225) or an IL-1 receptor antagonist (IL-1ra) and the cells were then treated with TNF. All 19 molecular signals were measured from 0–24 hr (Janes et al. 2006) and provided as input data to the PLS model. We then measured the actual TNF + C225- and TNF + IL-1ra-induced apoptotic signatures experimentally (*9*) and compared these with the model predictions. This experiment was a particularly stringent test of the model, because neither TGF-α nor IL-1α had been part of the original training set (Fig. 4.1F).

Strikingly, we observed a 90% correlation between the measured apoptotic outputs and the model predictions when the two autocrine loops were disrupted individually (Fig. 4.3B), indicating that the model could predict the contributions of cytokines other than TNF, EGF, and insulin. Furthermore, upstream molecular signals alone were highly predictive of downstream effector caspase activation after TNF + C225 and TNF + IL-1ra stimuli (prediction within 91% of measured values; Fig. 4.3C). Therefore, the contributions of autocrine TGF-α and IL-1α to TNF-induced apoptosis had been implicitly and correctly incorporated throughout models of apoptotic outputs as well as caspase activation.

Interestingly, disruption of the IL-1α autocrine loop decreased most apoptotic outputs in cells responding to TNF (Fig. 4.3D), suggesting that autocrine IL-1α was an extracellular positive-feedback circuit for TNF-induced apoptosis. In contrast, disruption of TGF-α signaling by C225 led to large changes in TNF-induced activation of the network but did not lead to any clear overall changes in apoptosis (Fig. 4.3D). Some outputs, like phosphatidylserine exposure, were increased in cells treated with C225 ($p < 10^{-5}$, two-way analysis of variance). Others, like caspase substrate cleavage, were decreased ($p < 0.05$), whereas six of the 12 individual apoptotic outputs did not change in a statistically significant manner.

TGF-α is a member of the EGF family (Rouse et al. 1994), and treatment of cells with EGF was shown to reduce apoptosis (Fig. 4.1, M and O). Why then did blocking autocrine TGF-α with C225 not increase apoptosis overall? First, in HT-29 cells, autocrine TGF-α activates a pro-death signal by inducing late (12 to 24 hr) release of autocrine IL-1α (Fig. 4.3A and Fig. 4.S4) (Janes et al. 2006). Second, we reasoned that the late, pro-death IL-1α signal must be offset by some unknown late, pro-survival signal. Concurrent pro-death and pro-survival signals at late times could then neutralize one another and explain the net lack of an effect of autocrine TGF-α on apoptosis. To help identify this late, pro-survival signal, we examined the coefficients within the PLS model that quantified the contribution of each signal to apoptosis (Fig. 4.2B), since the model correctly predicted the mixed apoptotic response resulting from autocrine TGF-α perturbation (Fig. 4.3B). Early MAPK-Activated Protein Kinase 2 (MK2) kinase activity in the model correlates with apoptosis; by contrast, the model revealed that MK2

signaling at times after 12 hr was strongly anticorrelated with apoptosis, implicating MK2 as a pro-survival kinase at later times. In agreement with this, when autocrine TGF-α was blocked by C225, MK2 activity at late times was inhibited (Fig. 4.3E) (Janes et al. 2006). Thus, both model and experiment suggested that late MK2 activity was a pro-survival signal activated by autocrine TGF-α.

If effectively pro-survival, then MK2 activity at late times should be present primarily in viable cells. MK2 signaling was therefore analyzed separately in live and apoptotic cells by measuring the floating and adherent subpopulations of TNF-treated cells. All MK2 activity was detectable only in the adherent (viable) cells (Fig. 4.3F). If we permitted the early phase of MK2 activity to occur in response to TNF but rapidly inhibited the late phase with SB202190, a small-molecule inhibitor of the MK2-activating kinase p38 (Lee et al. 1994; Yadav and Sarvetnick 2003), we observed a significant increase in cell death at 24 hr (Fig. 4.3G). Taken together, these experiments demonstrate that the signal to response linkages implicated by the PLS model can reveal new biological mechanisms that would not be easily recognized without a mathematical formalism.

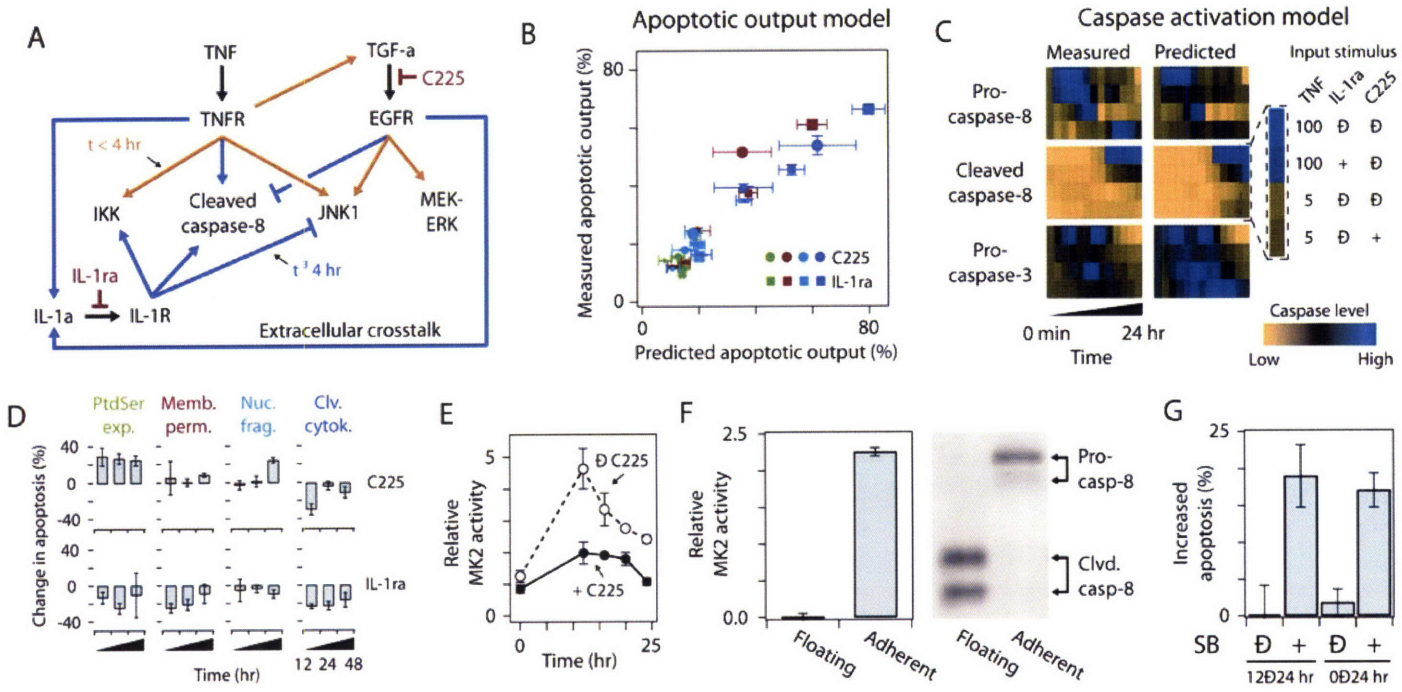

Figure 4.3. The principal components-based model captures hidden autocrine feedback in the signaling network and identifies late MK2 activity as a TGF-α-induced pro-survival signal **(A)** Diagram of TNF-induced autocrine circuits in HT-29 cells (Janes et. al 2006). Orange arrows indicate fast pathways (before four hours) and purple arrows indicate slow pathways (after four hours). C225 and IL-1ra were used as pharmacological inhibitors of autocrine TGF-α and IL-1α, respectively. **(B)** The model correctly predicts TNF-induced apoptosis when the autocrine feedback circuits are disrupted by C225 and IL-1ra. Apoptotic outputs were measured as in Fig. 4.1, G–O for cells treated with 5 ng/ml TNF and 10 μg/ml C225 (circle) and 100 ng/ml TNF plus 10 μg/ml IL-1ra (square). Marker color corresponds to the apoptotic index (c.f. Fig. 4.1, G–O) and size corresponds to the time point (c.f. Fig. 4.2, E–J). **(C)** The model correctly predicts caspase cleavage in response to TNF stimulation when the autocrine feedback circuits are disrupted. Comparisons between measured caspase levels and model predictions for the autocrine circuit perturbations. Each panel was normalized separately, and the unperturbed caspase dynamics were included for comparison. **(D)** The TNF→IL-1α autocrine circuit is proapoptotic, while the TNF→TGF-α circuit sends both pro- and

antiapoptotic signals. Comparison of TNF-induced apoptotic outputs with and without autocrine IL-1α and autocrine TGF-α. Data are shown as percent change in apoptosis in C225- and IL-1ra-treated cells compared with unperturbed TNF-stimulated cells (Janes et al. 2006). **(E)** TNF-induced late MK2 activity is TGF-α-dependent. Cells were stimulated with 5 ng/ml TNF in the presence or absence of 10 μg/ml C225 to block autocrine TGF-α, and MK2 activity was measured by in vitro kinase assay (Janes et al. 2003). **(F)** Late MK2 activity is restricted to surviving cells. Left panel: cells were treated with TNF for 20 hr, separated into floating and adherent subpopulations, and MK2 activity was assayed as in (E). Data were normalized to basal MK2 activity as described (Gaudet et al. 2005). Right panel: floating and adherent cells correspond to apoptotic and viable cells respectively, as indicated by caspase-8 cleavage and DAPI staining. **(H)** Late MK2 activity is a pro-survival signal. Cells were treated for 24 hr with 100 ng/ml TNF in the presence or absence of the inhibitor SB202190 during the indicated times and assayed for apoptosis by the presence of caspase substrate cleavage. For (E), (G), and (H), data are presented as the mean ± S.E.M. of triplicate biological experiments (Janes et al. 2006).

4.3.4 Redundant encoding of signaling components and critical roles of MAP kinases in PLS predictions of apoptosis.

In the full model, 660 metrics derived from 7980 signaling measurements were used to predict apoptosis (Fig. 4.2, E–J; 3B). In retrospect, it was not clear whether apoptotic outputs could be predicted equally well by a reduced number of metrics derived from smaller, more tractable experiments. We found that a model containing only the 20 most informative metrics, as determined by the relative magnitude of their coefficients in the model (Table 4. S2), was nearly as predictive of apoptosis as one that used all 660

metrics (Fig. 4.4A). A noteworthy feature of the top 20 metrics was that they were not the obvious metrics we would have chosen on the basis of our basic understanding of the regulation of apoptosis. Activation slopes of Akt and IRS1 phosphorylation and integrated peaks of JNK1 and IKK signaling were included, but caspase metrics were missing entirely (Table 4. S2). Use of fewer than these top 20 metrics, in isolation, gave significantly less effective predictions (data not shown), supporting our original hypothesis that individual signaling measurements would not broadly predict cell responses (Fig. 4.1, C–E).

High predictive ability of the top 20 metrics (Fig. 4.4A) suggested redundancy in the signaling information contained within the original 660-metric model. To investigate this, we sequentially removed various portions of the most informative metrics and then recalculated the prediction of apoptosis by cross-validation. Up to the top 350 metrics could be eliminated from the full list of 660 metrics before the apoptosis model lost all significant predictive ability (Fig. 4.4A). This implied that the full set of 660 biological metrics was redundantly encoded with the stimulus-specific information required to mediate all of the apoptotic outputs (Ozaki and Leonard 2002; Wiley et al. 2003). We also analyzed the contributions of individual proteins (that is, the 19 molecular signals) based on the average information contained in their derived metrics. The top three molecular signals, JNK1, MK2, and ERK, belonged to MAPK cascades (data not shown). A model given only metrics from these three signals performed nearly as well as the full PLS model in predicting the effects of autocrine perturbations (Fig. 4.4B). A model derived from the seven least informative molecular signals was also predictive (Fig.

4.4B). Together, these findings suggest that measurements of 3 to 7 relevant intracellular molecular signals are sufficient to predict network-dependent output responses. Prediction efficiency (defined as the relative predictive ability divided by the number of molecular signals included in the model) was maximal with 4 to 5 molecular signals (Fig. 4.4B, inset).

4.3.5 The PLS model identifies stress-apoptosis and survival signaling axes.

We examined the relationship between all of the signaling network measurements and the input treatments as signals propagated through the model's first two principal components (Janes et al. 2004), which predicted the apoptotic output within 92%. These components are the two main lumped contributions of the signaling metrics, which form a pair of orthogonal axes defining the optimal two-dimensional slice through the signaling dataset (Janes et al. 2004). We found that certain signals and treatments were clearly overrepresented in these dimensions. The first principal component, Axis #1, was oriented toward stress and apoptotic pathways and included early JNK1 activity, early MK2 activity, and late cleaved caspase-8 metrics (Table 4. S3). In contrast, the second principal component, Axis #2, appeared to constitute a global survival signal that included phosphorylated Akt (P-Akt), phosphorylated insulin receptor substrate 1 (P-IRS1), phosphorylated Forkhead transcription factor (P-FKHR), and procaspase-3 metrics (Table 4. S4). The specific molecular signals emphasized in these components were entirely consistent with the known molecular mechanisms that link these signaling proteins to apoptosis (Fig. 4.S1).

Using the principal component axes, we could now reanalyze the signaling contributions to apoptosis from cells exposed to single or combined cytokines. Certain signals, such as IKK, contributed differently to the stress-apoptosis and survival axes depending upon the time point when the molecular signal was measured. Early IKK activity induced directly by the TNF receptor (TNFR) was weighted predominantly along pro-survival Axis #2 (Fig. 4.4C). However, IKK activity after 12 hr, which occurs indirectly in response to an autocrine signal from IL-1α (Fig. 4.3A) (Janes et al. 2006), contributed more to the stress-apoptosis axis (Fig. 4.4C). Thus, the PLS model had revealed that the same molecule, such as IKK, can convey either pro- or anti-apoptotic messages depending on the timing and mechanism of activation.

For individual cytokines, we found that TNF treatment alone projected strongly along pro-death Axis #1, whereas isolated EGF and insulin treatments mapped exclusively on pro-survival Axis #2 (Fig. 4.4E). This reinforced our original intuition that TNF and EGF-insulin stimuli act upon orthogonal and antagonistic signaling axes for apoptosis. In contrast, the multi-input projections were remarkably different from what would be predicted by a summation of the single-input treatments (Fig. 4.4F, gray). TNF, EGF, and insulin each lost a fraction of their original projections along the two axes, indicating that the input stimuli were antagonized when added in combination (Fig. 4.4F). The TNF + EGF and TNF + insulin treatments were distinctly separated from one another: EGF appeared to antagonize TNF-induced apoptosis by specifically reducing the projection along the stress-apoptosis Axis #1 without any change along Axis #2 (Fig. 4.4F); in contrast, insulin actively promoted pro-survival signaling along Axis #2 while

also inhibiting stress-apoptosis signaling along Axis #1. Therefore, analyzing the multi-input stimuli through these model-derived biological "basis axes" (Fig. 4.4E) helped to reveal the different network strategies used by EGF and insulin to antagonize TNF-induced apoptosis.

Finally, to determine the contributions of TNF-induced autocrine circuits in the model, we mapped the TNF + C225 and TNF + IL-1ra treatments (Fig. 4.4G). The projection of TNF along the stress-apoptosis axis (Fig. 4.4G) was enforced by the autocrine circuits, which increased the contribution along Axis #1 and decreased the contribution along Axis #2. This is consistent with the notion that regulated autocrine circuits provide microenvironment-dependent feedback to cells during phenotypic decision processes, such as death-survival (Janes et al. 2004; Janes et al. 2006). Furthermore, it illustrated directly that effects of complex environmental stimuli were entirely contained within the two canoncial basis axes distilled from the original 660-dimensional signaling metric space by the PLS model (Fig. 4.4E).

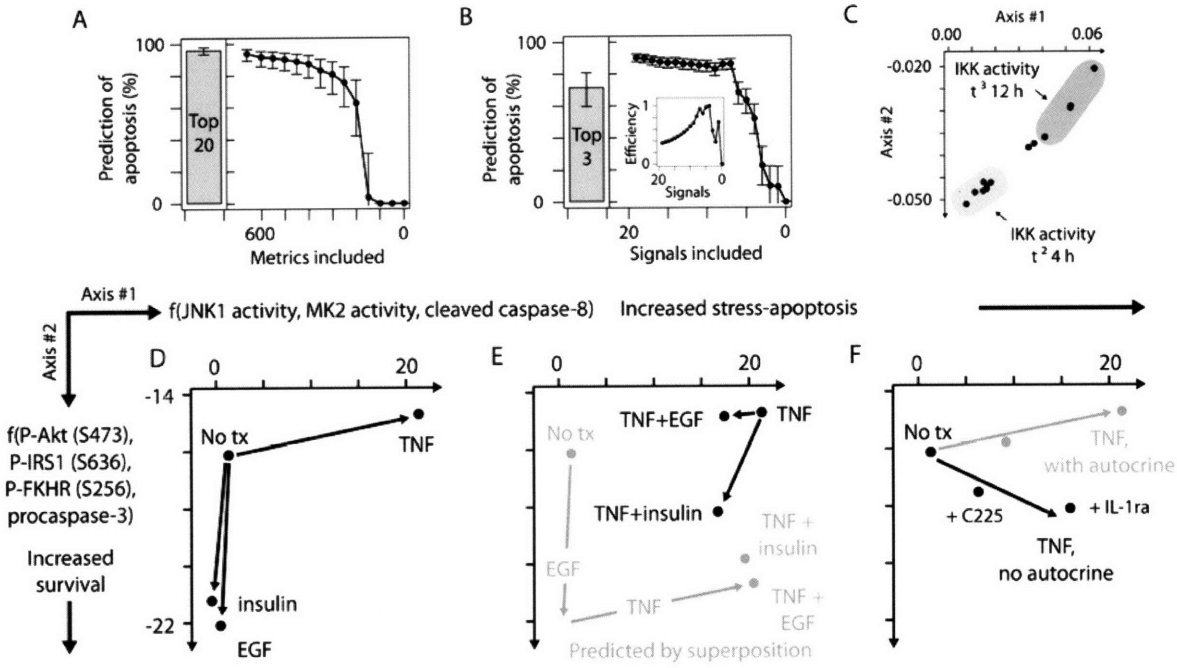

Figure 4.4. Two orthogonal stress and survival axes link complex stimuli to apoptosis. (A and B) The principal component-based model is redundantly encoded. (A) Decreased accuracy of prediction of apoptotic responses to TNF, EGF, and insulin with decreasing number of signaling metrics. (B) Decrease in accuracy of prediction of apoptotic responses to autocrine signals with decreasing number of molecular signals. Both metrics and molecular signals were eliminated sequentially from best to worst on the basis of their variable importance in the principal component projection (*9*). (inset) Predictive efficiency as a function of number of molecular signals included. To calculate efficiency, the TNF-EGF-insulin apoptotic predictions in (B) were divided by the number of molecular signals in the submodel. For (A) and (B), data are presented as the central prediction ± 90% Fisher Z-transformed confidence intervals. **(C)** The two principal components can correspond to distinct time-resolved mechanisms of molecular-signal activation. Contribution of IKK activity time-point metrics to Axis #1 and #2. Early and late IKK time points are shaded in light and dark gray, respectively. A reciprocal time-dependent change in projection along Axis #1 and #2 was observed for MK2 (data not shown). **(D–F)** The intracellular signaling network is defined by two orthogonal stress

and survival axes that link complex stimuli to apoptosis. (D) Cytokine inputs project along orthogonal stress and survival axes (Axis #1 and #2) of the PLS model. (E) Cytokine combinations project differently from linear superposition of isolated cytokine stimuli. EGF in combination with TNF directly antagonizes stress pathway signaling, while insulin in combination with TNF both antagonizes stress signaling and induces separate pro-survival signaling pathways. The linear superposition of single-input TNF, EGF, and insulin projections from Fig. 4.4E is shown in gray. (F) Autocrine feedback circuits rotate the TNF-induced signaling network to reinforce stress responses and suppress any signaling down the survival axis. For (E–G), samples were projected using the model scores as described (Janes et. al 2004).

4.4 Conclusion

In summary, by using a systems approach that combines quantitative experiments with data-driven modeling, we have identified two canonical axes—a stress-apoptosis axis and a survival axis—that together constitute a molecular basis set for the signaling network that controls apoptosis. These axes capture the dynamic intracellular signal processing of diverse stimuli, including autocrine-feedback circuits. Our work illustrates how a complex signaling network can be reduced empirically to a much simpler computational model that is directly tied to biological mechanism.

4.5 Materials and methods

P-JNK immunoblotting

HT-29 cells (ATCC) were plated and sensitized as described (Janes et al. 2005), then stimulated with combinations of 0, 1, 5, or 100 ng/ml TNF and EGF for 15 min and

lysed by standard techniques (Janes et al. 2003). 100 μg of each lysate was run on a 10% SDS-PAGE gel and transferred to PVDF (Millipore). The membranes were blocked with 5% nonfat skim milk in 20 mM Tris-HCl (pH 7.5), 137 mM NaCl, 0.1% Tween-20 and probed overnight with anti-phospho-SAPK/JNK (Cell Signaling) at 1:1000 dilution. The membranes were then probed with horseradish peroxidase conjugated anti-rabbit secondary antibody (Amersham) at 1:10,000 dilution and visualized by enhanced chemiluminescence (Amersham) on a Kodak Image Station (Perkin Elmer). Bands were selected and quantified according to the manufacturer's recommendations. To improve quantitation, each membrane was normalized to an internal positive control (100 ng/ml TNF, 15 min). The membranes were stripped and reprobed with anti-tubulin (Calbiochem) to confirm equal protein loading.

Large-scale apoptotic marker measurements

HT-29 cells were plated in 24-well plates and were sensitized and treated identically to the cells used in the corresponding signaling measurements on the same day (Janes et al. 2005). After 12, 24, or 48 hours of cytokine treatment, the cells were trypsinized until all cells were detached from the plate. The growth medium was combined with the trypsinized cells to ensure capture of both floating and adherent cells in each well. The combined pool of cells from each well was split into thirds; one third was analyzed for phosphatidylserine exposure and membrane permeability, one third was fixed with methanol and analyzed for cleaved caspase-cytokeratin, and one third was fixed with methanol (MeOH) and analyzed for nuclear fragmentation. For the

phosphatidylserine-membrane permeability analysis, the cells were washed once with Annexin Binding Buffer (ABB, 10 mM HEPES, 140 mM NaCl, 2.5 mM $CaCl_2$) and stained with Alexa Fluor 488-conjugated Annexin-V (Molecular Probes) and 1 ug/ml propidium iodide (PI) for 10 minutes at room temperature. Excess ABB was added and the cells were analyzed by a Becton Dickinson FACScan or FACSCalibur flow cytometer. For the cleaved caspase-cytokeratin assay, MeOH-fixed cells were stored at -20 C for up to 1 week. After centrifugation to remove the MeOH, cells were washed in PBS + 0.1% Tween-20 (PBS-T), and were then stained with anti-cleaved caspase-3 (Cell Signaling, Becton Dickinson) and anti-cleaved cytokeratin (Roche) antibodies in PBS-T + 1% bovine serum albumin (PBS-TB) for 1 hour at room temperature. The cells were washed and stained with secondary antibodies, Alexa Fluor 488-conjugated donkey anti-mouse IgG and Alexa Fluor 647-conjugated donkey anti-rabbit IgG (Molecular Probes) in PBS-TB for 1 hour at room temperature. The cells were then washed and analyzed on a Becton Dickinson FACSCalibur flow cytometer. For the nuclear fragmentation assay, MeOH cells were stored at -20 C for up to one week. After centrifugation to remove the MeOH, cells were washed once with PBS-T, and then incubated with 1 mg/ml RNAse A in PBS-T for 2.5 hours. PI was then added at a final concentration of 50 ug/ml, and the cells were analyzed on a FACSCalibur flow cytometer to quantify nuclear fragmentation. For all flow cytometry assays, data was analyzed using FlowJo software (TreeStar).

To fuse quantitative measurements on different days, 100 ng/ml TNF and mock treatments were always included as fixed positive and negative controls. Experimental samples were then scaled by the TNF (membrane permeability and cleaved caspase-

cytokeratin) or mock (phosphatidylserine exposure and nuclear fragmentation) index for that day. By cross-validation we verified that the magnitude and dynamics of these normalized apoptotic indices were highly reproducible, with $R^2 = 0.79–0.98$ (Gaudet et al. 2005b). The entire dataset of 1440 flow cytometry runs is available in the Supporting Online Material.

Signaling network measurements

Details of the signaling network measurements are described elsewhere (Gaudet et al. 2005b; Janes et al. 2005). Briefly, 19 quantitative signaling network measurements—IKK activity, JNK1 activity, MK2 activity, P-EGFR (Y1068), total EGFR, P/total EGFR, P-MEK (S217/221), ERK activity, P-IRS1 (S636), P-IRS1 (Y896), P-Akt (S473) by Western blot, total Akt, Akt activity, P-Akt (S473) by antibody microarray, total Akt, P/total Akt, P-FKHR (S256), procaspase-8, cleaved caspase-8, and procaspase-3—were compiled from triplicate biological samples treated with 0, 0.2, 5, 100 ng/ml TNF and 0, 1, 100 ng/ml EGF or 0, 1, 5, 500 ng/ml insulin for 5, 15, 30, 60, 90 min or 2, 4, 8, 12, 16, 20, 24 hr. With each treatment, sextuplicate 0-min samples were also prepared to measure the level of baseline signaling. Exact treatment combinations are shown in Fig. 4.1F and described in the legend. The total number of individual protein measurements in the initial compendium was 7980: 19 molecular signals x 3 replicate measures x 10 treatment combinations x the equivalent of 14 time points (i.e., zero in sextuplicate) = 7980 individual signals.

For autocrine perturbations, cells were pretreated with 10 μg/ml C225 for one hr or cotreated with 10 μg/ml IL-1ra, then stimulated with 5 or 100 ng/ml TNF (Janes et al. 2005). These data provided an additional 1596 protein measurements (19 molecular signals x 3 replicate measures x 2 treatment combinations x the equivalent of 14 time points) to test model predictions.

Signaling metric extraction

For each signaling time course, the following signaling metrics were derived:

a. Thirteen time-point metrics, defined as the mean signal at each point in the time course.

b. Thirteen instantaneous-derivative metrics, defined as the forward slope between the current time point and the subsequent time point. For the final time point (24 hr), the instantaneous derivative was set to zero.

c. Four summary metrics, which included the area under the curve for the entire time course, the maximum signal, the mean signal, and the steady-state signal (defined as the mean of the final four time points).

d. A variable number of peak metrics. For each signal a tolerance value (defined as a percentage of the dynamic range of the signal) was set for the algorithm to classify an upward fluctuation as a peak. Tolerances were set at: 50% for Akt activity, IKK activity, and all antibody microarray measurements; 5% for JNK1 activity and MK2

activity; and 20% for all other signaling network measurements. For each peak identified, three metrics were extracted: area under the curve, activation slope (defined as the best linear fit between the preceding local minimum and the peak maximum), and decay rate (defined as the best exponential fit between the peak maximum and the proceeding local minimum).

These signaling metrics are summarized in Table 4. S2. Metric extraction algorithms were coded in MATLAB and are available upon request.

PLS model construction and validation

Prior to all analyses, the signaling and apoptosis matrices were variance scaled to nondimensionalize the different measurements. The PLS model was constructed in the SIMCA-P 10.0 (Umetrics) software suite according to the following iterative formulas:

$$E_1 = X - t_1 p_1^T;\ E_2 = E_1 - t_2 p_2^T,\ t_2 = E_1 w_1;\ E_i = E_{i-1} - t_i p_i^T,\ t_i = E_{i-1} w_i$$

$$F_1 = Y - b_1 t_1 q_1^T;\ F_2 = F_1 - b_2 t_2 q_2^T;\ F_i = F_{i-1} - b_i t_i q_i^T$$

where E_i represents the residual of the i^{th} principal component, with score vector t_i, weight vector w_i, and loading vector p_i, and ^{T} represents transpose. F_i represents the residuals of the i^{th} dependent principal component, with score vector t_i and loading vector q_i, and b_i represents the coefficient characterizing the inner relation between the independent and dependent principal components. Model predictions were made by leave-one-out crossvalidation for the TNF-EGF-insulin treatments and by unbiased prediction for the autocrine perturbations (Gaudet et al. 2005b). Model uncertainties

were calculated by jack-knifing (Efron and Tibshirani). Signaling axes and treatment mappings (Fig. 4.4, E–G) were plotted using w_1, w_2 and t_1, t_2 respectively after a 60° subspace rotation (Alter et al.). Centered and scaled coefficients were used as the regression weights.

PLS model perturbations - Reduced metric submodels

For the reduced metric submodels, the information content of each signaling metric was assessed by its variable importance in the projection (VIP):

$$VIP_k = \sqrt{\frac{k\sum_{a=1}^{A} w_{ak} SS_a}{\sum_{a=1}^{A} SS_a}}$$

where k is the number of signaling metrics, w_{ak} is the weight of the k^{th} metric for principal component a, A is the total number of principal components, and SS_a is the sum of squares explained by principal component a (Wold 1994). For the reduced signal submodels, the mean VIP score for each signal calculated across all metrics was used as the central estimate of the pure-signal information content.

4.6 Supplementary Figures and Tables

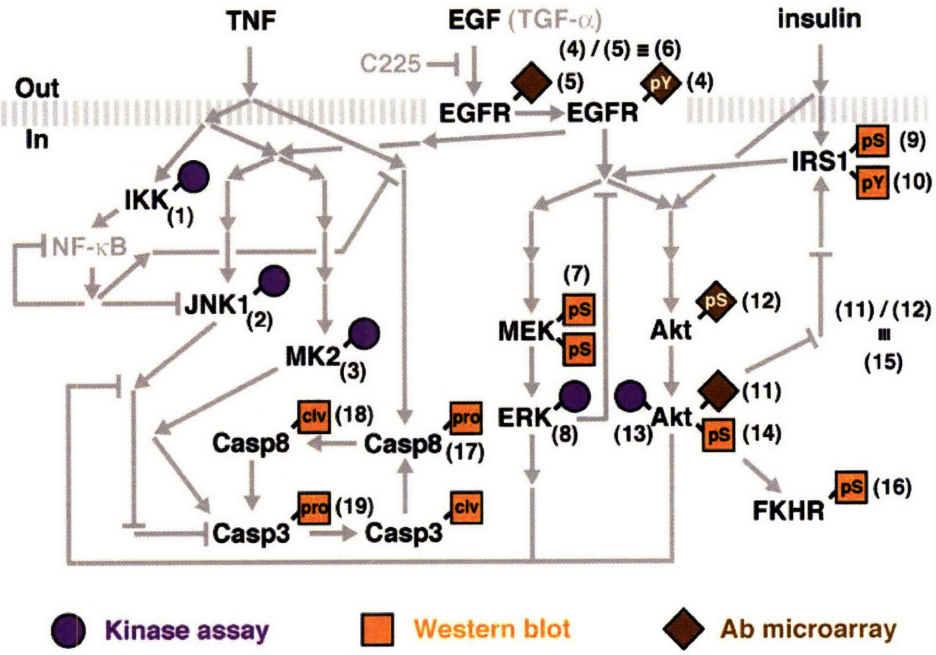

Figure 4.S1. Schematic of the shared TNF-EGF-insulin signaling network. Nineteen molecular signals (numbers) from protein nodes highlighted in black were measured by high-throughput kinase activity assays, quantitative Western blotting, or antibody microarrays as described (Janes et al. 2005).

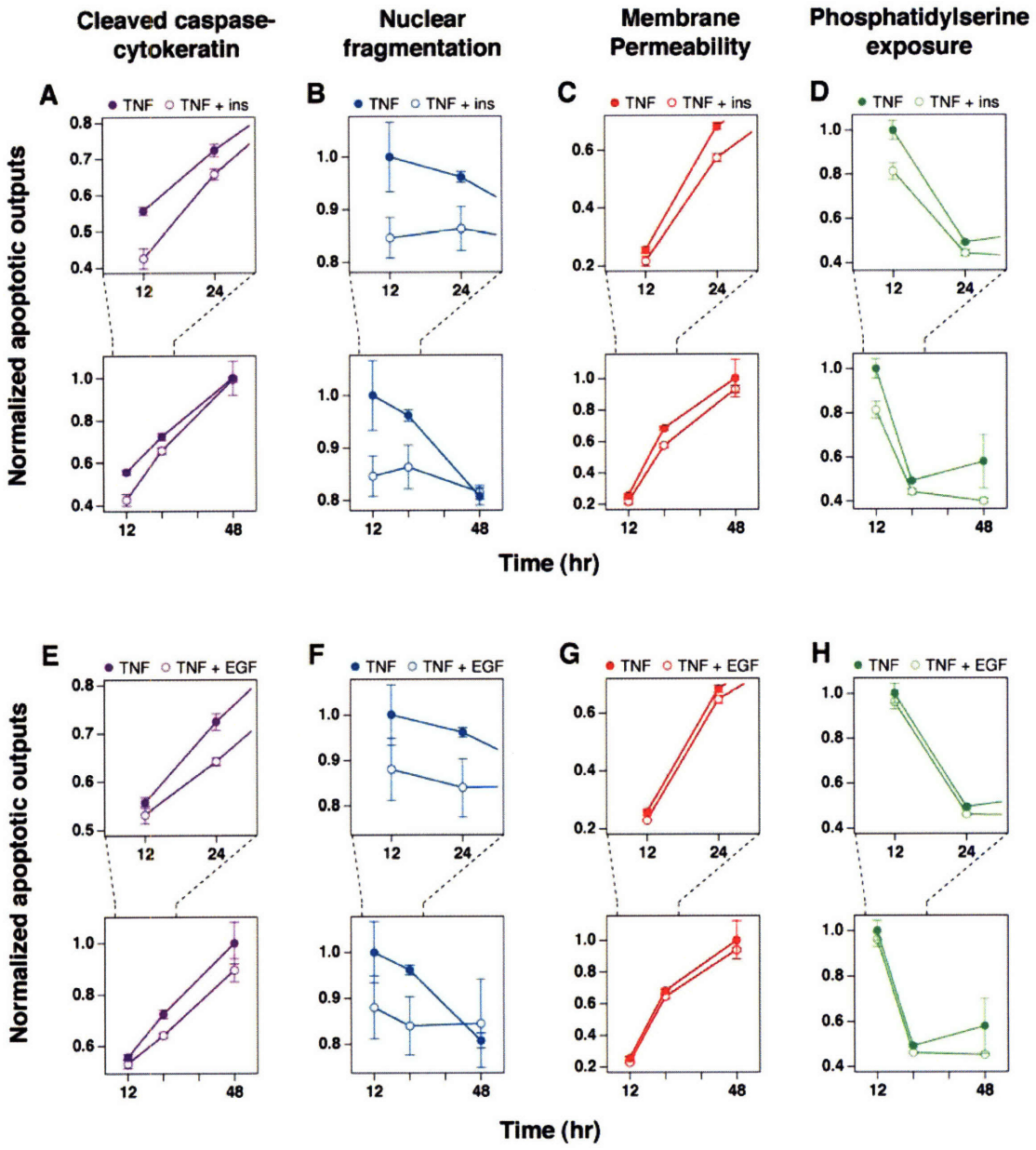

Figure 4.S2. Insulin and EGF antagonize TNF-induced apoptosis. **(A–D)** Insulin significantly reduces all four apoptotic outputs at 12 and 24 hr and reduces membrane permeability and phosphatidylserine exposure from 12 to 48 hr ($p < 0.05$, two-way analysis of variance). **(E–H)** EGF significantly reduces caspase substrate cleavage from 12 to 48 hr and membrane permeability at 12 and 24 hr ($p < 0.05$). Nuclear

fragmentation was also reduced but did not reach statistical significance ($p = 0.07$). Data are replotted from Fig. 4.1, M–O.

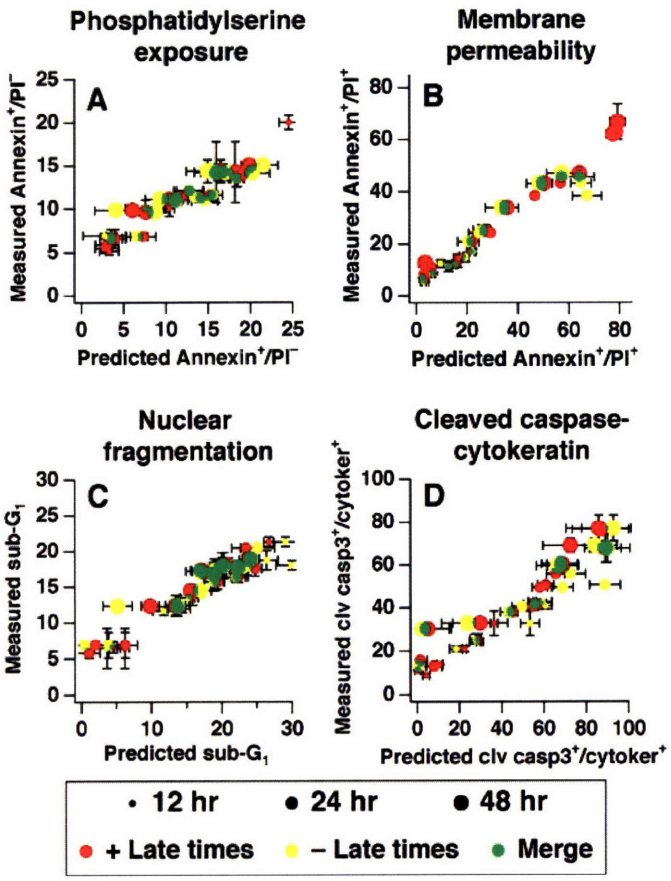

Figure 4.S3. The partial least squares model does not require late time points to make predictions of apoptosis. Correlation plots between measured apoptotic indices and cross-validated predictions of **(A)** phosphatidylserine exposure, **(B)** membrane permeability, **(C)** nuclear fragmentation, and **(D)** cleaved caspase-cytokeratin. The full PLS model (red) was compared with a truncated PLS model (yellow) that omitted signaling measurements after four hours. The merged overlay is shown in green, and marker size corresponds to the response time point. Data are presented as the mean ± S.E.M., and model uncertainties were estimated by jack-knifing.

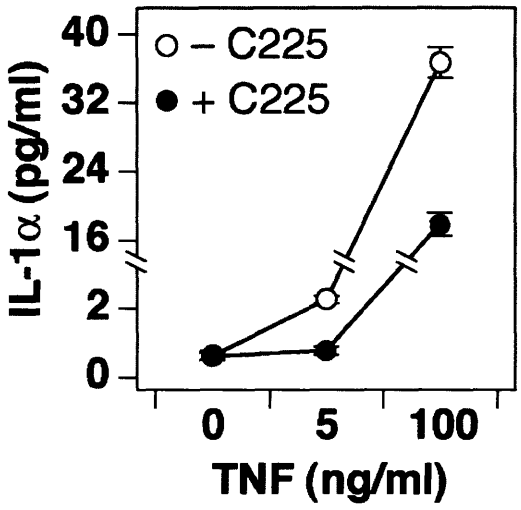

Figure 4.S4. TNF-induced autocrine TGF-α causes the release of autocrine IL-1α. Autocrine TGF-α was blocked with 10 μg/ml C225 antibody and HT-29 cells then stimulated with 0, 5, or 100 ng/ml TNF for 24 hr and analyzed for IL-1α release (Janes et al. 2004).

Table 4.S1. Signaling metrics extracted from dynamic network measurements

Metric class*	Metrics extracted
Time point	0 min
	5 min
	15 min
	30 min
	60 min
	90 min
	2 hr
	4 hr
	8 hr
	12 hr
	16 hr
	20 hr
	24 hr
Instantaneous derivative	0 min
	5 min
	15 min
	30 min
	60 min
	90 min
	2 hr
	4 hr
	8 hr
	12 hr
	16 hr
	20 hr
	24 hr
Summary metrics	Area under the curve
	Maximum signal
	Mean signal
	Steady-state signal
Peak metrics	Area under the curve
	Activation slope
	Decay rate

*See for a complete description and definition of the signaling metrics.

Table 4.S2. Top 20 most informative signaling metrics of the PLS model

VIP*	Protein†	Signal†	Metric‡
1.57	IRS-1	P-Ser636	Decay rate, peak #2
1.43	Akt	P-Ser473	Activation slope, peak #3
1.39	IRS-1	P-Ser636	Activation slope, peak #2
1.35	JNK1	Activity	Area under the curve, peak #2
1.35	IKK	Activity	Area under the curve, peak #2
1.30	MK2	Activity	4 hr time point
1.30	MK2	Activity	8 hr time point
1.29	JNK1	Activity	8 hr time point
1.29	IKK	Activity	Steady-state
1.29	JNK1	Activity	Decay rate, peak #2
1.29	MK2	Activity	Mean
1.28	MK2	Activity	30 min time point
1.28	MK2	Activity	Area under the curve
1.28	JNK1	Activity	Mean
1.28	MK2	Activity	Maximum
1.28	IKK	Activity	20 hr time point
1.28	IKK	Activity	Area under the curve
1.27	IKK	Activity	12 hr time point
1.27	IKK	Activity	16 hr time point
1.27	MK2	Activity	90 min time point§

*Variable importance in the projection .
†See Table 4. 1 and (Janes et al. 2005) for a complete description of the network measurements.
‡See Table 4. S1 and for a complete description of the signaling metrics.
§The top caspase metric, mean cleaved caspase-8, was only 34th overall .

Table 4.S3. Top 20 loadings in the first principal component of the PLS model

w_1c_1*	Protein†	Signal†	Metric‡
0.097	Caspase-8	Cleavage	2 hr derivative
0.095	EGFR	P-Tyr1068/total	16 hr derivative
0.095	MK2	Activity	5 min derivative
0.093	JNK1	Activity	5 min derivative
0.092	MK2	Activity	15 min time point
0.092	Akt	P-Ser473	Activation slope, peak #3
0.092	JNK1	Activity	Activation slope, peak #1
0.091	MK2	Activity	Area under the curve, peak #1
0.091	JNK1	Activity	15 min time point
0.090	JNK1	Activity	Maximum
0.090	Caspase-8	Cleavage	4 hr derivative
0.089	JNK1	Activity	30 min time point
0.089	MK2	Activity	90 min time point
0.088	MK2	Activity	60 min time point
0.088	Caspase-8	Cleavage	12 hr time point
0.087	MK2	Activity	30 min time point
0.087	Caspase-8	Cleavage	16 hr time point
0.087	Caspase-8	Cleavage	8 hr derivative
0.086	Akt	Total	20 hr derivative
0.086	MK2	Activity	Maximum
0.085	Caspase-8	Cleavage	Steady-state

*Loading weights of the first principal component .
†See Table 4. 1 and for a complete description of the network measurements.
‡See table S1 and for a complete description of the signaling metrics.

Table 4.S4. Top 20 loadings in the second principal component of the PLS model

w_2c_2*	Protein†	Signal†	Metric‡
-0.0695	IKK	Activity	Activation slope, peak #2
-0.0691	EGFR	Total	60 min derivative
-0.0622	Akt	P-Ser473	24 hr time point
-0.0615	MK2	Activity	Decay rate, peak #2
-0.0613	Akt	P-Ser473	8 hr derivative
-0.0608	FKHR	P-Ser256	16 hr time point
-0.0605	Akt	P-Ser473	16 hr time point
-0.0605	EGFR	Total	Area under the curve, peak #3
-0.0603	Akt	P-Ser473	Steady-state
-0.0600	Procaspase-3	Zymogen	12 hr time point
-0.0599	Procaspase-3	Zymogen	Steady-state
-0.0599	Procaspase-3	Zymogen	20 hr time point
-0.0596	Procaspase-3	Zymogen	24 hr time point
-0.0595	Procaspase-3	Zymogen	16 hr time point
-0.0593	Caspase-8	Cleavage	90 min time point
-0.0590	FKHR	P-Ser256	12 hr time point
-0.0587	Akt	P-Ser473	20 hr time point
-0.0586	FKHR	P-Ser256	Steady-state
-0.0583	Akt	P-Ser473	12 hr time point
-0.0581	IRS1	P-Tyr896	24 hr time point§

*Loading weights of the second principal component .
†See Table 4. 1 and (Janes et al. 2005) for a complete description of the network measurements.
‡See Table 4. S1 and for a complete description of the signaling metrics.
§Five P-IRS1 (Ser636) metrics were identified within the top 30 loadings of the second principal component .

4.7Acknowledgement

We thank Jason Kelly for programming the metric extraction algorithms.

4.8 References

Abreu-Martin MT, Vidrich A, Lynch DH, Targan SR (1995) Divergent induction of apoptosis and IL-8 secretion in HT-29 cells in response to TNF-alpha and ligation of Fas antigen. J Immunol 155(9): 4147-4154.

Abreu-Martin MT, Palladino AA, Faris M, Carramanzana NM, Nel AE et al. (1999) Fas activates the JNK pathway in human colonic epithelial cells: lack of a direct role in apoptosis. Am J Physiol 276(3 Pt 1): G599-605.

Alter O, Brown PO, Botstein D (2000) Singular value decomposition for genome-wide expression data processing and modeling. Proc Natl Acad Sci U S A 97(18): 10101-10106.

Bissell MJ, Radisky D (2001) Putting tumours in context. Nat Rev Cancer 1(1): 46-54.

Bouwmeester T, Bauch A, Ruffner H, Angrand PO, Bergamini G et al. (2004) A physical and functional map of the human TNF-alpha/NF-kappa B signal transduction pathway. Nat Cell Biol 6(2): 97-105.

Cruzalegui FH, Hardingham GE, Bading H (1999) c-Jun functions as a calcium-regulated transcriptional activator in the absence of JNK/SAPK1 activation. Embo J 18(5): 1335-1344.

Darzynkiewicz Z, Juan G, Li X, Gorczyca W, Murakami T et al. (1997) Cytometry in cell necrobiology: analysis of apoptosis and accidental cell death (necrosis). Cytometry 27(1): 1-20.

Del Bino G, Darzynkiewicz Z, Degraef C, Mosselmans R, Fokan D et al. (1999) Comparison of methods based on annexin-V binding, DNA content or TUNEL for evaluating cell death in HL-60 and adherent MCF-7 cells. Cell Prolif 32(1): 25-37.

Downward J (2001) The ins and outs of signalling. Nature 411(6839): 759-762.

Dumont JE, Dremier S, Pirson I, Maenhaut C (2002) Cross signaling, cell specificity, and physiology. Am J Physiol Cell Physiol 283(1): C2-28.

Efron B, Tibshirani RJ (1993) An Introduction to the Bootstrap. London: Chapman and Hall. 436 p.

Fadok VA, Bratton DL, Frasch SC, Warner ML, Henson PM (1998) The role of phosphatidylserine in recognition of apoptotic cells by phagocytes. Cell Death Differ 5(7): 551-562.

Gaudet S, Janes KA, Albeck JG, Pace EA, Lauffenburger DA et al. (2005a) A compendium of signals and responses triggered by prodeath and prosurvival cytokines. Mol Cell Proteomics 4(10): 1569-1590.

Gaudet S, Janes KA, Albeck JG, Pace EA, Lauffenburger DA et al. (2005b) A Compendium of Signals and Responses Triggered by Prodeath and Prosurvival Cytokines. Mol Cell Proteomics 4(10): 1569-1590.

Janes KA, Albeck JG, Peng LX, Sorger PK, Lauffenburger DA et al. (2003) A high-throughput quantitative multiplex kinase assay for monitoring information flow in signaling networks: application to sepsis-apoptosis. Mol Cell Proteomics 2(7): 463-473.

Janes KA, Kelly JR, Gaudet S, Albeck JG, Sorger PK et al. (2004) Cue-signal-response analysis of TNF-induced apoptosis by partial least squares regression of dynamic multivariate data. J Comput Biol 11(4): 544-561.

Janes KA, Gaudet S, Albeck JG, Nielsen UB, Lauffenburger DA et al. (2005) Autocrine crosstalk in the response of human cells to apoptotic and mitogenic stimuli. In preparation.

Janes KA, Gaudet S, Albeck JG, Nielsen UB, Lauffenburger DA et al. (2006) The response of human epithelial cells to TNF involves an inducible autocrine cascade. Cell 124(6): 1225-1239.

Kamata H, Honda S, Maeda S, Chang L, Hirata H et al. (2005) Reactive oxygen species promote TNFalpha-induced death and sustained JNK activation by inhibiting MAP kinase phosphatases. Cell 120(5): 649-661.

Lamb JA, Ventura JJ, Hess P, Flavell RA, Davis RJ (2003) JunD mediates survival signaling by the JNK signal transduction pathway. Mol Cell 11(6): 1479-1489.

Lee JC, Laydon JT, McDonnell PC, Gallagher TF, Kumar S et al. (1994) A protein kinase involved in the regulation of inflammatory cytokine biosynthesis. Nature 372(6508): 739-746.

Lei K, Davis RJ (2003) JNK phosphorylation of Bim-related members of the Bcl2 family induces Bax-dependent apoptosis. Proc Natl Acad Sci U S A 100(5): 2432-2437.

Nicholson DW, Thornberry NA (1997) Caspases: killer proteases. Trends Biochem Sci 22(8): 299-306.

Ozaki K, Leonard WJ (2002) Cytokine and cytokine receptor pleiotropy and redundancy. J Biol Chem 277(33): 29355-29358.

P.Geladi, Kowalski BR (1986) Partial Least Squares: A tutorial. Analytica Chimica Acta 185: 1-17.

Remacle-Bonnet MM, Garrouste FL, Heller S, Andre F, Marvaldi JL et al. (2000) Insulin-like growth factor-I protects colon cancer cells from death factor-induced apoptosis by potentiating tumor necrosis factor alpha-induced mitogen-activated protein kinase and nuclear factor kappaB signaling pathways. Cancer Res 60(7): 2007-2017.

Rouse J, Cohen P, Trigon S, Morange M, Alonso-Llamazares A et al. (1994) A novel kinase cascade triggered by stress and heat shock that stimulates MAPKAP kinase-2 and phosphorylation of the small heat shock proteins. Cell 78(6): 1027-1037.

Vanden Berghe T, Denecker G, Brouckaert G, Vadimovisch Krysko D, D'Herde K et al. (2004) More than one way to die: methods to determine TNF-induced apoptosis and necrosis. Methods Mol Med 98: 101-126.

Ventura JJ, Cogswell P, Flavell RA, Baldwin AS, Jr., Davis RJ (2004) JNK potentiates TNF-stimulated necrosis by increasing the production of cytotoxic reactive oxygen species. Genes Dev 18(23): 2905-2915.

Wiley HS, Shvartsman SY, Lauffenburger DA (2003) Computational modeling of the EGF-receptor system: a paradigm for systems biology. Trends Cell Biol 13(1): 43-50.

Wold S (1994) Exponentially Weighted Moving Principal Components-Analysis and Projections to Latent Structures. Chemometrics and Intelligent Laboratory Systems 23(1): 149-161.

Yadav D, Sarvetnick N (2003) Cytokines and autoimmunity: redundancy defines their complex nature. Curr Opin Immunol 15(6): 697-703.

Zhu X, Hart R, Chang MS, Kim JW, Lee SY et al. (2004) Analysis of the major patterns of B cell gene expression changes in response to short-term stimulation with 33 single ligands. J Immunol 173(12): 7141-7149.

Chapter 5

Conclusions and Future Directions

Chapter 5: Conclusions and Future Directions

Table of contents

5.1 Introduction

The study of apoptosis is important both from a basic biology and a clinical perspective. A thorough understanding of how, when, and to what extent cells commit to apoptosis will enable a better understanding of how multicellular organisms develop and, ideally make it possible to adjust the rate and extent of cell death so as to intervene in pathological processes. Part of this understanding will come from the continued discovery of additional components and interactions in the apoptotic pathways and a corresponding increase in the accuracy of the qualitative/descriptive models currently used to summarize our knowledge. However, it is increasingly apparent that a critical component of this understanding will be the integration of our knowledge in quantitative and mechanistic models. When I began this work, the prospect of developing such models seemed remote. Today the term "systems biology" and its goal of building formal quantitative models are widely recognized, although the approach is still viewed with skepticism by many traditional biologists. Critics note, quite rightly, that such modeling approaches will be of little use unless they are closely coupled to experimentation. Others remain unsure of how modeling approaches represent an advantage over more traditional experimental and analytical approaches. Thus, the crucial challenge, as systems biology comes of age, will be to effectively integrate data with models, not simply for the sake of building models but to answer questions that have remained inaccessible by experimental analysis alone. The work presented in this thesis aims to be such an integration, with the goal of gaining insight into a number of open questions in the fields of signal transduction and apoptosis. In this chapter, I summarize

the progress that my collaborators and I have made toward answering these questions, as well as the areas that remain in need of further exploration.

5.2 A quantitative mechanistic model of caspase substrate cleavage.

The model developed in Chapter 2 has served as an important tool throughout our single-cell studies. Our model served as a means for integrating data from various sources, including live-cell imaging, flow cytometry, and immunoblotting. Data from each of these sources were used as constraints on the model behavior, and thus the model effectively contains most of the information collected throughout our studies of TRAIL-induced apoptosis in HeLa cells. While numerous differential equation models of caspase networks have been developed, ours represents a significant advance in several ways. First, our model contains only mass-action equations; unlike several other models, there are no fitted forms or exponential equations that could enforce switch-like behavior (Bentele et al. 2004; Bagci et al. 2005). Thus, untested assumptions about the behavior of the biochemical network have not been hard-wired into the model. Second, our model has been extensively validated using single-cell data. While other models have been regressed against experimental data, population-average methods have been the main data source for these studies (Bentele et al. 2004). Mass-action biochemical models are based on the assumption that all reactions are occurring within the same physical compartment (or its sub-compartments). Therefore, comparing model behavior to population-average data rests on the assumption that the population-average behavior approaximates single-cell behavior. However, our live-cell experiments demonstrate that this assumption is not valid, and thus fitting the model to population average data

introduces a significant source of error into the model. Third, our model explicitly includes the cleavage of an effector caspase substrate (i.e. PARP). Most previous models have considered the network only up to caspase-3, and have assumed that the steady-state level of this enzyme can be equated to cell death. However, since there is a finite pool of effector caspase substrates in the cell, this simplification can be a significant problem. Under this simplification, the cleavage of caspase substrates induced by transient caspase-3 activation is not accurately accounted for. Moreover, we have observed in our model that participation of caspase-3 in enzyme-substrate complexes with its substrates can play a significant role in the extent to which it is accessible to its inhibitor XIAP. Thus, including caspase substrates such as PARP in the model, as we have done, substantially improves model accuracy.

Despite the progress that has been made in modeling caspase activation, there are clearly many aspects that have yet to be explored. Several known features of the signaling networks have been omitted from the current model; these could now be added to the model to explore whether they significantly alter the model behavior. For example, the formation of the DISC is a complex process involving the recruitment of multiple adaptor proteins. Additional complexities include a requirement for the interaction of adjacent receptor trimers (Holler et al. 2003), secondary complex formation (in the case of TNF, Micheau and Tschopp 2003), and signaling modulation by internalization (Schneider-Brachert et al. 2004). The cell-to-cell variability observed in caspase-8 activity (Chapter 3) could potentially arise from such a complex process, and numerous other forms of regulation are likely to modify the cellular response at this point. Secondly, additional details of proteasome-mediated protein degradation could be added,

which might improve the model's ability to predict the kinetics of PARP cleavage when a proteaseome inhibitor is added (Chapter 2). Thirdly, caspases considered redundant, such as caspase-7 and caspase-10, could be added to the model; caspase-7 could potentially act as a further amplifying step in effector caspase activation, since it has been reported to be activated downstream of caspase-3.

Other additions, which will require a substantial amount of experimental validation, are the inclusion of other pathways in the model. To fully model the response to TNF, for example, both the caspase pathway and the NF-κB survival pathway must be accounted for. The NF-κB pathway feeds back into the caspase pathway by transcriptionally regulating anti-apoptotic proteins such as FLIP, Bcl-X_L, and XIAP (Stehlik et al. 1998; Tsukahara et al. 1999; Micheau et al. 2001). Since each of these species is already present in the model, and models of TNF-induced NF-κB activation have also been developed (Hoffmann et al. 2002; Nelson et al. 2004), it would be relatively straightforward to integrate models of the two pathways. However, quantitative experimental data for the amount and timing of the transcriptional upregulation of each gene will be necessary to create an accurate link between the two pathways. The integration of other pathways, such as the Akt and ERK pathways, is also feasible, with similar requirements for data to calibrate the strength of crosstalk.

One final area into which the model could be extended is non-redundant parallel pathways. Several reports have suggested the existence of pathways that run in parallel to the canonical pathway included in the model, which are reported to be essential for TNF- or TRAIL-induced apoptosis (Deng et al. 2003; Chau et al. 2004; Baksh et al. 2005). For example, one study found that the tumor suppressor protein RASSF1A

activates the BH-3 protein MAP-1 at the DISC to stimulate mitochondrial permeabilization (Baksh et al. 2005). Blocking this pathway by gene knockout or siRNA greatly reduced death receptor-induced apoptosis, suggesting that this pathway may be equally as important as the well-known caspase-8/Bid pathway. However, this pathway is based only on one isolated report, and thus extensive experimental validation would be necessary before it could be included in the model with a high level of confidence. Nonetheless, this effort could be essential to fully capture the entire network.

5.3 Mechanism of all-or-none caspase activity

All-or-none caspase activity appears to be an important feature of apoptotic regulation. While several hypotheses have been put forward for this phenomenon, none have previously been tested experimentally (Eissing et al. 2004; Bagci et al. 2005). In our work, we identify the underlying mechanism of this regulation and demonstrate its breakdown under various conditions. This behavior has two essential components: first, XIAP acts to ensure that caspase-3 remains inactive despite being cleaved; second, the mitochondrial pathway produces a sudden, overwhelming signal that relieves XIAP inhibition and quickly leads to a sharp increase caspase-3 activity (Fig 2.6A). An important point to note is that caspase-3 *activation* is not literally all-or-none; even in the "all" case, our model indicates that only ~40% of the caspase-3 molecules in the cell are active at any one time. Rather, "all-or-none" most accurately describes the cleavage of the substrates downstream of caspase-3. When the switch functions properly, the amount of caspase-3 activity induced is far in excess of the amount needed to exhaustively cleave the cellular pool of substrates. Conversely, in the "none" case, the total cumulative

caspase-3 activity is low enough that less than 5% of cellular substrates are cleaved. An interesting consequence of the regulation of caspase-3 by XIAP is that, under some conditions, caspase-3 can be first activated and then degraded, creating a pulse of caspase-3 activity that is sufficient to cleave some, but not all, of the pool of caspase-3 substrates (Fig 2.3A). In some cases, this pulse causes damage (partial cleavage), but not death (Fig 2.2 G). We speculate that this could lead to genomic damage in the surviving cells, due to the activation of caspase-activated DNAses. However, we have yet to confirm the existence or the extent of such DNA damage; demonstrating this will be an essential test for the hypothesis that partial caspase substrate cleavage may lead to oncogenesis. Moreover, it will be important to examine the *in vivo* effects of partial caspase substrate cleavage. While it would be difficult to control caspase substrate cleavage precisely *in vivo*, perhaps one possibility would be a xenograft-type approach, in which cells are stimulated *in vitro* under conditions that result in partial caspase substrate cleavage, and then replaced into an animal to assess their tumorigenic potential.

It will also be interesting to explore situations in which partial caspase activation occurs for physiological reasons. There are numerous reports of caspases acting in non-apoptotic processes, such as differentiation and T-cell proliferation (Algeciras-Schimnich et al. 2002; Chun et al. 2002). Further work will be needed to determine whether the regulation of caspases under these circumstances is similar to the conditions we have described for partial caspase activation. The existence of situations in which the cell does not require full caspase activation may also suggest a reason why the all-or-none caspase activation is not more "robust". If the caspase network is required to fill multiple roles, some of which require full caspase activation and some which require partial activation,

these constraints could prevent the evolution of a system that can only operate in an all-or-none manner. While switching mechanisms could be envisioned in which it is much harder to cause partial caspase activation, these may not be practical because of the additional roles that the caspase network is required to fill.

5.4 Relationship of caspase-3 activity to cell fate.

Caspases kill the cell, but how lethal are these enzymes in quantitative terms? An interesting outcome of studying all-or-none caspase substrate cleavage is that it enabled us to create situations in which caspase activation does not result in exhaustive cleavage of cellular substrates. The final extent of effector caspase substrate cleavage can be adjusted by simultaneously inactivating the mitochondrial pathway by Bcl-2 overexpression and varying the XIAP level or the rate of proteasomal degradation (Fig 2.3). One advantage of this arrangement is that, by preventing mitochondrial permeabilization, a potential complicating source of cytotoxicity is removed, since it has been reported that mitochondrial permeabilization may result in cell death even in the absence of caspase activity (Ekert et al. 2004; Chipuk and Green 2005). Thus, the conditions of Bcl-2 overexpression and XIAP depletion allow the death-inducing power of the effector caspases to be examined in isolation of other cell death pathways. Based on these experiments we estimated that a pulse of caspase-3 activity sufficient to cleave ~10-20% of the cellular pool of substrates is lethal to ~50% of cells (Fig 2.2F,G and 2.S6). However, as noted in Chapter 1, there may be a number of redundant, or "backup", pathways leading to cell death (Golstein and Kroemer 2005). In the case of many cell deaths, caspase activation is only part of the lethal mix; substantial cell killing

results even if the caspases are inhibited. Much further study and quantitative modeling will be needed to understand these alternate death pathways. Nonetheless, a quantitative understanding of caspase-induced lethality is an important part of the overall cell death equation. The ultimate goal of understanding cell death in all its physiological forms will come when the independent contributions and synergistic behavior of multiple death mechanisms can be quantitatively modeled.

5.5 Single-cell apoptotic assays

The results presented here provide several good examples of why single-cell assays are important in studying many cell biological processes. Even within an isogenic population, individual cell responses can be highly variable (Tyas et al. 2000; Geva-Zatorsky et al. 2006). Furthermore, single-cell assays allow the distinction of different types of responses; e.g. a complete response in a subset of cells vs. a partial response in all cells. However, our findings also provide a good example of why it is also critical to integrate single-cell measurements with population-average methods. When using the DEVD-based FRET reporter in Chapter 2, its behavior accurately reflected the kinetics of endogenous caspase-3 substrates under the conditions examined. However, we later observed that this reporter was also cleaved at a much slower, but significant, rate in Bcl-2-overexpressing cells, a condition where the specificity of western blotting indicated unequivocally that endogenous substrates such as PARP are not cleaved (see Fig 2.2F and Appendix D). This enabled us to switch to a redesigned reporter with improved specificity for further studies (Chapter 3, Appendix D). Nonetheless, single-cell reporters, when carefully integrated with other data types, are an invaluable tool and an

exciting area for future development. Perhaps the most interesting area for exploration is the combination of multiple reporters within the same cell. As shown in chapter 3, multiple reporters can allow both an upstream and a downstream signal in the same pathway can be simultaneously assayed. This arrangement makes it possible to observe the input-output behavior of a portion of the pathway and, if a threshold exists, allows the quantification of the position of the threshold in individual cells. The cell-to-cell variability in input-output behavior and threshold position can then be assessed, providing insight into the molecular mechanisms of population heterogeneity. Another arrangement, which has not yet been explored in detail, is the use of reporters in parallel pathways; this arrangement would allow measurements of pathway correlation and cross-talk in single cells. This method could be very useful in developing integrated models of multiple pathways. For example, the pro-survival (NF-κB) and pro-apoptotic (caspase) pathways triggered by TNF could be simultaneously assayed by existing reporters; this would provide valuable quantitative information for the integrated TNF model discussed above (section 5.2).

5.6 Position of the threshold in the death receptor pathway

The ability of the mitochondrial pathway to act as an adjustable threshold and the point of no return in apoptosis has long been hypothesized. However, these hypotheses were based solely on observations of the behavior of cytochrome c/Smac release and the downstream events. A formally possible alternative to these hypotheses was that the final commitment to apoptosis was made by signals upstream of the mitochondria, and that cytochrome c/Smac release simply transmitted and amplified this binary decision. We

provide the first single-cell data confirming that the mitochondrial pathway is indeed the location of the threshold (Fig 3.3 B). Caspase-8 signaling upstream of the mitochondria appears to vary continuously with the amount of death ligand stimulation; the higher the concentration of ligand, the faster the cleavage of caspase-8 substrates. The mitochondrial pathway appears to play the role of an analog-to-digital converter, providing a uniformly rapid output (cytochrome c/Smac release) for all values of input (rate of caspase-8 activity). Moreover, the mitochondrial pathway effectively translates stimulus strength into the delay time of cell death, since the time at which permeabilization occurs depends on the rate of caspase-8 activity (Fig 3.4). Thus, the mitochondrial pathway appears to have the characteristics of a very sharp threshold. As noted in Chapter 1, such a threshold is not likely to result from a simple first order protein-protein interaction. Therefore, although the ability of Bcl-2 to bind and inhibit Bax prompted the original threshold model and is a necessary component of the threshold, the full mechanism is necessarily more complex. Our model will serve as a useful tool for understanding this mechanism, since it recapitulates the experimentally observed behavior. Preliminary analysis suggests that the threshold results from a combination of the rate at which Bax translocates to the mitochondrial compartment, the concentrating effect of the smaller mitochondrial volume (relative to the cytosol), the required oligomerization of Bax, and the high V_{max} of pore mediated cytochrome c/Smac release. A more formal mathematical analysis is underway, which will enable a clear definition of the feature of this pathway required for effective threshold behavior.

One significant advantage of the single-cell methods developed is that they enable sensitive discrimination of where pro-survival effects affect pro-apoptotic signaling –

upstream of, downstream of, or directly at the mitochondrial pathway. Since many survival factors, such as Akt, have been shown to intervene at multiple points in the apoptotic pathway (Datta et al. 1997; Cardone et al. 1998; Brunet et al. 1999), these methods will make it possible to identify which of the anti-apoptotic functions is most important in a given context. Thus, these methods will be important in the effort to understand how information from pro-survival signals is translated into changes in the signaling kinetics of the central death pathways.

5.7 Quantitative integration of information from multiple pro-survival pathways

In the work described in Chapter 4, we took a data-driven modeling approach to examine the integration of multiple pro- and anti- apoptotic signals in response to simultaneous stimulation by multiple ligands. While in Chapters 2 and 3 our approach was to use mechanistic modeling to understand the behavior of a more limited biochemical pathway, the sheer number of pathways and unknowns in the network under study in Chapter 4 make the mechanistic approach currently intractable. Therefore, this question required a modeling technique appropriate to the scale of the problem, and much information was gained from the principal component-based model that we developed. From the information encoded in a system-wide signaling data set, which was sufficient to predict the measured apoptotic signatures, we were able to identify the temporal molecular signals that were most important in determining the apoptotic response. While the model was correlative and not mechanistic, we were able to confirm a number of mechanistic hypotheses that were suggested by examining the key components of the model. Thus, in a situation where numerous pathways were active, many of which have

been shown to regulate apoptosis, this data-driven approach made it possible to quickly identify the subset of signals that were the most quantitatively important in controlling the cellular response. It is interesting to ask whether this model is specific to this particular cell context. In other words, would the same model successfully predict the apoptotic response, given the appropriate signaling data, in other cell types with other stimulation conditions? If the same principal-component model were broadly applicable, it would suggest that many different cell types have a similar processing mechanism for intracellular signals. The alternative hypothesis is that signal processing is highly context-dependent, meaning that the same Akt time course in two different cell types would influence the cellular response differently. These hypotheses are currently under investigation (K.A. Janes and K.E. Miller, unpublished data).

Another interesting direction will be to further link the highly significant signals in the principal component model to our mechanistic model. To harness the power of the data set already collected, further experiments could be performed in the HT-29 system, using the highly informative single-cell techniques developed in chapter 3. Then, a principal component model could be developed to connect the signaling data to specific molecular steps in the apoptotic pathway. It might be possible, for example, to connect the early peak in Akt signaling to a change in the mitochondrial threshold and the later peak to decreased signaling downstream of the mitochondria. Thus, by combining the mechanistic and data-driven approaches, it could be possible to develop a view of apoptotic signal integration that is both broad in signal diversity and deep in molecular mechanism.

Yet another interesting question is whether similar signaling processing occurs at the single cell level as occurs at the population level. To test this, multiple single-cell reporters corresponding to the highly significant signals in the model could be simultaneously monitored (for example, NF-κB GFP and FKHR-RFP). It would then be possible to determine whether the time points and signal strengths that were predictive in the population model were similarly predictive of the fate of each individual cell. Although it might seem that this should be the case, the presence of complex autocrine feedback loops would make it possible for population-level signal processing to differ significantly from the mechanism by which each individual cell chooses its fate.

5.8 Summary

Overall, my work presented here has contributed to the field of apoptosis by revealing the dynamic mechanisms by which the rate, completeness, and timing of caspase activation are controlled by the central apoptotic pathway and by survival signals that interface with the central pathway. This work has also contributed to the field of systems biology through the development of new mathematical models that are closely tied to experimental data. There are a number of interesting directions in which the integrated experimental and computational work begun here may continue.

5.9 References

Algeciras-Schimnich A, Barnhart BC, Peter ME (2002) Apoptosis-independent functions of killer caspases. Curr Opin Cell Biol 14(6): 721-726.

Bagci EZ, Vodovotz Y, Billiar TR, Ermentrout GB, Bahar I (2005) Bistability in Apoptosis: Roles of Bax, Bcl-2 and Mitochondrial Permeability Transition Pores. Biophys J.

Baksh S, Tommasi S, Fenton S, Yu VC, Martins LM et al. (2005) The tumor suppressor RASSF1A and MAP-1 link death receptor signaling to Bax conformational change and cell death. Mol Cell 18(6): 637-650.

Bentele M, Lavrik I, Ulrich M, Stosser S, Heermann DW et al. (2004) Mathematical modeling reveals threshold mechanism in CD95-induced apoptosis. J Cell Biol 166(6): 839-851.

Brunet A, Bonni A, Zigmond MJ, Lin MZ, Juo P et al. (1999) Akt promotes cell survival by phosphorylating and inhibiting a Forkhead transcription factor. Cell 96(6): 857-868.

Cardone MH, Roy N, Stennicke HR, Salvesen GS, Franke TF et al. (1998) Regulation of cell death protease caspase-9 by phosphorylation. Science 282(5392): 1318-1321.

Chau BN, Chen TT, Wan YY, DeGregori J, Wang JY (2004) Tumor necrosis factor alpha-induced apoptosis requires p73 and c-ABL activation downstream of RB degradation. Mol Cell Biol 24(10): 4438-4447.

Chipuk JE, Green DR (2005) Do inducers of apoptosis trigger caspase-independent cell death? Nat Rev Mol Cell Biol 6(3): 268-275.

Chun HJ, Zheng L, Ahmad M, Wang J, Speirs CK et al. (2002) Pleiotropic defects in lymphocyte activation caused by caspase-8 mutations lead to human immunodeficiency. Nature 419(6905): 395-399.

Datta SR, Dudek H, Tao X, Masters S, Fu H et al. (1997) Akt phosphorylation of BAD couples survival signals to the cell-intrinsic death machinery. Cell 91(2): 231-241.

Deng Y, Ren X, Yang L, Lin Y, Wu X (2003) A JNK-dependent pathway is required for TNFalpha-induced apoptosis. Cell 115(1): 61-70.

Eissing T, Conzelmann H, Gilles ED, Allgower F, Bullinger E et al. (2004) Bistability analyses of a caspase activation model for receptor induced apoptosis. J Biol Chem.

Ekert PG, Read SH, Silke J, Marsden VS, Kaufmann H et al. (2004) Apaf-1 and caspase-9 accelerate apoptosis, but do not determine whether factor-deprived or drug-treated cells die. J Cell Biol 165(6): 835-842.

Geva-Zatorsky N, Rosenfeld N, Itzkovitz S, Milo R, Sigal A et al. (2006) Oscillations and variability in the p53 system. Mol Syst Biol 2: 2006 0033.

Golstein P, Kroemer G (2005) Redundant cell death mechanisms as relics and backups. Cell Death Differ 12 Suppl 2: 1490-1496.

Hoffmann A, Levchenko A, Scott ML, Baltimore D (2002) The IkappaB-NF-kappaB signaling module: temporal control and selective gene activation. Science 298(5596): 1241-1245.

Holler N, Tardivel A, Kovacsovics-Bankowski M, Hertig S, Gaide O et al. (2003) Two adjacent trimeric Fas ligands are required for Fas signaling and formation of a death-inducing signaling complex. Mol Cell Biol 23(4): 1428-1440.

Micheau O, Tschopp J (2003) Induction of TNF receptor I-mediated apoptosis via two sequential signaling complexes. Cell 114(2): 181-190.

Micheau O, Lens S, Gaide O, Alevizopoulos K, Tschopp J (2001) NF-kappaB signals induce the expression of c-FLIP. Mol Cell Biol 21(16): 5299-5305.

Nelson DE, Ihekwaba AE, Elliott M, Johnson JR, Gibney CA et al. (2004) Oscillations in NF-kappaB signaling control the dynamics of gene expression. Science 306(5696): 704-708.

Schneider-Brachert W, Tchikov V, Neumeyer J, Jakob M, Winoto-Morbach S et al. (2004) Compartmentalization of TNF receptor 1 signaling: internalized TNF receptosomes as death signaling vesicles. Immunity 21(3): 415-428.

Stehlik C, de Martin R, Kumabashiri I, Schmid JA, Binder BR et al. (1998) Nuclear factor (NF)-kappaB-regulated X-chromosome-linked iap gene expression protects endothelial cells from tumor necrosis factor alpha-induced apoptosis. J Exp Med 188(1): 211-216.

Tsukahara T, Kannagi M, Ohashi T, Kato H, Arai M et al. (1999) Induction of Bcl-x(L) expression by human T-cell leukemia virus type 1 Tax through NF-kappaB in apoptosis-resistant T-cell transfectants with Tax. J Virol 73(10): 7981-7987.

Tyas L, Brophy VA, Pope A, Rivett AJ, Tavare JM (2000) Rapid caspase-3 activation during apoptosis revealed using fluorescence-resonance energy transfer. EMBO Rep 1(3): 266-270.

Appendix A

Reprinted from:

Gaudet, S., Janes, K. A., Albeck, J. G., Pace, E. A., Lauffenburger, D. A., and Sorger, P. K. (2005).

A compendium of signals and responses triggered by prodeath and prosurvival cytokines.

Mol Cell Proteomics *4*, 1569-1590.

In this study, I performed the cell death measurements shown in Figures 4B and 6B, which became an essential part of the compendium analysis. All other experiments and modeling were performed by Suzanne Gaudet, Kevin Janes, and Emily Pace.

A Compendium of Signals and Responses Triggered by Prodeath and Prosurvival Cytokines*[S]

Suzanne Gaudet‡, Kevin A. Janes§, John G. Albeck‡, Emily A. Pace¶, Douglas A. Lauffenburger‡§, and Peter K. Sorger‡§‖

Cell-signaling networks consist of proteins with a variety of functions (receptors, adaptor proteins, GTPases, kinases, proteases, and transcription factors) working together to control cell fate. Although much is known about the identities and biochemical activities of these signaling proteins, the ways in which they are combined into networks to process and transduce signals are poorly understood. Network-level understanding of signaling requires data on a wide variety of biochemical processes such as posttranslational modification, assembly of macromolecular complexes, enzymatic activity, and localization. No single method can gather such heterogeneous data in high throughput, and most studies of signal transduction therefore rely on series of small, discrete experiments. Inspired by the power of systematic datasets in genomics, we set out to build a systematic signaling dataset that would enable the construction of predictive models of cell-signaling networks. Here we describe the compilation and fusion of ~10,000 signal and response measurements acquired from HT-29 cells treated with tumor necrosis factor-α, a proapoptotic cytokine, in combination with epidermal growth factor or insulin, two prosurvival growth factors. Nineteen protein signals were measured over a 24-h period using kinase activity assays, quantitative immunoblotting, and antibody microarrays. Four different measurements of apoptotic response were also collected by flow cytometry for each time course. Partial least squares regression models that relate signaling data to apoptotic response data reveal which aspects of compendium construction and analysis were important for the reproducibility, internal consistency, and accuracy of the fused set of signaling measurements. We conclude that it is possible to build self-consistent compendia of cell-signaling data that can be mined computationally to yield important insights into the control of mammalian cell responses. ***Molecular & Cellular Proteomics 4:1569–1590, 2005.***

From the ‡Department of Biology and the §Biological Engineering Division, Massachusetts Institute of Technology, Cambridge, Massachusetts 02139 and ¶Merrimack Pharmaceuticals, Cambridge, Massachusetts 02142

Received, May 31, 2005, and in revised form, July 7, 2005

Published, MCP Papers in Press, July 18, 2005, DOI 10.1074/mcp.M500158-MCP200

The development of numerical models of complex biological processes such as signal transduction depends on the availability of accurate, self-consistent, and quantitative experimental data. Large scale collection and systematization of such data is likely to have as great an impact on cell biology as complete genome sequencing has had on genetics (1, 2). A few high throughput signaling datasets describing lymphokine-induced protein networks (3) and phosphotyrosine networks (4) have recently become available, and the Alliance for Cellular Signaling continues its efforts to collect data on large numbers of signaling proteins (5). However, the assembly of cell-signaling datasets is in its infancy and faces challenges not encountered in genomics. First, unlike gene sequences, signaling data are necessarily heterogeneous (6). Activation of intracellular signal transduction networks involves biochemical processes as distinct as receptor-ligand binding, protein modification, assembly of multicomponent complexes, translocation among cellular compartments, and protein synthesis and destruction (hereafter referred to as "signals"). Whereas the sequence of an entire genome can be determined using a single mature technology and genome-wide transcriptional profiling can be accomplished with microarray methods alone, monitoring cell signaling requires a wide variety of experimental techniques including enzymatic assays (7), immunoblotting (8), flow cytometry (3), immunofluorescence (9), and mass spectrometry (10). Only a subset of these approaches are currently used in large scale data collection (phosphoprotein mass spectrometry for example) in part because techniques that are mainstays of standard cell biology, such as immunoblotting and immunofluorescence, are not well adapted to high throughput analysis.

A second complication in systematizing cell-signaling measurements is the lack of inherent structure in the data. Structured data, such as DNA sequence, can be referenced to a single data model and systematized via relational databases. Manipulating unstructured data, such as microscopy and immunoblot images, is a significant informatic challenge to which current databases are not well suited (11). Third, unlike gene sequences, the meaning of data on kinase activation, receptor-ligand interaction, signalosome assembly, and phospholipid modification depends heavily on context (6, 11). Critical aspects of biological context include cell type,

nature and concentration of a cytokine stimulus, and cell cycle or growth phase. Experimental methods also contribute to context because quantitative measurements vary with reagent source and protocol. Finally signaling data are necessarily incomplete: whereas a genomic sequence has a well defined start and finish, the characterization of a complex signaling network is an open-ended process.

This study examined signaling networks that control the apoptosis-survival decision in HT-29 human colon adenocarcinoma cells treated with combinations of the prodeath cytokine tumor necrosis factor-α (TNF)[1] and the prosurvival growth factors epidermal growth factor (EGF) and insulin. TNF activates intracellular signals by binding to trimeric death receptors and promoting assembly of intracellular death-inducing signaling complexes (12, 13). Death-inducing signaling complexes then activate several parallel signaling pathways, including apoptotic caspases (14), stress-activated c-jun N-terminal kinase 1 (JNK1) and p38 pathways (15), and the proinflammatory IκB kinase (IKK)-nuclear factor-κB pathway (16).

Activation of the EGF receptor (EGFR) tyrosine kinase occurs through receptor dimerization, conformational change, and autophosphorylation (17, 18). Phosphorylated receptors recruit adaptor proteins, and these then activate multiple signaling proteins including extracellular signal-regulated kinase (ERK) via Ras and the Akt kinase via phosphatidylinositol 3-kinase (19). The binding of insulin to the insulin receptor also activates ERK and Akt, but in contrast to EGFR, the insulin receptor is constitutively dimerized, and most insulin-induced signaling involves modification of insulin receptor substrate 1 (IRS1), a multidomain adaptor protein (20). Antagonism between TNF and EGF or TNF and insulin is well documented and relevant to many diseases, including cancer, inflammatory bowel disease, and diabetes.[2] However, there exists only limited molecular level understanding of the strategies cells use to process conflicting cytokine stimuli and regulate responses such as apoptosis. The limitation arises in part because current practice in signal transduction research, as in other areas of cell biology, is to interpret data only with respect to contemporaneous controls. Categorical conclusions are drawn from direct comparison of experimental and control samples (*e.g.* ERK is more, less, or equally active between samples), and the next experiment is designed. In studies of complex networks, however, many variables must be measured, and the piecemeal accumulation and analysis of data become both cumbersome and limiting.

In this study we asked whether a validated and self-consistent dataset could be constructed from diverse biochemical measurements of cell-signaling proteins in human cells exposed to TNF, EGF, and insulin. Using techniques available in the average research laboratory, we normalized and fused into a single dataset ~10,000 data points collected over an 18-month period. We have not yet tackled the informatic challenge of building a database to hold the information, relying instead on a series of customized spreadsheets. We therefore refer to the assembled dataset as a compendium. The heterogeneity, lack of intrinsic structure, context dependence, and open-ended nature of the signaling data make the construction of this cytokine-signal-response (CSR) compendium nontrivial (22). However, we show that the compendium makes it possible to compare, with high reliability, data that were not collected contemporaneously. We also show that data can be mined for insights that would not be obvious from more conventional approaches. Finally because the value of a data compendium can only be unlocked computationally, we analyzed the full dataset by using a predictive statistical model based on partial least squares regression (PLSR).[3] We will describe elsewhere the use of modeling to elucidate the mechanisms by which cells process conflicting cytokine stimuli[3]; here we apply modeling to the more general problem of assessing the quality and information content of a CSR compendium. In contrast to many other proteomic efforts, we incorporated modeling early in the data collection process by linking protein signaling to relevant phenotypic responses. The inclusion of responses is necessary to constrain statistical models sufficiently to provide useful quantitative assessment of compendium design. Our key findings are that heterogeneous, time-resolved information is indeed critical for predictive power as is sampling broadly across the network. Nonetheless it appears sufficient to monitor a subset of network reactions, significantly reducing the data collection burden on future proteomic compendia.

EXPERIMENTAL PROCEDURES

Cell Culture and Treatments—HT-29 human colon adenocarcinoma cells (ATCC) were maintained in McCoy's 5A supplemented with 10% fetal bovine serum, 2 mM glutamine, 10 units/ml penicillin, and 10 units/ml streptomycin (Invitrogen). Cells were used within passage 10 after thaw for all experiments and passaged 2 days prior to plating. For each experiment, HT-29 cells were plated at 50,000 cells/cm^2. After 24 h, the cells were sensitized by changing to medium

[1] The abbreviations used are: TNF, tumor necrosis factor α; CSR, cytokine-signal-response; EGF, epidermal growth factor; EGFR, epidermal growth factor receptor; ERK, extracellular signal-regulated kinase; FKHR, Forkhead transcription factor; pFKHR, phospho-FKHR; FOXO3, Forkhead box O3a; IKK, IκB kinase; IL-1α, interleukin-1α; IL-1R, IL-1 receptor; IL-1ra, IL-1 receptor antagonist; IR, insulin receptor; IRS1, insulin receptor substrate 1; pIRS1, phospho-IRS1; JNK, c-jun N-terminal kinase; MEK, mitogen-activated protein kinase and extracellular signal-regulated kinase kinase; MK2, mitogen-activated protein kinase-activated protein kinase 2; PLSR, partial least squares regression; ptAkt, phospho-to-total Akt; ptEGFR, phospho-to-total EGFR; SGK, serum- and glucocorticoid-inducible kinase; TGF-α, transforming growth factor α; VIP, variable importance in the projection.

[2] K. A. Janes, S. Gaudet, J. G. Albeck, U. B. Nielsen, D. A. Lauffenburger, and P. K. Sorger, submitted for publication.

[3] K. A. Janes, J. G. Albeck, S. Gaudet, P. K. Sorger, D. A. Lauffenburger, and M. B. Yaffe, submitted for publication.

supplemented with 200 units/ml interferon-γ at a ratio of ~0.13 ml of medium/cm^2. The cultures were stimulated 24 h later by adding the stimulus diluted in 1/20 of the culture volume of serum-free medium for final concentrations of 0, 0.2, 5, or 100 ng/ml TNF (Peprotech); 0, 1, or 100 ng/ml EGF (Peprotech); and 0, 1, 5, or 500 ng/ml insulin (Sigma). The C225 anti-EGFR monoclonal antibody (H. S. Wiley laboratory) and IL-1ra (Amgen) inhibitors were used at 10 μg/ml. Triplicate plates were lysed at 0, 5, 15, 30, 60, and 90 min and 2, 4, 8, 12, 16, 20, and 24 h or prepared for flow cytometry at 12, 24, and 48 h.

Cell Lysis—Cell lysis had to be compatible with multiple assays and combine dead (floating) and viable cells. Floating cells were pelleted from culture supernatant and rinsed with ice-cold PBS. Adherent cells were lysed in ice-cold lysis buffer (as described in Ref. 7) and combined with the dead cells pelleted from the culture medium. An aliquot of the whole-cell homogenate was immediately frozen for use in immunoblot analysis. The lysates were clarified by centrifugation (10 min at 15,000 rpm) and aliquoted for antibody array and kinase assay. Total protein concentration was determined using the bicinchoninic acid assay (Pierce) for both the clarified lysates and the whole-cell homogenates (following addition of SDS-based lysis buffer to final concentrations of 112.5 mM Tris-Cl, pH 7.5, 4% SDS, 10 mM β-glycerophosphate, 10 mM NaF, 10 mM sodium pyrophosphate, 1 mM Na_3VO_4, 1 μg/ml leupeptin, 1 μg/ml pepstatin, and 1 μg/ml chymostatin).

Kinase Assays—Kinase assays were performed as described previously (7). All signaling measurements were normalized to total protein concentration in each lysate. For kinase assays, we also corrected for variations in ATP specific activity; all measurements are expressed in relative units of kinase activity. Relative units were calculated by comparing the day-specific ratio of t = 0 min (untreated) kinase activity/background activity to a compendium-wide average. The data were normalized so that one relative unit corresponded to the compendium-averaged t = 0 min activity for the kinase.

Antibody Microarray—Antibody microarrays were processed as described previously (24). For EGFR, the same antibodies were used (24), for Akt array measurements anti-Akt (Upstate Biotechnologies) was used as a capture antibody, and anti-phospho-Akt and anti-pan-specific Akt (catalog numbers 4051 and 9272, Cell Signaling Technologies) were used as detection antibodies. We obtained three measurements for EGFR and Akt, phosphoprotein levels, total protein level, and phosphorylated to total protein ratio, from triplicate spots for each lysate. The ratiometric measurement was used to account for spot-to-spot variation in printing. All three measures were normalized to total protein concentration and to the t = 0 min average for each time course and are therefore expressed as -fold activation over the base-line signals.

Immunoblots—For immunoblots, 75 μg of total cell homogenates were separated by SDS-PAGE and transferred to nitrocellulose. Reference samples of HT-29 cells treated with 200 units/ml interferon-γ for 24 h and then 500 ng/ml insulin for 30 min or 100 ng/ml TNF for 40 h were run on each gel for normalization purposes. Membranes were cut at specific molecular weights to allow probing with several antibodies for each gel. Immunoprobing was performed as described previously (25). Primary antibodies used were anti-phospho-Akt-Ser^{473} (catalog number 9271), anti-caspase-8 1C12 (catalog number 9746), anti-phospho-FKHR-Ser^{256} (catalog number 9461), anti-phospho-IRS-Ser^{636} (catalog number 2388), and anti-phospho-MEK1/2-Ser$^{217/221}$ (catalog number 9121) from Cell Signaling Technologies; anti-phospho-IRS1-Tyr^{896} (catalog number GF1003) from Calbiochem; and anti-caspase-3 (1:250, catalog number SC-7272) from Santa Cruz Biotechnologies. The fluorescence was assessed using a FluorImager 495 scanner (Amersham Biosciences) and quantitated using ImageQuant (Amersham Biosciences). Signal intensities were normalized to intensities in the reference samples to correct for differences in transfer and probing efficiencies. Signals where the t = 0 min average was consistently above background level were normalized to this basal level for each time course and expressed in -fold activation units.

Flow Cytometry—Cells were grown in 24-well plates and treated with the indicated cytokines as described above. For each experiment, triplicate reference samples (untreated, treated with 100 ng/ml TNF, and treated with 100 ng/ml TNF + the prosurvival factor used in that experiment) were collected for normalization purposes and to verify the bioactivity of the cytokines. The supernatant and rinse were saved and combined with the trypsinized cells to assay both floating and adherent cells. Live cells were stained with Alexa 488-labeled annexin V and 1 μg/ml propidium iodide (Molecular Probes). Fixed cells (4% formaldehyde for 10 min followed by 100% methanol) were stained with 50 μg/ml propidium iodide (for sub-G_1 DNA content) or with M30 monoclonal antibody against cleaved cytokeratin (Roche Applied Science) and anti-cleaved caspase-3 (Cell Signaling Technologies, BD Biosciences) followed by Alexa 488-conjugated donkey anti-mouse IgG and Alexa 647-conjugated donkey anti-rabbit IgG (Molecular Probes). Samples were analyzed on a BD Biosciences FACSCalibur or FACScan. Apoptosis measurements were normalized to average values found in contemporaneously treated and processed reference samples to account for variations in staining efficiency: 100 ng/ml TNF-treated reference samples were used for propidium iodide permeability and cleaved caspase-3 and cytokeratin staining assays, and untreated reference samples were used for annexin V binding and sub-G_1 DNA content assays.

Partial Least Squares Model—The descriptors of signaling dynamics and partial least squares models were generated using MATLAB® and SIMCA-P, respectively, as described elsewhere.[3] The fitness of values predicted by the model to the measured values for cell death was evaluated according to the equation,

$$R^2 = 1 - \left[\frac{\sum_{i=1}^{n} (\text{Predicted}_i - \text{Measured}_i)^2}{\sum_{i-1}^{n} (\text{Predicted}_i)^2 - \frac{\left(\sum_{i=1}^{n} \text{Predicted}_i \right)^2}{n}} \right] \quad \text{(Eq. 1)}$$

where n is the number of response measurements. The non-parametric 90% confidence intervals on the fitness to measured values were evaluated, based on the Fisher inversion, on the average R^2 value for seven models from cross-validation,

$$x = \frac{(e^{2y} - 1)}{(e^{2y} + 1)} \text{ where } y = \frac{1}{2}\left[\frac{(1 + R^2)}{(1 - R^2)}\right] \pm \frac{1.645}{\sqrt{n - 3}} \quad \text{(Eq. 2)}$$

The variable importance in the projection (VIP) was calculated using

$$\text{VIP}_k = \sqrt{\frac{k \sum_{a=1}^{A} w_{ak} \text{SS}_a}{\sum_{a\ 1}^{A} \text{SS}_a}} \quad \text{(Eq. 3)}$$

where k is the number of variables, w_{ak} is the weight of the kth variable for principal component a, A is the total number of principal components, and SS_a is the sum of squares explained by principal component a.

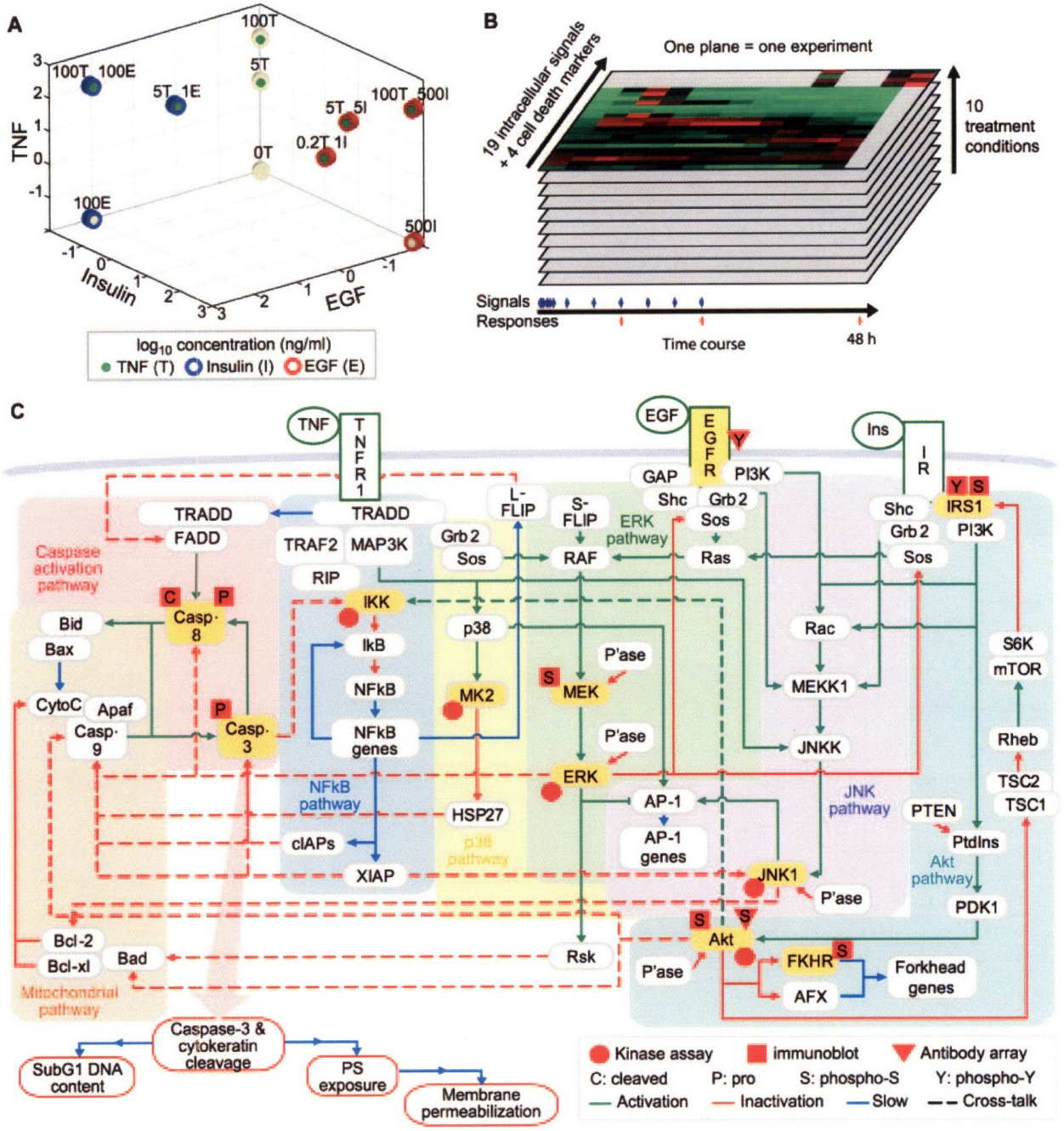
A
100T
100T 100E
5T
5T 1E
100T 500I
5T 5I
0.2T 1I
0T
100E
500I
TNF
Insulin
EGF
log10 concentration (ng/ml)
TNF (T) Insulin (I) EGF (E)
B
One plane = one experiment
19 intracellular signals + 4 cell death markers
10 treatment conditions
Signals
Responses
Time course
48 h
C
TNF
TNFR1
EGF
EGFR
Ins
IR
TRADD
FADD
Caspase activation pathway
Casp-8
Bid
Bax
CytoC
Apaf
Casp-9
Casp-3
TRAF2
MAP3K
RIP
IKK
IkB
NFkB
NFkB genes
NFkB pathway
cIAPs
XIAP
L-FLIP
S-FLIP
GAP
Shc
Grb2
Sos
RAF
ERK pathway
p38
MK2
HSP27
p38 pathway
P'ase
MEK
ERK
AP-1
AP-1 genes
PI3K
Ras
Rac
MEKK1
JNKK
JNK1
JNK pathway
PTEN
PtdIns
Akt pathway
PDK1
Akt
FKHR
AFX
Forkhead genes
Rsk
IRS1
S6K
mTOR
Rheb
TSC2
TSC1
Bcl-2
Bcl-xl
Bad
Mitochondrial pathway
Caspase-3 & cytokeratin cleavage
SubG1 DNA content
PS exposure
Membrane permeabilization
Kinase assay
immunoblot
Antibody array
C: cleaved
P: pro
S: phospho-S
Y: phospho-Y
Activation
Inactivation
Slow
Cross-talk
Signaling dynamics in cells treated with 100 ng/ml TNF + 500 ng/ml Insulin
D
ERK (KA)
E
pAkt (IB)
F
Cleaved caspase-8 (IB)
Relative activity
Time (h)

To mimic measurement error, random noise was added to the signaling measurements in the 5 ng/ml TNF + 1 ng/ml EGF treatment from a normal distribution centered at zero with a standard deviation of 0.1, 0.2, 0.3, 0.4, or 0.5 times the range of values for the time course in that signal. Time course descriptors were then extracted as described elsewhere.[3]

RESULTS

Data Generation

To explore systematically the relationships between cytokine-receptor interaction, activation of intracellular signaling cascades, and apoptosis-survival cell fate decisions, HT-29 human colon adenocarcinoma cells were exposed to a set of 10 cytokine treatments and monitored over a 48-h period. Each treatment consisted of a combination of TNF and either EGF or insulin (Fig. 1*A*). HT-29 cells respond to TNF, EGF, and insulin in a dose-dependent manner (26, 27),[2] and all three cytokines were therefore examined at subsaturating concentrations designed to mimic physiological conditions and at saturating concentrations at which essentially all receptors were ligand-bound. At 13 time points after cytokine addition, three replicate dishes of cells (six for the zero time point) were harvested to measure kinase activities, changes in protein phosphorylation, caspase cleavage, and changes in protein abundance. Altogether, 19 protein distinct signals were examined (Fig. 1*C* and Table I). Five kinases, ERK (28), Akt (29), JNK1 (28), IKK (16), and mitogen-activated protein kinase-activated protein kinase 2 (MK2) (30), were assayed *in vitro* using microtiter-based immunocomplex kinase activity assays (7). Five phosphorylation sites on four proteins and cleavage of caspase-3 and -8 were measured by quantitative immunoblotting. Phospho-, total, and phospho-to-total (pt) measures of EGFR and Akt were obtained by using antibody arrays (24). Because kinases such as Akt and ERK were maximally active 5–15 min after cytokine addition (Fig. 1, *D* and *E*), whereas caspase cleavage was evident only after 4 h (Fig. 1*F*), time points were spaced closely from 0–2 h (0, 5, 15, 30, 60, 90, and 120 min) and then more sparsely from 4–24 h (4, 8, 12, 16, 20, and 24 h) where $t = 0$ min is the time of cytokine addition. Nonuniform sampling made it possible to measure both early and late signals effectively (Fig. 1*B*).

To characterize the responses of cells to cytokine combinations, four measures of apoptosis were performed on triplicate plates 12, 24, and 48 h after stimulation (Fig. 1*B*). These four measures represent distinct stages or aspects of programmed cell death (Fig. 1*C*). Both adherent (viable) and floating (dying) cells were examined in all cases. In TNF-treated cells, procaspase-8, an initiator caspase, is activated by cleavage and then cleaves and activates the executioner caspase, caspase-3, leading to the degradation of a wide variety of essential proteins. The cleavage of procaspase-3 and -8 measured by immunoblots constituted signals in our dataset, whereas downstream events, measured by flow cytometry, were considered to be responses. The cleavage of caspase-3 and of its target, cytokeratin, was measured using cleavage-specific antibodies (Table I, response R1). DNA digestion by endonucleases and subsequent nuclear fragmentation were quantified by propidium iodide staining to detect cells with sub-G_1 DNA content (R2). Loss of plasma membrane asymmetry was assayed by the binding of annexin V to exposed phosphatidylserine, a phospholipid normally restricted to the inner membrane leaflet (R3). Finally, the complete loss of plasma membrane integrity was assayed using a vital stain (R4). Most of the apoptotic response measures are end points that increase steadily over time. However, phosphatidylserine exposure (R3) represents a transient state fairly early in apoptosis in which membrane structure is partially but not yet completely disrupted. The final product of the signal and response measurements was a set of 10 time courses, each describing the activities of 19 protein signals measured at 13 time points and four response measures at three time points, all in triplicate biological samples. The total number of measurements in this initial dataset was 8,340, collected over a period of 18 months by four scientists working in collaboration.

FIG. 1. **Design of a self-consistent compendium of TNF-, EGF-, and insulin-induced signals and responses in HT-29 cells.** *A*, three-dimensional representation of the 10 treatments used to generate the data compendium. TNF (*T*), EGF (*E*), and insulin (*I*) were used alone or in combination. *B*, data collection in single treatment planes. Each *plane* represents one contemporaneous set of measurements for 19 signals and four death markers on cells treated with a single cytokine combination. Signals were measured at 0, 5, 15, 30, 60, and 90 min and 2, 4, 8, 12, 16, 20, and 24 h. Cell death markers were assayed at 12, 24, and 48 h. *C*, schematic representation of the signaling network induced by TNF, EGF, and insulin. *Arrows* indicate the type of interaction: activation (*green*), inhibition (*red*), slow process (*blue*), or pathway cross-talk (*dashed*). The measured proteins are highlighted in *yellow*; *red circles*, *triangles*, and *rectangles* indicate kinase assay, antibody array, and immunoblot measurements, respectively. *D–F*, protein signals exhibit dramatically different dynamics of activation. Shown are time courses of ERK activity (*D*), immunoblot-measured phospho-Akt levels (*E*), and cleaved caspase-8 levels (*F*) in cells co-treated with 100 ng/ml TNF and 500 ng/ml insulin. Values are means of biological triplicate samples, and *error bars* show the S.E. *IB*, immunoblot; *KA*, kinase assay; *PS*, phosphatidylserine; *NFkB*, nuclear factor κB; *CytoC*, cytochrome *c*; *FADD*, Fas-associated death domain; *TRADD*, tumor necrosis factor receptor-associated death domain protein; *MAP3K*, mitogen-activated protein kinase kinase kinase; *XIAP*, X-linked inhibitor of apoptosis protein; *cIAP*, cellular inhibitor of apoptosis protein; *HSP*, heat shock protein; *RIP*, receptor-interacting protein; *PI3K*, phosphatidylinositol 3-kinase; *P'ase*, phosphatase; *GAP*, GTPase-activating protein; *FLIP*, FADD-like interleukin-1-converting enzyme (FLICE)-inhibitory protein; *MEKK1*, MEK kinase 1; *mTOR*, mammalian target of rapamycin; *Grb2*, growth factor receptor-bound 2; *JNKK*, JNK kinase; *Ins*, insulin; *PtdIns*, phosphatidylinositol; *pAkt*, phospho-Akt; *Casp.*, caspase; *TNFR1*, tumor necrosis factor receptor 1; *PDK1*, 3-phosphoinositide-dependent protein kinase 1; *S6K*, S6 kinase; *AP-1*, activator protein-1; *PTEN*, phosphatase and tensin homolog; *TRAF2*, tumor necrosis factor receptor-associated factor 2; *TSC*, tuberous sclerosis complex; *AFX*, ALL1 fused gene from chromosome X.

TABLE I

Measured protein signals and apoptosis markers

MAPK, mitogen-activated protein kinase; pAkt, phospho-Akt; tAkt, total Akt; ProC3, procaspase-3; ProC8, procaspase-8; ClvC8, cleaved caspase-8; AA, antibody array; IB, immunoblot; pEGFR, phospho-EGFR; tEGFR, total EGFR; pMEK, phospho-MEK; PI, propidium iodide; Ab, antibody; PKB, protein kinase B.

No.	Assay	Protein	Name	Function	Marker	Abbreviation
1	Kinase assay	Akt	Akt/PKB	Ser-Thr kinase	Activity	Akt[a]
2		ERK	Extracellular signal-regulated kinase	Ser-Thr kinase	Activity	ERK
3		IKK	Inhibitor of nuclear factor-κB kinase	Ser kinase	Activity	IKK
4		JNK1	c-Jun N-terminal kinase 1	Ser-Thr kinase	Activity	JNK1
5		MK2	MAPK-associated protein kinase 2	Ser-Thr kinase	Activity	MK2
6	Immunoblot	Akt	Akt/PKB	Ser-Thr kinase	Phospho-Ser^{473}	pAkt (IB)[a]
7		Casp.3	Caspase-3	Cysteine protease	Zymogen level	ProC3
8		Casp.8	Caspase-8	Cysteine protease	Zymogen level	ProC8
9					Cleaved level	ClvC8
10		FKHR	Forkhead	Transcription factor	Phospho-Ser^{256}	pFKHR
11		IRS1	Insulin receptor substrate 1	Adaptor-scaffold	Phospho-Ser^{636}	pIRS1-Ser^{636}
12					Phospho-Tyr^{896}	pIRS1-Tyr^{896}
13		MEK1/2	MAPK and ERK kinase	Dual specificity kinase	Phospho-$Ser^{217/221}$	pMEK
14	Ab array	Akt	Akt/PKB	Ser-Thr kinase	Phospho-Ser^{473}	pAkt (AA)
15					Total level	tAkt
16					Phospho/total ratio	ptAkt[a]
17		EGFR	Epidermal growth factor receptor	Receptor Tyr kinase	Phospho-Tyr^{1068}	pEGFR
18					Total level	tEGFR
19					Phospho/total ratio	ptEGFR
R1	Flow cytometry		Cleaved caspase-3 and cytokeratin	Cell rounding	Cleaved levels	CC3/CCK
R2			Sub-G_1 DNA content	Nuclear fragmentation	Low PI staining	Sub-G_1
R3			Phosphatidylserine exposure	Recognition by macrophages	Annexin V binding	PS exposure
R4			Membrane permeabilization	Secondary necrosis	PI permeability	Memb. perm.

[a] Signals used to validate measurements across assays.

Creation of a Cytokine-Signal-Response Data Compendium by Data Normalization, Fusion, and Validation

Our overall aim was to merge time course data collected at different times into a single self-consistent compendium. This involved a variety of experimental and data analysis techniques, some of which were obvious, whereas others were more subtle. One obvious step was to limit day-to-day and sample-to-sample variation by standardizing assay protocols, limiting cells to a narrow range of passage number, and ensuring uniformity in cell culture and treatment conditions through the use of lot-controlled sera, cytokines, and antibodies (supplemental material, Table S1). Raw data were corrected for other sources of variation by signal-specific normalization. As described in greater detail under "Experimental Procedures," normalization included the following: 1) correcting each signaling measurement for the total amount of cellular protein in the sample, 2) adjusting kinase activity measurements for changes in the specific activity of [γ-^{32}P]ATP, and 3) comparing immunoblot signals to contemporaneous positive controls to correct for variations in transfer efficiency and antibody binding. Signals with $t = 0$ min normalized averages that were consistently above background were divided by the $t = 0$ min average for that treatment to yield a measure of "-fold activation." Other signals were expressed in activity units referenced to a base line of zero. Apoptosis measurements were compared with contemporaneous positive and negative control cell populations to yield a normalized cell death fraction. We found that careful normalization was essential for data fusion: by minimizing the contributions of experimental variability on signal measurements, it was possible to reduce the median coefficient of variation among biological replicates to ~11%.

As one means to judge how reliably data from different assays had been fused in the CSR compendium, we examined correlations among three measures of Akt protein kinase activation. Immunoblots and antibody microarrays were used to monitor the levels of phospho-Ser^{473}, a modification that is associated with Akt activation (31, 32) (Table I and Fig. 2*A*). An *in vitro* immunocomplex kinase assay was used to monitor Akt-catalyzed phosphorylation of a sequence-optimized peptide substrate (Table I and Fig. 2*A*). After normalization, we found that all three measures of Akt were correlated across the full panel of cytokine combinations with pairwise Pearson coefficients of 0.80–0.87 (Fig. 2, *B–D*). Although experimental error may be partly responsible for the discrepancies among these measures, the biochemistry of Akt was also an important factor. Akt activation is known to involve two phosphorylation events: Ser^{473} modification by rictor-mTOR (mammalian target of rapamycin) (33) and modification of Thr^{308} by 3-phosphoinositide-dependent protein kinase 1 (34). Although fully activated only when doubly phosphorylated, Akt

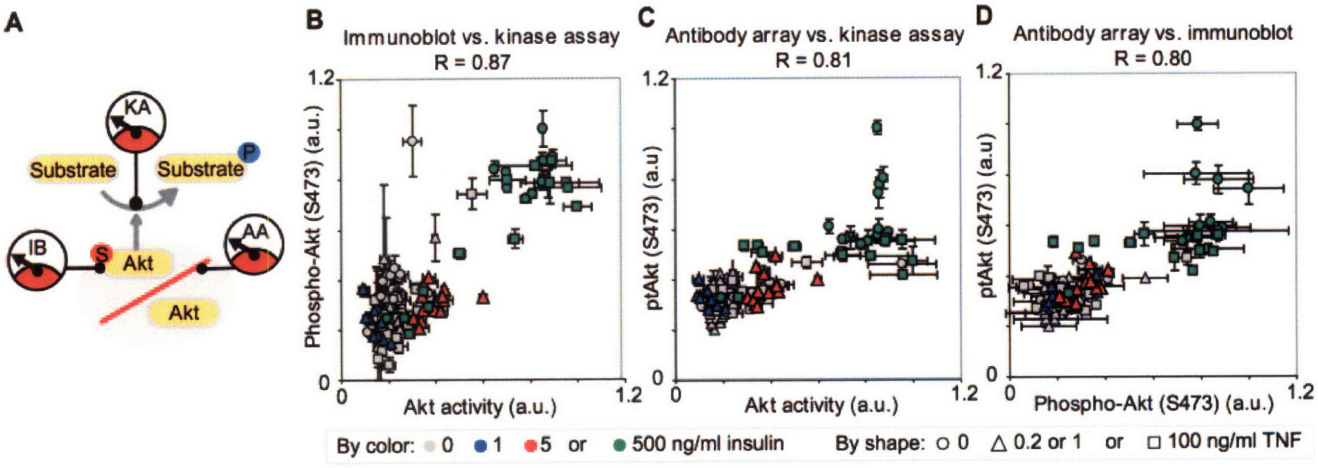

FIG. 2. **Heterogeneous Akt measurements are quantitatively comparable in the fused compendium.** *A*, schematic showing three measures of Akt activation: kinase activity assays (*KA*), phospho-Ser^{473} levels by immunoblot (*IB*), and ratio of phospho-Ser^{473} to total levels by antibody array (*AA*). *B–D*, scatter plots of pairwise comparisons of heterogeneous Akt activation measurements: immunoblot phospho-Akt-Ser^{473} assay compared with kinase activity (*B*), ptAkt ratio from antibody arrays compared with kinase activity (*C*), and immunoblot phospho-Akt-Ser^{473} assay compared with ptAkt ratio from antibody array (*D*). Pearson correlation coefficients are indicated above each plot (*R*). The ptAkt measurements by antibody microarray are the most distant because they are an aggregate measure of phospho-to-total levels of Akt. Values in *B–D* are means ± S.E. of biological triplicate samples normalized to the maximal value in the compendium for that signal. *a.u.*, arbitrary units.

is at least partially active with only one modification (35, 36). We might therefore expect to see situations in which Akt activity was relatively high but Ser^{473} phosphorylation was low; this is exactly what was observed in cells treated with saturating TNF + insulin at t = 2–12 h (Fig. 4*A*). Other discrepancies in measures of Akt activation could similarly be explained by current understanding of its regulation. In summary, the strong correlation among three different measures of Akt kinase activity argues that data from different biochemical assays can be fused into one compendium. It is important to note, however, that correlations among different measures of protein function are critically dependent on understanding the mechanisms of signal activation and inhibition.

Signals and responses were acquired as time course experiments, one cytokine combination at a time over a period of 18 months. To enable direct comparison of data collected non-contemporaneously, it was essential that the CSR compendium be self-consistent. Reproducibility over time is the most obvious criterion for self-consistency. To address the issue of reproducibility, we generated a validation dataset by using an experimental scheme orthogonal to that of the primary dataset. The validation data consisted of the 19 protein signals measured in triplicate at a single time point (t = 15 min) following exposure to eight different cytokine treatments; this corresponds to a single-time slice through the CSR data space (Fig. 3*A*). Apoptotic responses were also assayed at 12, 24, and 48 h in this experiment. We observed good correlations between values in the validation dataset and the initial CSR compendium: most signals and responses had correlation coefficients of 0.9 or higher. However, a subset of signals were poorly correlated. We noticed that these signals did not vary substantially from one treatment to the next, and thus the Pearson correlation coefficient was dominated by experimental noise. To distinguish high and low variance signals, we calculated their "dynamic range" by taking the variation in a signal (measured across treatments) and dividing by the measurement noise (from triplicate biological samples; see Fig. 3 legend for details). A signal such as phospho-Ser^{473} Akt (measured by immunoblotting) had a high dynamic range (7.5) at t = 15 min and was characterized by a high correlation between the single treatment and single time experiments (R = 0.98; Fig. 3*B*). IKK varied little among treatments (dynamic range, 1.5), and the correlation between compendium and validation data was low, although the absence of observable differences between the two datasets emphasizes that the issue was primarily one of noise and not inconsistency (Fig. 3*C*). Overall the great majority of signals and responses had a dynamic range above 2.5 and were well correlated between the compendium and the validating single time dataset (median Pearson coefficient of 0.95 for responses and 0.91 for signals; Fig. 3*D*). Monte Carlo simulations indicated that a Pearson coefficient of 0.9 corresponds to a ~14% coefficient of variation between measurements. This is only slightly larger than the 11% median coefficient of variation observed among biological replicates assayed at the same time, suggesting that day-to-day variation in compendium data was similar in magnitude to biological variation and measurement noise. We conclude that our experimental methods and data fusion techniques had therefore generated a self-consistent compendium in which data collected at different times could be compared with confidence.

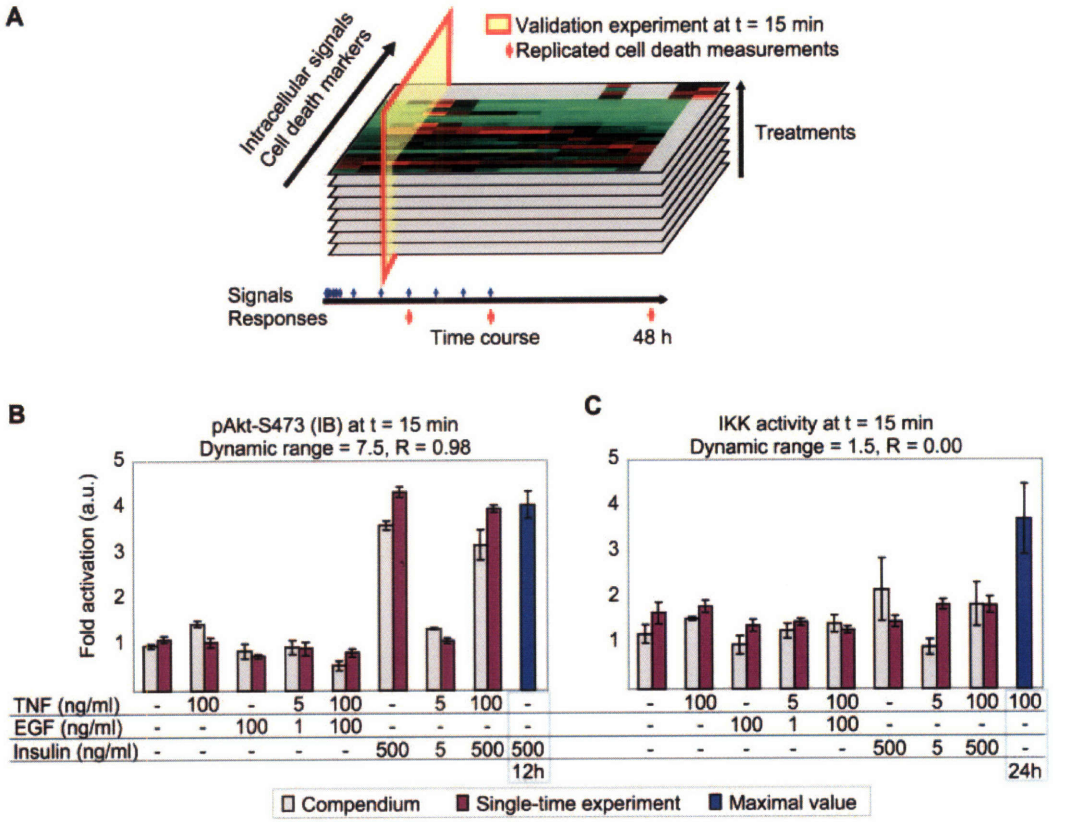
A
Validation experiment at t = 15 min
Replicated cell death measurements
Intracellular signals
Cell death markers
Treatments
Signals
Responses
Time course
48 h
B
pAkt-S473 (IB) at t = 15 min
Dynamic range = 7.5, R = 0.98
Fold activation (a.u.)
C
IKK activity at t = 15 min
Dynamic range = 1.5, R = 0.00
TNF (ng/ml)
EGF (ng/ml)
Insulin (ng/ml)
12h
24h
Compendium
Single-time experiment
Maximal value
D
From compendium
From single-time experiment
Signal values, normalized to max
Dynamic range
Pearson coefficient
JNK1 (KA) 57.7 0.95
MK2 (KA) 27.0 0.94
CC3/CCK (48h) 15.2 0.98
Memb. perm. (48h) 13.2 0.96
pIRS1-636 (IB) 10.9 0.73
ERK (KA) 10.8 0.85
Memb. perm. (24h) 8.6 0.96
CC3/CCK (24h) 8.3 0.98
pMEK (IB) 7.6 0.68
pAkt (IB) 7.5 0.98
CC3/CCK (12h) 7.4 0.97
PS exposure (12h) 7.0 0.95
Akt (KA) 6.2 0.92
pFKHR (IB) 5.3 0.40
SubG1 DNA (24h) 5.0 0.93
ptAkt (AA) 4.9 0.91
pIRS1-896 (IB) 4.9 0.98
Memb. perm. (12h) 4.8 0.79
SubG1 DNA (12h) 4.3 0.93
PS exposure (24h) 3.5 0.90
SubG1 DNA (48h) 2.5 N.A.
ptEGFR (AA) 2.4 N.A.
IKK (KA) 1.5 N.A.
ClvC8 (IB) 1.5 N.A.
PS exposure (48h) 1.1 N.A.
1-ProC3 (IB) 0.7 N.A.

Key Features of the Signaling Compendium Identified by Cytokine-Signal Covariates

To visualize the entire CSR compendium in a compact form, a heat map was constructed (Fig. 4, *A* and *B*). The error analysis described above (Fig. 3*D*) suggested that quantitative differences larger than ~30% between observed signals or responses were likely to be biologically significant. Most variation in the compendium was much larger than this, ranging from 3-fold changes in ptEGFR to over 50-fold changes in JNK and MK2 activity. Many of the patterns that could be discerned from the heat map were expected (*e.g.* EGF and insulin significantly inhibited TNF-induced caspase-8 cleavage at t = 8–24 h; $p < 10^{-4}$; Fig. 4*A*), but several were unanticipated (see supplemental material, Figs. S1–S4). In these cases the primary value of the CSR compendium was its ability to put each measured signal within the broader biological context of other signals, treatments, and time points.

In addition to visual inspection, the quality of the CSR data enabled us to examine quantitative correlations between cytokines and signals. We applied a previously described statistical mapping technique based on eigenvalue decomposition and rotation (25).[2] Briefly each protein signal in the compendium was integrated over its 24-h time course and then projected onto a set of classifiers describing the TNF and EGF or insulin treatment (see Ref. 25 for details). This projection generated a map in which the positions of 19 protein signals were plotted relative to the TNF, EGF, and insulin stimuli. The closer a protein signal is to a cytokine, the more strongly and specifically the signal is activated by that cytokine. For example, TNF strongly induces caspase-8 cleavage and JNK1 and MK2 activation (14, 15), and these signals were closest to TNF on the cytokine-signal map (Table II). Of particular interest were unanticipated map positions. We illustrate this point with two examples: one in which an unexpectedly close correlation was observed between EGF and pIRS1-Tyr^{896} and a second in which a lack of correlation was observed between the Akt kinase and its substrate, pFKHR.

IRS1-Tyr^{896} as a Candidate EGFR Phosphorylation Site—The signal that mapped closest to EGF was not a measure of EGF receptor activation but IRS1 phosphorylation at Tyr^{896} (Table II). IRS1 is a key adaptor protein associated with insulin signaling and is known to contain at least 12 functionally important phosphorylation sites (37, 38). IRS1 tyrosine phosphorylation, on sites such as Tyr^{612}, Tyr^{941}, and Tyr^{989}, is strongly induced by insulin and insulin-like growth factor receptor tyrosine kinases (37, 39). Whereas IRS1 tyrosine phosphorylation stimulates downstream signaling, serine phosphorylation is inhibitory (40, 41). The kinase that mediates IRS1-Tyr^{896} phosphorylation has not been identified, but the modification is known to create an Src homology 2 binding site for Grb2 (growth factor receptor-bound 2) and thus to serve as a positive regulator of signaling (39, 42) (Fig. 1*C*).

In agreement with results from the cytokine-signal map, strong IRS1-Tyr^{896} phosphorylation was observed in time courses of EGF-treated cells, but the modification was undetectable in the presence of insulin or TNF alone (Fig. 4, *A* and *C*). EGF-induced IRS1 modification was not unique to HT-29 cells: EGFR-dependent IRS1-Tyr^{896} phosphorylation was also observed in A431 epidermoid carcinoma cells.[4] EGF has previously been reported to promote tyrosine phosphorylation of IRS1, but specific sites of phosphorylation have not been identified (43–45). To search for candidate IRS1-Tyr^{896} kinases, we used the Scansite motif-based searching algorithm (46), which compares Swiss-Prot protein sequences to experimentally determined consensus sites for dozens of protein kinases. Strikingly the amino acid sequence surrounding IRS1-Tyr^{896} (EPKSPGEYVNIEFGS) conformed well to the EY(F/V/I) consensus site for the EGFR tyrosine kinase (47, 48) and ranked in the top 0.113% of potential EGFR substrates overall (Table III). This score is considerably better than the 0.2% cutoff recommended to avoid false positives with Scansite (49). Moreover only one known EGFR autophosphorylation site scored better than IRS1-Tyr^{896} (EGFR-Tyr^{1197} at 0.041%); conversely other well characterized EGFR sites had poorer scores than IRS1-Tyr^{896} (Table III). Several sequences within IRS1 were correctly identified as substrates for the insulin receptor (IR), but IRS1-Tyr^{896} scored only within the

[4] S. Gaudet and P. K. Sorger, unpublished observations.

FIG. 3. **An orthogonal single-time, multitreatment experiment validates that the compendium is fused properly.** *A*, schematic of the orthogonal validation experiment. Signals were measured contemporaneously in a series of eight representative treatments. All signaling measurements were made at a single time point 15 min after cytokine addition (*red vertical plane*). Cell death marker measurements were repeated in these eight conditions at 12, 24, and 48 h. *B* and *C*, bar graphs comparing immunoblot phospho-Ser^{473} Akt levels (*B*) or IKK activity (*C*) from the compendium (*gray*) with those obtained in the single time validation experiment (*red*) and with the maximal value in the full compendium (*blue*, treatment and time as indicated). Measurements are plotted as the mean of three biological replicates ± S.E. The dynamic range and Pearson correlation coefficient (*R*) are shown. The dynamic range was calculated as the ratio of the square root of the variance in the mean values across all treatments by the average standard deviation of replicate measures. *D*, heat map comparison of the average values from the compendium (*left*) and the single-time validation experiment (*right*). The average values from biological triplicates were normalized to the maximal value in the compendium for that assay (0, *green*; 0.5, *black*; 1, *red*). Protein signals were measured 15 min after cytokine addition, and the responses were measured at 12, 24, or 48 h as indicated. The signals and responses were ranked by dynamic range, and when applicable, the Pearson correlation coefficient between two datasets is listed. *KA*, kinase assay; *IB*, immunoblot; *AA*, antibody array; *Memb. perm.*, membrane permeability; *pMEK*, phospho-MEK; *PS*, phosphatidylserine; *ClvC8*, cleaved caspase-8; *pAkt*, phospho-Akt; *CC3/CCK*, cleaved caspase-3/cleaved cytokeratin; ProC3, procaspase-3; *a.u.*, arbitrary units.

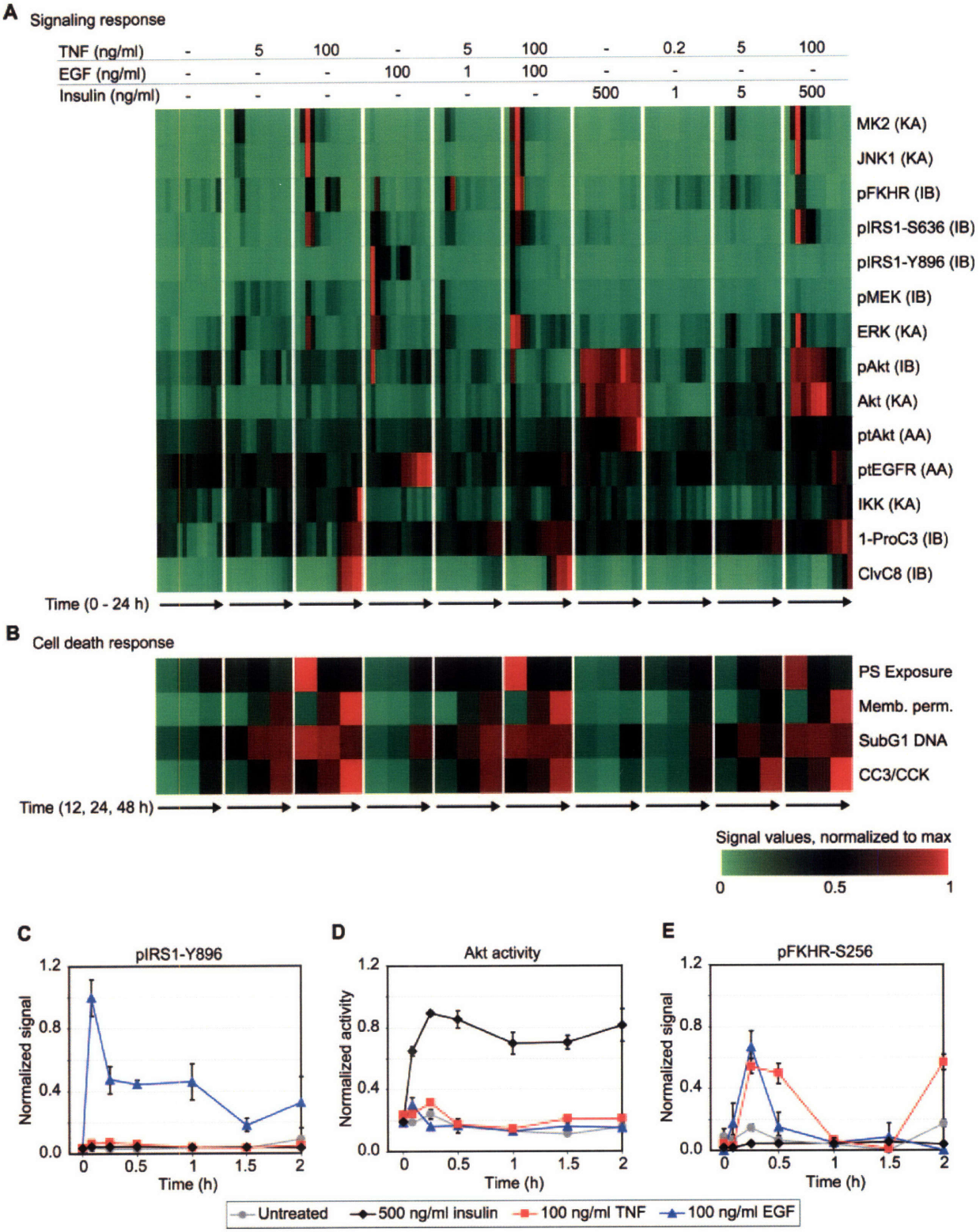

FIG. 4. **Compendium of signaling and cell death measurements in TNF-, EGF-, and insulin-treated HT-29 cells.** *A*, heat map of time-dependent signals in cells treated with 10 cytokine combinations. For each treatment, the average signal intensities were normalized to the maximal value obtained for that signal (0, *green*; 0.5, *black*; 1, *red*) and are plotted for the 13 time points. The signals were measured by kinase assay (*KA*), immunoblot (*IB*), or antibody microarray (*AA*). *B*, heat map of cell death responses for the 10 treatments. The average values from triplicate samples were normalized to the maximal value for that assay and are plotted for 12, 24, and 48 h of treatment (0, *green*; 0.5,

TABLE II
Top cytokine-signal covariates

Cytokine	Protein signal[a]	Map distance[b]	Pearson correlation[c]
TNF	ClvC8	0.18	0.83
	JNK1	0.24	0.75
	MK2	0.37	0.88
EGF	pIRS1-Tyr^{896}	0.20	0.69
	ptEGFR	0.39	0.63
	pIRS1-Ser^{636}	0.41	0.59
Insulin	Akt	0.21	0.95
	Akt (1B)	0.31	0.83
	ptAkt	0.44	0.88
	pFKHR	0.68	−0.39

[a] Proteins are abbreviated as described in Table I and ranked according to map distance.

[b] Euclidean cytokine-signal distances on the mapping described in Footnote 2. Distances were normalized to the farthest protein signal for each cytokine.

[c] Calculated between a scaled cytokine classifier (Footnote 2) and the integrated signal for each treatment.

TABLE III
EGFR and IRS1 phosphorylation sites for EGFR and insulin receptor tyrosine kinases

Protein[a]	Site	Substrate sequence	Tyrosine kinase score[b]	
			EGFR	Insulin receptor
IRS1	Tyr^{896}	EPKSPGEYVNIEFGS	0.113	2.820
	Tyr^{612}	TLHTDDGYMPMSPGV	N.S.[c]	0.056
	Tyr^{632}	GRKGSGDYMPMSPKS	2.574	0.002
	Tyr^{662}	QRVDPNGYMMMSPSG	2.507	0.021
	Tyr^{941}	EETGTEEYMKMDLGP	2.820	0.001
	Tyr^{989}	VPSSRGDYMTMQMSC	N.S.	0.050
EGFR	Tyr^{1016}	DVVDADEYLIPQQGF	1.543	N.S.
	Tyr^{1092}	TFLPVPEYINQSVPK	0.691	N.S.
	Tyr^{1110}	GSVQNPVYHNQPLNP	0.975	N.S.
	Tyr^{1172}	ISLDNPDYQQDFFPK	0.206	N.S.
	Tyr^{1197}	STAENAEYLRVAPQS	0.041	N.S.

[a] Proteins are abbreviated as described in Table I.

[b] Ranked percentile as EGFR and insulin receptor tyrosine kinase substrate motifs as scored by Scansite (46).

[c] N.S., not scored (too poor a substrate).

top 2.82% of sequences for IR tyrosine kinase (Table III and Ref. 39). IRS1-Tyr^{896} lacks a methionine in the +1 position that is important for IR-dependent modification (48) and is therefore less likely to be an *in vivo* IR kinase substrate. Intriguingly, IRS1-Tyr^{896} also scored highly as a potential substrate for the fibroblast growth factor receptor and platelet-derived growth factor receptor tyrosine kinases (data not shown). This raises the possibility that IRS1 functions downstream of EGFR and other growth factor receptors. Directed experiments *in vivo* and *in vitro* will be required to test this hypothesis and unravel the role played by IRS1 in cross-talk between EGFR, fibroblast growth factor receptor, platelet-derived growth factor receptor, and insulin receptors.

FKHR Phosphorylation Does Not Correlate with Akt Activation—The closest signals to insulin on the cytokine-signal map were the three measures of Akt activation (Table II) (50). One might expect that Akt substrates, like FKHR (51, 52) would also map closely to insulin. However, pFKHR-Ser^{256} was closer to TNF and EGF (map distances of 0.50 for TNF and 0.58 for EGF *versus* 0.68 for insulin), and there was no positive correlation with insulin treatment (Table II). When the dynamics of Akt activation and FKHR-Ser^{256} phosphorylation were examined, we found that EGF induced a sharp, transient Akt signal at t = 5 min, consistent with previous studies in myocytes (53), and an overlapping peak in pFKHR-Ser^{256} levels (Fig. 4, *A*, *D*, and *E*). TNF treatment also caused transient (but weaker and delayed) Akt activation, probably as a result of a TNF-inducible TGF-α autocrine loop,[2] and a transient pFKHR-Ser^{256} peak (Fig. 4, *A*, *D*, and *E*). In contrast, Akt was strongly induced in a sustained fashion by insulin, but no significant increase in pFKHR-Ser^{256} was observed (Fig. 4, *A*, *D*, and *E*). Thus, within the CSR compendium, Akt activation and FKHR-Ser^{256} phosphorylation are not always correlated ($-0.01 < R < 0.02$ overall with each of the three measures of Akt activation). The absence of a correlation between signals thought to be biochemically coupled is potentially as valuable as a strong correlation because it implies that mechanistic models are incomplete.

One simple explanation for the discordance between Akt activation and pFKHR-Ser^{256} modification is that, in TNF- and EGF-treated cells, FKHR is phosphorylated by a basophilic kinase other than Akt. Indeed two other FKHR phosphorylation sites (Thr^{24} and Thr^{316}), originally identified as Akt phosphoacceptor sites (52, 54), have recently been reported to be Akt-independent in hepatocytes (55). Furthermore the equivalent sites on a closely related transcription factor, FOXO3 (Thr^{32} and Ser^{315}), are not phosphorylated by Akt but rather by serum- and glucocorticoid-inducible kinase (SGK) (56). We therefore hypothesize that TNF- and EGF-induced FKHR-Ser^{256} phosphorylation is mediated by SGK or a similar kinase. It is noteworthy that FOXO3-Thr^{32}, targeted by SGK, ranks even higher than FKHR-Ser^{256} as a substrate motif for Akt (top 0.001% for FOXO3-Thr^{32} *versus* 0.049% for FKHR-Ser^{256} of all Akt substrate motif matches by Scansite) (46), illustrating the overlap between Akt and SGK substrate specificities. Distinguishing the roles of Akt and SGK has been difficult because both lie downstream of phosphatidylinositol

black; 1, *red*). The fractions of cells doubly positive for cleaved caspase-3 and cleaved cytokeratin (*CC3/CCK*) or with phosphatidylserine (*PS*) exposure, membrane permeability (*Memb. Perm.*), or sub-G_1 DNA content were measured by flow cytometry. *C–E*, time courses of pIRS1-Tyr^{896} (*C*), Akt activity (*D*), and pFKHR-Ser^{256} (*E*) in untreated cells (*gray*) or cells treated with 100 ng/ml TNF (*red*), 100 ng/ml EGF (*blue*), or 500 ng/ml insulin (*black*). Values in *C–E* are means ± S.E. of biological triplicate samples normalized to the maximal value in the compendium for that signal. *ClvC8*, cleaved caspase-8; *pAkt*, phospho-Akt; *pMEK*, phospho-MEK; *ProC3*, procaspase-3.

3-kinase and 3-phosphoinositide-dependent protein kinase 1 (34), but the compendium data may have determined conditions under which Akt is uncoupled from FKHR-Ser^{256} modification. Follow-up experiments can now be designed to test the idea that the critical FKHR kinase in TNF- and EGF-treated cells is SGK. Moreover novel mechanistic hypotheses can be derived by examining even well known signaling events within a broad biological context of compendium data.

A Linear Model of TNF-induced Cell Death

To evaluate rigorously our design strategy for the CSR compendium (*e.g.* selection of which signals to measure and time points to sample, assembly of multiple data types, choice of cytokine treatments, and approaches to data processing), we used a data-driven PLSR model. This model, designed to generate predictions of apoptotic responses based on measured intracellular signaling profiles, will be described in detail elsewhere.[3] Briefly, signal measurements were cast as independent (predictor) variables, and apoptotic responses were cast as dependent (predicted) variables. To maximize the information extracted from compendium data, the set of independent variables was expanded to include not only the actual measurements of each of the 19 signals at 13 time points (247 independent variables) but also 22–25 metrics describing the time-dependent dynamics of that signal. These derived metrics included "local descriptors" such as the instantaneous derivative of the signal at each time point, the area under the curve, and the activation and down-regulation rates for each peak in the time course. "Global descriptors" included the total area under the curve over a 24-h period and the global maximum, mean, and steady-state values of the signal. Together the time point measurements and the derived metrics for each signal constituted a set of 660 independent variables.[3] Changes in the independent variables were related to changes in the dependent variables (apoptosis measures) through regression coefficients that the PLSR algorithm calculates for the full range of cytokine treatments in the compendium. Cross-validation showed that the PLSR model could predict the apoptotic responses for any single treatment withheld from the training set with a squared Pearson correlation (R^2) of 0.94. Furthermore this model could predict data not in the training set with $R^2 = 0.91$.[3]

Maximizing Information Content in Models by Unit-Variance Scaling

PLSR models weigh independent and dependent variables with large covariance most heavily (57); this biases the models toward variables with the largest dynamic range. In the compendium, JNK1 activity at $t = 15$ min varied more than 200-fold across all treatments, whereas Akt activity never varied more than 5-fold at any time point. *A priori* it is not obvious that large changes in JNK1 activity are more important than more modest but sustained changes in Akt activity, yet regression-based models emphasize the former. To give all variables an equal likelihood of contributing to the PLSR model, we applied unit-variance scaling, a common preprocessing technique in regression analysis (57). Each variable (JNK1 activity at $t = 15$ min, for example) was divided by the square root of its variance calculated across all cytokine treatments. This maintained the relative variation in the CSR compendium (*e.g.* JNK1 activity at $t = 15$ min was still higher for TNF treatment when compared with insulin treatment), but the dataset was scaled so that all variables had the same "spread" of values. Some time courses were altered quite dramatically by unit-variance scaling. For example, high variance in JNK1 activity at $t = 5$, 15, and 30 min and lower (but potentially informative) variance across treatments at later time points led to a scaled TNF-induced time course in which the second wave of activation was emphasized (Fig. 5*A*). For caspase-8 activation, easily overlooked differences in the extent of cleavage at early times were amplified relative to cleavage at later times (Fig. 5*B*). As a general rule, we found that scaling enhanced the importance of signals at late time points relative to those at early times (Fig. 5*D*). However, a few signals with relatively uniform variance were minimally affected by scaling; raw and scaled phospho-Akt time courses were very similar for example (Fig. 5*C*).

Does unit-variance scaling increase the amount of information extracted from the compendium as measured by the number of independent variables incorporated into the model? To answer this, we constructed PLSR models from either scaled or unscaled data and then evaluated the contribution of each variable (*i.e.* measurements and derived metrics such as maximum, area under the curve, etc.) to the two models by examining the VIP. The VIP is a normalized expression for the magnitude of the regression coefficients for each variable (see Ref. 58 and "Experimental Procedures"). Variables with a high VIP value (VIP > 1) play an important role in the PLSR model, whereas variables with a low VIP value (VIP $\ll 1$) do not. For a model with unscaled variables (the "unscaled" model), only a small number of independent variables had a high VIP with most of the signals contributing negligibly to predictions (Fig. 5*E*). By contrast, a "scaled" model built from unit-variance scaled data incorporated far more signaling variables into the response prediction, and the signals were weighed more equally (Fig. 5*F*). This illustrates that the scaled model drew from data across the CSR compendium, whereas the unscaled model relied entirely on the highest variance signals.

Both scaled and unscaled models predicted cell death responses with good accuracy for single treatments withheld from the training set (squared Pearson correlation of 0.94 with measured values). As a more stringent test of performance, we examined how well the two models predicted death responses under conditions that were different from those used to generate training data. A first set of test data was obtained from cells treated with TNF in the presence of the EGFR-

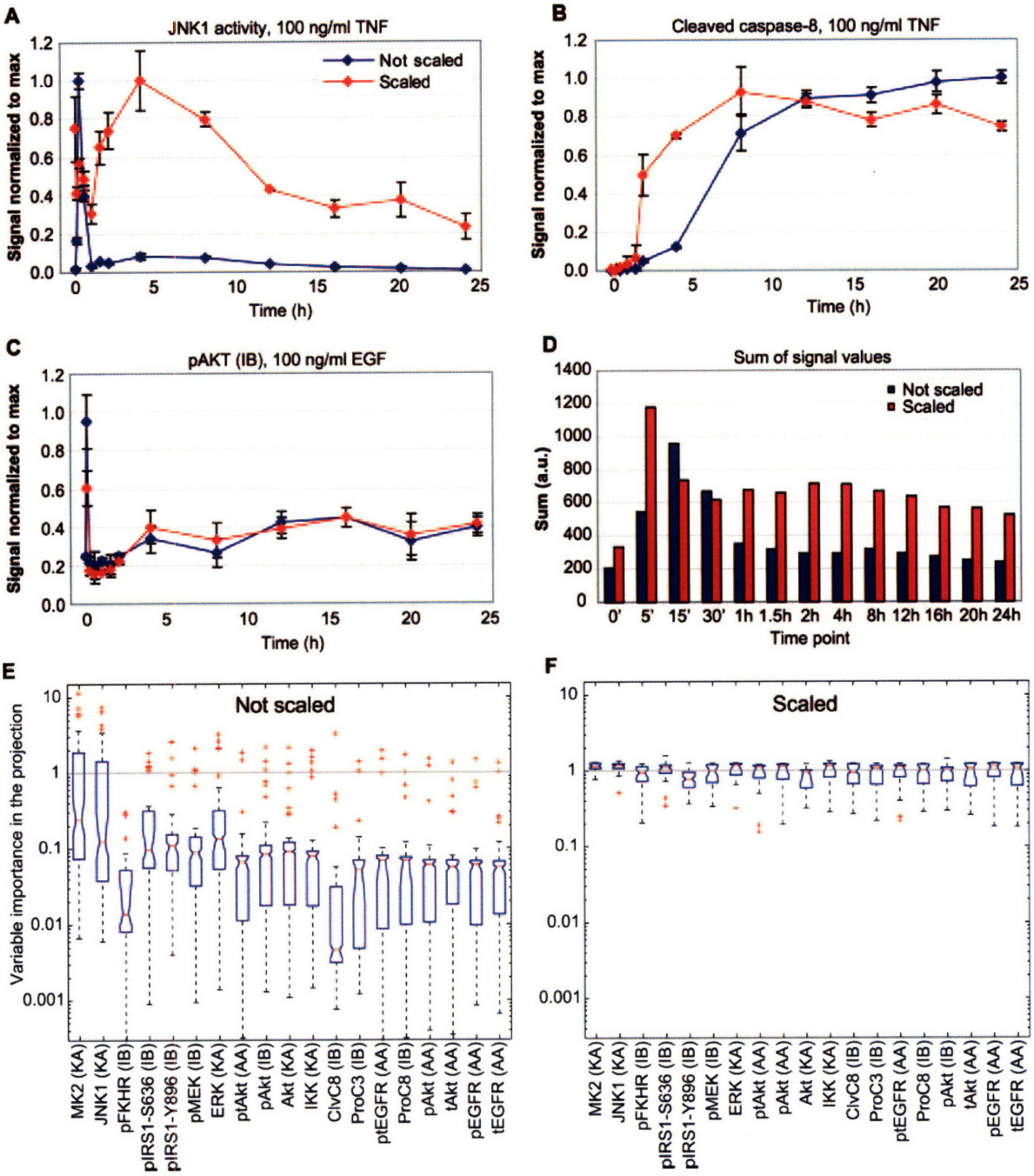

FIG. 5. **Unit-variance scaling enhances small but important features in the signaling time courses.** *A–C*, time courses of JNK1 activity (*A*) and cleaved caspase-8 levels (*B*) in cells treated with 100 ng/ml TNF and of phospho-Akt levels from cells treated with 100 ng/ml EGF (*C*). Normalized mean values from triplicate samples are shown in *blue*, and the values after scaling are shown in *red*. Error bars denote the S.E. *D*, bar graph comparing the sum of all signal values at each time point from normalized data (*Not scaled*, *blue*) or from unit-variance scaled data (*Scaled*, *red*). *E* and *F*, box-and-whisker plots showing the distribution of VIP for each signal in the PLSR models built using not scaled (*E*) or scaled (F) data. For each signal, the median is represented by a *red bar*, and its non-parametric 90% confidence interval is represented by the *notches* in the *box*. The *box* extends from the 25th to the 75th percentile values (*blue*), and the *whiskers* show the range of other data points (*black*). Outliers are shown as *red crosses*. *pAkt*, phospho-Akt; *KA*, kinase assay; *IB*, immunoblot; *AA*, antibody array; *pMEK*, phospho-MEK; *ClvC8*, cleaved caspase-8; *ProC3*, procaspase-3; *ProC8*, procaspase-8; *tEGFR*, total EGFR; *pEGFR*, phospho-EGFR; *a.u.*, arbitrary units; *′*, minutes.

blocking antibody C225 (59), and the second was obtained from cells treated with TNF in the presence of interleukin-1 receptor (IL-1R) antagonist (IL-1ra) (60). We show elsewhere that, at early times, the signaling and cell death response of cells to TNF is mediated in part by an TGF-α-EGFR autocrine loop and, at later times, by an IL-1α-IL-1R autocrine loop[2];

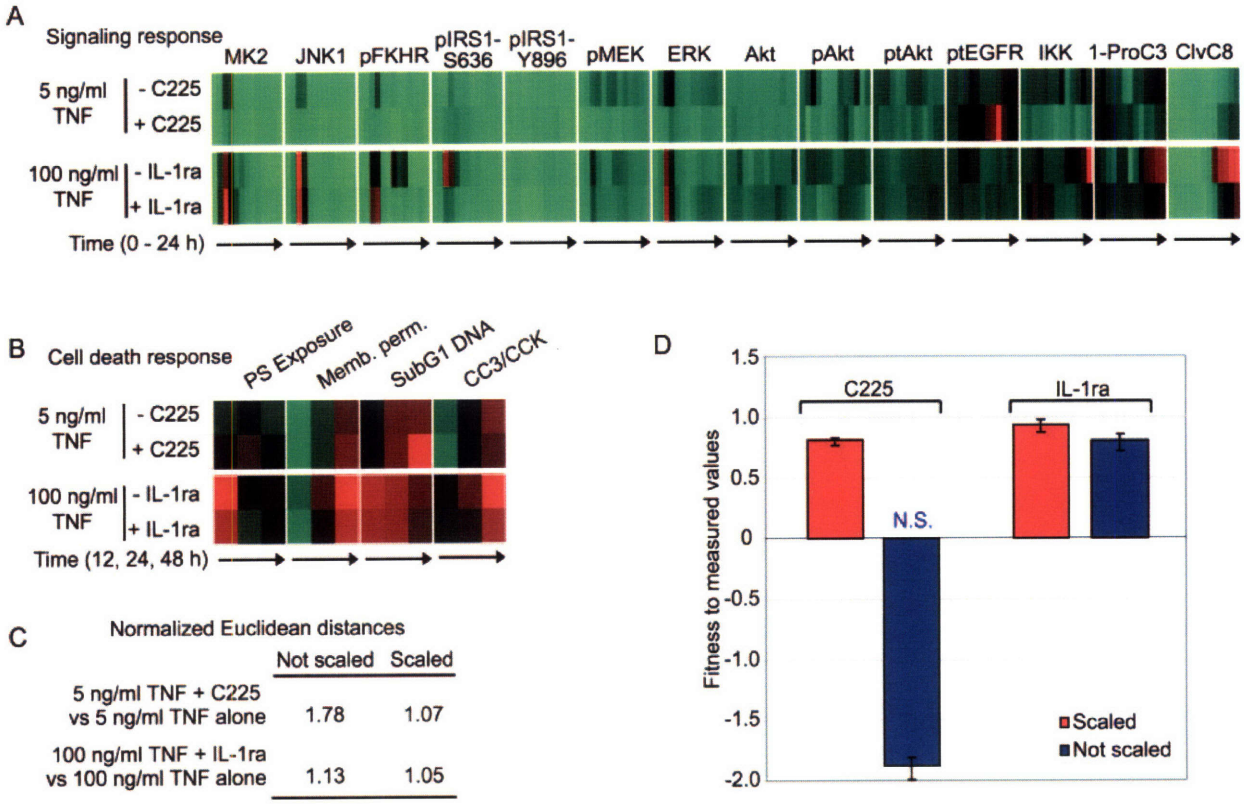

FIG. 6. **Unit-variance scaling is required for the model to correctly predict apoptosis induced by perturbations of autocrine signaling.** *A* and *B*, heat maps of the signals (*A*) and cell death responses (*B*) measured in two test datasets where TNF-induced autocrine loops were perturbed. Measurements were performed as in the single treatment experiments of the full compendium. Cells were stimulated with 100 ng/ml TNF + 10 μg/ml IL-1ra (*top*) or with 5 ng/ml TNF + 10 μg/ml C225 (*bottom*). In each case, the signaling profile is compared with the profile from the unperturbed treatment condition in the compendium. Averages from triplicate samples, normalized to the maximal value for that signal in the original compendium, are plotted for each time point (signals: 0, 5, 15, 30, 60, and 90 min and 2, 4, 8, 12, 16, 20, and 24 h; responses: 12, 24, and 48 h; 0, *green*; 0.5, *black*; 1, *red*). *C*, table showing the normalized Euclidean distances between the independent variables vector (time points and derived descriptors) of each of the test datasets and that of the corresponding unperturbed treatment before and after unit-variance scaling of the variables. The distances were normalized to the shortest distance in the full compendium for that unperturbed treatment. *D*, *bar graph* showing the least squares fitness of the apoptosis values predicted by the models to values measured in the two test datasets. The model from unit-variance scaled data (*red*) accurately predicts the cell death responses in the test data, whereas the model from data that was not scaled (*blue*) fails to predict the cell death responses from the C225 test dataset. *Error bars* denote the 90% confidence interval in the fitness estimate. *pMEK*, phospho-MEK; *pAkt*, phospho-Akt; *ProC3*, procaspase-3; *ClvC8*, cleaved caspase-8; *PS*, phosphatidylinositol; *Memb. perm.*, membrane permeability; *N.S.*, not significant; *CC3/CCK*, cleaved caspase-3/cleaved cytokeratin.

C225 and IL-1ra disrupt the TGF-α and IL-1α autocrine loops, respectively. Their importance for the current discussion is that C225 caused fairly dramatic changes in signaling as early as $t = 15$ min but only small changes in responses. Conversely IL-1ra elicited more modest changes in signaling (mostly at $t > 4$ h) but caused substantial changes in TNF-induced cell death responses (Fig. 6, *A–C*). When test data from cells treated with TNF + C225 were used as independent variables in the scaled PLSR model, cell death response predictions had a least squares fitness of 0.81 to experimental values (a perfect prediction would yield a fitness of 1; see "Experimental Procedures"). In contrast, the unscaled model performed very poorly, exhibiting no significant correlation between prediction and experiment (Fig. 6*D*). Although the impact of scaling was less dramatic for TNF + IL-1ra test data, we again found that the scaled model performed significantly better than the unscaled model (0.94 *versus* 0.81 least squares fit; Fig. 6*D*). We conclude that important information for predicting cell fate responses is contained in the small, consistent variations of low dynamic range signals and intermediate-to-late time points. Unit-variance scaling extracts this information from the CSR compendium and enables accurate prediction of cell death in treatments that are different from those within the training set data.

Aspects of the Compendium That Contribute to Prediction Accuracy and Model Robustness

The example above suggested a general approach for evaluating the importance of different aspects of the CSR compendium design using PLSR modeling. Scaled models lacking one or more data types were built and then compared with the

full scaled model to judge their ability to predict apoptotic responses in TNF + C225- and TNF + IL-1ra-treated cells.

The Value of Heterogeneous Signals Measured by Distinct Assays—To test our assumption that it was valuable to sample multiple features of a signaling network (Fig. 1*C*) we built PLSR models from subsets of the data. As expected, models built on measurements on a single protein performed poorly (Fig. 7*A*). More surprisingly, models built from multiple signals gathered using a single type of assay (*e.g.* immunoblots) were also inferior to the model based on the full compendium (Fig. 7*B*). For example, kinase activity data were as good as the full model at predicting apoptosis following TNF + IL-1ra treatment (0.94 least squares fit) but very poor at predicting the outcome of TNF + C225 treatment (no significant fit; Fig. 7*B*). Overall, immunoblot data yielded the best single assay model, but this model was still significantly less predictive than the full model (0.84 *versus* 0.94 for TNF + IL-1ra and 0.65 *versus* 0.81 for TNF + C225; Fig. 7*B*). We do not yet know whether the limitations of single-assay data can be overcome simply by measuring many more signals, using the same assay or whether something more fundamental is at work. However, given current technology, cell-signaling measurements are most powerful when different techniques are used in combination.

Efficient Data Collection by Combination Cytokine Treatments—In the design of a typical experiment, parameters are changed one at a time. In contrast, the CSR compendium included many treatments combining prodeath and prosurvival cytokines. To assess the value of combinatorial stimuli, we identified two models trained on few treatments that were still predictive of cell death in the test datasets: 1) a TNF-only model containing subsaturating and saturating TNF-alone treatments as well as the mock treatment and 2) a TNF-EGF-insulin model built from the saturating TNF + EGF and saturating TNF + insulin treatments (Fig. 7*C*). We then expanded the training data for the two models by including the low TNF + low EGF dataset. Both models predicted cell death in test data as accurately as the full model (fitness of 0.90 for model 1 and 0.94 for model 2; Fig. 7*D*). However, we reasoned that models trained on smaller datasets might be less robust to measurement noise in the training data. When random noise was added to the low TNF + low EGF signaling data and the models were recalculated, the TNF-only model performed poorly, whereas the TNF-EGF-insulin model and the full model remained reliable (Fig. 7*D*). We therefore conclude that inclusion of signaling data from cells exposed to multiple cytokines in combination yields models that are less sensitive to experimental noise.

Contributions from Derived Metrics—The full PLSR model was constructed using both signal measurements and derived metrics as independent variables. Was it important to include these derived metrics? Remarkably a model that included derived metrics but excluded actual signal measurements performed as well as the full model on both sets of test data (Fig. 7*E*, "*No time points*"). In contrast, a model built from signal measurements alone was unable to predict cell death in the C225 test dataset (Fig. 7*E*, "*Time points*"). Moreover activation rates and global descriptors of signaling dynamics (area under the curve, mean, maximal, and steady-state values) were among the most heavily weighted variables in the full model.[4] Why are derived metrics so important for model construction? In the PLSR approach described here, each time point is treated as a separate independent variable, and thus, derived metrics are the only variables that contain information on how measurements were ordered in time. To assess the relative value of each derived metric, we constructed models from single metric types. Several of the models accurately predicted apoptotic responses in the IL-1ra test data, but only one (based on activation rate, or on-slope) yielded predictions with a significant fitness to the measured apoptosis values in the C225 test data (Fig. 7*E*). Combining several derived metrics therefore seems to yield the most predictive power. Because derived metrics are more predictive than measurements themselves, we conclude that information encoded in time-dependent signaling is a critical aspect of the CSR compendium.

Predictive Information in Early and Late Signals—Can early signals predict late responses? Surprisingly, early time points between 5 and 90 min were predictive of cell death in the combined test datasets 12–48 h later (Fig. 7*F*), although they were significantly worse at predicting the C225 than IL-1ra test data (data not shown). This suggests that protein activities at early times encode much of the information needed to specify an apoptosis-survival cell fate decision. Late time points ($t > 12$ h) also had good overall predictive power (Fig. 7*F*), but this is to be expected because caspase activation at these late time points is mechanistically linked to cell death. Strikingly, a clear drop was observed in the predictive ability of the protein signals that were measured at $t = 2$, 4, and 8 h (Fig. 7*F*). It seems unlikely that information is really lost between 2 and 8 h; rather it may be encoded in transcriptional responses absent from our dataset (61). We hypothesize that the inclusion of transcriptional data in the compendium will reestablish the predictive power of models based on these time points. Taken together, compendium-based modeling results suggest that early signals immediately downstream of receptors contain much of the information needed to specify cell fate decisions up to 24 h later.

DISCUSSION

In this article, we describe the construction and validation of a cytokine-signal-response compendium with which to investigate the regulation of cell fate in cells exposed to combinations of the prodeath cytokine TNF and the prosurvival cytokines EGF and insulin. The compendium contains more than 10,000 biochemical measurements on the states and activities of cell-signaling proteins and apoptotic responses in human cells. At the outset of the work described here it was unclear whether heterogeneous data from immunoblots, an-

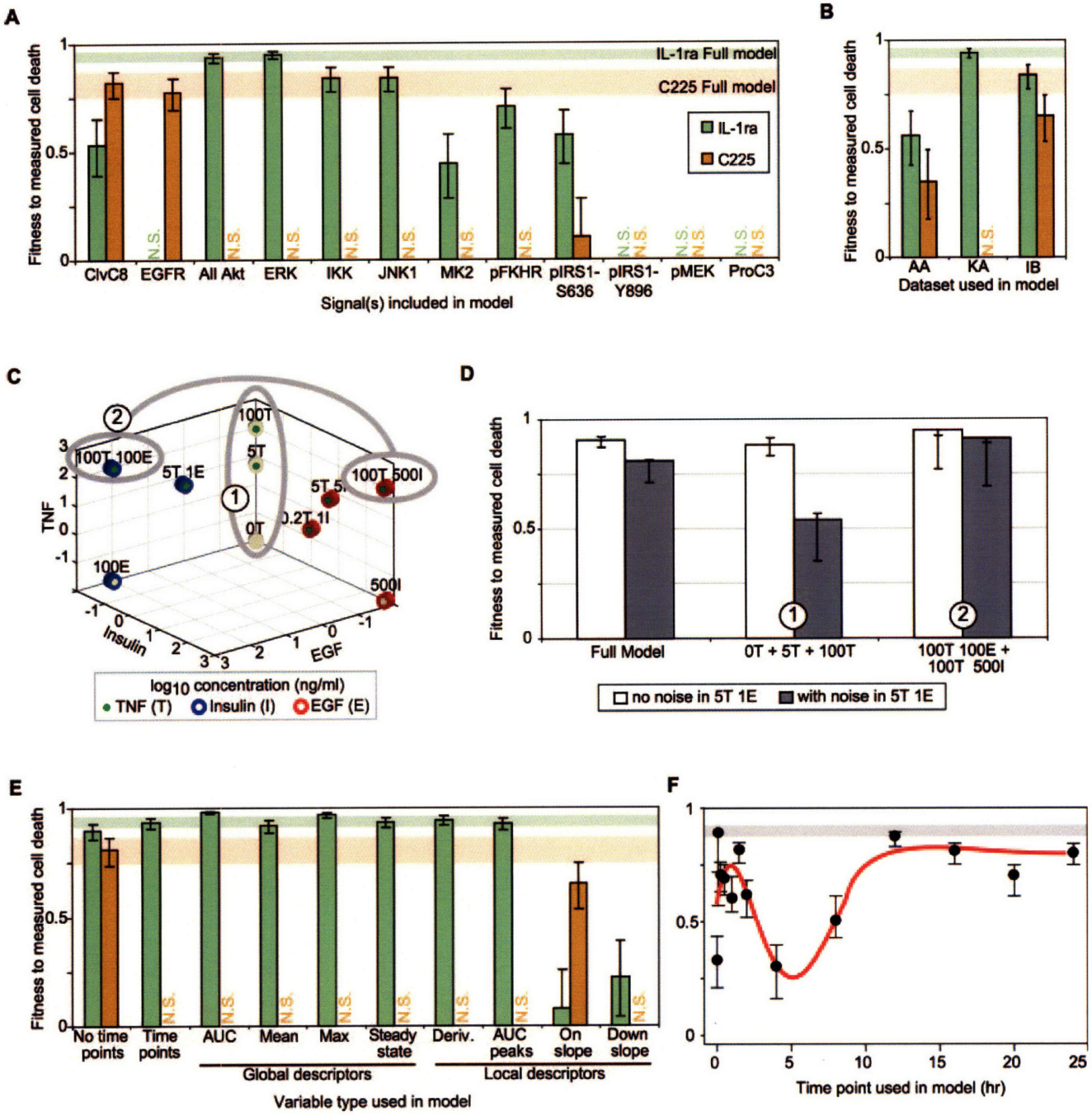

FIG. 7. **The PLSR model requires multiple, heterogeneous, time-dependent protein signals to predict apoptosis robustly.** Shown are bar graphs of the least-squares fitness of predicted-to-measured cell death responses in test datasets (IL-1ra, *green*; C225, *orange*) for models built from data subsets. *Light green* and *orange horizontal bands* mark the 90% confidence interval of the prediction fitness for the full compendium for the IL-1ra and C225 test datasets, respectively. Least-squares fitness values less than zero are marked as non-significant (*N.S.*). *Error bars* show the 90% confidence interval in the estimate. *A* and *B*, fitness values of predicted-to-observed cell death responses for models built from time course data on single protein signals (*A*) or from signaling data generated by a single assay (antibody arrays (*AA*), kinase assays (*KA*), or immunoblots (*IB*)) (*B*). Datasets that included cleaved caspase-8 (*ClvC8* in *A*, and immunoblots in *B*) performed best because this signal is the most directly linked, biochemically, to the outcomes. *C*, three-dimensional representation of the cytokine combinations used in models with subsets of treatment conditions. Model 1 used data from mock, 5 ng/ml TNF, and 100 ng/ml TNF treatments, whereas model 2 was built from data on 100 ng/ml TNF with either 100 ng/ml EGF or 500 ng/ml insulin. *D*, comparison of the fitness of predicted-to-measured apoptosis values in the IL-1ra and C225 test datasets combined for models with (*gray*) or without (*white*) simulated random normally distributed noise added to the 5 ng/ml TNF + 1 ng/ml EGF signal measurements. The fitness of models with noise represents the average predictive ability of three instances each at five noise levels (10, 20, 30, 40, or 50% of the range of values for each signal). *E*, fitness values of predicted-to-

tibody microarrays, kinase activity assays, and flow cytometry could be effectively assembled into a single dataset. However, we have now established that a carefully assembled CSR compendium enables the construction of informative statistical models and yields new hypotheses about the regulation of cell fate by cytokines. Elsewhere we describe some specific biological conclusions that can be inferred by mining compendium data[2]; here we concentrate on more general issues associated with the construction, validation, and mining of such datasets.

A key step in the construction of self-consistent datasets is data fusion. Heterogeneous measurements acquired at different times must be combined in such a way that they can be compared quantitatively across the full dataset. Experimental databases are common in genomics largely because sequence data are homogeneous and structured with a clear beginning and end, and data fusion is therefore straightforward. In contrast, cell-signaling data are heterogeneous and unstructured, lack an obvious completion point, and depend heavily on biological context. These features make fusion of signaling data challenging. Our approach to building a data compendium started with the definition of an experimental template that was applied repeatedly to the analysis of different cytokine combinations. The template specified standardized experimental protocols and optimized normalization procedures for determining the time-dependent activities of 19 protein signals and four cell death responses over a 48-h period. The template was applied to data collected from cells treated with 10 cytokine combinations and two combinations of a cytokine and a receptor inhibitor. Overall the raw cytokine-signal-response dataset contained ~10,000 quantitative measurements assembled from 12 independent experiments.

Accuracy and Self-consistency of the CSR Compendium—To support reliable hypothesis generation, data fusion must maintain measurement accuracy and self-consistency. A number of procedures were used to ensure the accuracy of the data, and these procedures were validated experimentally. First, the linearity of each assay was verified, and measurements were shown to be directly proportional to signal strength. Experimental protocols, cell treatments, and reagents were standardized, and measurements were adjusted for assay- and sample-specific fluctuations in factors such as reagent activities and lysate concentrations. For each treatment and time point, at least three replicate biological samples were measured, allowing formal statistical testing and assessment of the magnitude of biological variation and measurement noise.

Second, to rule out fluctuations in measurements during the 18-month data collection period, measurements in the primary compendium were compared with those in a validation dataset. The validation dataset replicated a subset of the compendium measurements but with an orthogonal experimental design. Whereas the primary compendium consisted of single treatments analyzed at different time points, validation data were collected at a single time from cells treated with different cytokine combinations. For most signals and responses, validation data matched primary data very well. A few signals could not be validated quantitatively because they lacked sufficient dynamic range to distinguish real variation from noise. Nonetheless we conclude that most signals and responses were consistent throughout the data collection process; validation experiments must be designed to maximize the number of signals showing significant variation across treatments.

As a third self-consistency check we asked whether different measures of the same biochemical process yielded similar data. In DNA sequencing this type of quality control is straightforward and involves checking the noncoding and coding sequences for complementarity. However, verifying the congruence of protein signals is more complex in part because a mechanistic model relating the different biochemical properties measured by each assay is necessary. For example, we assayed the activation of Akt both by kinase activity assay and by tracking its phosphorylation state at Ser^{473}, an activating site, using immunoblots and antibody arrays. Perfect correlations between these assays would require that phospho-Ser^{473} be essential for kinase activity and that all forms of phospho-Akt-Ser^{473} be fully active. Although kinase activity and phospho-Ser^{473} assays of Akt were generally well correlated, subtle discrepancies were observed. These discrepancies are consistent with the known mechanisms of Akt regulation (bisphosphorylated Akt is more active than Akt singly phosphorylated at Ser^{473} or Thr^{308} (35, 36)), but they also highlighted the challenges involved in validating the merger of data from heterogeneous assays into a single coherent representation.

Context-dependent Signaling Dynamics—The CSR compendium allowed us to compare signaling dynamics within a range of cytokine contexts. We used two approaches to mine compendium data for interesting signaling patterns: heat maps (see Supplementary Material) and cytokine-signal maps.[2] One surprising finding was that the treatment of cells with EGF, but not with insulin, was strongly associated with

observed cell death responses in each test dataset for models built from single variable types. The variables were grouped by time point values, global area under the curve (*AUC*), mean, maximal (*max*), or steady-state value over the time course, local area under the curve (*AUC peaks*), slope of activation phase (*On slope*) or of down-regulation phase (*Down slope*), and instant derivatives at each time point (*Deriv.*). *F*, plot of predictive ability of models built from single time point data as expressed by the least-squares fitness to the measured values for the two test datasets combined. Similar trends were observed with each perturbation alone. *Error bars* denote the 90% confidence interval, and the trend line (*red*) is a polynomial fit to the fitness values plotted against time. The 90% confidence interval in the fitness value for the full model is marked in *light gray*. *pMEK*, phospho-MEK.

phosphorylation of insulin receptor substrate 1 on Tyr^{896}. The sequence flanking IRS1-Tyr^{896} is a remarkably good match to an EGF receptor consensus phosphoacceptor site, leading us to hypothesize that EGF may be an important pIRS1-Tyr^{896} inducer and that EGFR may modify IRS1 directly. This hypothesis is now being tested experimentally. A second unexpected discovery was a lack of correlation between Akt activation and $Ser2^{256}$ phosphorylation of the Forkhead transcription factor, an Akt substrate (51, 52). The lack of correlation leads us to hypothesize that FKHR-Ser^{256} may be targeted by a kinase other than Akt in EGF- and TNF-treated cells. Consistent with this idea, the basophilic kinase SGK has recently been shown to modify the FKHR homologue FOXO3 on two phosphoacceptor sites previously thought to be Akt substrates (56). These two findings illustrate the value of comparing signal strengths quantitatively across a set of different biological conditions. Unexpected statistical correlations observed among signals are suggestive of new mechanistic links, whereas the absence of an expected correlation suggests that existing links may require reinvestigation.

Experimental Requirements for Signaling Compendia—The construction and validation of computational models of cell signaling was our primary goal in generating the CSR compendium. As a first step, we built a regression (PLSR) model that relates protein signals to cell death responses.[3] PLSR models built from data scaled to unit variance extracted the most information from the compendium and performed much better than models built from unscaled variables. The best PLSR data-driven model was surprisingly powerful: given signaling information from test data not included in the training set, the model predicted apoptotic responses to within the range of error for experimental measurements.[3] PLSR models were used to analyze the design and assembly of CSR data with the goal of developing optimized strategies for the construction of future compendia.

Would a simpler experimental scheme with fewer signals, treatments, or time points have yielded a CSR compendium with a similar ability to support PLSR modeling? Although the answer appears to be "yes" because some data scored low in the VIP (Fig. 5*F*), statistical modeling clearly benefited from heterogeneous measurements, information on signal dynamics, and the analysis of cells treated with combinations of cytokines. Models built from single signals were ineffective at predicting apoptosis, consistent with the idea that cells weigh the contributions from multiple signals when committing to survival or death (62). More interestingly, models built from any single type of assay were significantly less predictive than models based on the full compendium. Among the single-assay models, immunoblot data performed best probably because immunoblots were used to assay two distinct biochemical processes: protein phosphorylation and protein cleavage. Most proteomic efforts to date (63) have centered on the use of a single technology such as protein arrays (64) or mass spectrometry (10). However, our results suggest that it is highly advantageous to combine several different assay methods to capture the diversity of protein signals that mediate cell fate decisions.

If the analysis of single proteins is insufficient to predict cell fate, then how much coverage of a signaling network is required? The success of our CSR compendium shows that it is not necessary to strive for complete coverage: apoptosis was predicted within 94% accuracy given signaling information from only 11 of the roughly 75 protein nodes shown in Fig. 1*C* (15% coverage). However, we suspect that a sparse sampling of a network will only yield predictive models when nodes are repeatedly sampled under a variety of conditions. In a typical experiment one usually decides to vary one parameter at a time, but we have found that data from cells treated with a combination of cytokines were more informative than data from single cytokine treatments particularly when measurements were noisy. Combinations of prodeath and prosurvival cytokines evoke more complex signaling patterns than individual stimuli, and it seems likely that this provides a broader context within which to assess the role of each signal in cell death responses.

Which signals should be measured in the protein network? Although the answer clearly depends on the biological system, we found that upstream signals (*e.g.* receptors and adaptors) were easiest to relate to cytokine stimuli in statistical maps. For instance, IRS1-Tyr^{896} phosphorylation was prominent as an EGF-dependent signal on the cytokine-signal map.[2] With the PLSR model, however, downstream signals like ERK, JNK1, and MK2 were most predictive of apoptotic responses.[3] We also found that measuring connected nodes in the network, initially thought to represent somewhat redundant assays, provided useful insight into the propagation of signals through particular pathways. Akt-FKHR is one example of a densely sampled region of the network; another is the dual measurements of ERK activity and phospho-MEK level (Fig. 8*B*). The correlation between these two signals was reasonable (Pearson coefficient of 0.68 overall), but more in-depth analysis revealed that ERK and phospho-MEK were best correlated at the earliest time point after cytokine addition, implying that their activation was coincident (Fig. 8*A*, *5 min*). At later time points, MEK was inactivated more rapidly than ERK, and the correlation was lost probably as a result of differential dephosphorylation (Fig. 8, *A* and *B*) (65). The ERK-MEK disparity was exacerbated under conditions of saturating TNF treatment (Fig. 8*A*, *circles*). Thus, TNF may activate the Ser-Thr phosphatases that act on MEK or alternatively inactivate the dual specificity and Tyr phosphatases that act on ERK (Fig. 8*B*). Directed phosphomapping experiments and phosphatase assays should be able to test this prediction. More generally, the variability in MEK-ERK induction highlights how proteins that interact directly and function in the same pathway can exhibit time-dependent changes in relative activities.

Propagation of Signaling Information with Time—In the CSR

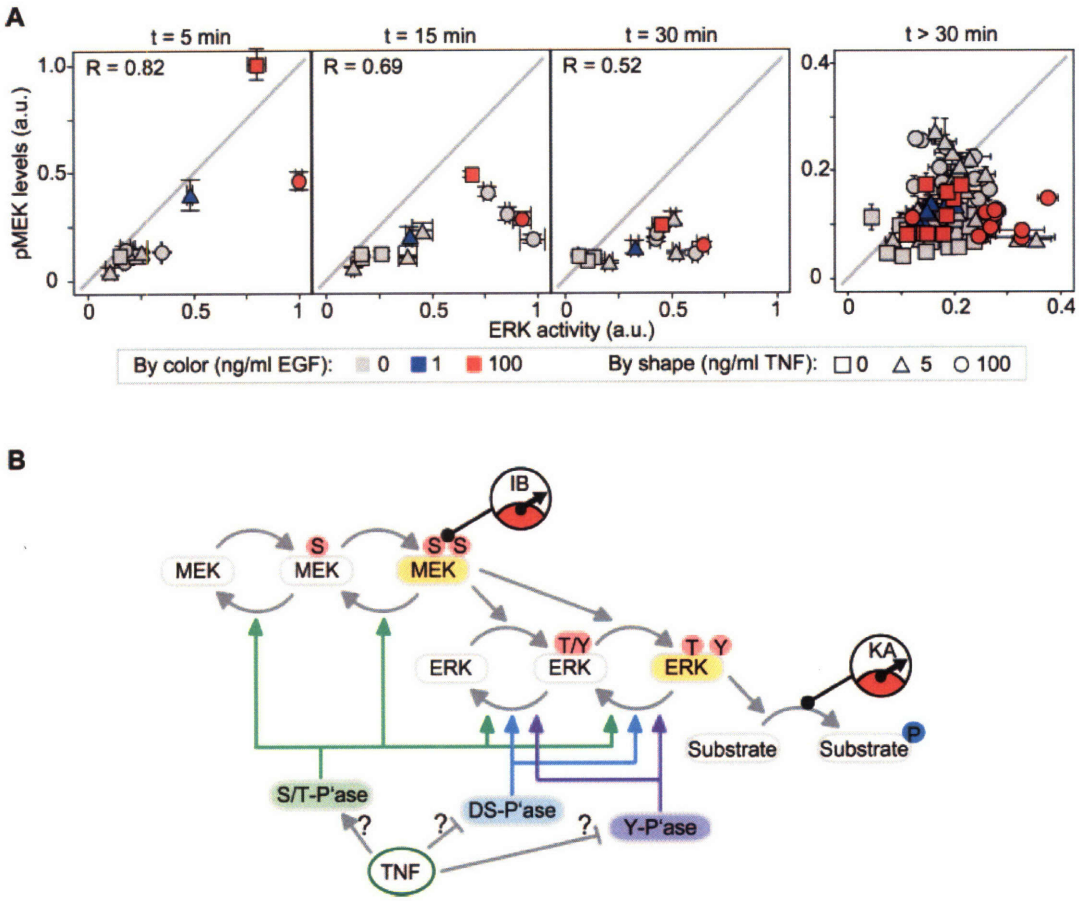

FIG. 8. **Differential regulation of MEK and ERK by phosphatases is context-dependent.** *A*, scatter plots of pairwise comparisons of ERK activity and phospho-MEK (*pMEK*) levels at 5, 15, and 30 min and at time points greater than 30 min as indicated. Values are means ± S.E. of biological triplicate samples normalized to the maximal value in the compendium for that signal. Pearson correlations are noted in the *upper left corner* when the dynamic range is greater than 2.5. *B*, schematic diagram showing the two measurement types, ERK kinase activity assays (*KA*) and phospho-MEK levels by immunoblot (*IB*), the differential regulation of ERK and MEK by phosphatases. MEK is targeted only by Ser-Thr phosphatases (*S/T-P'ase*) that may be activated by TNF treatment. ERK is additionally targeted by dual specificity phosphatases (*DS-P'ase*) and Tyr phosphatases (*Y-P'ase*) that may be inhibited by TNF treatment. *a.u.*, arbitrary units.

compendium, protein signals were encoded by two types of variables: discrete measurements collected at 13 points over a 24-h period and derived metrics describing the local and global dynamics of signaling. We found that these derived metrics were essential for constructing predictive PLSR models and that they could not be replaced by the measurements from which they were derived. PLSR treats each time point independently, and derived metrics were therefore the primary means by which time dependence was encoded. We presume that this explains the importance of the metrics for the PLSR model. Unexpectedly, however, when the CSR compendium was modeled using a multilinear regression technique (66) that constrains the sequence of time points by explicitly ordering signaling network "snapshots" in time, we were unable to construct predictive models.[5] One explanation for the success of derived metrics in PLSR and failure of multilinear regression is that critical signaling information is imbedded in the cumulative activities and rates of change of key signals, calculated as derived metrics, rather than in the ordering of signaling events. For example, the cumulative activity of caspase-8 is likely to be more important than the time at which activity is first detected. Indeed molecular integrators and differentiators have been previously identified in both prokaryotic and eukaryotic signaling networks (21, 23, 67).

PLSR models based on single time point snapshots between 5 and 90 min or 12 and 24 h were able to predict apoptotic responses with reasonable accuracy although not as well as the full model. A clear loss of information was observed with protein signals at t = 2–8 h. In HT-29 cells, TNF-induced apoptosis is not apparent until ~8 h after stimulus addition,[4] implying that cells must still be processing apoptosis-survival cues at those time points. One explanation for the loss of predictive power from 2 to 8 h is that informa-

[5] K. A. Janes and P. K. Sorger, unpublished observations.

tion processing involves changes in gene transcription, which were not measured in our experiments. Microarray experiments are currently underway to test this idea. Nonetheless it is clear that protein signals alone, when sampled over a time course, are sufficient for predicting HT-29 apoptotic responses induced by cytokines. It will be interesting to determine whether PLSR models based on the current CSR compendium will also be effective in predicting apoptosis induced by other stimuli or in different cell lines.

Conclusion—The data in this article show that cytokine-signal-response compendia should be constructed using measurements that are well distributed across a signaling network, although sparse coverage of the network is acceptable. Nonetheless resampling a subset of nodes using multiple assays helps to verify the consistency of heterogeneous data. Experimental validation of measurements is best carried out under conditions in which all signals have a sufficiently large dynamic range for correlation coefficients to be meaningful. In some cases this will involve two validation experiments, for example one at an early time point and one later. Measurement of signaling dynamics is clearly critical for CSR compendia, and uneven spacing of time points makes it possible to sample adequately both transient and sustained signals. Within the context of the regression-based models used here, it is important to rely not only on the data themselves but also to compute metrics that describe signal dynamics. Moreover scaling data to unit variance is necessary to optimize the extraction of information from compendium data.

In summary, we have described methods for compiling validated, self-consistent data compendia describing time-varying signals induced by cytokines and have demonstrated the value of compendium data in the study of mammalian signal transduction. We believe that similar CSR compendia coupled with both regression-based and mechanistic models will be valuable in the systematic analysis of other complex biological networks.

Acknowledgments—We thank members of the Sorger and Lauffenburger laboratories for helpful discussions.

* This work was supported by National Institutes of Health Grant P50-GM68762 and by the Whitaker Foundation (to K. A. J.). The costs of publication of this article were defrayed in part by the payment of page charges. This article must therefore be hereby marked "*advertisement*" in accordance with 18 U.S.C. Section 1734 solely to indicate this fact.

[S] The on-line version of this article (available at http://www.mcponline.org) contains supplemental material.

‖ To whom correspondence should be addressed: Dept. of Biology, Rm. 68-371, Massachusetts Inst. of Technology, 77 Massachusetts Ave., Cambridge, MA 02139. Tel.: 617-252-1648; E-mail: psorger@mit.edu.

REFERENCES

1. Lander, E. S., Linton, L. M., Birren, B., Nusbaum, C., Zody, M. C., Baldwin, J., Devon, K., Dewar, K., Doyle, M., FitzHugh, W., Funke, R., Gage, D., Harris, K., Heaford, A., Howland, J., Kann, L., Lehoczky, J., LeVine, R., McEwan, P., McKernan, K., Meldrim, J., Mesirov, J. P., Miranda, C., Morris, W., Naylor, J., Raymond, C., Rosetti, M., Santos, R., Sheridan, A., Sougnez, C., Stange-Thomann, N., Stojanovic, N., Subramanian, A., Wyman, D., Rogers, J., Sulston, J., Ainscough, R., Beck, S., Bentley, D., Burton, J., Clee, C., Carter, N., Coulson, A., Deadman, R., Deloukas, P., Dunham, A., Dunham, I., Durbin, R., French, L., Grafham, D., Gregory, S., Hubbard, T., Humphray, S., Hunt, A., Jones, M., Lloyd, C., McMurray, A., Matthews, L., Mercer, S., Milne, S., Mullikin, J. C., Mungall, A., Plumb, R., Ross, M., Shownkeen, R., Sims, S., Waterston, R. H., Wilson, R. K., Hillier, L. W., McPherson, J. D., Marra, M. A., Mardis, E. R., Fulton, L. A., Chinwalla, A. T., Pepin, K. H., Gish, W. R., Chissoe, S. L., Wendl, M. C., Delehaunty, K. D., Miner, T. L., Delehaunty, A., Kramer, J. B., Cook, L. L., Fulton, R. S., Johnson, D. L., Minx, P. J., Clifton, S. W., Hawkins, T., Branscomb, E., Predki, P., Richardson, P., Wenning, S., Slezak, T., Doggett, N., Cheng, J. F., Olsen, A., Lucas, S., Elkin, C., Uberbacher, E., Frazier, M., Gibbs, R. A., Muzny, D. M., Scherer, S. E., Bouck, J. B., Sodergren, E. J., Worley, K. C., Rives, C. M., Gorrell, J. H., Metzker, M. L., Naylor, S. L., Kucherlapati, R. S., Nelson, D. L., Weinstock, G. M., Sakaki, Y., Fujiyama, A., Hattori, M., Yada, T., Toyoda, A., Itoh, T., Kawagoe, C., Watanabe, H., Totoki, Y., Taylor, T., Weissenbach, J., Heilig, R., Saurin, W., Artiguenave, F., Brottier, P., Bruls, T., Pelletier, E., Robert, C., Wincker, P., Smith, D. R., Doucette-Stamm, L., Rubenfield, M., Weinstock, K., Lee, H. M., Dubois, J., Rosenthal, A., Platzer, M., Nyakatura, G., Taudien, S., Rump, A., Yang, H., Yu, J., Wang, J., Huang, G., Gu, J., Hood, L., Rowen, L., Madan, A., Qin, S., Davis, R. W., Federspiel, N. A., Abola, A. P., Proctor, M. J., Myers, R. M., Schmutz, J., Dickson, M., Grimwood, J., Cox, D. R., Olson, M. V., Kaul, R., Shimizu, N., Kawasaki, K., Minoshima, S., Evans, G. A., Athanasiou, M., Schultz, R., Roe, B. A., Chen, F., Pan, H., Ramser, J., Lehrach, H., Reinhardt, R., McCombie, W. R., de la Bastide, M., Dedhia, N., Blocker, H., Hornischer, K., Nordsiek, G., Agarwala, R., Aravind, L., Bailey, J. A., Bateman, A., Batzoglou, S., Birney, E., Bork, P., Brown, D. G., Burge, C. B., Cerutti, L., Chen, H. C., Church, D., Clamp, M., Copley, R. R., Doerks, T., Eddy, S. R., Eichler, E. E., Furey, T. S., Galagan, J., Gilbert, J. G., Harmon, C., Hayashizaki, Y., Haussler, D., Hermjakob, H., Hokamp, K., Jang, W., Johnson, L. S., Jones, T. A., Kasif, S., Kaspryzk, A., Kennedy, S., Kent, W. J., Kitts, P., Koonin, E. V., Korf, I., Kulp, D., Lancet, D., Lowe, T. M., McLysaght, A., Mikkelsen, T., Moran, J. V., Mulder, N., Pollara, V. J., Ponting, C. P., Schuler, G., Schultz, J., Slater, G., Smit, A. F., Stupka, E., Szustakowski, J., Thierry-Mieg, D., Thierry-Mieg, J., Wagner, L., Wallis, J., Wheeler, R., Williams, A., Wolf, Y. I., Wolfe, K. H., Yang, S. P., Yeh, R. F., Collins, F., Guyer, M. S., Peterson, J., Felsenfeld, A., Wetterstrand, K. A., Patrinos, A., Morgan, M. J., de Jong, P., Catanese, J. J., Osoegawa, K., Shizuya, H., Choi, S., and Chen, Y. J. (2001) Initial sequencing and analysis of the human genome. *Nature* **409,** 860–921
2. Botstein, D., and Risch, N. (2003) Discovering genotypes underlying human phenotypes: past successes for mendelian disease, future approaches for complex disease. *Nat. Genet.* **33,** (suppl.) 228–237
3. Irish, J. M., Hovland, R., Krutzik, P. O., Perez, O. D., Bruserud, O., Gjertsen, B. T., and Nolan, G. P. (2004) Single cell profiling of potentiated phospho-protein networks in cancer cells. *Cell* **118,** 217–228
4. Blagoev, B., Ong, S. E., Kratchmarova, I., and Mann, M. (2004) Temporal analysis of phosphotyrosine-dependent signaling networks by quantitative proteomics. *Nat. Biotechnol.* **22,** 1139–1145
5. Gilman, A. G., Simon, M. I., Bourne, H. R., Harris, B. A., Long, R., Ross, E. M., Stull, J. T., Taussig, R., Arkin, A. P., Cobb, M. H., Cyster, J. G., Devreotes, P. N., Ferrell, J. E., Fruman, D., Gold, M., Weiss, A., Berridge, M. J., Cantley, L. C., Catterall, W. A., Coughlin, S. R., Olson, E. N., Smith, T. F., Brugge, J. S., Botstein, D., Dixon, J. E., Hunter, T., Lefkowitz, R. J., Pawson, A. J., Sternberg, P. W., Varmus, H., Subramaniam, S., Sinkovits, R. S., Li, J., Mock, D., Ning, Y., Saunders, B., Sternweis, P. C., Hilgemann, D., Scheuermann, R. H., DeCamp, D., Hsueh, R., Lin, K. M., Ni, Y., Seaman, W. E., Simpson, P. C., O'Connell, T. D., Roach, T., Choi, S., Eversole-Cire, P., Fraser, I., Mumby, M. C., Zhao, Y., Brekken, D., Shu, H., Meyer, T., Chandy, G., Heo, W. D., Liou, J., O'Rourke, N., Verghese, M., Mumby, S. M., Han, H., Brown, H. A., Forrester, J. S., Ivanova, P., Milne, S. B., Casey, P. J., Harden, T. K., Doyle, J., Gray, M. L., Michnick, S., Schmidt, M. A., Toner, M., Tsien, R. Y., Natarajan, M., Ranganathan, R., and Sambrano, G. R. (2002) Overview of the Alliance for Cellular Signaling. *Nature* **420,** 703–706
6. Papin, J. A., Hunter, T., Palsson, B. O., and Subramaniam, S. (2005) Reconstruction of cellular signalling networks and analysis of their prop-

erties. *Nat. Rev. Mol. Cell. Biol.* **6,** 99–111
7. Janes, K. A., Albeck, J. G., Peng, L. X., Sorger, P. K., Lauffenburger, D. A., and Yaffe, M. B. (2003) A high-throughput quantitative multiplex kinase assay for monitoring information flow in signaling networks: application to sepsis-apoptosis. *Mol. Cell. Proteomics* **2,** 463–473
8. Sambrano, G. R., Chandy, G., Choi, S., Decamp, D., Hsueh, R., Lin, K. M., Mock, D., O'Rourke, N., Roach, T., Shu, H., Sinkovits, B., Verghese, M., and Bourne, H. (2002) Unravelling the signal-transduction network in B lymphocytes. *Nature* **420,** 708–710
9. Perlman, Z. E., Slack, M. D., Feng, Y., Mitchison, T. J., Wu, L. F., and Altschuler, S. J. (2004) Multidimensional drug profiling by automated microscopy. *Science* **306,** 1194–1198
10. Aebersold, R., and Mann, M. (2003) Mass spectrometry-based proteomics. *Nature* **422,** 198–207
11. Swedlow, J. R., Goldberg, I., Brauner, E., and Sorger, P. K. (2003) Informatics and quantitative analysis in biological imaging. *Science* **300,** 100–102
12. Wajant, H., Pfizenmaier, K., and Scheurich, P. (2003) Tumor necrosis factor signaling. *Cell. Death Differ.* **10,** 45–65
13. Micheau, O., and Tschopp, J. (2003) Induction of TNF receptor I-mediated apoptosis via two sequential signaling complexes. *Cell* **114,** 181–190
14. Nicholson, D. W., and Thornberry, N. A. (1997) Caspases: killer proteases. *Trends Biochem. Sci.* **22,** 299–306
15. Kyriakis, J. M., and Avruch, J. (2001) Mammalian mitogen-activated protein kinase signal transduction pathways activated by stress and inflammation. *Physiol. Rev.* **81,** 807–869
16. Karin, M., and Ben-Neriah, Y. (2000) Phosphorylation meets ubiquitination: the control of NF-κB activity. *Annu. Rev. Immunol.* **18,** 621–663
17. Yarden, Y., and Sliwkowski, M. X. (2001) Untangling the ErbB signalling network. *Nat. Rev. Mol. Cell. Biol.* **2,** 127–137
18. Jorissen, R. N., Walker, F., Pouliot, N., Garrett, T. P., Ward, C. W., and Burgess, A. W. (2003) Epidermal growth factor receptor: mechanisms of activation and signalling. *Exp. Cell. Res.* **284,** 31–53
19. Schlessinger, J. (2004) Common and distinct elements in cellular signaling via EGF and FGF receptors. *Science* **306,** 1506–1507
20. White, M. F. (1994) The IRS-1 signaling system. *Curr. Opin. Genet. Dev.* **4,** 47–54
21. Sasagawa, S., Ozaki, Y., Fujita, K., and Kuroda, S. (2005) Prediction and validation of the distinct dynamics of transient and sustained ERK activation. *Nat. Cell. Biol.* **7,** 365–373
22. von Mering, C., Krause, R., Snel, B., Cornell, M., Oliver, S. G., Fields, S., and Bork, P. (2002) Comparative assessment of large-scale data sets of protein-protein interactions. *Nature* **417,** 399–403
23. Alon, U., Surette, M. G., Barkai, N., and Leibler, S. (1999) Robustness in bacterial chemotaxis. *Nature* **397,** 168–171
24. Nielsen, U. B., Cardone, M. H., Sinskey, A. J., MacBeath, G., and Sorger, P. K. (2003) Profiling receptor tyrosine kinase activation by using Ab microarrays. *Proc. Natl. Acad. Sci. U. S. A.* **100,** 9330–9335
25. Janes, K. A., Kelly, J. R., Gaudet, S., Albeck, J. G., Sorger, P. K., and Lauffenburger, D. A. (2004) Cue-signal-response analysis of TNF-induced apoptosis by partial least squares regression of dynamic multivariate data. *J. Comput. Biol.* **11,** 544–561
26. Abreu-Martin, M. T., Vidrich, A., Lynch, D. H., and Targan, S. R. (1995) Divergent induction of apoptosis and IL-8 secretion in HT-29 cells in response to TNF-alpha and ligation of Fas antigen. *J. Immunol.* **155,** 4147–4154
27. Remacle-Bonnet, M. M., Garrouste, F. L., Heller, S., Andre, F., Marvaldi, J. L., and Pommier, G. J. (2000) Insulin-like growth factor-I protects colon cancer cells from death factor-induced apoptosis by potentiating tumor necrosis factor α-induced mitogen-activated protein kinase and nuclear factor κB signaling pathways. *Cancer Res.* **60,** 2007–2017
28. Johnson, G. L., and Lapadat, R. (2002) Mitogen-activated protein kinase pathways mediated by ERK, JNK, and p38 protein kinases. *Science* **298,** 1911–1912
29. Datta, S. R., Brunet, A., and Greenberg, M. E. (1999) Cellular survival: a play in three Akts. *Genes Dev.* **13,** 2905–2927
30. Roux, P. P., and Blenis, J. (2004) ERK and p38 MAPK-activated protein kinases: a family of protein kinases with diverse biological functions. *Microbiol. Mol. Biol. Rev.* **68,** 320–344
31. Scheid, M. P., Marignani, P. A., and Woodgett, J. R. (2002) Multiple phosphoinositide 3-kinase-dependent steps in activation of protein kinase B. *Mol. Cell. Biol.* **22,** 6247–6260
32. Yang, J., Cron, P., Thompson, V., Good, V. M., Hess, D., Hemmings, B. A., and Barford, D. (2002) Molecular mechanism for the regulation of protein kinase B/Akt by hydrophobic motif phosphorylation. *Mol. Cell* **9,** 1227–1240
33. Sarbassov, D. D., Guertin, D. A., Ali, S. M., and Sabatini, D. M. (2005) Phosphorylation and regulation of Akt/PKB by the rictor-mTOR complex. *Science* **307,** 1098–1101
34. Toker, A., and Newton, A. C. (2000) Cellular signaling: pivoting around PDK-1. *Cell* **103,** 185–188
35. Alessi, D. R., Andjelkovic, M., Caudwell, B., Cron, P., Morrice, N., Cohen, P., and Hemmings, B. A. (1996) Mechanism of activation of protein kinase B by insulin and IGF-1. *EMBO J.* **15,** 6541–6551
36. Feng, J., Park, J., Cron, P., Hess, D., and Hemmings, B. A. (2004) Identification of a PKB/Akt hydrophobic motif Ser-473 kinase as DNA-dependent protein kinase. *J. Biol. Chem.* **279,** 41189–41196
37. White, M. F. (1998) The IRS-signalling system: a network of docking proteins that mediate insulin action. *Mol. Cell. Biochem.* **182,** 3–11
38. Harrington, L. S., Findlay, G. M., and Lamb, R. F. (2005) Restraining PI3K: mTOR signalling goes back to the membrane. *Trends Biochem. Sci.* **30,** 35–42
39. Sun, X. J., Crimmins, D. L., Myers, M. G., Jr., Miralpeix, M., and White, M. F. (1993) Pleiotropic insulin signals are engaged by multisite phosphorylation of IRS-1. *Mol. Cell. Biol.* **13,** 7418–7428
40. Paz, K., Hemi, R., LeRoith, D., Karasik, A., Elhanany, E., Kanety, H., and Zick, Y. (1997) A molecular basis for insulin resistance. Elevated serine/threonine phosphorylation of IRS-1 and IRS-2 inhibits their binding to the juxtamembrane region of the insulin receptor and impairs their ability to undergo insulin-induced tyrosine phosphorylation. *J. Biol. Chem.* **272,** 29911–29918
41. White, M. F. (2002) IRS proteins and the common path to diabetes. *Am. J. Physiol.* **283,** E413–E422
42. Valverde, A. M., Mur, C., Pons, S., Alvarez, A. M., White, M. F., Kahn, C. R., and Benito, M. (2001) Association of insulin receptor substrate 1 (IRS-1) y895 with Grb-2 mediates the insulin signaling involved in IRS-1-deficient brown adipocyte mitogenesis. *Mol. Cell. Biol.* **21,** 2269–2280
43. Fujioka, T., and Ui, M. (2001) Involvement of insulin receptor substrates in epidermal growth factor induced activation of phosphatidylinositol 3-kinase in rat hepatocyte primary culture. *Eur. J. Biochem.* **268,** 25–34
44. Fujioka, T., Kim, J. H., Adachi, H., Saito, K., Tsujimoto, M., Yokoyama, S., and Ui, M. (2001) Further evidence for the involvement of insulin receptor substrates in epidermal growth factor-induced activation of phosphatidylinositol 3-kinase. *Eur. J. Biochem.* **268,** 4158–4168
45. Gogg, S., and Smith, U. (2002) Epidermal growth factor and transforming growth factor α mimic the effects of insulin in human fat cells and augment downstream signaling in insulin resistance. *J. Biol. Chem.* **277,** 36045–36051
46. Obenauer, J. C., Cantley, L. C., and Yaffe, M. B. (2003) Scansite 2.0: proteome-wide prediction of cell signaling interactions using short sequence motifs. *Nucleic Acids Res.* **31,** 3635–3641
47. Saxinger, C., Conrads, T. P., Goldstein, D. J., and Veenstra, T. D. (2005) Fully automated synthesis of (phospho)peptide arrays in microtiter plate wells provides efficient access to protein tyrosine kinase characterization. *BMC Immunol.* **6,** 1
48. Songyang, Z., Carraway, K. L., III, Eck, M. J., Harrison, S. C., Feldman, R. A., Mohammadi, M., Schlessinger, J., Hubbard, S. R., Smith, D. P., Eng, C., Lorenzo, M. J., Ponder, B. A. J., Mayer, B. J., and Cantley, L. C. (1995) Catalytic specificity of protein-tyrosine kinases is critical for selective signalling. *Nature* **373,** 536–539
49. Yaffe, M. B., Leparc, G. G., Lai, J., Obata, T., Volinia, S., and Cantley, L. C. (2001) A motif-based profile scanning approach for genome-wide prediction of signaling pathways. *Nat. Biotechnol.* **19,** 348–353
50. Avruch, J. (1998) Insulin signal transduction through protein kinase cascades. *Mol. Cell. Biochem.* **182,** 31–48
51. Tang, E. D., Nunez, G., Barr, F. G., and Guan, K. L. (1999) Negative regulation of the forkhead transcription factor FKHR by Akt. *J. Biol. Chem.* **274,** 16741–16746
52. Rena, G., Guo, S., Cichy, S. C., Unterman, T. G., and Cohen, P. (1999) Phosphorylation of the transcription factor forkhead family member FKHR by protein kinase B. *J. Biol. Chem.* **274,** 17179–17183
53. Cross, D. A., Watt, P. W., Shaw, M., van der Kaay, J., Downes, C. P.,

Holder, J. C., and Cohen, P. (1997) Insulin activates protein kinase B, inhibits glycogen synthase kinase-3 and activates glycogen synthase by rapamycin-insensitive pathways in skeletal muscle and adipose tissue. *FEBS Lett.* **406,** 211–215

54. Nakae, J., Park, B. C., and Accili, D. (1999) Insulin stimulates phosphorylation of the forkhead transcription factor FKHR on serine 253 through a Wortmannin-sensitive pathway. *J. Biol. Chem.* **274,** 15982–15985
55. Nakae, J., Kitamura, T., Ogawa, W., Kasuga, M., and Accili, D. (2001) Insulin regulation of gene expression through the forkhead transcription factor Foxo1 (Fkhr) requires kinases distinct from Akt. *Biochemistry* **40,** 11768–11776
56. Brunet, A., Park, J., Tran, H., Hu, L. S., Hemmings, B. A., and Greenberg, M. E. (2001) Protein kinase SGK mediates survival signals by phosphorylating the forkhead transcription factor FKHRL1 (FOXO3a). *Mol. Cell. Biol.* **21,** 952–965
57. Geladi, P., and Kowalski, B. R. (1986) Partial least-squares regression—a tutorial. *Anal. Chim. Acta* **185,** 1–17
58. Wold, S. (1994) Exponentially weighted moving principal components—analysis and projections to latent structures. *Chemom. Intell. Lab. Syst.* **23,** 149–161
59. Sato, J. D., Kawamoto, T., Le, A. D., Mendelsohn, J., Polikoff, J., and Sato, G. H. (1983) Biological effects in vitro of monoclonal antibodies to human epidermal growth factor receptors. *Mol. Biol. Med.* **1,** 511–529
60. Dinarello, C. A. (2000) The role of the interleukin-1-receptor antagonist in blocking inflammation mediated by interleukin-1. *N. Engl. J. Med.* **343,** 732–734
61. Manos, E. J., and Jones, D. A. (2001) Assessment of tumor necrosis factor receptor and Fas signaling pathways by transcriptional profiling. *Cancer Res.* **61,** 433–438
62. Lowe, S. W., Cepero, E., and Evan, G. (2004) Intrinsic tumour suppression. *Nature* **432,** 307–315
63. Service, R. F. (2003) Proteomics. Public projects gear up to chart the protein landscape. *Science* **302,** 1316–1318
64. Melton, L. (2004) Protein arrays: proteomics in multiplex. *Nature* **429,** 101–107
65. Tamura, S., Hanada, M., Ohnishi, M., Katsura, K., Sasaki, M., and Kobayashi, T. (2002) Regulation of stress-activated protein kinase signaling pathways by protein phosphatases. *Eur. J. Biochem.* **269,** 1060–1066
66. Bro, R. (1996) Multiway calibration. Multilinear PLS. *J. Chemom.* **10,** 47–61
67. Yi, T. M., Huang, Y., Simon, M. I., and Doyle, J. (2000) Robust perfect adaptation in bacterial chemotaxis through integral feedback control. *Proc. Natl. Acad. Sci. U. S. A.* **97,** 4649–4653

Appendix B

Reprinted from:

Janes, K. A., Gaudet, S., Albeck, J. G., Nielsen, U. B., Lauffenburger, D. A., and Sorger, P. K. (2006).

The response of human epithelial cells to TNF involves an inducible autocrine cascade.

Cell *124*, 1225-1239.

In this study I performed the experiments shown in Figures 1B, 1C, 1D, 4D, 4E, 4F, 5F, 5G, and 5J. All other experiments were performed by Kevin Janes, Suzanne Gaudet, and Ulrik Nielsen.

The Response of Human Epithelial Cells to TNF Involves an Inducible Autocrine Cascade

Kevin A. Janes,[1,2] Suzanne Gaudet,[1,3] John G. Albeck,[1,3] Ulrik B. Nielsen,[4] Douglas A. Lauffenburger,[1,2,3] and Peter K. Sorger[1,2,3,*]
[1] Center for Cell Decision Processes
[2] Department of Biological Engineering
[3] Department of Biology
Massachusetts Institute of Technology, 77 Massachusetts Avenue, Cambridge, MA 02139, USA
[4] Merrimack Pharmaceuticals, Cambridge, MA 02139, USA
*Contact: psorger@mit.edu
DOI 10.1016/j.cell.2006.01.041

SUMMARY

Tumor necrosis factor (TNF) is a proinflammatory cytokine that induces conflicting pro- and antiapoptotic signals whose relative strengths determine the extent of cell death. TNF receptor (TNFR) has been studied in considerable detail, but it is not known how crosstalk among antagonistic pro- and antiapoptotic signals is achieved. Here we report an experimental and computational analysis of crosstalk between prodeath TNF and prosurvival growth factors in human epithelial cells. By applying classifier-based regression to a cytokine-signaling compendium of ~8000 intracellular protein measurements, we demonstrate that cells respond to TNF both directly, via activated TNF receptor, and indirectly, via the sequential release of transforming growth factor-α (TGF-α), interleukin-1α (IL-1α), and IL-1 receptor antagonist (IL-1ra). We refer to the contingent and time-varying series of extracellular signals induced by TNF as an "autocrine cascade." Time-dependent crosstalk of synergistic and antagonistic autocrine circuits may serve to link cellular responses to the local environment.

INTRODUCTION

Cytokines and their receptors activate complex signaling networks composed of diverse proteins whose overall function is to control cell fate and function (Downward, 2001). Understanding these intracellular networks is complicated in part because many receptors generate competing, and even antagonistic, intracellular signals. For example, tumor necrosis factor (TNF) promotes cell death by inducing activation of the cysteine proteases caspase-8 and caspase-3 (Nicholson and Thornberry, 1997) but also promotes cell survival by activating the nuclear factor-κB (NF-κB) transcription factor (Karin and Ben-Neriah, 2000). In tissues, the connection between signals and cell fate is even more complex because cells are exposed to multiple cytokines that act together in synergistic and antagonistic combinations. Conflicting stimuli often arise when cells are exposed to paracrine cytokines from neighboring cells together with autocrine cytokines secreted by the cell itself. In colonic epithelia, for example, TNF secreted by inflammatory cells is a key mediator of inflammatory bowel disease (Rutgeerts et al., 2004) and can lead to epithelial cell death, whereas locally produced epidermal growth factor (EGF) and insulin-like growth factor (IGF) are critical for cell division and repair of the mucosa (Chailler and Menard, 1999; Singh and Rubin, 1993).

Individual cytokines and receptors have been studied extensively, but relatively little is known about intracellular processing of antagonistic signals. It is likely that crosstalk between individual receptors and their downstream signaling pathways is important. We reasoned that crosstalk could be studied effectively by using a large-scale systematic approach in which cells were treated with antagonistic cytokines and multiple downstream signals were then measured to create a data compendium. We anticipated that most crosstalk would be intracellular and involve the joint regulation of signaling proteins such as mitogen-activated protein kinases, caspases, etc. We therefore assayed intracellular signaling proteins for which reliable quantitative measurements were available (Janes et al., 2003; Nielsen et al., 2003). By focusing on known pathways and proteins, the compendium approach does not seek to identify new signaling proteins but rather to uncover how the activities of known molecules are coordinated during a physiological stimulus. For TNF, our systematic analysis revealed the surprising importance of crosstalk via extracellular autocrine signaling in specifying cell fate.

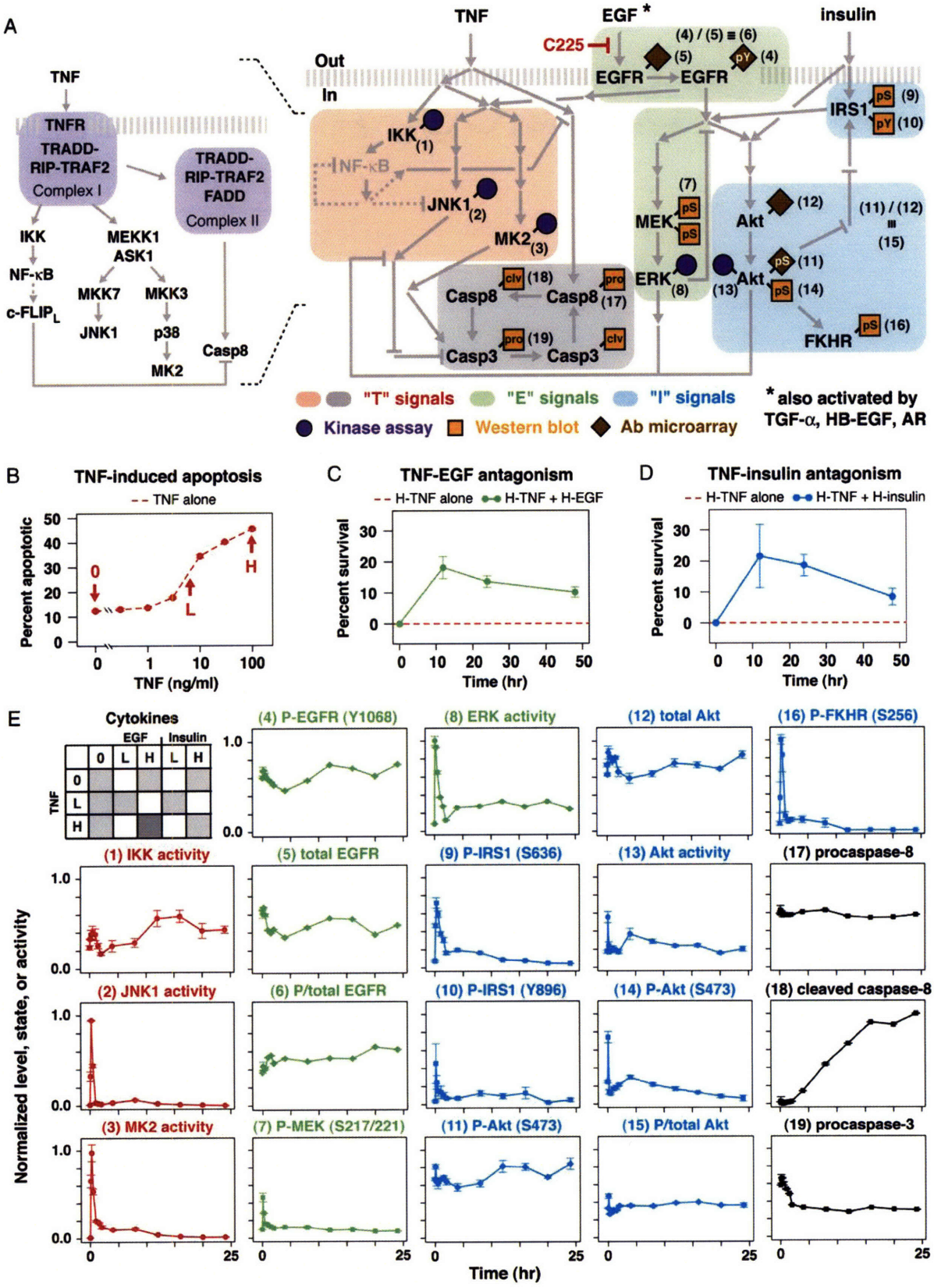
A
TNF
EGF *
insulin
C225
(4) / (5) ≡ (6)
(5)
(4)
pY
EGFR
EGFR
Out
In
TNF
TNFR
TRADD-
RIP-TRAF2
Complex I
TRADD-
RIP-TRAF2
FADD
Complex II
IKK
(1)
NF-κB
JNK1
(2)
MK2
(3)
IRS1
pS
(9)
pY
(10)
(7)
MEK
pS
pS
ERK
(8)
(12)
Akt
(11) / (12)
≡
(15)
(13)
Akt
pS
(11)
pS
(14)
FKHR
pS
(16)
IKK
NF-κB
c-FLIP$_L$
MEKK1
ASK1
MKK7
MKK3
JNK1
p38
MK2
Casp8
clv
(18)
Casp8
pro
(17)
Casp3
pro
(19)
Casp3
clv
"T" signals
"E" signals
"I" signals
Kinase assay
Western blot
Ab microarray
* also activated by
TGF-α, HB-EGF, AR
B
TNF-induced apoptosis
TNF alone
Percent apoptotic
0
L
H
TNF (ng/ml)
C
TNF-EGF antagonism
H-TNF alone
H-TNF + H-EGF
Percent survival
Time (hr)
D
TNF-insulin antagonism
H-TNF alone
H-TNF + H-insulin
Percent survival
Time (hr)
E
Cytokines
EGF
Insulin
TNF
0
L
H
(4) P-EGFR (Y1068)
(8) ERK activity
(12) total Akt
(16) P-FKHR (S256)
(1) IKK activity
(5) total EGFR
(9) P-IRS1 (S636)
(13) Akt activity
(17) procaspase-8
(2) JNK1 activity
(6) P/total EGFR
(10) P-IRS1 (Y896)
(14) P-Akt (S473)
(18) cleaved caspase-8
(3) MK2 activity
(7) P-MEK (S217/221)
(11) P-Akt (S473)
(15) P/total Akt
(19) procaspase-3
Normalized level, state, or activity
Time (hr)

TNF is the prototypical member of a family of 19 related proapoptotic and proinflammatory cytokines (Aggarwal, 2003; Chen and Goeddel, 2002). Trimeric TNF binds to a TNF receptor (TNFR) trimer, leading to intracellular assembly of two multicomponent death-inducing signaling complexes, DISC-I and DISC-II (Figure 1A; Barnhart and Peter, 2003; Micheau and Tschopp, 2003). DISC-I is an early membrane bound complex that signals through the NF-κB, JNK, and p38 pathways, whereas DISC-II is a later cytoplasmic complex that activates caspases-8 and -3 (Micheau and Tschopp, 2003). NF-κB signaling from DISC-I antagonizes caspase signaling from DISC-II by inducing transcription of survival factors, such as c-FLIP$_L$, which regulate caspase-8 activation (Micheau et al., 2001, 2002). In many cell types, the proapoptotic functions of TNF are also antagonized by mitogenic cytokines such as EGF, insulin, and IGFs (Garcia-Lloret et al., 1996; Qian et al., 2001; Wu et al., 1996). EGF, insulin, and IGFs bind dimeric receptors that signal via adaptor proteins to ERK, Akt, and other kinase pathways (Figure 1A; Avruch, 1998; Schlessinger, 2004). Growth-factor receptors respond acutely to changes in exogenous ligands and also transduce chronic signals arising from constitutive autocrine stimulation. Autocrine signaling is critically important for the survival and the progression of many cancers (Hambek et al., 2001; Torrance et al., 2000), and small-molecule- and antibody-based therapies have therefore been developed to disrupt receptor-ligand binding, receptor dimerization, and signaling (Hofmann and Garcia-Echeverria, 2005; Mendelsohn and Baselga, 2000). The possibility that these drugs have secondary effects on inflammatory signaling has not been investigated extensively, despite evidence linking inflammation and cancer (Karin and Greten, 2005).

In this paper, we combine conventional and high-throughput experimental methods with numerical analysis to uncover mechanisms of crosstalk involving pro- and antiapoptotic signals induced by TNF. Time-dependent profiles of 19 intracellular signals were measured in cells costimulated with TNF and either EGF or insulin (two prototypical survival factors) to create a cytokine-signaling compendium of ~8000 measurements. We describe elsewhere the experimental methods used to collect, validate, and systematize the compendium (Gaudet et al., 2005) and focus here on the surprising finding that a large fraction of TNF-induced crosstalk occurs extracellularly via regulated shedding of autocrine cytokines. We find that TNF activates a multistep, time-varying "autocrine cascade" in which three secreted factors other than TNF play pro- and antiapoptotic roles: transforming growth factor-α (TGF-α), interleukin-1α (IL-1α), and interleukin-1 receptor antagonist (IL-1ra). Intracellular signaling activated by these cytokines specifies the extent of TNF-induced apoptosis in a self-limiting fashion. While elucidation of the TNF-TGF-α-IL-1α-IL-1ra autocrine cascade involved statistical analysis of a large data compendium, key hypotheses were independently validated using a combination of neutralizing antibodies, small-molecule drugs, and receptor antagonists. We conclude from both large-scale and directed experiments that extracellular autocrine crosstalk plays as important a role as intracellular crosstalk in coordinating cellular responses to TNF.

RESULTS

To explore crosstalk between conflicting mitogenic and apoptotic signals, HT-29 human colonic adenocarcinoma cells were stimulated with TNF in combination with either EGF or insulin. The potency of TNF as a proapoptotic factor in epithelial cells is most apparent when combined with immunostimulatory cytokines such as interferon-γ (IFN-γ; Fransen et al., 1986). Thus, ten combinations of TNF, insulin, and EGF, at either subsaturating ("low" or "L-") or saturating ("high" or "H-") concentrations, were added to HT-29 cells pretreated with IFN-γ for 24 hr (see Experimental Procedures; Figures 1B–1D). A "mock" treatment ("0"), in which cells were manipulated as in other experiments but without added cytokine, served as a baseline control (Figure 1B and data not shown). Triplicate cell extracts were prepared at 13 time points spanning 0 min (before stimulus) to 24 hr, and 19 protein measurements made from each extract. Since many kinase signals

Figure 1. Design and Collection of a TNF-EGF-Insulin Signaling Compendium

(A) Schematic of well-recognized intracellular signaling proteins shared by TNF, EGF, and insulin. Nineteen signals (parentheses) were selected throughout the network and measured by high-throughput kinase assay (Janes et al., 2003), Western blotting, or antibody (Ab) microarray (Nielsen et al., 2003). P/total EGFR (signal 6) and P/total Akt (signal 15) signals were defined by taking the ratio of the phospho- and total signals measured by antibody microarray. Signals were defined as "T" signals (red or black), "E" signals (green), or "I" signals (blue) as described in the text. Dashed arrows indicate transcriptional pathways.

(B) Dose response for HT-29 apoptosis induced by various concentrations of TNF. Apoptosis was measured at 24 hr by annexin V-propidium iodide staining and flow cytometry as described in Experimental Procedures. Mock (0), low (L), and high (H) TNF concentrations were defined at 0, 5, and 100 ng/ml (red).

(C and D) Growth-factor antagonism of TNF-induced apoptosis. HT-29 cells were costimulated with 100 ng/ml TNF (H-TNF) and 100 ng/ml EGF (H-EGF, [C]) or 500 ng/ml insulin (H-insulin, [D]) and compared against 100 ng/ml TNF alone (red) for apoptosis at 12, 24, and 48 hr as described in (B). Percent survival was calculated as described (Janes et al., 2003). Baseline apoptosis values for H-TNF alone were 17%, 36%, and 60% at 12, 24, and 48 hr, respectively.

(E) Signaling network response to 100 ng/ml TNF (H-TNF) and 100 ng/ml EGF (H-EGF). Signals are referenced by number to the targets specified in (A). Data are presented as the mean ± SEM of triplicate biological samples as described in Experimental Procedures. Nine combinations of TNF, EGF, and insulin (shaded boxes, with H-TNF + H-EGF shaded dark gray), as well as a tenth combination of 0.2 ng/ml TNF + 1 ng/ml insulin, were similarly measured and are available in the Supplemental Data.

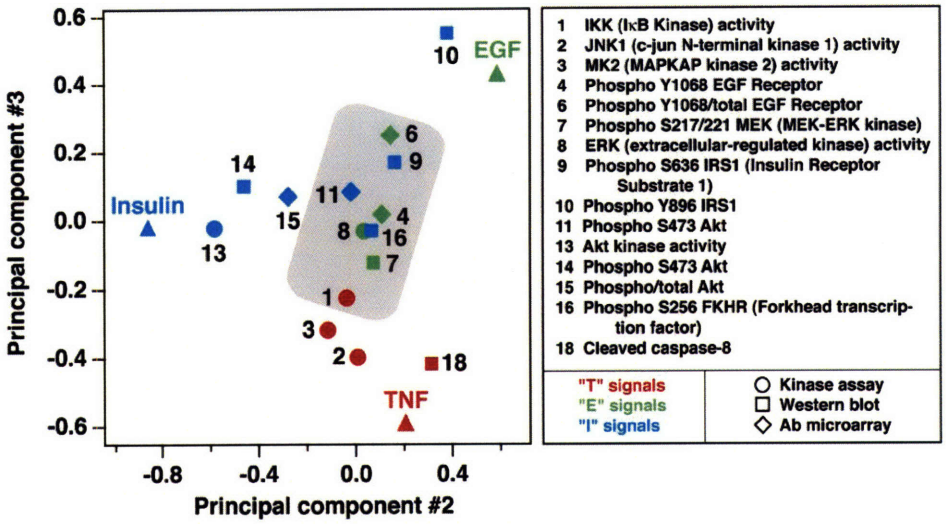

Figure 2. DPLSR Mapping of Intracellular Crosstalk in the Network Shared by TNF, EGF, and Insulin

Data were mapped as described in Experimental Procedures and in Figure S1 (Janes et al., 2004). The numbers, colors, and markers are identical to those in Figure 1E, except for cleaved caspase-8 (signal 18), which has been changed from black to red for clarity. The gray box indicates the crosstalk region shared by TNF, EGF, and insulin.

exhibit rapid changes between 0 and 30 min, whereas caspases rise slowly in activity over many hours, the 13 time points were distributed unevenly, with seven "early" time points concentrated at t = 0–2 hr and six "late" time points spread from t = 4–24 hr. The net result was a multidimensional data set describing time-dependent changes in protein activities following the stimulation of cells with ten distinct cytokine cues.

Considerable effort was expended to ensure the reproducibility and self-consistency of the data (Gaudet et al., 2005). The median coefficient of variation for biological repeats across the full data set was ~11%, making it possible to detect changes in protein state or activity as small as ±15%–25%, even between experiments performed on different days. Inspection of the complete 7980-measurement data set revealed several distinct time courses of signaling. We observed fast-acting "transient" signals, such as c-Jun N-terminal kinase 1 (JNK1) activity, which peaked at 15 min and returned to baseline by 1 hr (Figure 1E, signal 2). Many examples of "sustained" or slow-rising signals were also observed, such as cleaved caspase-8 levels, which began to increase at t > 2 hr and remained high for the duration of the observation period (Figure 1E, signal 18). Based on information in the literature, the 19 measurements acquired at each time point were roughly characterized as TNF-dependent ("T" signals), EGF-dependent ("E" signals), or insulin-dependent ("I" signals; see Figure 1A). Importantly, each cytokine treatment elicited multiple classes of signals: high TNF activated both T and E signals, and high TNF + high EGF elicited T, E, and I signals (Figure 1E and data not shown). We therefore conclude that, as expected, TNF, EGF, and insulin exhibit significant crosstalk at the level of intracellular protein signals.

Mapping Intracellular Crosstalk onto a Shared Cytokine-Signal Space

To visualize connections between intracellular signals and cytokine treatments in a simple and intuitive way, we constructed a compact representation of the entire compendium by using discriminant partial least squares regression (DPLSR; Janes et al., 2004). A DPLSR map was created such that the signaling proteins and cytokines were projected onto a set of "principal components" that maximized covariation between the time-integrated signaling profiles and the corresponding cytokine treatment (see Figure S1 in the Supplemental Data available with this article online for details). The first principal component in the DPLSR map corresponded to a baseline that distinguished all cytokine treatments from mock stimulation, whereas the second and third principal components discriminated among TNF, EGF, and insulin treatments (Figure S1 and data not shown). The latter two principal components therefore identified cytokine-specific signals as well as instances where two or more cytokine pathways had converged upon a common signaling protein.

By plotting cytokine treatments and integrated signals along the two dimensions defined by the second and third principal components, the extent of covariance among signals and treatments could be evaluated. Some cases of covariation were expected: For example, the cleavage of caspase-8 mapped close to TNF (Figure 2, signal 18), consistent with evidence that caspase-8 is activated by TNFR via formation of DISC-II (Micheau and Tschopp, 2003). Similarly, three measures of Akt activity (signals 13–15) mapped close to insulin, which is a powerful inducer of Akt signaling (Avruch, 1998). Sometimes, the map position suggested unexpected biological regulation: For example, the phosphorylation of IRS1 on Y896

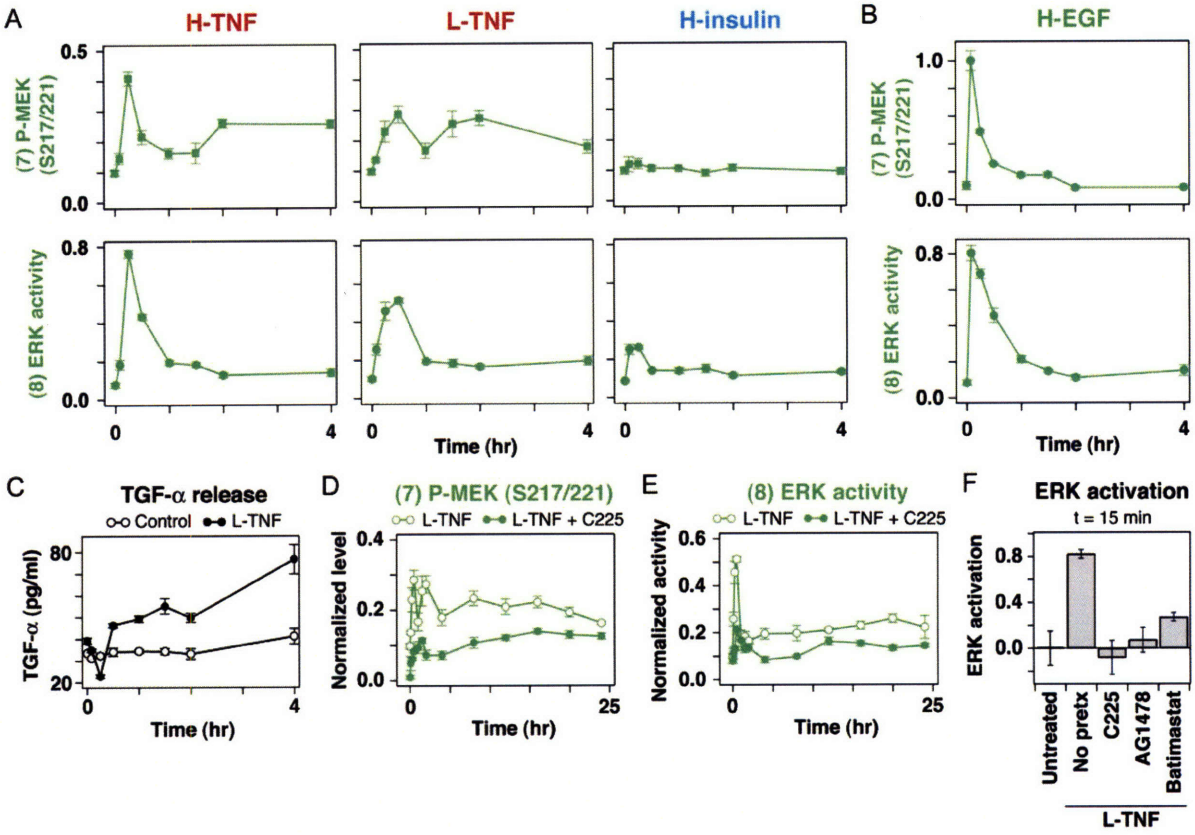

Figure 3. TNF Activates an Early-Phase TGF-α Autocrine Circuit to Crosstalk through the EGFR-MEK-ERK Signaling Pathway

(A) Comparison of P-MEK (upper) and ERK (lower) signaling dynamics induced by 100 ng/ml TNF (H-TNF, left), 5 ng/ml TNF (L-TNF, center), and 500 ng/ml insulin (H-insulin, right). EGFR phosphorylation was similarly increased in response to TNF (data not shown).

(B) Comparison of P-MEK (upper) and ERK (lower) signaling dynamics induced by 100 ng/ml EGF (H-EGF).

(C) TGF-α release in response to 5 ng/ml TNF (L-TNF) in the presence of 10 μg/ml C225 pretreatment for 1 hr before stimulation. The control treatment was a mock stimulation with carrier only. Similar results were obtained in the absence of C225 (data not shown).

(D and E) TNF-induced E signaling through EGFR. pMEK (D) and ERK (E) signaling were measured after stimulation with 5 ng/ml TNF (L-TNF) in the presence or absence of 10 μg/ml C225 pretreatment.

(F) Perturbation of TNF-induced ERK activation by pretreatment with 10 μg/ml C225, 1 μM AG1478, or 10 μM batimastat for 1 hr before stimulation with 5 ng/ml TNF (L-TNF) for 15 min. 0.1% DMSO was added as a control pretreatment (No pretx). ERK activity from untreated cells was included as a baseline, and ERK activation was defined as the increase in ERK activity compared to these untreated cells.

Data are presented as the mean ± SEM of triplicate biological samples as described in Experimental Procedures.

(P-IRS1(Y896); signal 10) was closely associated with EGF but not insulin (Gaudet et al., 2005). Of greatest interest was the clustering of signals midway between TNF, EGF, and insulin, possibly implying covariance of the signals with two or more cytokines (Figure 2, gray box). When the Euclidean distance between cytokine cues and signals in this central cluster was calculated, E signals such as EGFR (Figure 2, signal 4), ERK (signal 8), and MAPK-ERK kinase (MEK, signal 7), were found to be roughly equidistant to TNF and EGF cytokine stimuli but significantly farther from insulin ($p < 0.05$). Inspection of individual cytokine time courses confirmed that TNF treatment activated EGFR, ERK, and MEK to a similar extent as EGF itself, whereas insulin did not (Figures 3A and 3B and data not shown). Others have noted crosstalk between TNF and EGF (Chen et al., 2004; Izumi et al., 1994), supporting the paradoxical conclusion that TNF activates EGFR and its downstream targets MEK and ERK with strength and kinetics similar to EGF.

Rapid Activation of a TGF-α Autocrine Circuit by TNF

A direct intracellular link from activated TNFR to ERK has not been established, but TNF can induce the shedding of EGF-family ligands in mammary epithelial cells following 24 hr of stimulation (Chen et al., 2004). HT-29 cells also shed ligands of the EGF family (Anzano et al., 1989), so we asked whether TNF could stimulate this shedding with the rapid kinetics observed for MEK, ERK, and EGFR activation (Figure 3A and data not shown). EGF-family ligands known to act as autocrine factors include TGF-α, amphiregulin (AR), and heparin binding epidermal growth factor (HB-EGF). Quantitative ELISA measurements of

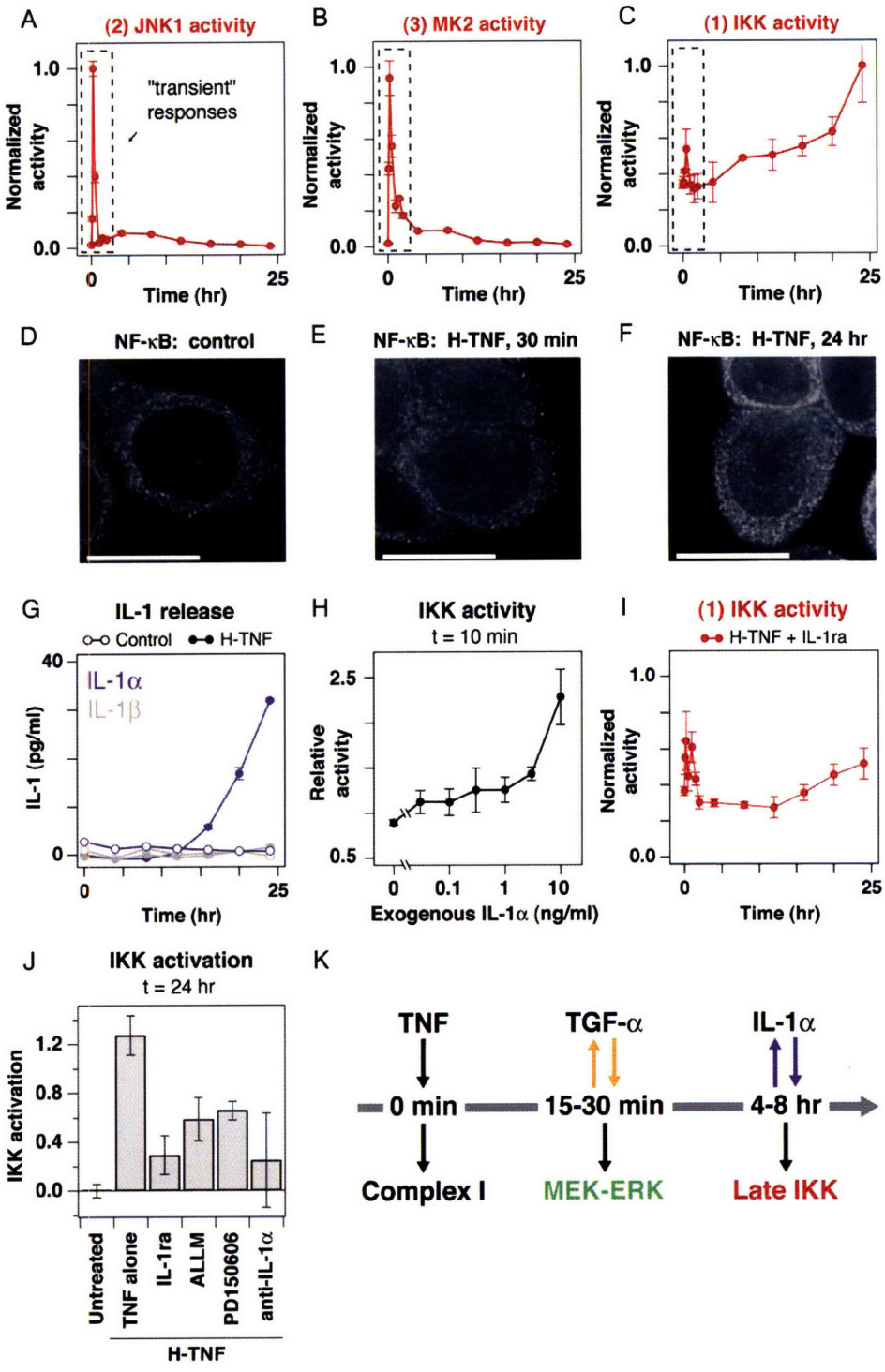

Figure 4. TNF Activates a Late-Phase IL-1α Autocrine Circuit to Crosstalk through the IKK-NF-κB Signaling Pathway

(A–C) TNF-induced signaling after stimulation with 100 ng/ml TNF. JNK1 activity (A), MK2 activity (B), and IKK activity (C) dynamics are shown, with a dotted box highlighting transient responses ($t < 2$ hr).

(D–F) Indirect immunofluorescence images of the p65 subunit of NF-κB in untreated cells (D) and in cells stimulated with 100 ng/ml TNF (H-TNF) for 30 min (E) and 24 hr (F). Scale bar = 15 μm.

(G) IL-1α (purple) and IL-1β (gray) release in response to 100 ng/ml TNF (H-TNF) in the presence of 10 μg/ml IL-1ra costimulation. The control treatment was a mock stimulation with carrier only. Similar results were obtained in the absence of IL-1ra (data not shown).

EGF-family ligands in conditioned medium of HT-29 cells before and after TNF addition showed all three to be present, but only TGF-α was upregulated by TNF (Figure 3C and Figure S2). TNF-induced TGF-α release in HT-29 cells was much faster than previously reported (Chen et al., 2004), peaking 1 hr after TNF addition (Figure 3C). Thus, TNF stimulation is associated with near-immediate release of an EGFR ligand, TGF-α, into the medium. Although transcriptional upregulation of TGF-α by growth-factor signaling pathways has been reported (Schulze et al., 2001), the rapidity of TGF-α release after TNF treatment suggests a posttranslational mechanism.

Addition of exogenous EGF rapidly activated MEK and ERK in HT-29 cells (Figure 3B). We therefore asked whether TNF-stimulated release of endogenous TGF-α also activated MEK and ERK in an EGFR-dependent fashion. When cells were treated with C225 antibody to block the interaction of EGFR with its ligands (Figure S3), dramatic inhibition of both acute (t = 0–2 hr) and sustained (t = 2–24 hr) MEK-ERK activation was observed after TNF treatment (Figures 3D and 3E). The significant and persistent reduction in MEK-ERK signaling following TNF stimulation (4-fold lower at t = 30 min, $p < 0.005$ and 2-fold lower at t = 4–24 hr, $p < 10^{-6}$) demonstrates a predominantly EGFR-dependent pathway. ERK activation was also blocked by a small-molecule inhibitor of the EGFR kinase (AG1478) and an inhibitor of the matrix metalloproteases that mediate TGF-α shedding from the plasma membrane (batimastat; Peschon et al., 1998; Figure 3F). Taken together, these data show that an autocrine circuit involving TGF-α and EGFR is the primary mechanism by which TNF activates MEK-ERK signaling at both short (t < 1 hr) and long (t > 4 hr) timescales in HT-29 cells. The delay between the peak of direct ERK activation by EGF at t = 5 min and indirect activation by TNF at t = 15 min is an estimate of the minimum time required to establish the TNF-induced TGF-α autocrine circuit (Figure 3A).

TNF Activates a Late-Phase IL-1α Autocrine Circuit

Further inspection of the DPLSR map revealed that IKK activity (Figure 2, signal 1) was also unexpectedly distant from its presumed inducer, TNF. JNK1 and MK2 are two well-recognized TNF-induced signals that, unlike IKK, were close to TNF on the DPLSR map (Figure 2, signals 2 and 3; Wajant et al., 2003). We therefore compared the dynamics of their activation to that of IKK. All three T signals were strongly induced 5–30 min after TNF addition, but IKK was unique in exhibiting a second, sustained phase of activation, rising from 4–24 hr (Figures 4A–4C). In the classical TNF-induced pathway, IKK phosphorylates and inactivates IκB, an NF-κB inhibitor, which allows NF-κB to translocate into the nucleus and induce gene expression (Karin and Ben-Neriah, 2000). By immunofluorescence, we found that the p65 subunit of NF-κB—which was largely cytoplasmic before TNF stimulation, reflecting its sequestration by IκB (Figure 4D)—was present at high levels in the nucleus in TNF-treated cells during early (t = 30 min) and late (t = 24 hr) peaks of IKK activation (Figures 4E and 4F). Thus, the two distinct phases of IKK signaling both appear to activate NF-κB. However, since JNK1 and MK2 activities had returned to low levels by t = 1 hr (Figures 4A and 4B), it seemed unlikely that sustained IKK and NF-κB signaling at t > 4 hr was mediated directly by TNF.

One circumstance in which sustained NF-κB activation is well described is in ultraviolet-irradiated keratinocytes, where late NF-κB signaling is known to depend on secondary release of IL-1α (Bender et al., 1998). Because IL-1 cytokines are potent IKK agonists (Dinarello, 1997), we asked whether TNF treatment of HT-29 cells might lead to IL-1 release and whether IL-1 would provoke sustained IKK activation. We observed an 8-fold increase in soluble IL-1α, but not IL-1β, in conditioned medium from TNF-treated cells 12–24 hr after TNF addition (Figure 4G). HT-29 cells are known to express the IL-1 receptor (IL-1R; Panja et al., 1998), and we found that exogenous IL-1α activated IKK at concentrations as low as 30 pg/ml (Figure 4H), consistent with the recognized ligand sensitivity of IL-1R (Dinarello, 1997). Thus, HT-29 cells are IL-1 responsive and secrete IL-1α after TNF stimulation, suggesting that IL-1α might constitute a TNF-dependent activator of IKK.

To determine whether IKK activation in TNF-treated cells was dependent on secreted IL-1α, IKK activity was measured in cells treated with high TNF in the presence of saturating levels of IL-1ra, a naturally occurring IL-1R antagonist (Figure S3; Dinarello, 2000). We observed that activation of IKK 15–30 min after TNF addition was unaltered by IL-1ra, consistent with a direct pathway via TNFR (Figure 4I). However, sustained IKK activation 4–24 hr after TNF addition was significantly reduced by IL-1ra addition ($p < 0.001$; Figures 4C and 4I). Substantial reductions in TNF-induced IKK activity at 24 hr were also observed with ALLM and PD150606, two structurally distinct calpain inhibitors that block processing and release

(H) IKK activity induced by recombinant IL-1α. HT-29 cells were stimulated with various concentrations of exogenous IL-1α for 10 min and analyzed for IKK activity.

(I) IKK response to 100 ng/ml TNF (H-TNF) with 10 μg/ml IL-1ra cotreatment. Cells were treated and measured for IKK activity as shown in (C) but in the presence of IL-1ra.

(J) Perturbation of TNF-induced IKK activation by cotreatment with 10 μg/ml IL-1ra, 25 μM ALLM, 25 μM PD150606, or 1 μg/ml anti-IL-1α during stimulation with 100 ng/ml TNF (H-TNF) for 24 hr. IKK activity from untreated cells was included as a baseline, and IKK activation was defined as the increase in IKK activity compared to these untreated cells.

(K) Timeline of TNF-induced TGF-α and IL-1α autocrine circuits and autocrine-dependent signals.

For (A)–(C) and (G)–(J), data are presented as the mean ± SEM of triplicate biological samples as described in Experimental Procedures.

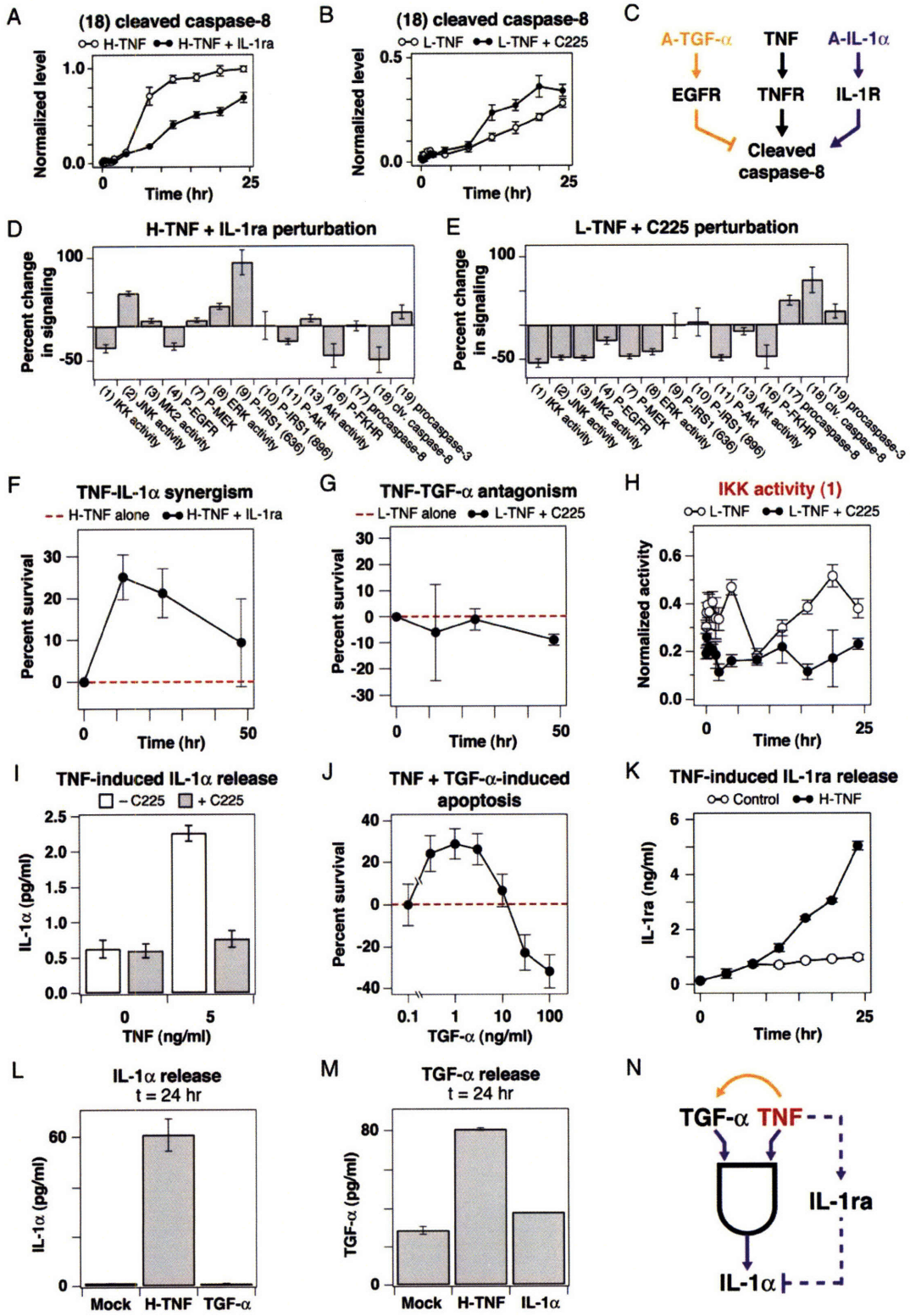

Figure 5. The TNF-Induced TGF-α and IL-1α Circuits Are Coupled with an IL-1ra Circuit to Form an Autocrine Cascade

(A and B) Quantitative changes in TNF-induced caspase signaling after perturbation of the TGF-α and IL-1α autocrine circuits. Cleaved caspase-8 responses to 5 ng/ml TNF (L-TNF) with or without 10 μg/ml C225 pretreatment (A) or 100 ng/ml TNF (H-TNF) with or without 10 μg/ml IL-1ra cotreatment (B). TNF-induced procaspase-3 signaling was also affected by IL-1ra (data not shown).

of IL-1α from cells (Kobayashi et al., 1990), as well as with IL-1α-neutralizing antibodies (Figure 4J). Together, these data show that IKK signaling at $t < 4$ hr is independent of IL-1α but that sustained IKK activation at $t > 4$ hr (which is quantitatively more significant in HT-29 cells; Figure 4C) is mediated primarily by the binding of IL-1α to IL-1R (Figure 4K). Thus, the early and late phases of IKK activation in TNF-treated HT-29 cells involve distinct direct and autocrine-indirect mechanisms.

Coupling of Sequential Autocrine Circuits into an Autocrine Cascade

The data described above establish that TGF-α and IL-1α autocrine circuits play important roles in the activation of MEK-ERK and IKK by TNF, but it remained unclear whether autocrine-dependent signaling altered the activity of caspases directly implicated in apoptosis. To study this, we blocked TGF-α- and IL-1α-dependent circuits individually and measured the cleavage of caspase-8, an important initiator caspase downstream of TNFR (Chen and Goeddel, 2002). Blocking IL-1R with IL-1ra significantly reduced TNF-stimulated cleavage of caspase-8 compared to TNF alone ($p < 10^{-9}$; Figure 5A). Conversely, blocking EGFR with C225 significantly increased TNF-induced caspase-8 cleavage ($p < 0.001$; Figure 5B). Thus, TNF-induced TGF-α and IL-1α exert opposing control on caspase-8 (Figure 5C). To determine how broad an effect EGFR or IL-1R blockade had on TNF-induced signaling, full time courses were collected for the 19 signals after TNF stimulation in the presence of IL-1ra or C225. When autocrine-perturbed time courses were compared to data in the original cytokine-signaling compendium, we found that the durations or magnitudes of roughly half of the measured signals were altered (Figures 5D and 5E). Thus, discrete perturbation of an autocrine circuit causes a system-wide alteration in the underlying intracellular signaling network.

The opposing contributions of TGF-α and IL-1α to TNF-induced caspase-8 cleavage implied that blocking EGFR-mediated signaling should decrease cell survival, whereas blocking IL-1R-mediated signaling should decrease cell death (Figure 5C). Consistent with this, we observed that TNF was less effective as a prodeath stimulus when IL-1α signaling was blocked with IL-1ra (Figure 5F). The potency of IL-1ra as a prosurvival factor in TNF-treated cells was comparable to that of saturating EGF or insulin (Figures 1C and 1D). In contrast, blocking TGF-α signaling with C225 antibody did not substantially increase TNF-induced cell death (Figure 5G). This was paradoxical because it implied that the ability of autocrine TGF-α to reduce caspase-8 cleavage (Figure 5C) did not translate into reduced cell death. In an attempt to resolve this paradox, the 19 signals measured for TNF + C225 treatment were examined more closely (Figure 5E). We observed that IKK activity was reduced to baseline levels throughout the time course, exhibiting neither early- nor late-phase activation ($p < 10^{-10}$; Figure 5H). The attenuation of late-phase IKK signaling ($t = 4$–24 hr) by C225 was particularly interesting because our results indicated that late-phase IKK signaling required an autocrine IL-1α circuit (Figures 4C and 4I). Therefore, it seemed possible that induction of the IL-1α circuit (and thus late IKK signaling) might depend upon prior release of TGF-α. To determine whether TGF-α and IL-1α release were linked, we blocked TGF-α-EGFR signaling with C225 and measured IL-1α levels following TNF stimulation. EGFR blockade with C225 completely prevented IL-1α release at low TNF concentrations (Figure 5I) and significantly reduced IL-1α release at high

(C) Autocrine TGF-α (A-TGF-α) and autocrine IL-1α (A-IL-1α) exert opposing control on TNF-induced caspase-8 cleavage.

(D and E) Network-level changes in TNF-induced signaling in the presence of 10 μg/ml C225 pretreatment (D) or 10 μg/ml IL-1ra cotreatment. Selected intracellular signals from C225- and IL-1ra-treated cells were integrated from 0–24 hr and compared to the integrated signals from 5 ng/ml TNF (L-TNF) and 100 ng/ml TNF (H-TNF) treatments without autocrine perturbation, respectively. Uncertainty in the integrated signaling profiles was calculated by bootstrapping with the original signaling replicates (Efron and Tibshirani, 1993).

(F) IL-1α-mediated synergism with TNF-induced apoptosis. HT-29 cells were cotreated with 100 ng/ml TNF (H-TNF) and 10 μg/ml IL-1ra and compared against H-TNF alone (red) for apoptosis at 12, 24, and 48 hr as described in Figure 1B (Janes et al., 2005). Baseline apoptosis values for H-TNF alone were 17%, 45%, and 67% at 12, 24, and 48 hr, respectively.

(G) TGF-α-mediated antagonism of TNF-induced apoptosis. HT-29 cells were pretreated with 10 μg/ml C225, stimulated with 5 ng/ml TNF (L-TNF), and compared against L-TNF alone (red) for apoptosis at 12, 24, and 48 hr as described in Figure 1B (Janes et al., 2005). Baseline apoptosis values for L-TNF alone were 11%, 24%, and 47% at 12, 24, and 48 hr, respectively.

(H) IKK response to 5 ng/ml TNF (L-TNF) with or without 10 μg/ml C225 pretreatment.

(I) IL-1α release induced by 0 or 5 ng/ml TNF with or without 10 μg/ml C225 pretreatment. The control treatment was a mock stimulation with carrier only.

(J) TGF-α-mediated antagonism for TNF-induced apoptosis. HT-29 cells were treated with various concentrations of TGF-α and 5 ng/ml TNF (L-TNF) and compared against L-TNF alone (red) for apoptosis at 24 hr as described in Figure 1B (Janes et al., 2005). Baseline apoptosis for L-TNF alone was 33%.

(K) IL-1ra release in response to 100 ng/ml TNF (H-TNF). The control treatment was a mock stimulation with carrier only.

(L) The IL-1α autocrine circuit is induced by TNF but not by TGF-α. HT-29 cells were treated with 100 ng/ml TNF (H-TNF) or 100 ng/ml TGF-α for 24 hr and analyzed for IL-1α release.

(M) The TGF-α autocrine circuit is induced by TNF but not by IL-1α. HT-29 cells were treated with 100 ng/ml TNF (H-TNF) or 10 ng/ml IL-1α for 24 hr and analyzed for TGF-α release.

(N) The molecular logic of the TNF-induced autocrine cascade. TNF, TGF-α, and IL-1α are coupled via an "AND" gate.

For (A)–(B) and (F)–(M), data are presented as the mean ± SEM of triplicate biological samples as described in Experimental Procedures. For (D) and (E), data are presented as the mean percent change ± SD from 1000 resamplings of the original data set.

TNF concentrations (Figure S4). Thus, proper function of the IL-1α autocrine circuit was dependent on the prior establishment of an EGFR-mediated TGF-α circuit.

The observed coupling between TGF-α and IL-1α autocrine circuits explains the inability of EGFR blockade to alter TNF-induced cell death significantly. In TNF-treated cells, C225 increased cleaved caspase-8 levels and reduced MEK-ERK signaling (which is generally regarded as a prosurvival signal; Ballif and Blenis, 2001), but C225 also prevented IL-1α release (Figure 5I), which mediates proapoptotic signals via IL-1R (Figure 5F). The ability of C225 to block the offsetting TGF-α- and IL-1α-dependent pathways implied that conditions could be found in which EGFR and IL-1R signals were not perfectly balanced. At some concentrations, TGF-α might act as a prosurvival factor and at others as a proapoptotic factor. To test this idea, cells were exposed to TNF in combination with exogenous TGF-α at 0.3–100 ng/ml, and the fraction of dying cells was measured. We observed that, at low concentrations, TGF-α was proapoptotic in combination with TNF, whereas at higher concentrations, it was prosurvival (Figure 5J), confirming our prediction.

The link between the TGF-α and IL-1α autocrine circuits raised the possibility that additional extracellular factors might contribute to TNF signaling and cellular responses. In recent microarray studies, we observed that transcription of the *IL-1ra* gene was strongly upregulated by TNF (K.A.J. and P.K.S., unpublished data). ELISA measurements on conditioned medium of HT-29 cells revealed that IL-1ra protein accumulated to significant levels 12 hr after TNF stimulation (Figure 5K). However, unlike IL-1α, TNF-induced IL-1ra release was unaffected by pretreatment with C225 antibody, indicating that IL-1ra induction does not require autocrine TGF-α (Figure S5). Thus, IL-1ra constitutes a third TNF-inducible autocrine factor, one with a prosurvival function (Figure 5F; Dinarello, 2000).

The successive waves of extracellular signaling circuits induced by TNF suggest the existence of an autocrine cascade involving TNF, TGF-α, IL-1α, and IL-1ra. The most interesting features of the cascade are the connections between individual autocrine circuits: TGF-α is required for IL-1α release, and IL-1ra inhibits the action of IL-1α. Is there a contingent logic underlying the order in which these signals are released? We found that the link between TGF-α and IL-1α (Figure 5I) was not reciprocal because addition of exogenous IL-1α did not induce shedding of TGF-α (Figure 5L). Moreover, exogenous TGF-α was not sufficient to provoke IL-1α release (Figure 5M), implying that signals from both TNFR and EGFR are required. The TGF-α and IL-1α circuits are therefore linked together unidirectionally. TNF and TGF-α comprise inputs to an "AND" function that induces IL-1α, which is subsequently inactivated by IL-1ra (Figure 5N).

Evidence for a TNF-Induced Autocrine Cascade in Diverse Epithelial Cell Types

To examine whether TNF-induced autocrine cascades are a conserved feature of TNF-responsive cells, we tested other epithelial cell lines for the essential features of the TGF-α-IL-1α-IL-1ra cascade. Specifically, we asked whether TNF would stimulate (1) release of TGF-α (Figure 6A), (2) release of IL-1α in an EGFR-dependent manner (Figure 6B), and (3) release of IL-1ra (Figure 6C). We focused on two human cell lines known to have receptors for TNF, EGF, and IL-1: A431 epidermoid carcinoma cells and nontransformed 184A1 human mammary epithelial cells (HMEC; Chen et al., 2004; Masui et al., 1993).

Both A431 and immortalized HMEC cells were treated with TNF, and cytokine levels were measured at t = 0, 2, and 24 hr by ELISA (Figures 6D–6I). We found that TGF-α, IL-1α, and IL-1ra levels all increased in A431 cells after TNF treatment. In particular, TGF-α release was nearly as rapid as in HT-29 cells. TNF-stimulated IL-1α release in A431 cells was inhibited significantly but not completely by C225, probably reflecting incomplete blockade of high EGFR levels on the surface of these cells (Masui et al., 1993). In analogous experiments with TNF-simulated HMEC cells, we found that TGF-α levels increased dramatically over a 24 hr period, IL-1α levels increased >2.5-fold, and IL-1ra levels increased >4-fold. Moreover, TNF-induced release of IL-1α into the medium was blocked almost completely by C225 anti-EGFR antibody. Thus, all three extracellular components of the TNF-stimulated TGF-α-IL-1α-IL-1ra autocrine cascade are present in HMEC cells, and induction of the IL-1α circuit is almost completely dependent on prior establishment of the TGF-α-EGFR circuit. The primary difference between HT-29 and HMEC cells is in the timing of TGF-α release, which was considerably slower in HMECs, perhaps reflecting a requirement for protein synthesis. Together, these data indicate that a TNF-induced autocrine cascade consisting of TGF-α, IL-1α, and IL-1ra cytokines exists in multiple epithelial cell types.

DISCUSSION

In this paper, we show that TNF induces three successive autocrine circuits, which together form an autocrine cascade that plays out over 24 hr (Figure 7A). Working in combination with TNF itself, the cascade adds layers of pro- and antiapoptotic signaling to set the level of apoptosis in a self-limiting fashion. Shortly after TNF addition, proapoptotic signals immediately downstream of TNFR binding are induced. About 10 min later, an autocrine TGF-α circuit is established, leading to prosurvival signaling through EGFR. The combination of TNF and TGF-α causes release of IL-1α starting at 4 hr, which in turn activates prodeath signaling through IL-1R. Finally, upregulation of the IL-1R antagonist IL-1ra by 8–12 hr negatively regulates IL-1R signaling and presumably constitutes a final antiapoptotic stimulus. Our work highlights the important but underappreciated role of autocrine crosstalk in determining cell fate. Individual autocrine circuits have previously been studied in multiple cellular contexts. However, extended connectivity between inducible autocrine circuits has not been reported previously, perhaps because

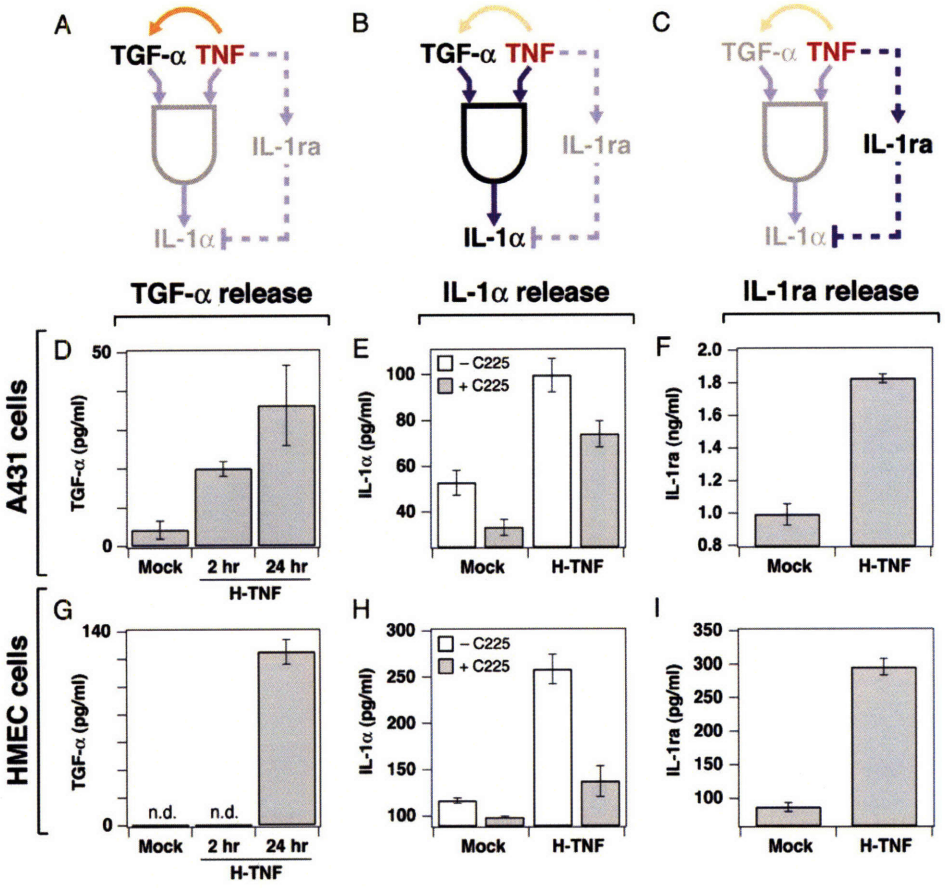

Figure 6. The Basic Elements of the TNF-Induced Autocrine Cascade Are Present in Other Epithelial Cell Types

(A–C) Main elements of the TNF-induced autocrine cascade: release of TGF-α (A), release of IL-1α in a TGF-α-dependent manner (B), and release of IL-1ra (C).

(D and E) The TNF-induced autocrine cascade exists in A431 cells. A431 cells were stimulated with 100 ng/ml TNF + 10 μg/ml C225 (H-TNF) (D–F) or 100 ng/ml TNF alone (E) and analyzed for TGF-α at 2 and 24 hr (D), IL-1α at 24 hr (E), and IL-1ra at 24 hr (F). The control treatment was a mock stimulation with carrier only.

(G–I) The TNF-induced autocrine cascade exists in human mammary epithelial cells (HMEC). HMEC cells were stimulated with 100 ng/ml TNF (H-TNF) (G–I) or 100 ng/ml TNF (H-TNF) + 10 μg/ml C225 (H) and analyzed for TGF-α at 2 and 24 hr (G), IL-1α at 24 hr (H), and IL-1ra at 24 hr (I). The control treatment was a mock stimulation with carrier only.

For (D)–(I), data are presented as the mean ± SEM of triplicate biological samples as described in Experimental Procedures. n.d., not detectable.

such linkages are only evident when large, multidimensional signaling data sets are examined.

Data, Statistical Mining, and Hypotheses

The construction of a systematic time-dependent compendium of cellular signals has been essential to our analysis of TNF. The 7980-measurement compendium contains quantitative information on 19 activities and states of kinases, caspases, transcription factors, adaptors, and other signaling proteins distributed across signaling networks downstream of TNFR, EGFR, and insulin receptor (Figure 1A). An advantage of constraining measurements to a limited number of proteins is that it becomes practical to examine many different cytokine combinations at multiple points in time. The experimental precision and reproducibility of the measurements also made it possible to study small (i.e., less than 2-fold) but biologically significant differences in signals from one cytokine treatment to the next. Our proteomic compendium is far from comprehensive, but, in the context of signal transduction, the multicomponent, multicytokine time courses represent a useful advance over more focused studies because they place dynamic information within a broader physiological context.

A major challenge with large experimental compendia is generating experimentally testable biological hypotheses. Here, we use DPLSR to derive a visually intuitive map from time-integrated signals (Janes et al., 2004). In related work, we construct alternative models that explicitly incorporate time-course data (Janes et al., 2005). Both analyses show that a TNF-induced autocrine cascade is critical in determining cell fate. However, it is important to note

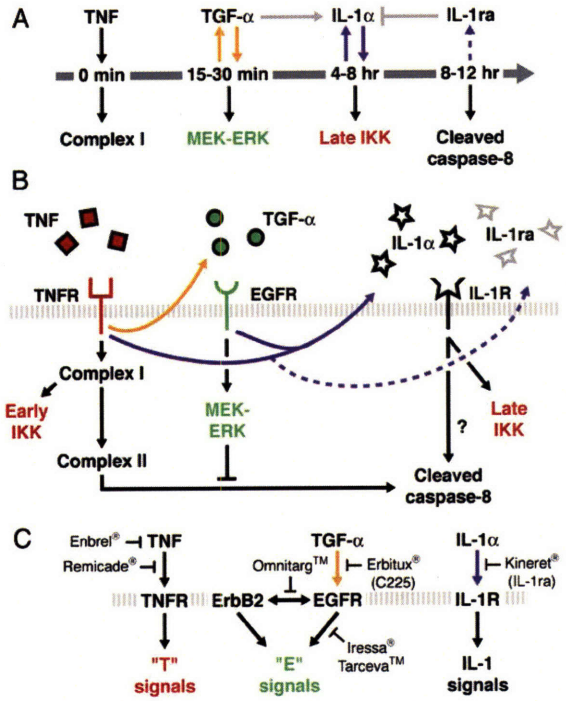

Figure 7. Model of TNF-Induced Extracellular Crosstalk

(A) Sequence of the time-dependent TNF-induced autocrine cascade established by TGF-α, IL-1α, and IL-1ra.

(B) Direct and autocrine-indirect intracellular signals activated by TNF.

(C) Approved pharmaceuticals that target different points of the TNF-induced autocrine cascade.

that, despite the importance of compendium data for hypothesis generation, critical features of the TNF-induced autocrine cascade were confirmed by independent experimentation without reference to DPLSR analysis. Hypothesis-testing experiments took advantage of highly specific (and clinically important) inhibitors of EGF and IL-1 signaling.

Intracellular Regulators of the TNF-Induced Autocrine Cascade

This study focuses on the role played by extracellular crosstalk in the response of cells to TNF (Figure 7B). However, intracellular crosstalk is equally important for regulating signaling proteins by two or more receptor types. We estimate that ~50% of signaling in HT-29 cells is attributable to autocrine factors induced by TNF and ~50% is dependent on direct signals downstream of TNFR. One clear point of intersection between internal and external signals is the regulation of metalloproteases and calpains, which cleave inactive membrane bound precursors to promote TGF-α and IL-1α shedding (Kobayashi et al., 1990; Peschon et al., 1998). The importance of metalloprotease and calpain activity for the TNF autocrine cascade is demonstrated by the effectiveness of small-molecule protease inhibitors in blocking autocrine ligand release. Regulation of membrane proteases is an area of active research (Goll et al., 2003), and increasing evidence suggests a role for protease phosphorylation (Fan and Derynck, 1999; Glading et al., 2004). However, current understanding of metalloprotease and calpain phosphorylation is insufficient to explain the dynamics of the TNF-induced autocrine cascade in HT-29 cells. For example, ERK has been implicated in cytokine-stimulated shedding of TGF-α (Fan and Derynck, 1999). However, most TNF-induced ERK activation occurs as a consequence (rather than a cause) of TGF-α release. Detailed analysis of protease regulation will be critical to understanding the autocrine cascades described here.

Molecular Logic of the Autocrine Cascade

TNF is known to stimulate the release of many soluble factors, but most are thought to act in a paracrine fashion (Pahl, 1999); very few studies have established a role for TNF in autocrine signaling (Chen et al., 2004). Likewise, crosstalk in intracellular networks is well recognized (Dumont et al., 2002), but extracellular crosstalk involving multiple autocrine signals has not been explicitly documented. The most striking feature of the TNF-induced autocrine cascade described here is its conditional "molecular logic." Activation of the IL-1α circuit requires prior TGF-α release, but TGF-α-IL-1α interaction depends on the presence of TNF because exogenous TGF-α alone does not cause IL-1α release. TGF-α-IL-1α crosstalk is also unidirectional: exogenous IL-1α does not cause TGF-α release. Likewise, IL-1ra is presumed to inhibit IL-1α signaling (Dinarello, 2000), but IL-1ra release is almost completely TNF dependent: it is only slightly decreased by EGFR blockade and only slightly induced by exogenous IL-1α (K.A.J. and P.K.S., unpublished data). These and other data reemphasize the complexity and current lack of understanding of the metalloprotease and calpain regulation in autocrine signaling.

Biological and Clinical Significance

Why does the response of cells to TNF involve complex self-limiting extracellular signals? Overlapping positive and negative feedback has been proposed as a means to optimize the sensitivity and stability of biological systems (Stelling et al., 2004). A role for autocrine circuits in sensing spatial ranges and local environmental cues has also been documented (Wiley et al., 2003). In agreement with this, we have found that the precise magnitude of autocrine-dependent apoptotic responses is cell-density dependent (J.G.A. and P.K.S., unpublished data). Our data suggest that TNF-induced cytokines do not travel far before rebinding to cells, but we have not yet established whether they bind to the original secreting cell in true-autocrine mode or whether they diffuse to adjacent cells in a paracrine fashion. Regardless, it seems likely that the TNF-TGF-α-IL-1α-IL-1ra cascade functions to link cell-death decisions to extracellular cues and thereby achieve microenvironment-sensitive control over cell fate (Figure 7A).

In the current work, we rely entirely on immortalized cells grown in vitro. It will now be important to study TNF-induced autocrine cascades in primary cells, such as hepatocytes and adipocytes, in which TNF has established physiological and pathological roles (Ruan and Lodish, 2003; Streetz et al., 2000). However, the TNF-induced autocrine cascade discovered in HT-29 cells clearly operates in a variety of other transformed and nontransformed cell lines. Like HT-29 cells, A431 and HMEC cells have inducible TNF-TGF-α-IL-1α-IL-1ra circuits, although the timing and magnitude of each loop in the cascade appears to vary. This suggests that the extent of crosstalk between autocrine and intracellular networks, and their relative physiological importance, may depend on cell type and stimulus. The cell-type specificity of the TNF-induced autocrine cascade clearly warrants further investigation.

Since its discovery three decades ago as an endotoxin-induced serum factor with tumoricidal activity, TNF has remained an important therapeutic target in a variety of human diseases (Carswell et al., 1975; Palladino et al., 2003). Neutralizing anti-TNF antibodies (e.g., Remicade) and decoy receptors (e.g., Enbrel) are now used to treat inflammatory bowel disease and rheumatoid arthritis (Figure 7C; Rutgeerts et al., 2004; Sfikakis and Kollias, 2003). However, clinical trials on sepsis and cancer, once promising targets for TNF treatment, have been disappointing and have highlighted the puzzling inefficacy and side effects of cytokine-directed therapy (Anderson et al., 2004; Reinhart and Karzai, 2001). Our experiments provide some insight into why therapeutics targeted against self-limiting autocrine systems are so difficult to design. For example, the treatment of TNF-stimulated HT-29 cells with the anti-EGFR antibody C225 (known commercially as Erbitux) does not increase the level of apoptosis, even though it causes extensive changes in both intracellular and extracellular signaling. It is not that Erbitux is inactive against HT-29 cells, but rather that proapoptotic effects of blocking TGF-α are offset by a reduction in IL-1α levels. Understanding how autocrine cascades operate in normal and diseased tissues seems likely to yield significant therapeutic insight, particularly with respect to multidrug therapies. Indeed, combination treatments involving anti-TNF biologics and IL-1ra are already being explored for the treatment of rheumatoid arthritis (Zwerina et al., 2004).

EXPERIMENTAL PROCEDURES

Cell-Line Treatments and Lysis

HT-29 cells were grown, plated, and sensitized with IFN-γ as described previously (Janes et al., 2003). Sensitized cells were then spiked with 0, 0.2, 5, 100 ng/ml TNF (Peprotech) + 0, 1, 100 ng/ml EGF (Peprotech) or 0, 1, 5, 500 ng/ml insulin (Sigma) as a 20× stock in serum-free medium. Triplicate plates were lysed at the indicated times as described (Gaudet et al., 2005; Janes et al., 2003). For TGF-α perturbation, C225, batimastat (both gifts from H.S. Wiley), AG1478 (Calbiochem), and anti-TGF-α antibody (R&D Systems) were added 1 hr before stimulation. For IL-1α perturbation, IL-1ra (R&D Systems), ALLM, PD150606 (both from Calbiochem), and anti-IL-1α antibody (R&D Systems) were added at the same time as stimulation. A431 cells (ATCC) and the HMEC line (Stampfer and Yaswen, 1993) were maintained in recommended growth medium, plated at 20,000 cells/cm^2, and sensitized and treated as described for HT-29 cells.

Network-Level Signaling Measurements

Kinase assays, Western blotting, and antibody microarrays were essentially performed as described (Janes et al., 2003, 2004; Nielsen et al., 2003). The full quantitative details of the network-level signaling measurements are reported elsewhere (Gaudet et al., 2005). The final processed data were normalized to the maximum value (across all conditions) for that signal to aid comparison of signals with different dynamic ranges.

DPLSR Mapping

Nine of ten cytokine treatments (all except 0.2 ng/ml TNF + 1 ng/ml insulin) were used for the DPLSR mapping. The signaling network dynamics were integrated by trapezoidal rule to calculate a composite metric for each signal within each time course. The integrated signals and treatment classes were mapped by DPLSR as described previously (Janes et al., 2004) and in Figure S1.

Enzyme-Linked Immunosorbent Assays

Conditioned medium from HT-29, A431, and HMEC cultures was analyzed for TGF-α, AR, HB-EGF, IL-1α, IL-1β, and IL-1ra according to manufacturer's recommendations (R&D Systems).

Indirect Immunofluorescence

Cells were fixed with 4% paraformaldehyde in PBS for 10 min at room temperature, then permeabilized with Perm/Wash (BD Biosciences) and stained with anti-RelA (Santa Cruz, 1:100) and Alexa 594 anti-rabbit IgG (Molecular Probes, 1:250). Coverslips were mounted with VectaShield, and imaging was performed with a 63× Plan-Apochromat objective and a Photometrics CoolSnap HQ camera on a DeltaVision RT Restoration microscope. 0.2 μm Z sections were acquired and deconvolved using Applied Precision SoftWorx software. Images are shown as individual slices from the reconstructed 3D image.

Apoptosis Measurements

Cells that scored double positive for cleaved cytokeratin (a caspase-3/6/7 substrate) and cleaved-caspase-3 were measured by flow cytometry or by annexin V-propidium iodide staining as described previously (Janes et al., 2003). Changes in survival were calculated as before (Janes et al., 2003).

Statistical Analysis

Covariations within the TNF-EGF-insulin network were calculated as the Euclidean distance between the signals and the cytokine cues on the DPLSR mapping (Figure 2); a Bonferroni-corrected Student's paired t test was used to compare Euclidean distances. For comparing two individual means, a Student's t test was used. For comparing two time courses, a two-way analysis of variance was used. All tests were performed at a significance level of $\alpha = 0.05$ with Bonferroni correction for multiple hypothesis testing when appropriate.

Supplemental Data

Supplemental Data include Supplemental References, five figures, and three tables and can be found with this article online at http://www.cell.com/cgi/content/full/124/6/1225/DC1/.

ACKNOWLEDGMENTS

We thank Michael Yaffe (MIT) and Steve Wiley (PNNL) for providing critical reagents and for helpful discussions, Emily Pace (Merrimack) for technical assistance with the antibody microarrays, and members of the Sorger and Lauffenburger laboratory who helped with experiments. This work was supported by NIH grant P50-GM68762 (P.K.S. and D.A.L.) and the Whitaker Foundation (K.A.J.). P.K.S. is a founder and chair of the Scientific Advisory Board of Merrimack

Pharmaceuticals. D.A.L. is a member of the Scientific Advisory Board of Merrimack Pharmaceuticals.

Received: May 26, 2005
Revised: October 19, 2005
Accepted: January 5, 2006
Published: March 23, 2006

REFERENCES

Aggarwal, B.B. (2003). Signalling pathways of the TNF superfamily: a double-edged sword. Nat. Rev. Immunol. *3*, 745–756.

Anderson, G.M., Nakada, M.T., and DeWitte, M. (2004). Tumor necrosis factor-alpha in the pathogenesis and treatment of cancer. Curr. Opin. Pharmacol. *4*, 314–320.

Anzano, M.A., Rieman, D., Prichett, W., Bowen-Pope, D.F., and Greig, R. (1989). Growth factor production by human colon carcinoma cell lines. Cancer Res. *49*, 2898–2904.

Avruch, J. (1998). Insulin signal transduction through protein kinase cascades. Mol. Cell. Biochem. *182*, 31–48.

Ballif, B.A., and Blenis, J. (2001). Molecular mechanisms mediating mammalian mitogen-activated protein kinase (MAPK) kinase (MEK)-MAPK cell survival signals. Cell Growth Differ. *12*, 397–408.

Barnhart, B.C., and Peter, M.E. (2003). The TNF receptor 1: a split personality complex. Cell *114*, 148–150.

Bender, K., Gottlicher, M., Whiteside, S., Rahmsdorf, H.J., and Herrlich, P. (1998). Sequential DNA damage-independent and -dependent activation of NF-kappaB by UV. EMBO J. *17*, 5170–5181.

Carswell, E.A., Old, L.J., Kassel, R.L., Green, S., Fiore, N., and Williamson, B. (1975). An endotoxin-induced serum factor that causes necrosis of tumors. Proc. Natl. Acad. Sci. USA *72*, 3666–3670.

Chailler, P., and Menard, D. (1999). Ontogeny of EGF receptors in the human gut. Front. Biosci. *4*, D87–D101.

Chen, G., and Goeddel, D.V. (2002). TNF-R1 signaling: a beautiful pathway. Science *296*, 1634–1635.

Chen, W.N., Woodbury, R.L., Kathmann, L.E., Opresko, L.K., Zangar, R.C., Wiley, H.S., and Thrall, B.D. (2004). Induced autocrine signaling through the epidermal growth factor receptor contributes to the response of mammary epithelial cells to tumor necrosis factor alpha. J. Biol. Chem. *279*, 18488–18496.

Dinarello, C.A. (1997). Interleukin-1. Cytokine Growth Factor Rev. *8*, 253–265.

Dinarello, C.A. (2000). The role of the interleukin-1-receptor antagonist in blocking inflammation mediated by interleukin-1. N. Engl. J. Med. *343*, 732–734.

Downward, J. (2001). The ins and outs of signalling. Nature *411*, 759–762.

Dumont, J.E., Dremier, S., Pirson, I., and Maenhaut, C. (2002). Cross signaling, cell specificity, and physiology. Am. J. Physiol. Cell Physiol. *283*, C2–C28.

Efron, B., and Tibshirani, R.J. (1993). An Introduction to the Bootstrap (London: Chapman and Hall).

Fan, H., and Derynck, R. (1999). Ectodomain shedding of TGF-alpha and other transmembrane proteins is induced by receptor tyrosine kinase activation and MAP kinase signaling cascades. EMBO J. *18*, 6962–6972.

Fransen, L., Van der Heyden, J., Ruysschaert, R., and Fiers, W. (1986). Recombinant tumor necrosis factor: its effect and its synergism with interferon-gamma on a variety of normal and transformed human cell lines. Eur. J. Cancer Clin. Oncol. *22*, 419–426.

Garcia-Lloret, M.I., Yui, J., Winkler-Lowen, B., and Guilbert, L.J. (1996). Epidermal growth factor inhibits cytokine-induced apoptosis of primary human trophoblasts. J. Cell. Physiol. *167*, 324–332.

Gaudet, S., Janes, K.A., Albeck, J.G., Pace, E.A., Lauffenburger, D.A., and Sorger, P.K. (2005). A compendium of signals and responses triggered by prodeath and prosurvival cytokines. Mol. Cell. Proteomics *4*, 1569–1590.

Glading, A., Bodnar, R.J., Reynolds, I.J., Shiraha, H., Satish, L., Potter, D.A., Blair, H.C., and Wells, A. (2004). Epidermal growth factor activates m-calpain (calpain II), at least in part, by extracellular signal-regulated kinase-mediated phosphorylation. Mol. Cell. Biol. *24*, 2499–2512.

Goll, D.E., Thompson, V.F., Li, H., Wei, W., and Cong, J. (2003). The calpain system. Physiol. Rev. *83*, 731–801.

Hambek, M., Solbach, C., Schnuerch, H.G., Roller, M., Stegmueller, M., Sterner-Kock, A., Kiefer, J., and Knecht, R. (2001). Tumor necrosis factor alpha sensitizes low epidermal growth factor receptor (EGFR)-expressing carcinomas for anti-EGFR therapy. Cancer Res. *61*, 1045–1049.

Hofmann, F., and Garcia-Echeverria, C. (2005). Blocking the insulin-like growth factor-I receptor as a strategy for targeting cancer. Drug Discov. Today *10*, 1041–1047.

Izumi, H., Ono, M., Ushiro, S., Kohno, K., Kung, H.F., and Kuwano, M. (1994). Cross talk of tumor necrosis factor-alpha and epidermal growth factor in human microvascular endothelial cells. Exp. Cell Res. *214*, 654–662.

Janes, K.A., Albeck, J.G., Peng, L.X., Sorger, P.K., Lauffenburger, D.A., and Yaffe, M.B. (2003). A high-throughput quantitative multiplex kinase assay for monitoring information flow in signaling networks: application to sepsis-apoptosis. Mol. Cell. Proteomics *2*, 463–473.

Janes, K.A., Kelly, J.R., Gaudet, S., Albeck, J.G., Sorger, P.K., and Lauffenburger, D.A. (2004). Cue-signal-response analysis of TNF-induced apoptosis by partial least squares regression of dynamic multivariate data. J. Comput. Biol. *11*, 544–561.

Janes, K.A., Albeck, J.G., Gaudet, S., Sorger, P.K., Lauffenburger, D.A., and Yaffe, M.B. (2005). A predictive systems model of signaling identifies a molecular basis set for cytokine-induced apoptosis. Science *310*, 1646–1653.

Karin, M., and Ben-Neriah, Y. (2000). Phosphorylation meets ubiquitination: the control of NF-[kappa]B activity. Annu. Rev. Immunol. *18*, 621–663.

Karin, M., and Greten, F.R. (2005). NF-kappaB: linking inflammation and immunity to cancer development and progression. Nat. Rev. Immunol. *5*, 749–759.

Kobayashi, Y., Yamamoto, K., Saido, T., Kawasaki, H., Oppenheim, J.J., and Matsushima, K. (1990). Identification of calcium-activated neutral protease as a processing enzyme of human interleukin 1 alpha. Proc. Natl. Acad. Sci. USA *87*, 5548–5552.

Masui, H., Castro, L., and Mendelsohn, J. (1993). Consumption of EGF by A431 cells: evidence for receptor recycling. J. Cell Biol. *120*, 85–93.

Mendelsohn, J., and Baselga, J. (2000). The EGF receptor family as targets for cancer therapy. Oncogene *19*, 6550–6565.

Micheau, O., and Tschopp, J. (2003). Induction of TNF receptor I-mediated apoptosis via two sequential signaling complexes. Cell *114*, 181–190.

Micheau, O., Lens, S., Gaide, O., Alevizopoulos, K., and Tschopp, J. (2001). NF-kappaB signals induce the expression of c-FLIP. Mol. Cell. Biol. *21*, 5299–5305.

Micheau, O., Thome, M., Schneider, P., Holler, N., Tschopp, J., Nicholson, D.W., Briand, C., and Grutter, M.G. (2002). The long form of FLIP is an activator of caspase-8 at the Fas death-inducing signaling complex. J. Biol. Chem. *277*, 45162–45171.

Nicholson, D.W., and Thornberry, N.A. (1997). Caspases: killer proteases. Trends Biochem. Sci. *22*, 299–306.

Nielsen, U.B., Cardone, M.H., Sinskey, A.J., MacBeath, G., and Sorger, P.K. (2003). Profiling receptor tyrosine kinase activation by using Ab microarrays. Proc. Natl. Acad. Sci. USA *100*, 9330–9335.

Pahl, H.L. (1999). Activators and target genes of Rel/NF-kappaB transcription factors. Oncogene *18*, 6853–6866.

Palladino, M.A., Bahjat, F.R., Theodorakis, E.A., and Moldawer, L.L. (2003). Anti-TNF-alpha therapies: the next generation. Nat. Rev. Drug Discov. *2*, 736–746.

Panja, A., Goldberg, S., Eckmann, L., Krishen, P., and Mayer, L. (1998). The regulation and functional consequence of proinflammatory cytokine binding on human intestinal epithelial cells. J. Immunol. *161*, 3675–3684.

Peschon, J.J., Slack, J.L., Reddy, P., Stocking, K.L., Sunnarborg, S.W., Lee, D.C., Russell, W.E., Castner, B.J., Johnson, R.S., Fitzner, J.N., et al. (1998). An essential role for ectodomain shedding in mammalian development. Science *282*, 1281–1284.

Qian, H., Hausman, D.B., Compton, M.M., Martin, R.J., Della-Fera, M.A., Hartzell, D.L., and Baile, C.A. (2001). TNFalpha induces and insulin inhibits caspase 3-dependent adipocyte apoptosis. Biochem. Biophys. Res. Commun. *284*, 1176–1183.

Reinhart, K., and Karzai, W. (2001). Anti-tumor necrosis factor therapy in sepsis: update on clinical trials and lessons learned. Crit. Care Med. *29*, S121–S125.

Ruan, H., and Lodish, H.F. (2003). Insulin resistance in adipose tissue: direct and indirect effects of tumor necrosis factor-alpha. Cytokine Growth Factor Rev. *14*, 447–455.

Rutgeerts, P., Van Assche, G., and Vermeire, S. (2004). Optimizing anti-TNF treatment in inflammatory bowel disease. Gastroenterology *126*, 1593–1610.

Schlessinger, J. (2004). Common and distinct elements in cellular signaling via EGF and FGF receptors. Science *306*, 1506–1507.

Schulze, A., Lehmann, K., Jefferies, H.B., McMahon, M., and Downward, J. (2001). Analysis of the transcriptional program induced by Raf in epithelial cells. Genes Dev. *15*, 981–994.

Sfikakis, P.P., and Kollias, G. (2003). Tumor necrosis factor biology in experimental and clinical arthritis. Curr. Opin. Rheumatol. *15*, 380–386.

Singh, P., and Rubin, N. (1993). Insulinlike growth factors and binding proteins in colon cancer. Gastroenterology *105*, 1218–1237.

Stampfer, M.R., and Yaswen, P. (1993). Culture systems for study of human mammary epithelial cell proliferation, differentiation and transformation. Cancer Surv. *18*, 7–34.

Stelling, J., Sauer, U., Szallasi, Z., Doyle, F.J., 3rd, and Doyle, J. (2004). Robustness of cellular functions. Cell *118*, 675–685.

Streetz, K., Leifeld, L., Grundmann, D., Ramakers, J., Eckert, K., Spengler, U., Brenner, D., Manns, M., and Trautwein, C. (2000). Tumor necrosis factor alpha in the pathogenesis of human and murine fulminant hepatic failure. Gastroenterology *119*, 446–460.

Torrance, C.J., Jackson, P.E., Montgomery, E., Kinzler, K.W., Vogelstein, B., Wissner, A., Nunes, M., Frost, P., and Discafani, C.M. (2000). Combinatorial chemoprevention of intestinal neoplasia. Nat. Med. *6*, 1024–1028.

Wajant, H., Pfizenmaier, K., and Scheurich, P. (2003). Tumor necrosis factor signaling. Cell Death Differ. *10*, 45–65.

Wiley, H.S., Shvartsman, S.Y., and Lauffenburger, D.A. (2003). Computational modeling of the EGF-receptor system: a paradigm for systems biology. Trends Cell Biol. *13*, 43–50.

Wu, Y., Tewari, M., Cui, S., and Rubin, R. (1996). Activation of the insulin-like growth factor-I receptor inhibits tumor necrosis factor-induced cell death. J. Cell. Physiol. *168*, 499–509.

Zwerina, J., Hayer, S., Tohidast-Akrad, M., Bergmeister, H., Redlich, K., Feige, U., Dunstan, C., Kollias, G., Steiner, G., Smolen, J., and Schett, G. (2004). Single and combined inhibition of tumor necrosis factor, interleukin-1, and RANKL pathways in tumor necrosis factor-induced arthritis: effects on synovial inflammation, bone erosion, and cartilage destruction. Arthritis Rheum. *50*, 277–290.

Appendix C

Reprinted from:

Janes, K. A., Albeck, J. G., Peng, L. X., Sorger, P. K., Lauffenburger, D. A., and Yaffe, M. B. (2003).

A high-throughput quantitative multiplex kinase assay for monitoring information flow in signaling networks: application to sepsis-apoptosis.

Mol Cell Proteomics *2*, 463-473.

In this study I performed the microscopy and flow cytometry experiments shown in Figure 6 and Figure 8 B and C. All other experiments were performed by Kevin Janes and Lilly Peng.

A High-throughput Quantitative Multiplex Kinase Assay for Monitoring Information Flow in Signaling Networks

APPLICATION TO SEPSIS-APOPTOSIS*

Kevin A. Janes‡, John G. Albeck§, Lili X. Peng‡, Peter K. Sorger‡§¶, Douglas A. Lauffenburger‡§¶, and Michael B. Yaffe‡§¶‖

To treat complex human diseases effectively, a systems-level approach is needed to understand the interplay of environmental cues, intracellular signals, and cellular behaviors that underlie disease states. This approach requires high-throughput, multiplex techniques that measure quantitative temporal variations of multiple protein activities in the intracellular signaling network. Here, we describe a single microtiter-based format that simultaneously quantifies protein kinase activities in the phosphatidylinositol 3-kinase pathway (Akt), nuclear factor-κB pathway (IKK), and three core mitogen-activated protein kinase pathways (ERK, JNK1, MK2). These parallel high-throughput assays are stringently linear, redundantly specific, reproducible, and sensitive compared with classical low-throughput techniques. When applied to a model of sepsis-induced colon epithelial apoptosis, this approach identified a late phase of Akt activity as a critical mediator of cell survival that quantitatively contributed to the efficacy of insulin as an anti-apoptotic cue. Thus, sampling parallel nodes in the intracellular signaling network identified part of the molecular mechanism underlying the efficacy of insulin in the treatment of human sepsis. ***Molecular & Cellular Proteomics 2:463–473, 2003.***

Complex patterns of signal transduction arise when cells are exposed to combinations of extracellular cues that vary in onset, duration, origin, and synchrony. Cells process these cues through an interconnected network of multifunctional, redundant molecules to elicit a set of phenotypic responses that subsequently impact function at the cell, tissue, and organ level. In order to develop a molecular understanding of the complex pathophysiology underlying human diseases and utilize this information for prognosis and therapy, a systems-level, network-biology approach should be applied to the signaling networks governing the relevant cell responses (1). This approach will require frequent temporal sampling of protein activity at critical nodes within parallel signaling pathways inside the cell in a quantitative manner to characterize the flow of information accurately. Such functional measurements are likely to be as valuable, or more valuable, than measurements of simple protein abundance. By quantitatively exploring the functional response of the signaling network to distinct extracellular cues and correlating these molecular events with phenotypic responses, one can construct predictive models of cue-signal and signal-response relationships.

Evolving proteomic approaches to network biology have largely focused on measuring abundances of many proteins at only a few time points or under a limited number of experimental conditions (2). Complementary information on functional protein characteristics, such as enzyme activity, has been lacking in these systematic analyses, in large part because there do not exist quantitatively robust, high-throughput techniques that simultaneously measure multiple protein activities in cells. Initially, this type of data collection on protein functional status should focus on frequent sampling of a limited number of key molecules that sit at critical nodes in different signaling pathways (Fig. 1*A*).

To begin to address this, we have developed a generalized assay for the multiplex analysis of multiple protein kinase activities in a 96-well format. The procedure utilizes parallel kinase-specific immunopurification steps, followed by rapid quantitative high-throughput activity measurements within the linear-rate regime for each kinase. We applied this technique to measure the activities of five kinases (extracellular-regulated kinase (ERK)[1] (3), Akt, Iκ-B kinase (IKK), c-jun N-terminal kinase 1 (JNK1), and mitogen-activated protein kinase-associated protein kinase 2 (MK2)) in a sepsis/systemic inflammatory response syndrome (SIRS) model system for tumor necrosis factor-alpha (TNF-α)-induced colon epithelial cell death.

From the ‡Biological Engineering Division, §Department of Biology, and ¶Center for Cancer Research, Massachusetts Institute of Technology, 400 Main Street, Cambridge, MA 02139

Received, May 16, 2003, and in revised form, June 25, 2003

Published, MCP Papers in Press, June 26, 2003, DOI 10.1074/mcp.M300045-MCP200

[1] The abbreviations used are: ERK, extracellular-regulated kinase; IKK, Iκ-B kinase; JNK1, c-jun N-terminal kinase 1; MK2, mitogen-activated protein kinase-associated protein kinase 2; PC, phosphocellulose; PI 3-K, phosphatidylinositol 3-kinase; SIRS, systemic inflammatory response syndrome; TNF-α, tumor necrosis factor-alpha; DTT, dithiothreitol; IFN-γ, interferon gamma; GST, glutathione *S*-transferase; CPM, counts per minute.

We chose this experimental model because, clinically, sepsis is the most common cause of death in critically ill patients and is a prime example of acute, systemic disease mediated by molecular network dysfunction (4, 5). Despite the multifaceted etiology of sepsis, the colonic epithelium represents a common final effector organ and is a major site for programmed cell death following injury (6). Epithelial apoptosis is believed to cause gut barrier dysfunction (7), leading to leakage of cytokines and possibly bacteria into the systemic circulation, thereby exacerbating the inflammatory state. Thus, the bowel has been postulated to be the "motor" driving the septic state (8). TNF-α levels are drastically elevated in a number of forms of human sepsis, and levels correlate with increased mortality (9). The five kinases whose activities we measured function downstream of TNF-α as canonical hubs for signaling pathways that control cell survival, stress responses, and the onset of programmed cell death (Fig. 1*A*, gray nodes) (10–13). Quantitative sampling of the activity of these kinases in time with the high-throughput multiplex assays provided a window into the state of the signaling network in this model of cytokine-induced human disease.

Due to the complexity of the disease, treatments for sepsis have proven elusive, with certain monotherapies (*e.g.* TNF antagonists (14)) actually worsening patient survival. Intriguingly, intensive insulin therapy has recently been found to reduce morbidity in critical illness substantially (15), though the mechanism underlying this effect is unknown (4). A number of possibilities have been proposed, including tight regulation of glucose levels (16), antagonism of proinflammatory molecules (17), and reduction of circulating C-reactive protein levels (18).

At the molecular level, TNF-α and insulin activate a number of common signaling pathways that are highly interconnected (Fig. 1*A*), and it is difficult to predict *a priori* how these conflicting cues are processed intracellularly to determine cell fate in physiologically relevant cell types. We hypothesized that quantitative, dynamic measurement of information flow through these critical signaling nodes might clarify how network information is processed and reveal new signal-response relationships involving insulin's mechanism of action in sepsis.

We implemented an *in vitro* model of TNF-induced programmed cell death in a human colon epithelial cell line that survives TNF-α treatment when costimulated with insulin. The network response to TNF-α and insulin as combinatorial cues in this model system was then explored by performing over 400 independent kinase activity measurements with the high-throughput assays. A significant reduction in TNF-induced colon epithelial death was observed upon insulin treatment. This correlated with a profound change in the pattern of Akt kinase activity, with only minor perturbations observed in the activities of other kinases that were assayed. We were able to attribute at least half of the insulin-induced survival effect to the specific activation of the Akt pathway at late times. Importantly, we found that the addition of insulin 4 h after TNF-α addition provided sufficient late-phase Akt activity to elicit the same survival effect as when insulin was added simultaneously with TNF-α, suggesting a molecular mechanism for how insulin improves patient survival in sepsis even when administered hours after the initial insult. The assay format and approach that we report here provides a common platform that can now be used to systematically probe multiple signal transduction pathways at moderate sampling rates under diverse experimental conditions of broad scientific and medical interest.

EXPERIMENTAL PROCEDURES

Cell Culture, Stimulation, and Lysis—HT-29 and HeLa cells (ATCC, Manassas, VA) were grown according to the manufacturer's recommendations. For the time courses, HT-29 cells were seeded at 50,000 cells/cm^2, grown for 24 h, and then treated with 200 U/ml IFN-γ (Roche) for an additional 24 h. After sensitization, cells were rinsed once with PBS and treated with 50 ng/ml TNF-α (Peprotech, Rocky Hill, NJ) with or without 100 nM insulin (Sigma) for the indicated times. Cells were washed once with ice-cold PBS and lysed in 1% Triton X-100, 50 mM Tris-HCl (pH 7.5), 150 mM NaCl, 50 mM β-glycerophosphate, 10 mM sodium pyrophosphate, 30 mM NaF, 1 mM benzamidine, 2 mM EGTA, 100 μM $NaVO_4$, 1 mM dithiothreitol (DTT), 1 mM phenylmethylsulfonyl fluoride, 10 μg/ml aprotinin, 10 μg/ml leupeptin, 1 μg/ml pepstatin, 1 μg/ml microcystin-LR. Whole cell lysates were incubated on ice for 15 min, then clarified by centrifugation at 16,000 $\times$ *g* for 15 min at 4 °C. Protein concentrations of clarified extracts were determined with a bicinchoninic acid assay (Pierce).

High-throughput Kinase Activity Assays—The microtiter-based kinase activity assays were performed with the following antibodies: anti-ERK1/2 CT (Upstate Biotechnology, Lake Placid, NY), anti-Akt PH domain (Upstate Biotechnology), anti-JNK1 (Santa Cruz Biotechnology, Santa Cruz, CA), anti-IKKα/β (Santa Cruz Biotechnology) or anti-MK2 (Upstate Biotechnology). Protein A or G microtiter strips (Pierce) were coated overnight with 10 μg/ml anti-kinase antibody and washed three times with blocking buffer (1% bovine serum albumin (Sigma) in 50 mM Tris-HCl (pH 7.5), 150 mM NaCl, 0.05% Triton X-100). Cell lysates (50 μg for ERK, 500 μg for Akt, 200 μg for JNK1, 200 μg for MK2, 600 μg for IKK) were added for 3 h (ERK, Akt, JNK1, and MK2) or overnight (IKK), then washed two times with wash buffer (50 mM Tris-HCl (pH 7.5), 150 mM NaCl) and two times with kinase wash buffer (20 mM Tris-HCl (pH 7.5), 15 mM $MgCl_2$, 5 mM β-glycerophosphate, 1 mM EGTA, 0.2 mM Na_3VO_4, 0.2 mM DTT). The wells were resuspended in 20 μl kinase wash buffer and warmed to 37 °C. Then 20 μl kinase assay buffer (kinase wash buffer plus 0.4 μM protein kinase A inhibitor, 4 μM protein kinase C inhibitor, 4 μM calmidazolium, 0–25 μM cold ATP, 1–5 μCi [γ-^{32}P]ATP) was added to the wells, followed by 20 μl of substrate (40 μg myelin basic protein for ERK, 10 μM Aktide (19) for Akt, 3 μg glutathione *S*-transferase (GST)-ATF2 (1–109) (20) for JNK1, 10 μM MK2tide[2] for MK2, 10 μg GST-IκBα (1–62) (21) for IKK) to initiate the reaction. The kinase reactions were allowed to proceed for 15–120 min at 37 °C, then terminated by 60 μl 75 mM H_3PO_4 or 20 mM EDTA. Exact conditions for each kinase assay are detailed in Table I. For EDTA-terminated reactions, 40 μl of the terminated reaction was transferred to a phosphocellulose filter plate (Millipore, Bedford, MA) containing 100 μl 75 mM H_3PO_4 and mixed, whereas H_3PO_4-terminated reactions were added directly to the filter plates. The terminated reaction con-

[2] I. A. Manke and M. B. Yaffe, manuscript in preparation.

TABLE I

Experimental conditions for the individual in vitro kinase assays

Other experimental parameters were maintained as described in "Experimental Procedures."

Kinase	Antibody	Substrate	ATP (μM)	[γ-^{32}P]ATP (μCi)	Reaction time (min)	Termination
ERK	Anti-ERK1/2 CT	Myelin basic protein	25	1	60	H_3PO_4
Akt	Anti-Akt PH dom.	Aktide	10	5	30	H_3PO_4
JNK1	Anti-JNK1	GST-ATF2 (1-109)	10	2	60	H_3PO_4
IKK	Anti-IKKα/β	GST-IκBα (1-62)	0	5	120	EDTA
MK2	Anti-MAPKAP K2	MK2tide	25	2	15	EDTA

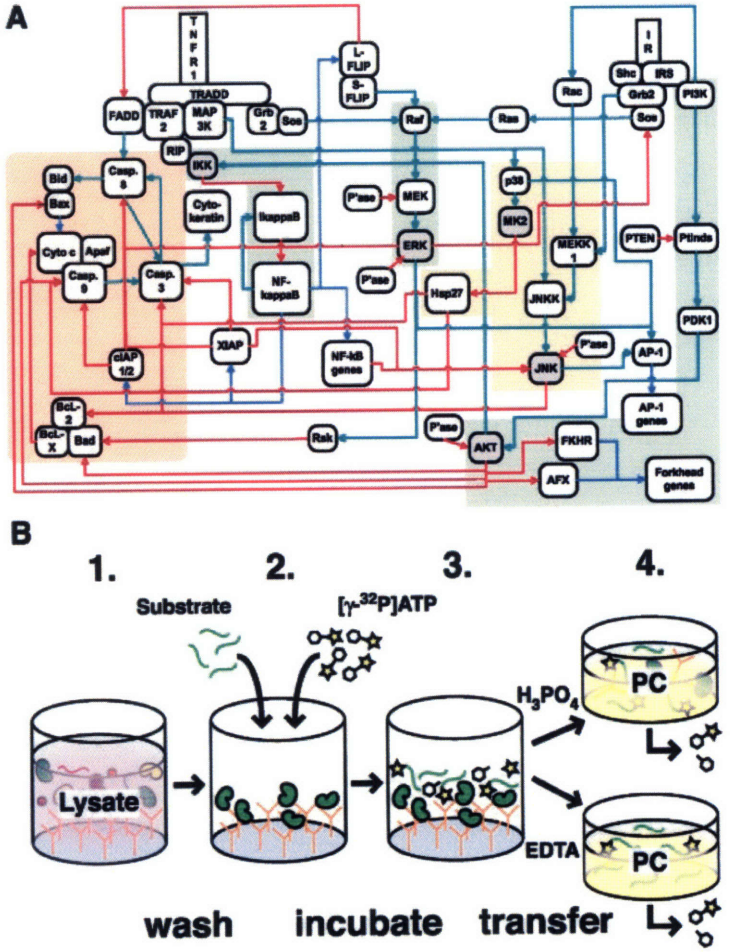

FIG. 1. **A high-throughput assay of multiple endogenous kinase activities can monitor information flow through critical nodes in a signaling network.** *A*, generalized network diagram describing pathways activated downstream of TNF-α and insulin: activating interactions (*green arrows*), inhibitory interactions (*red arrows*), transcriptional interactions (*blue arrows*). *Gray nodes* highlight kinases that are measured by the high-throughput multiplex kinase activity assay. *Red regions* indicate apoptotic pathways, *green regions* indicate survival pathways, and *orange regions* indicate stress pathways that can function to promote or inhibit apoptosis, depending on context. Note the extent of crosstalk in the network. Diagram is not implied to be comprehensive (*e.g.* location-dependent interactions have been abstracted). *B*, general schematic of the high-throughput multiplex kinase activity assay format. Lysates are incubated with Protein A or G microtiter wells precoated with anti-kinase antibody. After several washes, an appropriate substrate and [γ-^{32}P]ATP are added to the plate to initiate an *in vitro* phosphorylation reaction. The reaction is terminated with H_3PO_4 (for Akt and JNK1 assays) or EDTA (for IKK and MK2 assays), and a fraction of the reaction mix is transferred to a PC filter plate and washed to remove free ^{32}P.

tents were vacuum-filtered and washed five times with 75 mM H_3PO_4 and three times with 70% EtOH. The filters were punched into vials and the radioactivity incorporated was measured by liquid scintillation (Cytoscint; ICN Pharmaceuticals, Costa Mesa, CA). The results from blank wells, containing only lysis buffer during the immunopurification step, were subtracted to remove nonspecific contributions, with the exception of Akt, where this was not necessary.

Western Blotting—For determination of target capture, assays were stopped before the kinase reaction step and resuspended in 40 μl sample buffer (62.5 mM Tris-HCl (pH 6.8), 2% SDS, 10% glycerol, 100 mM DTT, 0.01% bromphenol blue). Wells were boiled for 5 min, and the samples were resolved on a 10% polyacrylamide gel and transferred to polyvinylidene difluoride (Millipore). Membranes were blocked with 5% nonfat skim milk in 20 mM Tris-HCl (pH 7.5), 137 mM NaCl, 0.1% Tween-20, and probed with the following primary antibodies at 1:1000 dilution: anti-Akt (Upstate Biotechnology), anti-JNK1 (Santa Cruz Biotechnology), anti-MAPKAPK2 (StressGen Biotechnologies, Victoria, British Columbia, Canada), and anti-IKKα/β (Santa Cruz Biotechnology). The membranes were then probed with horseradish peroxidase conjugated anti-mouse or anti-rabbit secondary antibody (Amersham Pharmacia Biotech) at 1:10,000 dilution and visualized by enhanced chemiluminescence (Amersham Pharmacia Biotech) on a FluorS (Bio-Rad) or Kodak Image Station (Perkin Elmer). Bands were selected and quantified according to the manufacturer's recommendations.

Autoradiography—Thirty microliters of the terminated kinase reactions were mixed with 10 μl 4$\times$ sample buffer and resolved on a 10% polyacrylamide glycine gel for protein substrates or a 16% polyacrylamide tricine gel for peptide substrates (22). The dye front was excised, and the gel exposed overnight to a multisensitive BaFBr:

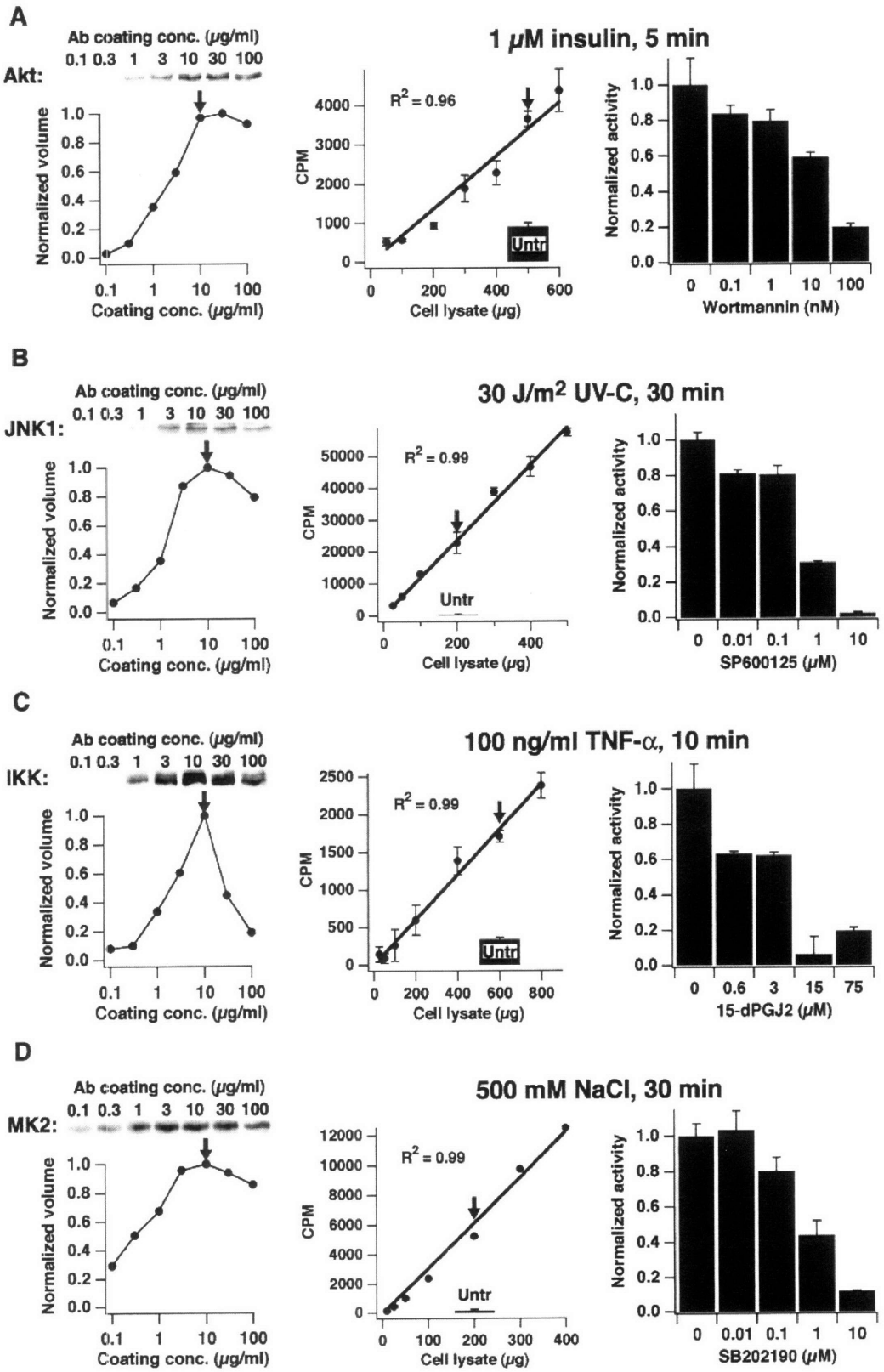

FIG. 2. **High-throughput multiplex kinase activity assays are optimally sensitive, quantitatively linear, and specific for the target kinase.** *A*, *Left panel*, Akt was immunopurified from 500 μg of HT-29 lysate on Protein G microtiter plates coated with 50 μl of anti-Akt at various coating concentrations. Plate-bound Akt was analyzed by Western blotting, as described under "Experimental Procedures," and

Eu^{2+} screen (Perkin Elmer). The screen was visualized using a Cyclone Storage Phosphor system (Perkin Elmer).

Cell Imaging—HT-29 cells were seeded in Delta T glass culture dishes (Bioptechs). After 30 h, cells were pretreated with IFN-γ as described, then rinsed and treated with 50 ng/ml TNF-α or 50 ng/ml TNF-α + 100 nM insulin for 18 h. Then 6 μg/ml Hoechst 33342 (Molecular Probes, Eugene, OR) was added to the medium, and phase and fluorescence images were collected. Cells were then fixed with 100% MeOH and stored at −20 °C overnight. After primary staining with anti-cleaved caspase 3 (Cell Signaling, Beverly, MA) and secondary staining with Alexa 594-conjugated anti-rabbit IgG (Molecular Probes), fluorescence images were collected.

Apoptosis Assays—HT-29 cells were seeded in 96-well plates and sensitized with IFN-γ as described. For inhibitor studies, 20 μM LY294002 was added to the medium 1 h before or 3 h after cytokine stimulation. During washout experiments, the medium was removed and the wells washed once with PBS. The medium was then replaced with medium conditioned by cells treated with the same cytokine concentrations without inhibitor. After 18 h, cells were rinsed with PBS and trypsinized. The supernatant and rinse were saved and combined with the trypsinized cells to ensure capture of both floating and adherent cells. The cells were washed with PBS, then fixed in 100% MeOH and stored at −20 °C. The fixed cells were stained with a fluorescein-labeled monoclonal antibody against caspase-cleaved cytokeratin (M30; Roche), plus anti-cleaved-caspase-3 (Asp 175; Cell Signaling) with Alexa 647-conjugated anti-rabbit secondary (Molecular Probes), according to the manufacturers' instructions. Cells were washed once after staining, then analyzed by flow cytometry (FACScalibur; Becton-Dickinson, Mountain View, CA). Cells positive for cleaved cytokeratin, cleaved caspase-3, or both were scored as apoptotic. Three separate biological samples were analyzed for each treatment condition. Percent increased survival was calculated according to the following formula: [1 − (% apoptotic cells in the presence of insulin)/(% apoptotic cells in the absence of insulin under the same pretreatment conditions)] × 100%.

RESULTS AND DISCUSSION

High-throughput Kinase Activity Assay Development—The generalized assay format involves four steps, shown in Fig. 1*B*: i) parallel purification of endogenous kinase from whole cell lysates by immunoprecipitation onto Protein A or G microtiter plates that have been precoated with kinase-specific antibodies, ii) low stringency washes to remove nonpurified lysate components, iii) addition of [γ-^{32}P]ATP and a kinase-specific substrate to initiate an *in vitro* kinase reaction, and iv) termination of the *in vitro* reaction either by H_3PO_4 or EDTA and liquid transfer to a 96-well phosphocellulose (PC) filter plate to isolate phosphoproteins and remove free [γ-^{32}P]ATP. We developed assays for ERK (3), Akt, JNK1, IKK, and MK2 activity in cell extracts after rigorous optimization and quantitative validation.

To develop the parallel immunopurification step, we experimentally screened multiple commercially available products and identified for each kinase a single, high-affinity antibody that retained enzymatic activity. Coating conditions for each anti-kinase antibody on Protein A/G microtiter plates were individually optimized, revealing that the antibodies maximally bound their intended targets when 50 μl of 10 μg/ml antibody was applied to each well (Fig. 2, *A–D*, *left panels*), consistent with our estimates of the number of antibody binding sites on the plate surface. Higher coating concentrations of polyclonal antibodies (anti-JNK1, anti-IKKα/β, and anti-MK2) reduced the solid-phase avidity for the kinase and caused a net decrease in purification efficiency (Fig. 2, *B–D*, *left panels*). At the optimized coating concentration (Fig. 2, *A–D*, *left panels, arrows*), the immunopurification was always linear in the amount of kinase purified over a substantial range of lysate concentrations (Fig. 3, *A–D*). This demonstrates that the antibody capture step linearly reflects kinase abundance in the lysate.

Next, kinase reaction conditions for each assay were optimized by modifying the following *in vitro* parameters: choice of substrate, concentration of substrate, radioactive-to-nonradioactive ATP ratio, and reaction duration (see "Experimental Procedures"). When an individual kinase was determined to phosphorylate multiple substrates effectively (Fig. 4, *A*, *B*, and *D* and data not shown), the substrate showing the highest

quantified by densitometry of the band intensity to calculate a normalized volume. *Middle panel*, 50–600 μg of lysate from HT-29 cells treated with 1 μM insulin for 5 min was measured with the high-throughput Akt activity assay using 10 μM Aktide as substrate, as described under "Experimental Procedures." The stimulated lysate (*arrow*) was compared with 500 μg untreated control lysate (*solid bar*). *Right panel*, HT-29 cells were pretreated with various concentrations of wortmannin (Sigma) for 1 h then stimulated with 1 μM insulin for 5 min and lysed. Akt activity was quantified as described under "Experimental Procedures." *B*, Left panel, JNK1 was immunopurified from 200 μg of HT-29 lysate on Protein A microtiter plates coated with 50 μl of anti-JNK1 at various coating concentrations and analyzed as described in *A*. *Middle panel*, 25–500 μg of lysate from HT-29 cells harvested 30 min after treatment with 30 J/m^2 UV-C was measured with the high-throughput JNK1 activity assay using 3 μg GST-ATF2 (1-109) as substrate, as described under "Experimental Procedures." The stimulated lysate (*arrow*) was compared with 200 μg untreated control lysate (*solid bar*). *Right panel*, plate-bound JNK1 from UV-stimulated HT-29 cells was incubated for 10 min with various concentrations of SP600125 (Calbiochem), and JNK1 activity was quantified as described under "Experimental Procedures." *C*, Left panel, IKK was immunopurified from 800 μg of HT-29 lysate on Protein A microtiter plates coated with 50 μl of anti-IKKα/β at various coating concentrations and analyzed as described in *A*. *Middle panel*, 50–800 μg of lysate from HeLa cells treated with 100 ng/ml TNF-α for 10 min was measured with the high-throughput IKK activity assay using 10 μg GST-IκBα (1-62) as substrate, as described under "Experimental Procedures." The stimulated lysate (*arrow*) was compared with 600 μg untreated control lysate (*solid bar*). *Right panel*, plate-bound IKK from TNF-stimulated HeLa cells was incubated for 1 h with various concentrations of 15-deoxy-$\Delta^{12,14}$-prostaglandin J_2 (*15d-PGJ_2*; Calbiochem), and IKK activity was quantified as described under "Experimental Procedures." *D*, Left panel, MK2 was immunopurified from 200 μg of HT-29 lysate on Protein G microtiter plates coated with 50 μl of anti-MK2 at various coating concentrations and analyzed as described in *A*. *Middle panel*, 10–400 μg of lysate from HT-29 cells treated with 500 mM NaCl for 30 min was measured with the high-throughput MK2 activity assay using 10 μM MK2tide as substrate, as described under "Experimental Procedures." The stimulated lysate (*arrow*) was compared with 200 μg untreated control lysate (*solid bar*). *Right panel*, HT-29 cells were pretreated with various concentrations of SB202190 (Calbiochem) for 1 h then stimulated with 500 mM NaCl for 30 min and lysed. MK2 activity was quantified as described under "Experimental Procedures." All kinase activities are reported as the mean ± S.E. of triplicate samples (error bars for the MK2 assay were smaller than the size of the marker). Western blots were repeated at least twice with similar results; representative images are shown. *Arrows* indicate fixed experimental conditions for the adjacent experiment.

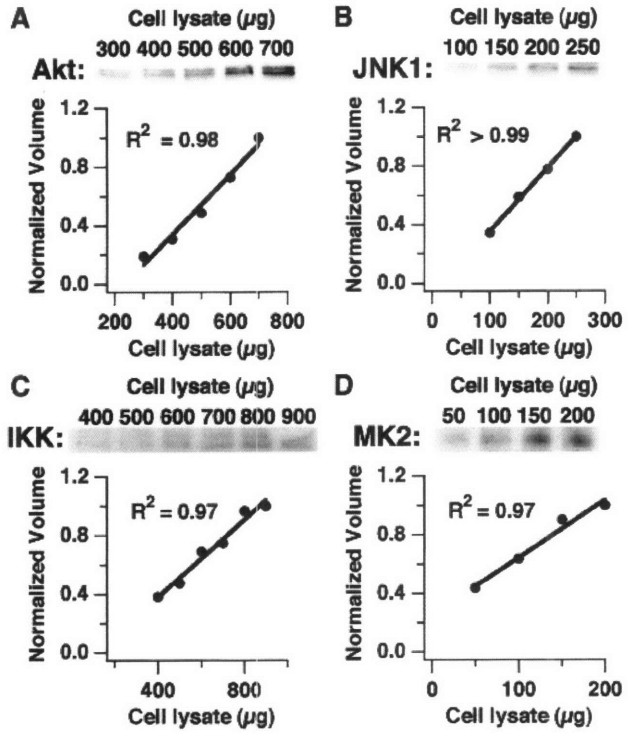

FIG. 3. **Purification of endogenous kinases is linear on antibody-coated microtiter plates.** *A*, 300–700 μg of HT-29 lysate was incubated for 3 h on Protein G microtiter plates coated with 10 μg/ml of anti-Akt. Plate-bound Akt was analyzed by Western blotting, as described under "Experimental Procedures," and quantified by densitometry of the band intensity to calculate a normalized volume. *B*, 100–250 μg of HT-29 lysate was incubated for 3 h on Protein A microtiter plates coated with 10 μg/ml of anti-JNK1 and analyzed as described in *A*. *C*, 400–900 μg of HT-29 lysate was incubated overnight on Protein A microtiter plates coated with 10 μg/ml of anti-IKKα/β and analyzed as described in *A*. *D*, 50–200 μg of HT-29 lysate was incubated for 3 h on Protein G microtiter plates coated with 10 μg/ml of anti-MK2 and analyzed as described *A*. Western blots were performed at least twice with similar results; representative images are shown.

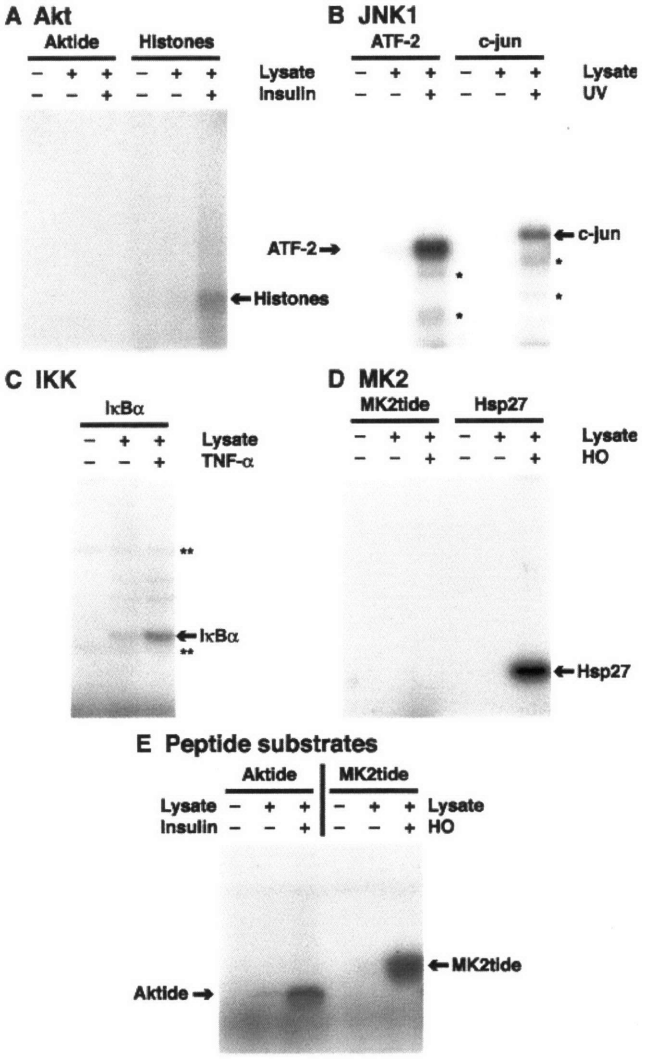

FIG. 4. **Terminated *in vitro* reaction products specifically contain the phosphorylated substrate.** *A*, the high-throughput Akt assay, using 10 μM Aktide or 40 μg partially purified histones (Sigma) as substrate, was analyzed by SDS-PAGE and autoradiography after termination of the *in vitro* reaction as described under "Experimental Procedures." Note that the phosphopeptide has run off the gel and no other phosphorylated bands are evident. *B*, the high-throughput JNK1 assay, using 3 μg ATF-2 or 2 μg c-jun (Upstate Biotechnology) as substrate, was analyzed as described in *A*. *Single asterisks* indicate ^{32}P incorporation into partially cleaved substrates. *C*, the high-throughput IKK assay, using 10 μg IκBα as substrate, was analyzed as described in *A*. *Double asterisks* indicate nonspecific ^{32}P incorporation (note that these bands are of equal intensity in the blank sample, such that background subtraction will remove their contribution). *D*, the high-throughput MK2 assay, using 10 μM MK2tide or 5 μg Hsp27 (Upstate Biotechnology) as substrate, was analyzed as described in *A*. Note that the phosphopeptide has run off the gel and no other phosphorylated bands are evident. *E*, the peptide substrates (10 μM Aktide for the Akt assay and 10 μM MK2tide for the MK2 assay) were analyzed on a 16% tricine-polyacrylamide gel and autoradiographed after termination of the *in vitro* reaction as described under "Experimental Procedures." The migration position of a 5-kDa marker is indicated.

specific activity (counts per minute (CPM)/μmol) was selected to maximize sensitivity. Other reaction parameters, such as buffer composition and reaction temperature, were intentionally kept constant to enable assays of different kinases to be performed in parallel on the same microtiter plate in a single step.

ERK, Akt, and JNK1 assays were terminated by adding an equal volume of 75 mm H_3PO_4 to the microtiter reaction well and transferring the well contents to a parallel 96-well PC filter plate for washing and quantitation. MK2 and IKK assays were terminated by adding an equal volume of 20 mM EDTA to the microtiter reaction well and transferring the contents to the 96-well PC filter plate preacidified with 75 mM H_3PO_4 in each well. SDS-PAGE analysis of the terminated reaction mixtures transferred to the PC filter verified that phosphorylation was only occurring on the added substrate (Fig. 4, *A–E*). Therefore, individual filters in the wells of the PC plate could be punched out for scintillation counting to accurately quantify kinase

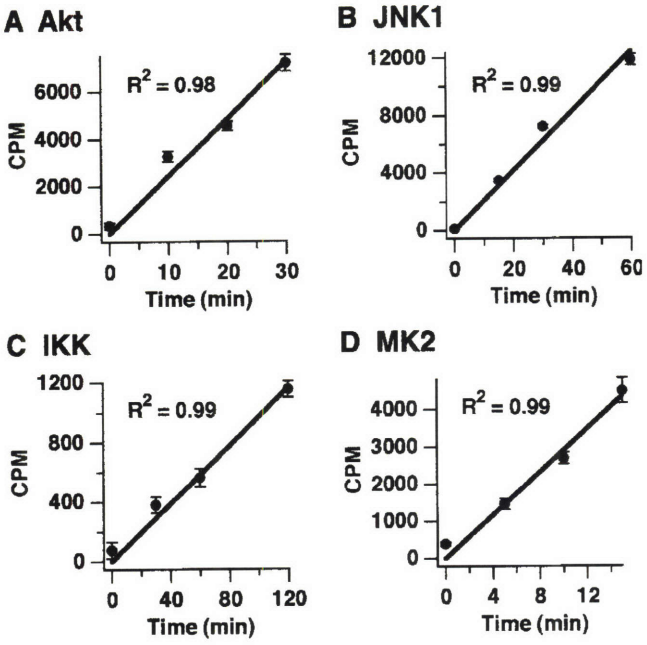

FIG. 5. **Kinetics of the *in vitro* kinase reactions are linear with time.** Assays were incubated with fixed amounts of HT-29 or HeLa lysates treated with known activators of the pathway of interest (for details, see Fig. 2, *A–D*). *In vitro* reactions were allowed to proceed for the indicated times and analyzed as described under "Experimental Procedures." *A*, Akt assay kinetics with Akt from 500 μg of HT-29 lysate. *B*, JNK1 assay kinetics with with JNK1 from 200 μg of HT-29 lysate. *C*, IKK assay kinetics with IKK from 800 μg of HeLa lysate. *D*, MK2 assay kinetics with MK2 from 200 μg of HT-29 lysate.

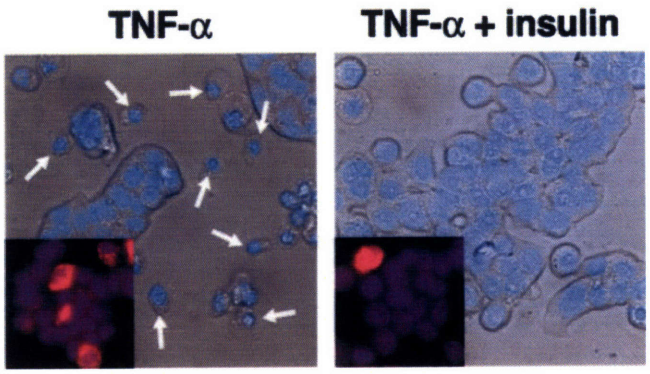

FIG. 6. **IFN-sensitized HT-29 cells undergo programmed cell death in response to TNF-α and can be rescued by cotreatment with insulin.** *Main panels*, phase contrast images of HT-29 cells treated with 100 ng/ml TNF-α alone (*left*) and both 100 ng/ml TNF-α + 100 nM insulin (*right*) as described under "Experimental Procedures." Note the increased number of shrunken cells with condensed nuclei in cells treated with TNF-α alone (*arrows*). *Insets*, indirect immunofluorescence images of cleaved caspase 3 (*red*) in HT-29 cells treated with 100 ng/ml TNF-α alone (*left*) and both 100 ng/ml TNF-α + 100 nM insulin (*right*). Note the increased number of cleaved caspase 3-positive cells in the TNF-α alone image. Hoechst 33342 (*blue*) is overlaid in all images to show nuclei.

activity, eliminating the low-throughput, SDS-PAGE-and-autoradiography step required in classical immune complex kinase assays.

To investigate the sensitivity, dynamic range, and linearity of these assays, HT-29 and HeLa cells were treated with known activators of each kinase, and the kinase activities (CPM on the PC filter) measured as a function of different dilutions of the activated lysates (Fig. 2, *A–D*, *middle panels*). The ^{32}P incorporation was linear over at least an order of magnitude in activity, and the absolute sensitivities of the assays were always below 200 μg, with some assays capable of measuring activity from as little as 10–25 μg of total lysate. This result is comparable to, or better than, existing assays that usually require several hundred micrograms of lysate for analysis (23–25). The aggregate sensitivity of the format was more than sufficient to measure ERK, Akt, JNK1, MK2, and IKK activity simultaneously from a single 10-cm plate of HT-29 cells.

The signal-to-noise and reproducibility characteristics for each kinase assay were examined by selecting a single concentration in the middle of the dynamic range of each assay (Fig. 2, *A–D*, *middle panels, arrows*) and comparing the kinase activities between lysates from stimulated and unstimulated cells. For each agonist, this revealed a relative activation of each endogenous kinase that was comparable in magnitude to that reported in the literature, with intra-assay coefficients of variation always $\leq$10%. Thus, the assays clearly reflected activation of the endogenous pathways, and the end point measures of activity were highly sensitive and reproducible.

In order for these assays to reflect information flow through the signaling network accurately, it was crucial to confirm that our end point CPM measurement linearly reflected the kinase activity in the lysate. Therefore, the kinetics of the *in vitro* reaction were examined in detail at a selecting fixed lysate concentration within the linear range (Fig. 2, *A–D*, *middle panels, arrows*). As shown in Fig. 5, *A–D*, each phosphorylation reaction displayed linear kinetics up to the time of termination, suggesting that neither the [γ-^{32}P]ATP nor the substrate was significantly depleted over the course of the reaction. Thus, the linearity at every step in the assay procedure (kinase capture, *in vitro* reaction kinetics, and end point CPM measurement) strongly suggests that these assays are a linear reflection of endogenous kinase activity *in vivo*.

As a final confirmation of assay specificity, we examined the effect of various small molecule inhibitors that have been reported to be specific for each of the measured kinases or the directly upstream kinase (26–29). At a fixed lysate concentration (Fig. 2, *A–D*, *middle panels, arrows*), a dose-dependent decrease in the measured activity (Fig. 2, *A–D*, *right panels*) was observed, consistent with the reported IC_{50} values for the target kinase. Taken together with the redundant antibody-kinase and kinase-substrate specificity inherent to the measurement format, these results strongly suggest that the assays specifically quantify the endogenous activity of the intended kinase. We conclude that the high-throughput

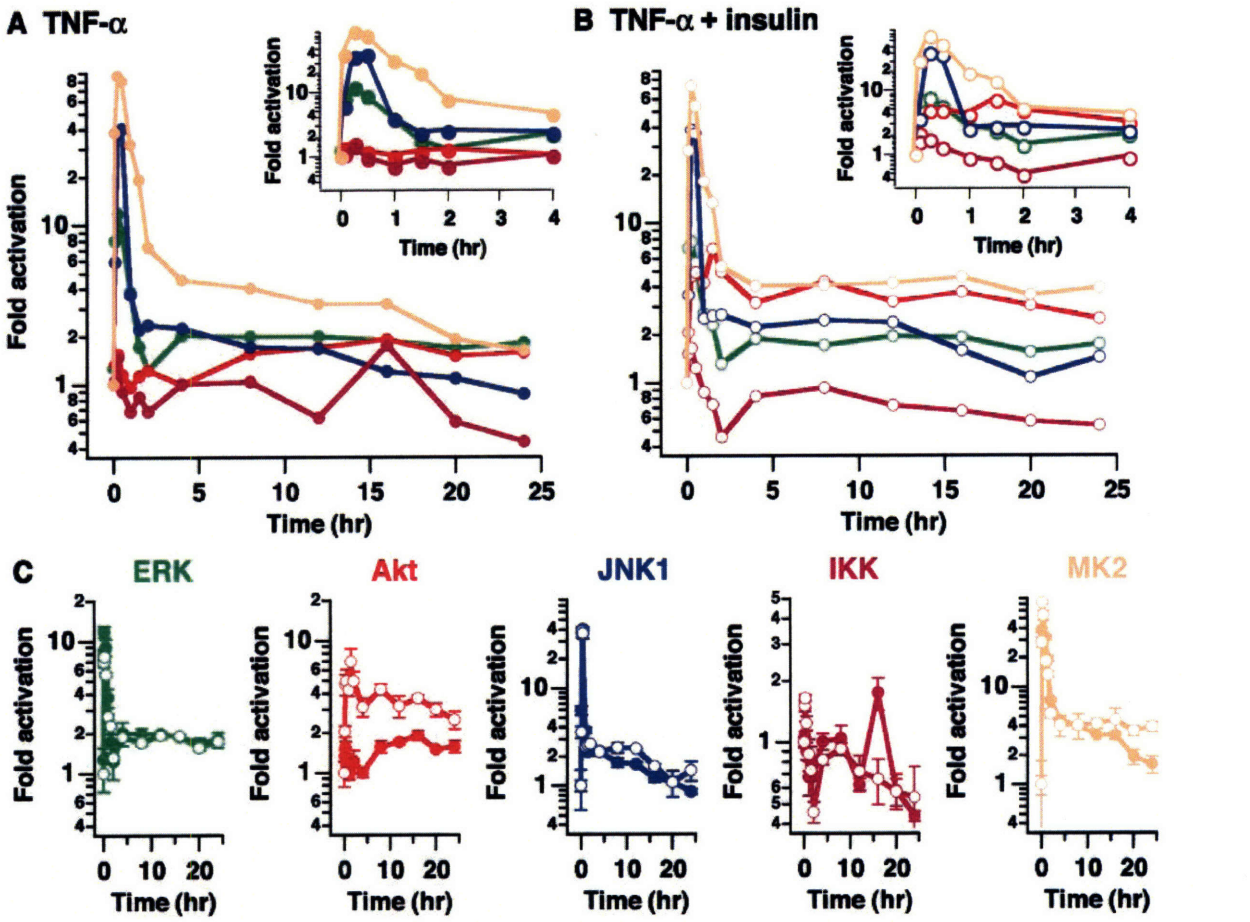

FIG. 7. **TNF-α and TNF-α + insulin treatments elicit quantitatively distinct signaling patterns in HT-29 cells.** Endogenous ERK (*green*), Akt (*red*), JNK1 (*blue*), IKK (*purple*), and MK2 (*orange*) activities in HT-29 cells in response to: *A*, 50 ng/ml TNF-α (*filled circles*) and *B*, 50 ng/ml TNF-α + 100 nM insulin (*open circles*). Lysates were generated at 0, 5, 15, 30, 60, 90 min and 2, 4, 8, 12, 16, 20, 24 h, then measured for kinase activity with the high-throughput multiplex kinase assay. Results are plotted as the mean fold activation of three independent cell extracts. Error bars are omitted for clarity, but are shown in panel *C*. *C*, comparison of ERK, Akt, JNK1, IKK and MK2 activities in response to TNF-α (*filled circles*) and TNF-α + insulin (*open circles*) from *A* and *B*, plotted as mean fold activation ± S.E. of triplicate samples.

multiplex assays provide reliable, quantitative measurements that are directly reflective of specific protein kinase activities in cell extracts.

Application to an In Vitro Model of Sepsis-induced Colon Epithelial Apoptosis—HT-29 cells are a human colon carcinoma cell line that die in response to TNF-α, following sensitization with interferon gamma (IFN-γ) (30). We confirmed that TNF-treated HT-29 cells exhibit many features of apoptosis, such as cell shrinkage, membrane blebbing, nuclear condensation, and caspase 3 activation (Fig. 6, *left*). Intriguingly, we found that TNF-induced cell death can be reduced by ~30% if HT-29 cells are costimulated with insulin (Fig. 6, *right*), in agreement with previous reports (31). Given the importance of proinflammatory cytokines, such as TNF-α and IFN-γ, in sepsis (4) and the emerging role of insulin as a therapeutic for critically ill patients (15), we considered HT-29 cells as an appropriate model system for exploring the signaling network dynamics activated by TNF-α and TNF-α + insulin in relation to a relevant cell phenotype: colon epithelial cell death, as observed during the onset of sepsis (6).

IFN-sensitized HT-29 cells were treated with 50 ng/ml TNF-α, in the presence or absence of 100 nM insulin cotreatment, and triplicate lysates were prepared at 13 time points over 24 h. Because much of the signaling induced by these cues occurs shortly after cytokine addition, time points were more densely sampled in the first 4 h (Fig. 7, *A* and *B*, *inset*). From these cell extracts, quantitative measurements of ERK, Akt, JNK1, MK2, and IKK kinase activity were performed using the high-throughput multiplex kinase activity assays (Fig. 7, *A* and *B*). To our knowledge, this set of time courses, consisting of over 400 independent activity measurements, represents the most comprehensive, rigorously quantitative study of functional signaling dynamics performed to date. To achieve this depth of quantitative, replicated network sampling by traditional techniques would have been extraordinarily laborious and technically impractical.

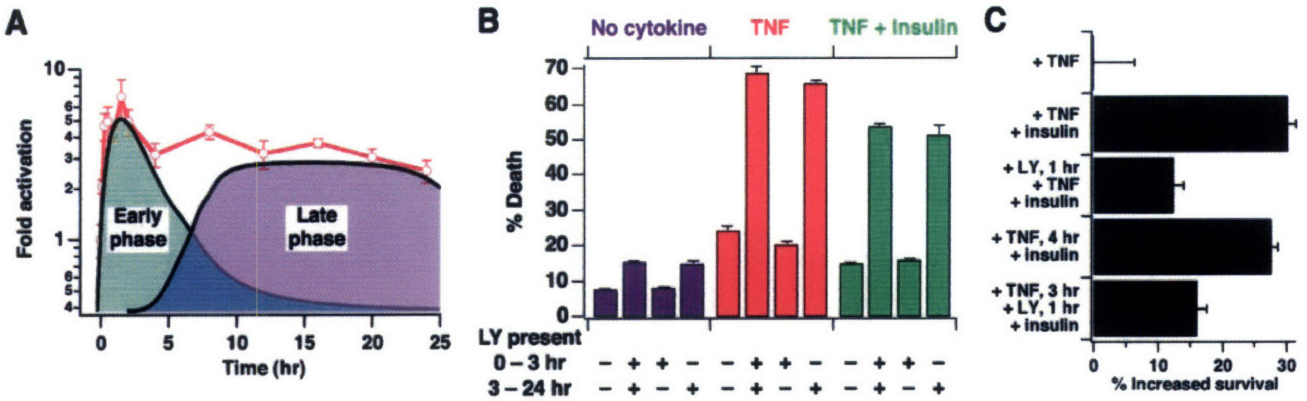

FIG. 8. **Insulin elevates two phases of Akt activity, and the late-phase of Akt activity provides a critical anti-apoptotic signal in HT-29 cells.** *A*, hypothetical two-phase contribution to the sustained Akt activity that was observed in the presence of insulin (Fig. 7, *B* and *C*). *B*, HT-29 cell death in response to no cytokines (■), 50 ng/ml TNF-α (■), or 50 ng/ml TNF-α + 100 nM insulin (■) in the presence of 20 μM LY294002 (*LY*) at the indicated times. Cells were stained for cleaved cytokeratin and cleaved caspase 3 and analyzed by flow cytometry as described under "Experimental Procedures." Values represent the percentage of apoptotic cells ± S.E. of triplicate samples. *C*, HT-29 cell survival in response to timed combinations of 50 ng/ml TNF-α, 100 nM insulin, and 20 μM LY294002. Values represent the percentage of increased survival ± S.E. of triplicate samples, computed as described under "Experimental Procedures." The carrier (0.1% DMSO) was kept constant for control experiments.

Furthermore, to deconstruct the effects of insulin therapy on the signaling network in the context of TNF-α signaling, a pairwise comparison was performed for each kinase under TNF-α with and without insulin costimulation. As shown in Fig. 7*C*, the dynamics of activation of some pathways, such as the ERK pathway (Fig. 7*C*, *green*), were essentially superimposable. Thus insulin does not appear to influence activation of the ERK pathway by TNF-α under these conditions. Other TNF-induced kinase activities were affected by insulin in a time-dependent manner. JNK1 activity, for example, was larger at intermediate times (8–16 h), while IKK activity was smaller at 16 h, and MK2 activity was larger at late times (16–24 h). Although potentially important, these transient signaling differences did not clearly reflect the insulin-induced survival phenotype observed at the cellular level (Fig. 6).

Late-phase Akt Activity as a Critical Pro-survival Signal—In contrast to the subtle influences of insulin on ERK, JNK1, IKK, and MK2 signaling, it was readily apparent that insulin dramatically augmented Akt activity, inducing a rapid increase within 5 min and sustaining activation for 24 h, whereas with TNF-α alone, the Akt response was much smaller in magnitude (Fig. 7*C*, *red*). In addition to these quantitative differences, we noted that the dynamic TNF-induced Akt response was also qualitatively different without insulin, in that the course of activation was clearly biphasic, with a brief initial peak, followed by a small (*i.e.* 2-fold), sustained increase in activity after 4 h. If these data had not been rigorously quantitative, or had the signaling network not been sampled frequently in time, this increase in activity would likely have been missed. By virtue of the high-throughput activity assays, however, it was clear that Akt activity after 4 h was significantly up-regulated in comparison to baseline activity ($p < 0.05$ for all times after 4 h, Student's *t* test).

These findings suggested that a significant component of the insulin-induced anti-apoptotic effect was mediated by the high sustained Akt activity, and that this activity profile was derived from the superposition of an early, elevated phase of activity that was transient with a late, elevated phase of activity that was sustained (Fig. 8*A*). Conversely, in cells treated with TNF-α alone, these two phases were reduced in intensity and separated in time. Because Akt is thought to provide strong pro-survival signals (10), we hypothesized that one or both of these temporal components of Akt activation were involved in controlling the phenotypic response of HT-29 cells to TNF-α and insulin.

To investigate this, we used a reversible, selective inhibitor (LY294002 (32)) of phosphatidylinositol 3-kinase (PI 3-K), an upstream activator of Akt. LY294002 was added or removed at critical times to eliminate the early phase of Akt activity, the late phase of Akt activity, or both, and apoptosis was quantified by flow cytometry with an anti-cleaved caspase 3 antibody and the M30 antibody (33) against caspase-cleaved cytokeratin. We have found this double stain to be the most sensitive, quantitatively reproducible measure of apoptosis in HT-29 cells.[3]

When LY294002 was added 1 h before cytokine addition and tonically maintained to block Akt activity over the entire time course, a dramatic increase in TNF-induced cell death was observed (Fig. 8*B*, *red*). Surprisingly, if LY294002 was present only for the first 3 h of TNF-α addition, thus permitting only the late phase of Akt activity, there was no increased cell death relative to treatments without inhibitor. In contrast, when LY294002 was first added at 3 h after cytokine addition to selectively abolish late-phase Akt activity, we observed an increase in cell death equivalent to that observed when the

[3] J. G. Albeck, unpublished observations.

inhibitor was present for the entire 24 h. An identical pattern was observed in response to TNF-α + insulin (Fig. 8*B*, *green*), whereas LY294002 had only a small effect on basal apoptosis (Fig. 8*B*, *blue*). These data suggest that late-phase Akt activation is necessary to restrain the percentage of cells undergoing programmed cell death in response to TNF-α in the presence or absence of insulin.

The importance of late Akt activity in controlling TNF-induced cell death, in conjunction with the strong, sustained late Akt activation in the presence of insulin, led to the hypothesis that the insulin-induced increase in cell survival was due, in part, to this increase in late-phase Akt signaling. If true, then addition of insulin up to 4 h after the pro-death stimulus should elicit an equivalent reduction in the extent of TNF-induced apoptosis. Indeed, this was observed; the delayed addition of insulin 4 h following TNF-α addition resulted in the same increase in HT-29 cell survival as observed when insulin was added simultaneously with TNF-α (Fig. 8*C*). Moreover, pretreatment with LY294002 1 h before insulin addition significantly reduced the survival response, regardless whether insulin was added simultaneously or 4 h after TNF-α treatment (Fig. 8*C*).

These experiments strongly implicate late-phase signaling, along a PI 3-K-dependent/Akt pathway, as a critical pro-survival mechanism of insulin in colon epithelia. Excessive apoptosis in the gut leads to disruption of the epithelial permeability barrier (7) that drives many of the complications of the septic state (8). Our results provide a partial molecular explanation why intensive insulin therapy, administered hours after the initial septic insult, is capable of reducing sepsis-induced apoptosis of gastrointestinal epithelia and improving the prognostic outcome in critically ill patients.

We stress that it was the ability to robustly sample the dynamics of multiple nodes in the signaling network with the high-throughput multiplex kinase assay format described in this paper that enabled the identification of Akt as an important signal for modulating cell response. Other insulin-induced, PI 3-K independent pathways must also attenuate the TNF-induced apoptotic phenotype in HT-29 cells, because inhibition of PI 3-K/Akt by LY294002 did not completely abrogate the rescue response of insulin (Fig. 8*C*). Thus, i) there may exist additional response-determining pathways that our measurements did not capture, or ii) the subtle, time-dependent quantitative differences we measured in the JNK1, IKK, and MK2 pathways (Fig. 7*C*) may modulate phenotypic response. We are currently investigating both these possibilities.

The current knowledge of intracellular signal transduction is staggeringly complex. To identify network-level properties that affect cell function, it will be necessary to mathematically model the dynamic, multivariate characteristics of signaling proteins within cells (34). For such models to be realized, quantitative experimental techniques that are both high-throughput and multiplex are needed. The kinase activity assay format presented here represents a first step in this direction. The 96-well, microtiter format is highly versatile, in that it is amenable to scale-up and automated liquid handling, yet tractable for individual scientists and more moderate studies. Importantly, these assays possess linearity, reproducibility, specificity, and sensitivity characteristics as good as, or better than, the corresponding low-throughput technique. We anticipate that these functional assays will complement existing proteomic approaches (2) and find broad applicability toward biological and clinical problems involving signal transduction and human disease.

Acknowledgments—We thank Isaac Manke for providing the MK2tide sequence ahead of publication, as well as Roger Davis and Warner Greene for providing various plasmids.

* This work was supported by the Defense Advanced Research Planning Agency Bio-Info-Micro Program, the National Institute of General Medical Sciences Cell Migration Consortium (to D. A. L.), and National Institutes of Health Grant GM59281 (to M. B. Y.). Additional financial support was provided by the Whitaker Foundation (to K. A. J.). The costs of publication of this article were defrayed in part by the payment of page charges. This article must therefore be hereby marked "*advertisement*" in accordance with 18 U.S.C. Section 1734 solely to indicate this fact.

‖ To whom correspondence should be addressed: Center for Cancer Research, Massachusetts Institute of Technology, 77 Massachusetts Ave. E18–580, Cambridge, MA 02139. Tel.: 617-452-2103, Fax: 617-452-4978; E-mail: myaffe@mit.edu.

REFERENCES

1. Nguyen, A., and Yaffe, M. B. (2003) Proteomics and systems biology approaches to signal transduction in sepsis. *Crit. Care Med.* **31,** S1–S6
2. Tyers, M., and Mann, M. (2003) From genomics to proteomics. *Nature* **422,** 193–197
3. Asthagiri, A. R., Horwitz, A. F., and Lauffenburger, D. A. (1999) A rapid and sensitive quantitative kinase activity assay using a convenient 96-well format. *Anal. Biochem.* **269,** 342–347
4. Hotchkiss, R. S., and Karl, I. E. (2003) The pathophysiology and treatment of sepsis. *N. Engl. J. Med.* **348,** 138–150
5. Strassheim, D., Park, J. S., and Abraham, E. (2002) Sepsis: Current concepts in intracellular signaling. *Int. J. Biochem. Cell Biol.* **34,** 1527–1533
6. Hotchkiss, R. S., Schmieg, R. E., Jr., Swanson, P. E., Freeman, B. D., Tinsley, K. W., Cobb, J. P., Karl, I. E., and Buchman, T. G. (2000) Rapid onset of intestinal epithelial and lymphocyte apoptotic cell death in patients with trauma and shock. *Crit. Care Med.* **28,** 3207–3217
7. Bojarski, C., Bendfeldt, K., Gitter, A. H., Mankertz, J., Fromm, M., Wagner, S., Riecken, E. O., and Schulzke, J. D. (2000) Apoptosis and intestinal barrier function. *Ann. N. Y. Acad. Sci.* **915,** 270–274
8. Wattanasirichaigoon, S., Menconi, M. J., Delude, R. L., and Fink, M. P. (1999) Effect of mesenteric ischemia and reperfusion or hemorrhagic shock on intestinal mucosal permeability and ATP content in rats. *Shock* **12,** 127–133
9. Hatherill, M., Tibby, S. M., Turner, C., Ratnavel, N., and Murdoch, I. A. (2000) Procalcitonin and cytokine levels: relationship to organ failure and mortality in pediatric septic shock. *Crit. Care Med.* **28,** 2591–2594
10. Lawlor, M. A., and Alessi, D. R. (2001) PKB/Akt: a key mediator of cell proliferation, survival and insulin responses? *J. Cell Sci.* **114,** 2903–2910
11. Davis, R. J. (2000) Signal transduction by the JNK group of MAP kinases. *Cell* **103,** 239–252
12. Karin, M., and Ben-Neriah, Y. (2000) Phosphorylation meets ubiquitination: The control of NF-κB activity. *Annu. Rev. Immunol.* **18,** 621–663
13. Stokoe, D., Engel, K., Campbell, D. G., Cohen, P., and Gaestel, M. (1992) Identification of MAPKAP kinase 2 as a major enzyme responsible for the phosphorylation of the small mammalian heat shock proteins. *FEBS Lett.* **313,** 307–313
14. Fisher, C. J., Jr., Agosti, J. M., Opal, S. M., Lowry, S. F., Balk, R. A., Sadoff,

J. C., Abraham, E., Schein, R. M., and Benjamin, E. (1996) Treatment of septic shock with the tumor necrosis factor receptor:Fc fusion protein. The Soluble TNF Receptor Sepsis Study Group. *N. Engl. J. Med.* **334,** 1697–1702

15. van den Berghe, G., Wouters, P., Weekers, F., Verwaest, C., Bruyninckx, F., Schetz, M., Vlasselaers, D., Ferdinande, P., Lauwers, P., and Bouillon, R. (2001) Intensive insulin therapy in the critically ill patients. *N. Engl. J. Med.* **345,** 1359–1367
16. Van den Berghe, G., Wouters, P. J., Bouillon, R., Weekers, F., Verwaest, C., Schetz, M., Vlasselaers, D., Ferdinande, P., and Lauwers, P. (2003) Outcome benefit of intensive insulin therapy in the critically ill: Insulin dose versus glycemic control. *Crit. Care Med.* **31,** 359–366
17. Hirsch, I. B., and Coviello, A. (2002) Intensive insulin therapy in critically ill patients. *N. Engl. J. Med.* **346,** 1586–1588
18. Hansen, T. K., Thiel, S., Wouters, P. J., Christiansen, J. S., and Van den Berghe, G. (2003) Intensive insulin therapy exerts antiinflammatory effects in critically ill patients and counteracts the adverse effect of low mannose-binding lectin levels. *J. Clin. Endocrinol. Metab.* **88,** 1082–1088
19. Obata, T., Yaffe, M. B., Leparc, G. G., Piro, E. T., Maegawa, H., Kashiwagi, A., Kikkawa, R., and Cantley, L. C. (2000) Peptide and protein library screening defines optimal substrate motifs for AKT/PKB. *J. Biol. Chem.* **275,** 36108–36115
20. Gupta, S., Campbell, D., Derijard, B., and Davis, R. J. (1995) Transcription factor ATF2 regulation by the JNK signal transduction pathway. *Science* **267,** 389–393
21. Geleziunas, R., Ferrell, S., Lin, X., Mu, Y., Cunningham, E. T., Jr., Grant, M., Connelly, M. A., Hambor, J. E., Marcu, K. B., and Greene, W. C. (1998) Human T-cell leukemia virus type 1 Tax induction of NF-kappaB involves activation of the IkappaB kinase alpha (IKKalpha) and IKKbeta cellular kinases. *Mol. Cell. Biol.* **18,** 5157–5165
22. Judd, R. C. (1994) Electrophoresis of peptides, in *Methods in Molecular Biology* (Walker, J. M., ed.) p. 32, Humana Press, Totowa, NJ
23. Whitmarsh, A. J., and Davis, R. J. (2001) Analyzing JNK and p38 mitogen-activated protein kinase activity. *Methods Enzymol.* **332,** 319–336
24. Hill, M. M., and Hemmings, B. A. (2002) Analysis of protein kinase B/Akt. *Methods Enzymol.* **345,** 448–463
25. Kupfer, R., and Scheinman, R. I. (2002) Measurement of IKK activity in primary rat T cells: rapid activation and inactivation. *J. Immunol. Methods.* **266,** 155–164
26. Arcaro, A., and Wymann, M. P. (1993) Wortmannin is a potent phosphatidylinositol 3-kinase inhibitor: the role of phosphatidylinositol 3, 4, 5-trisphosphate in neutrophil responses. *Biochem. J.* **296 (Pt 2),** 297–301
27. Bennett, B. L., Sasaki, D. T., Murray, B. W., O'Leary, E. C., Sakata, S. T., Xu, W., Leisten, J. C., Motiwala, A., Pierce, S., Satoh, Y., Bhagwat, S. S., Manning, A. M., and Anderson, D. W. (2001) SP600125, an anthrapyrazolone inhibitor of Jun N-terminal kinase. *Proc. Natl. Acad. Sci. U. S. A.* **98,** 13681–13686
28. Rossi, A., Kapahi, P., Natoli, G., Takahashi, T., Chen, Y., Karin, M., and Santoro, M. G. (2000) Anti-inflammatory cyclopentenone prostaglandins are direct inhibitors of IkappaB kinase. *Nature* **403,** 103–108
29. Lee, J. C., Laydon, J. T., McDonnell, P. C., Gallagher, T. F., Kumar, S., Green, D., McNulty, D., Blumenthal, M. J., Heys, J. R., Landvatter, S. W., Strickler, J. E., McLaughlin, M. M., Siemens, J. R., Fisher, S. M., Livi, G. P., White, J. R., Adams, J. L., and Young, P. R. (1994) A protein kinase involved in the regulation of inflammatory cytokine biosynthesis. *Nature* **372,** 739–746
30. Abreu-Martin, M. T., Vidrich, A., Lynch, D. H., and Targan, S. R. (1995) Divergent induction of apoptosis and IL-8 secretion in HT-29 cells in response to TNF-alpha and ligation of Fas antigen. *J. Immunol.* **155,** 4147–4154
31. Remacle-Bonnet, M. M., Garrouste, F. L., Heller, S., Andre, F., Marvaldi, J. L., and Pommier, G. J. (2000) Insulin-like growth factor-I protects colon cancer cells from death factor-induced apoptosis by potentiating tumor necrosis factor alpha-induced mitogen-activated protein kinase and nuclear factor kappaB signaling pathways. *Cancer Res.* **60,** 2007–2017
32. Vlahos, C. J., Matter, W. F., Hui, K. Y., and Brown, R. F. (1994) A specific inhibitor of phosphatidylinositol 3-kinase, 2-(4-morpholinyl)-8-phenyl-4H-1-benzopyran-4-one (LY294002). *J. Biol. Chem.* **269,** 5241–5248
33. Leers, M. P., Kolgen, W., Bjorklund, V., Bergman, T., Tribbick, G., Persson, B., Bjorklund, P., Ramaekers, F. C., Bjorklund, B., Nap, M., Jornvall, H., and Schutte, B. (1999) Immunocytochemical detection and mapping of a cytokeratin 18 neo-epitope exposed during early apoptosis. *J. Pathol.* **187,** 567–572
34. Asthagiri, A. R., and Lauffenburger, D. A. (2000) Bioengineering models of cell signaling. *Annu. Rev. Biomed. Eng.* **2,** 31–53

Appendix D

Improved fluorescent protein reporters for observing the apoptotic network

This work was performed in collaboration with Bree Aldridge, who constructed the novel caspase-3 reporter described here and performed the experiment shown in Fig. D1 with my supervision

Introduction

To examine the relationship of various signals in the apoptotic pathway, reliable single-cell reporters are required. A reliable reporter must be 1) specific for the intended molecular event, and 2) non-invasive, leaving endogenous signaling dynamics unaltered. While several reporters for caspases (Luo et al. 2001; Rehm et al. 2002; Luo et al. 2003; Takemoto et al. 2003; Kawai et al. 2004) and the mitochondrial pathway (Goldstein et al. 2000; Rehm et al. 2003; Munoz-Pinedo et al. 2006) have been previously described, it is not clear that these reporters meet the requirements for specificity and signaling neutrality. For example, the caspase FRET reporter containing the cleavage sequence DEVD is often used as a reporter of caspase-3/7 activity, since DEVD is the optimal cleavage sequence for caspase-3/7 (Thornberry et al. 1997). However, it is clear from numerous publications that the sequence DEVD can serve as a substrate for other caspases, most notably caspase-8 (Blanchard et al. 2000; Rehm et al. 2002). Thus, this FRET reporter may not be a highly specific indicator of effector caspase activity. In the case of the mitochondrial pathway, fluorescent protein fusions to cytochrome c, Smac, and other mitochondrial intermembrane space proteins have been used to observe the process of mitochondrial permeabilization (Goldstein et al. 2000; Rehm et al. 2003; Munoz-Pinedo et al. 2006). It has been observed that each of these fusion proteins, like the endogenous versions, are typically localized to the mitochondria but simultaneously redistribute to the cytosol when the mitochondrial outer membrane is permeabilized in response to pro-apoptotic stimuli. However, as the work in this thesis has indicated, the kinetics of caspase activity are critically dependent on the levels and ratios of proteins such as Smac that are released from the mitochondria. Consequently, overexpressing

GFP-fused versions of these proteins is likely to have a significant effect on the functioning of the system. Thus, there are several features of existing reporters that need to be improved before in-depth studies of apoptotic signaling can be performed.

A caspase-3 reporter with improved specificity

To create a caspase-3/7-specific reporter, we turned to the literature to identify a peptide sequence that would be an efficient substrate for the effector caspases but a poor substrate for other caspases such as caspase-8. Caspase consensus sequences are typically designed as tetrapeptide motifs whose C-terminal residue is the aspartate at which the peptide backbone is cleaved. However, a detailed study of the specificity of caspase-8 and caspase-3 for residues at each of the traditional four positions suggested few possibilities that would screen out caspase-8 cleavage while allowing efficient caspase-3 cleavage. We then examined the P(-1) position, which follows the tetrapeptide motif, and has been shown to have significant influence on cleavage specificity (Stennicke et al. 2000). In the original DEVD reporter (and most other published reporters), the P(-1) position is occupied by G, which is the optimal residue for this position for both caspase-3 and caspase-8 . However, if this G is converted to an R, the kcat/Km for caspase-3 is reduced by ~14-fold, while the kcat/Km for caspase-8 is reduced by ~300-fold (Stennicke et al. 2000). Thus, a peptide substrate with the sequence of DEVDR should substantially increase its suitability as a substrate of caspase-3 relative to caspase-8. Therefore, we constructed a new FRET reporter, in which ECFP and Venus-YFP proteins were linked by a peptide containing the sequence DEVDR.

To test the specificity of the DEVDR FRET reporter, we examined its behavior in cells where caspase-8 was active but caspase-3 was not. In previous work, we noted that in Bcl-2-overexpressing HeLa cells treated with TRAIL+CHX, caspase-3 was efficiently cleaved by caspase-8, but the caspase-3/7 substrate PARP remained entirely uncleaved due to the inhibitory activity of XIAP (Fig 2.2 F). Thus, a reporter that is highly specific for caspase-3/7 activity would show no cleavage in Bcl-2 overexpressing cells, but would be cleaved rapidly in wild type HeLa cells. Therefore, we transfected Bcl-2-overexpressing HeLa cells with both the conventional DEVDG-containing FRET reporter, and our DEVDR-containing FRET reporter and examined the change in FRET ratio in response to TRAIL treatment. Under these conditions, a gradual but substantial increase in cleavage of the DEVDG reporter was observed, indicating its cleavage by caspase-8. Conversely the DEVDR reporter displayed very little increase in signal, indicating that it is insensitive to caspase-8-mediated cleavage. In other work, we found that in standard HeLa cells, both DEVDG and DEVDR reporters were cleaved with similar kinetics. Thus, it appears that the DEVDR reporter effectively serves as a caspase-3 reporter and is a substantial improvement over DEVDG in resisting cleavage by caspase-8.

A caspase-8 FRET reporter with improved pH insensitivity

Reporters of caspase-8 activity have been previously reported (Luo et al. 2003; Kawai et al. 2004). The cleavage sequence in these reporters is IETD, the optimal peptide substrate for caspase-8. This sequence is a poor substrate of caspase-3 due to the isoleucine in the P1 position (Thornberry et al. 1997). The general difficulty in creating

caspase-8 reporters is that caspase-8 is catalytically less efficient than caspase-3; this problem has been solved by including tandem IETD sites in the linker peptide, creating a higher likelihood of linker cleavage by caspase-8 (Luo et al. 2003). This design for a caspase-8 reporter is likely to be fairly specific to caspase-8 and other initiator caspases. However, the existing reporters were constructed using an older version of YFP (EYFP) that displays substantial sensitivity to pH changes, complicating the interpretation of its behavior. Therefore, we constructed a FRET reporter using the tandem-IETD linker, but in which the pH-insensitive YFP variant Venus was substituted for EYFP.

A non-invasive reporter for mitochondrial permeabilization

Another key even in apoptotic signaling is the permeabilization of the mitochondria. One method that has long been used for observing mitochondrial events during apoptosis is the use of dyes such as tetramethylrhodamine that are sensitive to the mitochondrial membrane potential. Such dyes indicate a drastic drop in mitochondrial membrane potential (membrane depolarization) that is simultaneous with effector caspase activity. However, recent research has shown that mitochondrial permeabilization and depolarization are two independent and separable events. Mitochondrial permeabilization is the crucial first step in which signaling molecules such as Smac and cytochrome c are released to the cytosol, while depolarization is a later event that is at least partially dependent on effector caspase activation. Thus, to observe the signaling behavior of the mitochondria, it is crucial to measure permeabilization rather than depolarization. Permeabilization can be observed by tracking proteins such as cytochrome c and Smac fused to fluorescent proteins. However, as noted above,

apoptotic behavior is highly sensitive to the expression levels of these proteins. Therefore, it would be advantageous to develop a non-signaling version of such proteins, which could act as indicators without altering signaling behavior. One such possibility is presented by Smac. The precursor of Smac is transported into the mitochondria by an N-terminal signal peptide of 60 amino acids. Once inside the mitochondria, this peptide is cleaved to generate mature Smac; this cleavage is necessary for Smac activity, since the XIAP-binding motif of mature Smac, consisting of the four residues immediately following the signal peptide, is only functional when this motif has been exposed by cleavage (Verhagen et al. 2000; Zou et al. 2003). To create a non-signaling reporter of Smac localization, we generated a gene fusion in which the signal sequence of Smac is immediately upstream of monomeric red fluorescent protein (RFP). In theory, this fusion protein would be imported into the mitochondrial intermembrane space by the signal peptide, where it would be cleaved to generate free RFP. Since permeabilization appears to be a non-selective event in which all soluble proteins in the mitochondrial intermembrane space are released through large pores, RFP should also be released simultaneously with endogenous Smac, cytochrome c, and other proteins. However, this fusion protein would not affect signaling, since it lacks the XIAP-binding motif and all other signaling domains of mature Smac. We named this reporter IMS-RFP, since it generates RFP localized to the intermembrane space of the mitochondria.

To test the ability of IMS-RFP to accurately report mitochondrial permeabilization, we transiently transfected HeLa cells with this construct. As expected, IMS-RFP displayed a predominantly mitochondrial localization pattern and co-localized with cytochrome c, as assessed by immunofluorescence for cytochrome c (Fig D2 A).

When IMS-RFP-expressing cells were treated with TNF, the localization pattern of both cytochrome c and IMS-RFP changed, reflecting release from the mitochondria to the cytosol. Importantly, all cells in which cytochrome c was redistributed to the cytosol also showed IMS-RFP release, indicating that release of IMS-RFP and cytochrome c were simultaneous (Fig D2A). However, in contrast to cytochrome c, some mitochondrial localization of IMS-RFP was retained even after release. This suggests that, unlike cytochrome c, IMS-RFP is not completely released upon permeabilization; a potential explanation is that IMS-RFP is not efficiently cleaved within the mitochondria and thus cannot be fully released. Nonetheless, IMS-RFP could be expressed at high levels without toxicity, and in time-lapse image sequences, the first frame of IMS-RFP release could be clearly identified in every case (Fig D2 B). This frame indicates the onset of mitochondrial permeabilization, a key event in apoptosis; it can be inferred that this time point also marks the onset of the release of endogenous Smac, cytochrome c, and other proteins of the intermebrane space. (Janes et al. 2003; Gaudet et al. 2005; Janes et al. 2006)

References

Blanchard H, Donepudi M, Tschopp M, Kodandapani L, Wu JC et al. (2000) Caspase-8 specificity probed at subsite S(4): crystal structure of the caspase-8-Z-DEVD-cho complex. J Mol Biol 302(1): 9-16.

Gaudet S, Janes KA, Albeck JG, Pace EA, Lauffenburger DA et al. (2005) A compendium of signals and responses triggered by prodeath and prosurvival cytokines. Mol Cell Proteomics 4(10): 1569-1590.

Goldstein JC, Waterhouse NJ, Juin P, Evan GI, Green DR (2000) The coordinate release of cytochrome c during apoptosis is rapid, complete and kinetically invariant. Nat Cell Biol 2(3): 156-162.

Janes KA, Albeck JG, Peng LX, Sorger PK, Lauffenburger DA et al. (2003) A high-throughput quantitative multiplex kinase assay for monitoring information flow in signaling networks: application to sepsis-apoptosis. Mol Cell Proteomics 2(7): 463-473.

Janes KA, Gaudet S, Albeck JG, Nielsen UB, Lauffenburger DA et al. (2006) The response of human epithelial cells to TNF involves an inducible autocrine cascade. Cell 124(6): 1225-1239.

Kawai H, Suzuki T, Kobayashi T, Mizuguchi H, Hayakawa T et al. (2004) Simultaneous imaging of initiator/effector caspase activity and mitochondrial membrane potential during cell death in living HeLa cells. Biochim Biophys Acta 1693(2): 101-110.

Luo KQ, Yu VC, Pu Y, Chang DC (2001) Application of the fluorescence resonance energy transfer method for studying the dynamics of caspase-3 activation during UV-induced apoptosis in living HeLa cells. Biochem Biophys Res Commun 283(5): 1054-1060.

Luo KQ, Yu VC, Pu Y, Chang DC (2003) Measuring dynamics of caspase-8 activation in a single living HeLa cell during TNFalpha-induced apoptosis. Biochem Biophys Res Commun 304(2): 217-222.

Munoz-Pinedo C, Guio-Carrion A, Goldstein JC, Fitzgerald P, Newmeyer DD et al. (2006) Different mitochondrial intermembrane space proteins are released during apoptosis in a manner that is coordinately initiated but can vary in duration. Proc Natl Acad Sci U S A 103(31): 11573-11578.

Rehm M, Dussmann H, Prehn JH (2003) Real-time single cell analysis of Smac/DIABLO release during apoptosis. J Cell Biol 162(6): 1031-1043.

Rehm M, Dussmann H, Janicke RU, Tavare JM, Kogel D et al. (2002) Single-cell fluorescence resonance energy transfer analysis demonstrates that caspase activation during apoptosis is a rapid process. Role of caspase-3. J Biol Chem 277(27): 24506-24514.

Stennicke HR, Renatus M, Meldal M, Salvesen GS (2000) Internally quenched fluorescent peptide substrates disclose the subsite preferences of human caspases 1, 3, 6, 7 and 8. Biochem J 350 Pt 2: 563-568.

Takemoto K, Nagai T, Miyawaki A, Miura M (2003) Spatio-temporal activation of caspase revealed by indicator that is insensitive to environmental effects. J Cell Biol 160(2): 235-243.

Thornberry NA, Rano TA, Peterson EP, Rasper DM, Timkey T et al. (1997) A combinatorial approach defines specificities of members of the caspase family and granzyme B. Functional relationships established for key mediators of apoptosis. J Biol Chem 272(29): 17907-17911.

Verhagen AM, Ekert PG, Pakusch M, Silke J, Connolly LM et al. (2000) Identification of DIABLO, a mammalian protein that promotes apoptosis by binding to and antagonizing IAP proteins. Cell 102(1): 43-53.

Zou H, Yang R, Hao J, Wang J, Sun C et al. (2003) Regulation of the Apaf-1/caspase-9 apoptosome by caspase-3 and XIAP. J Biol Chem 278(10): 8091-8098.

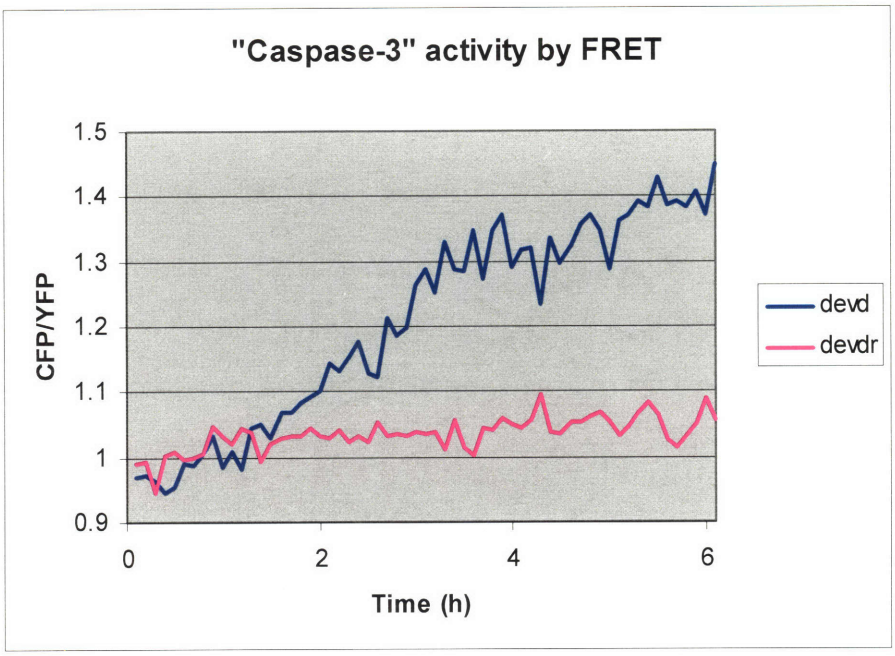

Figure D1. A FRET reporter containing the sequence DEVDR provides improved specificity for caspase-3. Bcl-2-overexpressing HeLa cells were transfected with the plasmids pECFP-DEVD-Venus or pECFP-DEVDR-Venus. Cells were then treated with TRAIL, and reporter cleavage was monitored by measuring the CFP/YFP ratio by live-cell microscopy.

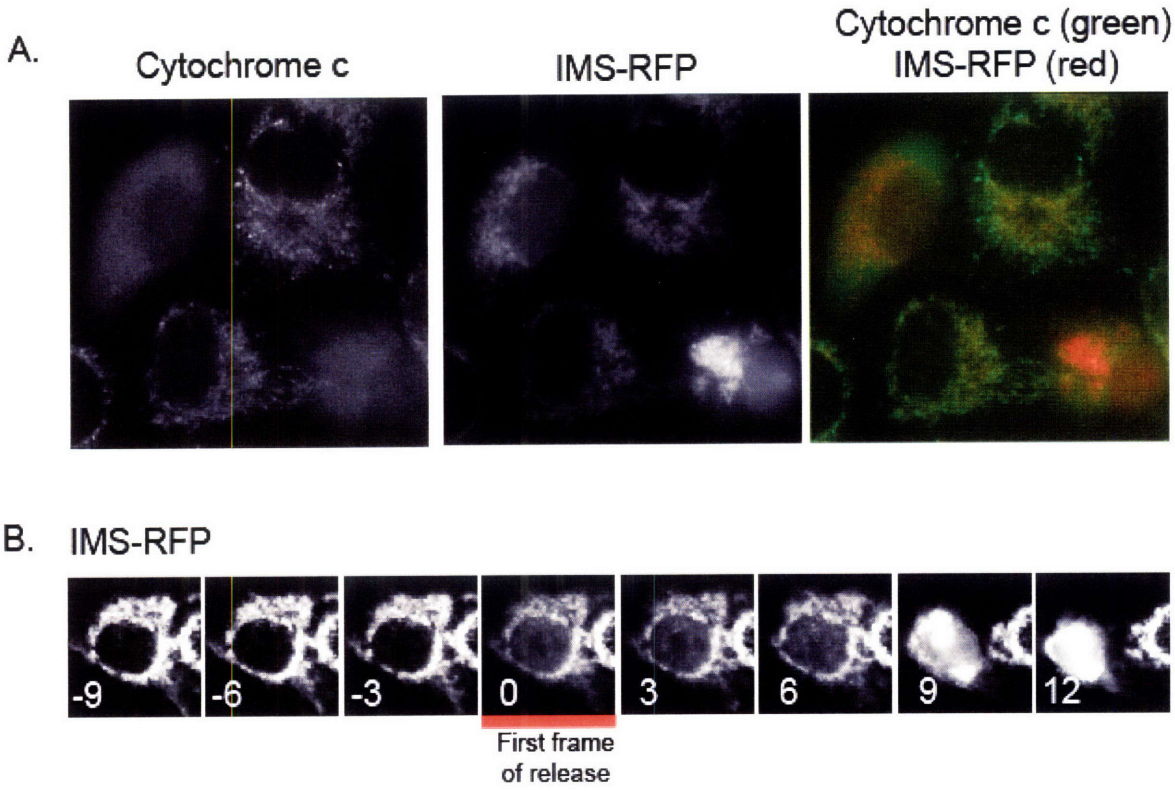

Figure D2. IMS-RFP release from the mitochondria coincides with cytochrome c release and indicates the onset of mitochondrial permeabilization. A. HeLa cells transfected with pExchange1-IMS-RFP were treated with TNF+CHX for 4 hours. Cells were then fixed, and cytochrome c was detected by immunofluorescence and compared to IMS-RFP fluorescence. B. HeLa cells transfected with pExchange1-IMS-RFP were treated with TNF+CHX, and IMS-RFP was tracked by live cell microscopy. Numbers in each panel indicate the time, in minutes, relative to the first frame in which IMS-RFP release is apparent (red bar).

Appendix E

A MATLAB routine for generating simulated flow cytometry data based on a hypothetical population of cells

To simulate the expected flow cytometry patterns of cPARP cleavage, the following Matlab procedure was used:

First, the number of cells, c, in the simulation is defined. Most cytometry experiments measure 10,000 cells.

```
cells=10000;
```

Each single cell will be represented by a Boltzmann equation, as described in Chapter 2. First, we choose a characteristic time (tchar) and a maximum fraction of PARP cleaved (Fmax); these parameters will be applied to all cells in the population, since single-cell experiments indicate little cell-to-cell variation in these parameters.

```
tchar=20;  %(minutes)
Fmax=1.0;  %(fraction, ranging from 0 to 1)
```

Next, we define the mean and standard deviation for a distribution of delay times. For each cell, a delay time will be chosen randomly from a normal distribution with these parameters, to reflect the experimentally observed approximately normal distribution of delay times in cells treated with 50 ng/ml TRAIL.

```
meandelay=200;  %(minutes)
delaystdev=40;  %(minutes)
delays=meandelay+delaystdev*randn(c,1);
```

The number of timepoints for flow cytometry measurement (in addition to the zero time point), and the spacing between timepoints, are defined:

```
numtimepoints=3;
timespacing=120; %(minutes)
```

Initialize a matrix to hold the raw signal (the fraction of PARP cleaved) of each cell at each timepoint. Then, at each time point, determine the raw signal of each cell by calculating the value of the Boltzmann equation for that cell's delay, tchar, and Fmax.

```
rawsignals=zeros(c,numtimepoints);

for t=0:numtimepoints
    for i=1:cells
        rawsignals(i,t)=(Fmax-(Fmax)/(1+exp((t*timespacing-
delays(i))/(tchar/4))));
    end
end
```

Next, we need to account for the processing of signals by the flow cytometer.

Our flow cytometry measurements were made on a flow cytometer with a 4-decade logarithmic amplifier with 1024 detection channels.

```
channels=linspace(0,4,1024);
```

The voltage of the amplifier can be adjusted, so that cells with a raw signal of 1 may fall at any arbitrary point in the amplifier's range. In most of our experiments, the fluorescence intensity of cells with complete PARP cleavage was around 1000.

```
amplification=1000;
```

All cells have background fluorescence, so that even cells with a raw signal of 0 display a non-zero fluorescence intensity; in our experiments, this value was approximately10.

```
background=10;
```

Instrument noise and cell-to-cell variation in cell size and staining intensity lead to a distribution of measured signals centered around the actual raw signal. This distribution is approximated by a lognormal distribution. Empirically, the variance of this lognormal distribution ranges from 0.4 to 0.5. We then assign a noise value for each cell chosen at random from this distribution.

```
noisevariance=0.4;
noisevalues=lognrnd(0,noisevariance,c,numtimepoints);
```

We then calculate the actual observed signal for each cell by adding the background signal to each and multiplying by the noise value:

```
measuredsignals=noisevalues.*(rawsignals.*amplification+background);
```

The measured signals are then binned into the appropriate channels, and the resulting histogram is plotted.

```
for tf=0:numtimepoints

    subplot(numtimepoints+1,1,tf+1);
    p=hist(log10(measuredsignals(:,tf+1)),channels);
    hold on;


    axis([0,1024,0,histy]);
    set(gca,'xtick',[0,256,512,768,1024]);

end
```

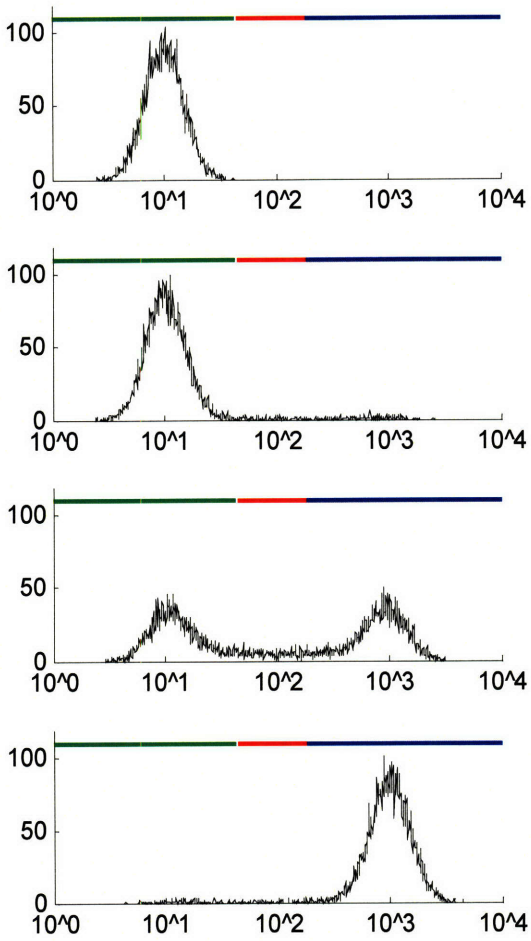

To facilitate comparisons to actual experiments, gates are created to contain the negative, intermediate, and positive cells. This is done by defining the boundaries for each gate. A matrix named 'frequencies' is created to hold the percentage of cells in each gate at each timepoint.

```
neg_start=1;
neg_end=420;
int_start=421;
int_end=580;
pos_start=581;
pos_end=1024;

frequencies=zeros(3,numtimepoints+1);
```

The fraction of cells falling into each gate is calculated by simply summing across the appropriate regions of the histogram.

```
for t=0:numtimepoints
    temphist=hist(log10(x(:,t+1)),bins);
    popgates(1,t+1)=sum(temphist(neg_start:neg_end))/cells;
    popgates(2,t+1)=sum(temphist(int_start:int_end))/cells;
    popgates(3,t+1)=sum(temphist(pos_start:pos_end))/cells;
end
```

These frequencies are then plotted:

```
popgates(2,:)=-popgates(2,:);
bar(popgates','grouped');
axis([0.5 4.5 -11000 11000]);
```

For actual experimental data, gate positions were determined as follows. First, the intermediate gate was defined to be 160 channels wide, and was positioned on control samples to lie between the positive and negative peaks at a point where the number of cells in the intermediate gate was approximately at a minimum. Negative and positive gates were then defined as the remaining regions below and above the intermediate gate, respectively.

A graphical interface was created that produces simulated data for any input set of parameters. This interface was used to adjust the parameters to best match the experimental data, providing an estimate of single cell parameters.

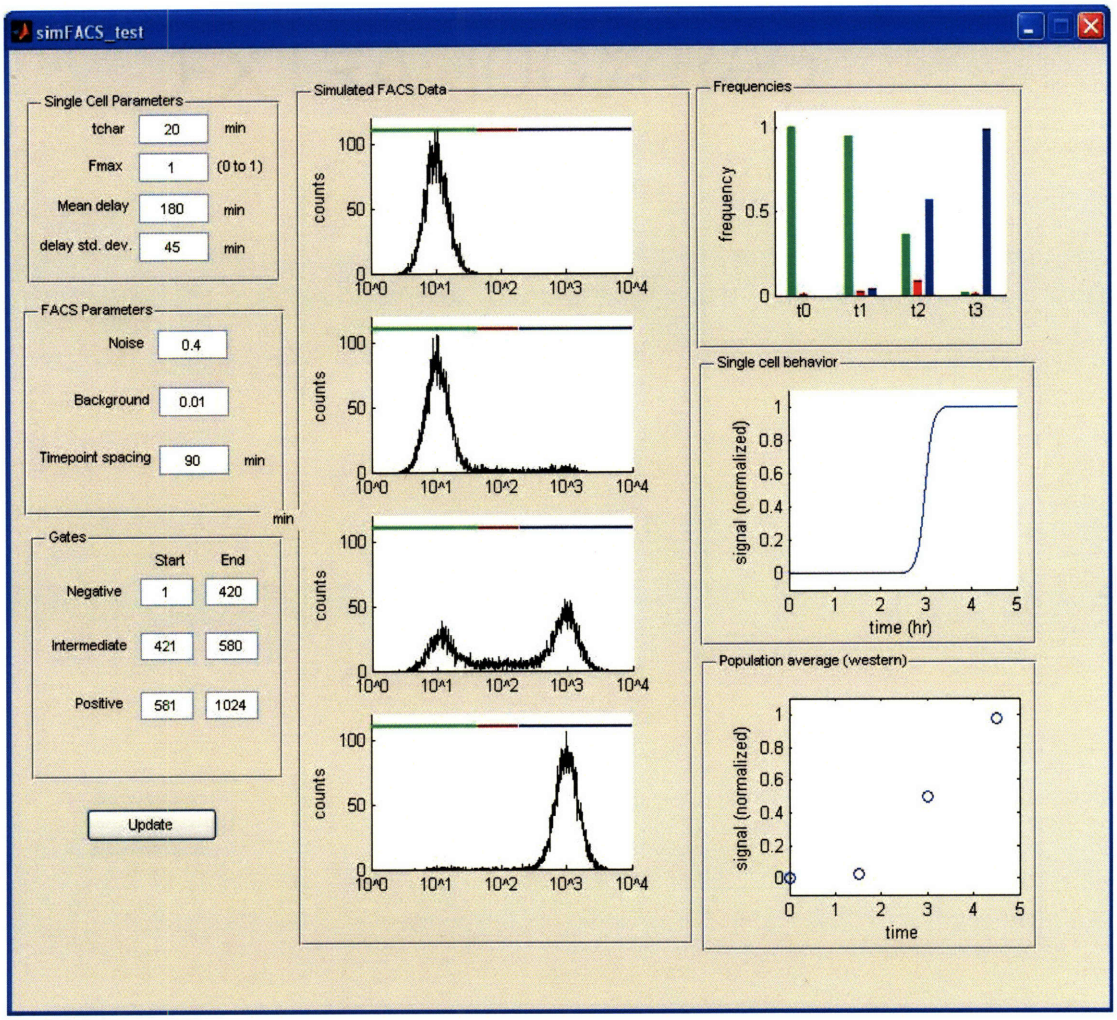

From these simulations, we can also produce the expected results of a western blot time course experiment. Since a western blot of PARP cleavage represents the average fraction of PARP cleavage across the entire population, this type of data can be simulated by summing the raw signals of all cells at each time point and then dividing by the total number of cells to obtain the population average:

```
for t=0:numtimepoints
    for i=1:cells
        rawsignals(i,t)=(Fmax-(Fmax)/(1+exp((t*timespacing-
delays(i))/(tchar/4))));
    end
    popavg(t)=sum(rawsignals)/cells;

end
```

Note that the population average does not contain all of the information that is present in flow cytometry data. For example, the population average data resulting from cells in which tchar is 20 minutes is nearly identical to poplation average data from cells with a tchar of 100 minutes. Moreover, partial cleavage of PARP at the single cell level in the entire population cannot be distinguished from complete cleavage at the single cell level in only some of the population. For example, consider the two cases below. In the first case, Fmax is 0.2, and thus 20% of PARP is cleaved in each cell, resulting in a population average of 20% PARP cleavage. In the second case, Fmax is 1.0, but due to the broad distribution of delay times centered at x hours, only ~20% of the cells have responded at 4.5 hours. Therefore, the population average PARP cleavage is again 20%, even though the situation at the single-cell level is entirely different.

Many more examples like this may be found by simply exploring the simulated behavior of flow cytometry and western blot data using the graphical interface, underscoring the need for examining both population average and single-cell data to correctly assess the behavior of PARP cleavage in the cell. The Matlab tool presented here may be a useful resource for those examining the relationship of flow cytometry, single-cell, and population data.